

# Luminous, High Redshift, Obscured Galaxies and their Environments

Jordan I. Penney

A thesis presented for the degree of  
Doctor of Philosophy



X-ray & Observational Astronomy Group

School of Physics and Astronomy

University of Leicester

UK

March 2020

# Luminous, High Redshift, Obscured Galaxies and their Environments

Jordan I. Penney

## Abstract

This thesis presents observations of dusty, luminous, high redshift galaxies using mid Infra-Red and radio observations of samples of galaxies uncovered using the Wide-Field Infra-Red Survey Explorer (WISE) All-Sky Mission. Observations of these galaxies are critical to understanding the evolution of galaxies during the epoch of the peak in mergers and star formation activity. Two samples of galaxies are investigated in Chapter 3 and Chapter 4.

The galaxies in Chapter 3 were selected using the WISE-All Sky mission, with additional constraints at 1.4 GHz (21 cm) to select for radio-intermediate emission. These galaxies are expected to have radio jets still embedded in their galactic hosts, and the sample within this thesis resides between redshifts of  $1.3 < z < 2.9$ . To understand the nature of the environments that these powerful, luminous galaxies inhabit, the possibility of mergers between nearby galaxies is estimated using mid Infra-Red *Spitzer* observations over square  $5.12' \times 5.12'$  fields.

The galaxies in Chapter 4 were also discovered using the WISE-All Sky mission, but with no constraints on their radio power. These galaxies are among the most luminous known, with Infra-Red luminosities in excess of  $10^{14} L_{\odot}$ , placing them in the HyLIRG regime. These luminous, dusty galaxies are expected to contain extremely powerful AGN in their centres, heating the surrounding dust to temperatures  $\gtrsim 60$  K. Using  $\sim 30$  GHz observations of a sample of these galaxies, estimates of their radio properties can be determined to understand the level of free-free and synchrotron emission, and the rates of star formation in the galaxy hosts.

# Declaration

I hereby declare that no part of this thesis has been previously submitted to this or any other University as part of the requirement for a higher degree. The work herein was conducted by the undersigned except for contributions as acknowledged in the text.

Jordan I. Penney

# Acknowledgements

First and foremost, I would like to thank my partner, Maria for being a constant inspiration, a source of emotional support and safety without whom I can not imagine how I would have survived the last few years. Second, to my loving and insane family for being there whenever I have needed you, and sometimes when I haven't. Thanks to my Dad for always being the inspiration, the one who was that wall to bounce ideas off even when neither of us knew what was going on, and thanks to Mum, for being there and helping in things great and small.

I want to thank all of the staff and my fellow PhD students, especially Sarah Gibson for the constant help with Python, sorry once again! Thank you to Adam, Roger and Sam, the people I started my time at Leicester with all those years ago. Thanks to Claudia, for making 2<sup>nd</sup> Year Labs bearable. And thank you to Emily and Rob, for a sanity check in the last few months. I should thank my supervisor, Prof. Andrew Blain; without him the PhD would never have happened. Thanks also to Prof. Nial Tanvir, for kindly looking through this thesis.

Thank you to everyone at the University of Leicester Karate Club for making the last 8 years of training the most amazing experience I could have hoped for. To Nathan, Nikol and Zac for being great training partners inside and out of the dojo, and to Sensei Rick for being equal parts terrifying and inspirational.

To Eddie, the dog who found his way onto every one of my presentations, whether I wanted him there or not, the true hero of my PhD. Finally, to everyone I've lost and found along the way at my time of Leicester, be it friends or loved ones, you are in my heart and mind always.

# Contents

<b>1</b>	<b>Introduction</b>	<b>1</b>
1.1	Overview and Motivation . . . . .	1
1.2	Diversity of Galaxies . . . . .	2
1.3	Active Galactic Nuclei . . . . .	4
1.3.1	Types of AGN . . . . .	5
1.4	Evolution of Galaxies . . . . .	9
1.4.1	Major Mergers . . . . .	9
1.4.2	Minor Mergers and Galaxy Interactions . . . . .	12
1.5	Clusters of Galaxies . . . . .	13
1.6	Infra-Red Observations . . . . .	16
1.6.1	IR Selected Dust Obscured Galaxies . . . . .	17

1.7	Sub-Millimeter Observations . . . . .	20
1.8	Radio Observations . . . . .	23
1.8.1	Radio Continuum Observations . . . . .	25
1.8.2	Radio Line Spectra . . . . .	27
1.9	Structure of Thesis . . . . .	28
<b>2</b>	<b>Instrumentation</b>	<b>29</b>
2.1	Spitzer . . . . .	29
2.2	WISE . . . . .	34
2.3	JWST . . . . .	38
2.4	Herschel . . . . .	39
2.5	JCMT SCUBA-2 . . . . .	41
2.6	VLA . . . . .	42
2.6.1	JVLA . . . . .	42
2.6.2	NVSS . . . . .	46
2.6.3	FIRST . . . . .	46
2.7	ALMA . . . . .	47

<b>3</b>	<b>The Environments of Luminous Radio-WISE selected Infrared Galaxies</b>	<b>49</b>
3.1	Introduction . . . . .	50
3.2	<i>Spitzer</i> Observations . . . . .	54
3.2.1	Data Reduction . . . . .	54
3.2.2	Source Extraction . . . . .	56
3.2.3	Completeness Limits . . . . .	58
3.3	Properties of Radio-WISE Galaxies . . . . .	60
3.4	Object Selection Criteria . . . . .	64
3.4.1	SpUDS and S-COSMOS Comparison Fields . . . . .	66
3.4.2	Photometric Redshifts . . . . .	68
3.5	Results . . . . .	72
3.5.1	Group-I Selected <i>Spitzer</i> Galaxies . . . . .	72
3.5.2	Group-II <i>Spitzer</i> -Selected Galaxies . . . . .	78
3.6	Angular Auto-Correlation Function . . . . .	86
3.7	Discussion . . . . .	91

3.7.1	Overdensity of Galaxies in Radio-WISE Selected Fields . . . . .	92
3.7.2	Radial Distribution . . . . .	93
3.8	Summary . . . . .	96
<b>4</b>	<b>JVLA Observations of Cold Gas around Hot DOGs</b>	<b>99</b>
4.1	Introduction . . . . .	99
4.2	Observations and Data Reduction . . . . .	103
4.3	Observational Results . . . . .	105
4.3.1	CO(1–0) Luminosity . . . . .	109
4.3.2	30-GHz Continuum . . . . .	114
4.3.3	Spectral Energy Distributions . . . . .	116
4.4	Discussion . . . . .	130
4.4.1	30-GHz Emission from Hot DOGs . . . . .	130
4.4.2	FIR-Radio Correlation . . . . .	131
4.5	Summary . . . . .	138
<b>5</b>	<b>Conclusions and Future Prospects</b>	<b>141</b>

## CONTENTS

---

A Abbreviations	145
B Properties of <i>Spitzer</i> -observed Radio-WISE Selected Galaxies	150

# List of Figures

1.1	Hubble Sequence . . . . .	3
1.2	Unified AGN Model . . . . .	6
1.3	Star Formation and AGN Accretion Rate with respect to Redshift . . .	12
1.4	Galaxy Lensing . . . . .	15
1.5	IRAC Colour vs. Redshift . . . . .	18
1.6	Radio-WISE Galaxy WISE Colour Selection . . . . .	21
1.7	Negative K-Correction . . . . .	23
1.8	Radio Interferometer Fourier Transform . . . . .	25
2.1	Spitzer Telescope . . . . .	31
2.2	SERVS IRAC Colour vs. Photometric Redshift . . . . .	32
2.3	Sensitivity of WISE, <i>Spitzer</i> , Herschel and JWST . . . . .	33

## LIST OF FIGURES

---

2.4	WISE Telescope Schematic . . . . .	35
2.5	WISE and cold- <i>Spitzer</i> IRAC bands . . . . .	37
2.6	Sensitivity of ALMA, JVLA and SKA . . . . .	43
2.7	JVLA Layout . . . . .	44
3.1	MOPEX Drizzle Image . . . . .	55
3.2	Matching Radius Distribution . . . . .	57
3.3	Radio-WISE Field Simulated Completeness . . . . .	59
3.4	Radio-WISE Field Completeness . . . . .	59
3.5	IRAC Properties of Hot DOGs and Radio-WISE Galaxies . . . . .	62
3.6	WISE Properties of Hot DOGs and Radio-WISE Galaxies . . . . .	63
3.7	Example Radio-WISE Selected Field . . . . .	65
3.8	Radio-WISE Galaxies and Centered Comparison Fields . . . . .	67
3.9	Group-I Field Density Comparison . . . . .	67
3.10	Photometric Redshift Distribution of Group-I Galaxies . . . . .	69
3.11	Radio-WISE Magnitude-Density Comparison . . . . .	73
3.12	Radio-WISE Group-I Density Per Field . . . . .	74

## LIST OF FIGURES

---

3.13	Radio-WISE Group-I Radial Profile . . . . .	75
3.14	Radio-WISE Inner 0.25' Comparison . . . . .	76
3.15	Radio-WISE Colour-Density Comparison . . . . .	77
3.16	Radio-WISE Reddening Calculation . . . . .	79
3.17	Group-II Comparison Field Contrast . . . . .	80
3.18	Radio-WISE Group-II Density per Field Comparison . . . . .	81
3.19	Radio-WISE Group-II Radial Profile . . . . .	83
3.20	Radio-WISE Field Density Comparison . . . . .	85
3.21	Radio-WISE Auto-Correlation Function . . . . .	88
3.22	Radio-WISE Assef et al. (2010) Radial Distribution Comparison . . . . .	92
4.1	Poor W1322 Image . . . . .	104
4.2	Hot DOG $\sim$ 30 GHz Spectra . . . . .	106
4.3	Hot DOG Emission Centred JVLA Images . . . . .	107
4.4	Hot DOG Velocity Fields . . . . .	108
4.5	$L_{\text{CO}(1-0)}$ properties of Hot DOGs . . . . .	112
4.6	Hot DOG JVLA Continuum Images . . . . .	115

## LIST OF FIGURES

---

4.7	Hot DOG Single Broken Power-law SEDs . . . . .	117
4.8	Hot DOG Corner Plot Single Broken Power-law . . . . .	120
4.9	Hot DOG Double Broken Power-law SEDs . . . . .	122
4.10	Hot DOG Double Broken SED Corner Plot . . . . .	123
4.11	Hot DOG Blackbody SEDs . . . . .	125
4.12	Hot DOG Blackbody SED Corner Plot . . . . .	126
4.13	Hot DOG FIRST Cutouts . . . . .	132
4.14	Stacked FIRST Images of Hot DOGs . . . . .	135
4.15	$q_{\text{IR}}$ Comparison with Different Galaxy Types . . . . .	137
4.16	$q_{\text{IR}}$ Comparison Hot DOGs vs. Radio-WISE Galaxies . . . . .	139

# List of Tables

2.1	<i>Spitzer</i> Bands and Bandwidths . . . . .	30
2.2	WISE Wavelengths and Bandwidths . . . . .	36
2.3	WISE Conversion Factors . . . . .	38
2.4	Herschel Instruments and Bands . . . . .	40
2.5	JVLA Bands and Frequencies . . . . .	45
2.6	ALMA Bands, Wavelengths and Frequencies . . . . .	48
3.1	Radio-WISE ISAAC Field Detections . . . . .	71
4.1	JVLA-Selected Hot DOG Properties . . . . .	102
4.2	CO(1–0) Hot DOG Luminosity and H II mass . . . . .	113
4.3	$\chi^2$ values for SED fits . . . . .	127

**LIST OF TABLES**

---

4.4 Modified Blackbody Fit Parameters for Hot DOGs . . . . . 129

B.1 Radio-WISE Selected Galaxies and Mid-IR Properties . . . . . 151

# Chapter 1

## Introduction

### 1.1 Overview and Motivation

The focus of the research presented in this thesis is to understand the environments of high-redshift, luminous Infra-Red (IR) galaxies. To this end, the thesis presents follow-up observations of galaxies selected using the Wide Field Infra-red Survey Explorer (WISE; Wright et al., 2010) All-Sky Survey. Deeper measurements of some of the reddest-selected galaxies in this survey can be used to build an understanding of how these galaxies formed and what processes are occurring in their local environment. By doing so, one can determine the mechanisms producing these extremely luminous IR galaxies.

It is now believed that many local galaxies were formed at high-redshift via major mergers between galaxies (Toomre & Toomre, 1972; Toomre, 1977; Mihos & Hernquist, 1994; Somerville et al., 2001; Tacconi et al., 2008; Conselice, 2014). During these

mergers, gas from the progenitor galaxies is distorted via tidal torques and shocked (Hernquist, 1989), forming bars and spiralling into the central regions of the galaxy as it loses angular momentum (Hernquist, 1989; Barnes & Hernquist, 1996; Hopkins et al., 2008). Some of this gas is accreted onto the central Supermassive Black Hole (SMBH) of the newly formed galaxy, while some increases the star formation rate of the host galaxy (Elbaz & Cesarsky, 2003). Further, simulations of clusters of galaxies by Chiang et al. (2017) suggest that within the entire 10 – 20 Mpc of the simulated clusters of galaxies at  $1.5 < z < 5$  there appears to be an excess density of star-forming galaxies. To fully understand this period of rapid growth, observations of obscured, luminous galaxies in the IR and their environments are necessary. Through shallow, wide-field surveys and specific selection criteria, deeper follow-up observations can determine properties of these galaxies, such as star formation rates, galaxy masses, dust masses and temperatures. This thesis will constitute part of such a study.

## 1.2 Diversity of Galaxies

The diversity of observed galaxies has been well established since Edwin Hubble’s observations, which suggested a “Hubble Sequence” (Hubble, 1936), classifying galaxies into several morphological groups (see Fig. 1.1). These galaxies can be arranged into three morphological types; spiral galaxies with columns of stars, gas and dust in spirals emerging from central regions of the galaxy and a bulge towards the galactic centre, elliptical galaxies appearing as generally featureless orb-like structures of stars, and lenticular galaxies, which appear with a central bulge similar to spiral galaxies, albeit with no spiral structure and a simple disk of stars orbiting the central region. These galaxy classes have various subsets to define additional observed features (e.g. strength of ellipticity for elliptical galaxies), and can classify other galaxy types, such as irregu-

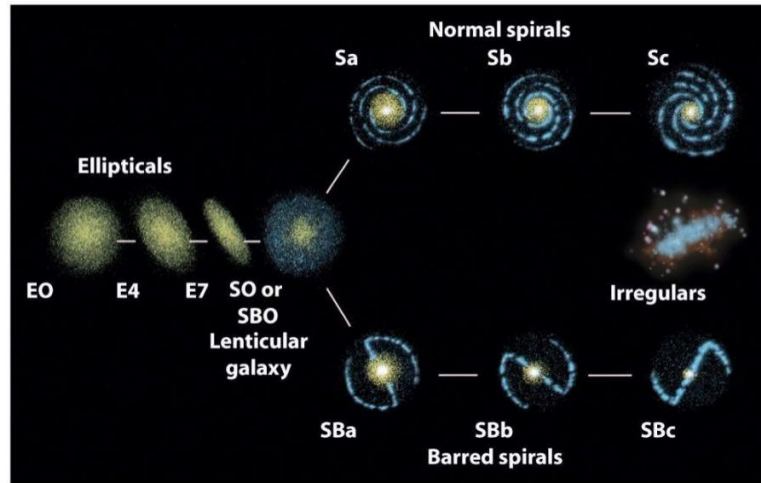


Figure 1.1: Figure shows the Hubble Sequence, a morphological classification system devised by Edwin Hubble in the 1920s to explain the observed difference between galaxies. The Hubble Sequence shows the transitions between different morphologies, suggesting galaxy evolution. Current theories of galaxy evolution have utilised galaxy merger theory and dark matter to understand the observed differences.

lar/peculiar galaxies, which have neither bars, spirals nor disks.

The different morphologies are expected to be produced via interactions with the environment or processes within the galaxies (Barnes & Hernquist, 1998). “Red and dead” galaxies, which have little ongoing star formation appear red from the emission of older stars. The lack of younger stellar emission is most likely produced via winds from the central SMBH, causing star forming gas to be expelled from the galaxy (Lynden-Bell, 1969), suppressing star formation. For many galaxies, therefore, the morphologies can be explained via the motion of gas and dust, such that understanding these properties at high-redshifts is useful in determining how galaxies formed.

### 1.3 Active Galactic Nuclei

Some of the first observations of Active Galactic Nuclei (AGN) were made using spectroscopic observations which revealed emission lines from NGC 1068 and Messier 81 by Edward Fath in 1909 (Fath, 1909). Instead of a continuous spectrum of stellar absorption lines, these objects showed composite spectra of bright absorption and emission lines, and later work showed that these emission lines were spread across a wide range of frequencies (Slipher, 1917). In 1943, Carl Seyfert discussed broad emission lines emanating from the nuclei of several spiral galaxies, and galaxies with these emission lines are commonly known as Seyfert Galaxies (Seyfert, 1943). Over the following decades, further types of AGN were discovered, all unusually compact and extremely bright but with faint or no host emission. Analysing these objects at various different wavelengths produce Spectral Energy Distributions (SEDs) of the central regions of the galaxies, which showed broad and narrow emission lines, suggesting that these AGN were extremely powerful objects.

Accretion of matter onto a central SMBH has been used to explain the feeding mechanism for AGN (Salpeter, 1964) and a paper published by Lynden-Bell (1969) showed that accretion onto the SMBH was the source of non-stellar emission in Seyfert galaxies (see Section 1.3.1). Accretion onto the central SMBH has long been argued to be the most efficient method to transport energy onto these compact objects and convert it to radiation. The Eddington Limit (see Eqn. 1.1), calculated by equating the radiation pressure with the gravitational attraction from a massive body, shows the output from accretion onto a black hole has an extremely large maximum energy. This is in general agreement with estimates of AGN, suggesting that accretion onto a SMBH is the main mechanism by which AGN are powered. With matter-energy conversion efficiencies of

$\epsilon \lesssim 40\%$ , compared with an efficiency of  $\epsilon \sim 0.7\%$  for stars, this shows that accretion onto a black hole is the most efficient process for emitting energy from matter.

$$L_{Edd} = \frac{4\pi GMm_p c}{\sigma_T} \quad (1.1)$$

where  $L_{Edd}$  is the Eddington luminosity,  $M$  is the mass of the central black hole,  $m_p$  is the mass of the proton and  $\sigma_T$  is the Thomson scattering cross-section.  $G$  and  $c$  are the gravitational constant and speed of light respectively. Typically, the value of the Eddington luminosity is between  $1 \times 10^{40} < L_{Edd} < 1 \times 10^{45}$  W, and requires  $> 1 \times 10^{24}$  kg of matter to produce this luminosity.

### 1.3.1 Types of AGN

In the following section, I briefly discuss the different types of AGN and how they are classified. The differences are observed at a wide range of frequencies, in which the central AGN will vary with luminosity. Models have been used to explain the observed difference between the variety of AGNs. Urry & Padovani (1995) suggests that the main difference between Type 1 and Type 2 AGN is the orientation of the obscuring torus with respect to the observer (Kellermann et al., 1989), shown in Fig. 1.2. This is expected to produce the observed broad and narrow line emission observed at optical and UV wavelengths in Type 1 AGN, whereby the central nucleus is visible, while only faint, narrow line emission is observed from Type 2 AGN. In the instance of Type 2 AGN, the broad line emission is blocked by the obscuring torus (see Netzer, 2013, for a complete review), and the faint, narrow line emission is from narrow-line emitting clouds. The model shown in Fig. 1.2 does not explain the differences between all

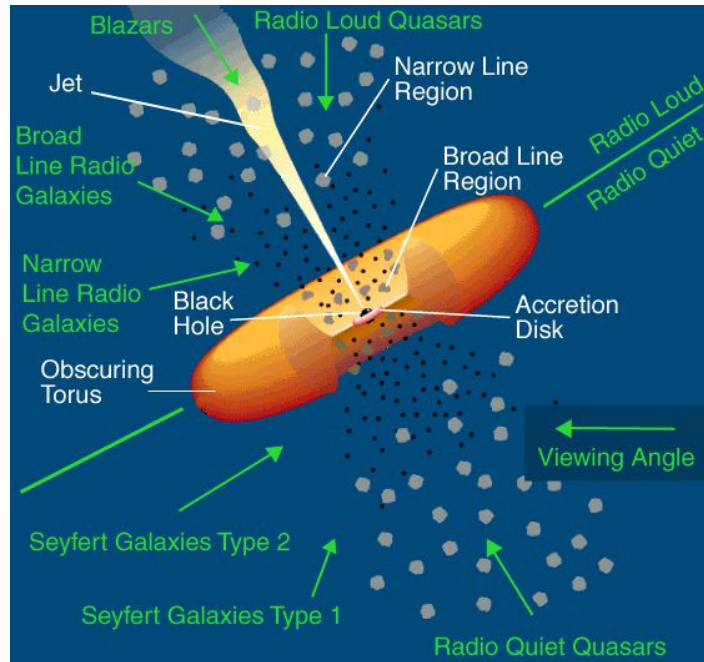


Figure 1.2: Figure from Urry & Padovani (1995) illustrating the unified model of AGN, whereby the viewing angle of the observer affects the observed characteristics of the AGN. The model shows (green arrows) the different viewing angle which could produce the observed AGN and (white arrow) the features produced by the AGN.

AGN, but suggests that all AGN have the same internal structure within the innermost nucleus.

Radio-Loud galaxies are generally split into three subclasses: Radio-Galaxies, Quasars and Blazars. Radio-Galaxies, as the name suggests, are galaxies with high radio luminosities ( $\gtrsim 10^{39}$  W; Fanaroff & Riley, 1974) between 10 MHz and 100 GHz. Radio emission is generally associated with synchrotron processes, such as those observed in radio-jets. This is caused by the acceleration of electrons and other charged particles by magnetic fields, causing them to emit radiation. Radio emission is generally observed from a pair of distinct jets emanating from the central regions of the galaxies, interacting with the Inter-Galactic Medium (IGM). Depending on the orientation of the jet with respect to the observer, one of the jets can appear much brighter than the

other jet. This is caused by an effect known as beaming (Blandford & Königl, 1979), in which the observed luminosity of jets of particles appears to be significantly brighter when moving close to the speed of light when the jet is inclined towards the observer. Compared to normal galaxies, which emit  $10^{-4}\%$  of their total luminosity at radio frequencies (Condon, 1992), radio-galaxies emit 0.1 to 10 times their optical flux in the radio. Emission lines in radio-galaxies are variable, such that they can have both broad and narrow line emission.

Quasars were first discovered in the 1950s as sources of intense radio emission from point-like objects (Matthews & Sandage, 1963; Schmidt, 1963), with optical counterparts known as Quasi-Stellar Objects (QSOs). Further higher resolution images centred on positions of known quasars showed that these objects were extremely compact, residing in the central regions of galaxies (Sanders et al., 1988a). These objects are defined by their broad emission lines in the Ultra-Violet (UV) (see Davidson & Netzer, 1979, for a review), have bright emission lines in the optical and have luminosities which are variable on timescales of hours to days, suggesting a compact accretion disk near to the source. Due to the bright emission from these AGN, high redshift quasars can be used as indicators of properties of the early universe at  $z \gtrsim 3$ , aiding in the understanding of the density of galaxies at these redshifts, and the manner in which galaxies formed (e.g. Madau et al., 1996; Fan et al., 2001; Mortlock et al., 2011).

Blazars are also extremely luminous objects, and generally show signs of relativistic beaming, suggesting that the central AGN jet axis is observed close to or directly on the line of sight (Urry & Padovani, 1995). High resolution imaging of these objects show that they reside within elliptical galaxies (e.g. Padovani & Giommi, 1995; Falomo & Ulrich, 2000), and have variations in both their spectra and observed output energy on short timescales of hours to days (Blandford & Rees, 1978). Unlike Quasars, these AGN do not generally display narrow line features and only weak broad line emission

(Blandford & Rees, 1978; Urry & Padovani, 1995). Blazars can be broken down into two sub-classes: BL Lacertae (BL Lac) and Flat-Spectrum Radio Quasars (FSRQs), which are thought to be, under the AGN Unification paradigm, low- and high-luminosity radio-galaxies (Sambruna, 1997; Willott et al., 2001).

First discovered by Carl Seyfert in 1944, Seyfert galaxies are one of the two largest groups of known active galaxies alongside Quasars. The AGN in these galaxies were first uncovered due to their broad emission lines in the cores of the host galaxies, producing a large stellar-like component in the central regions. While extremely luminous, like Quasars, Seyfert host galaxies are also clearly detectable, with variations in their brightness on timescales of days. Seyfert galaxies can be subdivided into two classes; Seyfert I galaxies include both broad ( $1 \times 10^3 \text{ km s}^{-1}$ ) and narrow line ( $\lesssim 1 \times 10^3 \text{ km s}^{-1}$ ) doppler-shifted components, and Seyfert II galaxies are expected to be obscured counterparts to Seyfert I galaxies, with an obscuring torus that blocks much of the broad line component from the centre of these galaxies from view (see Fig. 1.2). A key piece of evidence for the difference came from Antonucci & Miller (1985), which showed that the polarization spectra of the Seyfert II galaxy, NGC 1068, had similar broad line spectra to Seyfert I galaxies. This finding showed that some Seyfert II galaxies contained broad emission lines, albeit significantly reduced below the continuum, such that it could only be viewed in polarized light (Peterson & Wilkes, 2000).

The AGN Unification Model can be used to further sub-divide AGN classes, as shown in the case of Blazars. Low Ionisation Nuclear Emission-line Regions (LINERS; Heckman, 1980) generally resemble Seyfert II galaxies, albeit with strong O[I] and N[II] lines. These galaxies are one of the most common types of AGN, making up roughly a third of observed local galaxies. These AGN also reside within a wide range of galaxies; including Spiral, Lenticular and Ellipticals, although they appear to rarely reside within Irregular galaxies (Ho et al., 1997).

## 1.4 Evolution of Galaxies

Galaxies seem to evolve over billions of years; through stages of star formation, periods of varying AGN activity and interactions with nearby galaxies. Galaxies are expected to evolve through one of two methods; either passively, evolving into redder galaxies that appear isolated from other galaxies, or via mergers/interactions with other nearby galaxies. Evolution via mergers has been theorised to produce the disturbed Spiral galaxies and Ultra-Luminous IR Galaxies (ULIRGs) in the local universe (Toomre & Toomre, 1972), which has been evidenced by observations of trails of matter in opposite directions, and the chaotic positions and velocity distributions of gas and dust (Springel & Hernquist, 2005; Naab et al., 2006; Robertson et al., 2006; Cox et al., 2008; Khalatyan et al., 2008; Lotz et al., 2008). The arm-like features observed in Spiral galaxies are likely to be produced as dust and gas is displaced through the merger process, producing the younger stars compared to the bulge (Springel & Hernquist, 2005; Foyle et al., 2010). The theory of the assembly of galaxies via hierarchical growth through mergers has been observed in numerical models and simulations (Barnes & Hernquist, 1992, 1998; Hernquist, 1992, 1993), producing the observed elliptical galaxies at lower redshifts. The effect of merger events is discussed below.

### 1.4.1 Major Mergers

Major mergers are typically defined as collisions between two or more galaxies with similar luminosities (e.g. Barnes & Hernquist, 1992; Lambas et al., 2012a) and are believed to be the main method through which galaxies acquire gas and dust to accrete onto the central SMBH (Eggen et al., 1962; White & Rees, 1978) and form stars (Joseph &

Wright, 1985; Sanders & Mirabel, 1996; Evans et al., 2010; Hopkins et al., 2013). In the bottom-up theory of galaxy mergers, the initial perturbations of the matter density field would have collapsed via gravitational attraction to produce the first galaxies, before forming larger structures with other galaxies along the cosmic web via gravitational attraction (White & Rees, 1978). These mergers would have substantially changed the activity of the newly formed galaxy, including the star formation rate (Toomre & Toomre, 1972) and the activity of the central SMBH. By understanding these mergers, one can build a better understanding of the formation of galaxies observed in the local universe and the processes that produced observed ULIRGs at low redshifts ( $z < 1$ ) (Lonsdale et al., 2006; Tacconi et al., 2008).

Depending on the size of the central SMBH and the gas reservoirs in the constituent galaxies before the merger, the star formation and activity of the central AGN will, in the first instances, dramatically increase. These mergers initially lead to collisions of clouds of cold gas, condensing to produce star forming regions and establishing the starburst phase observed at redshifts  $2 < z < 3$  (Barnes & Hernquist, 1992). During this period, however, the quantity of matter accreted onto the central SMBH also increases, obscured by the increased levels of dust and gas within the newly formed galaxy. Eventually, the luminosity of the AGN comes to dominate the host galaxy, becoming obscured quasars (Stevens et al., 2003; Alexander & Hickox, 2012). The AGN then enters what has been coined the “Blowout” phase, wherein feedback mechanisms from winds of the central SMBH (Veilleux et al., 2005; King, 2003) will drive out gas, halting any further star formation. The AGN then becomes directly visible as the obscuring material is flushed from the surrounding environment, and the AGN becomes an optical quasar. Without further matter to accrete or form stars, the AGN and its host galaxy begin to fade in luminosity, passively evolving to the “Dead Elliptical” phase.

The host galaxy during a merger is also significantly affected, evidenced by the observed chaotic motion of gas, long tidal tails, and additional spectral components (Schweizer, 1982; van Dokkum, 2005; Tacconi et al., 2008; Bennert et al., 2008). During the stages of mergers, the most striking observational characteristic is the change in the morphology of the constituent galaxies. Indeed, initial simulations by Toomre (1977) show that spiral galaxies are converted into elliptical galaxies via mergers, transforming the gas-rich spirals into “red and dead” elliptical galaxies through rapid quenching of gas needed for star formation. The observed morphologies of local ellipticals are thought to have been formed from interactions and major mergers between galaxies earlier in their evolution (e.g. Toomre & Toomre, 1972; Farouki & Shapiro, 1982; Negroponte & White, 1983; Schweizer & Seitzer, 1998). During their earlier stages, merging galaxies produce far more complex morphologies (Hwang & Chang, 2009), with tails, additional nuclei, shells and dust lanes (e.g. Schweizer, 1982; Heckman et al., 1986; Smith et al., 1986), indicative of potential sites of major mergers or interactions between galaxies. Due to chance alignment of galaxies at different redshift, one cannot simply use radial profiles to determine the merger rates at different redshifts. Spectroscopic/photometric observations of potentially interacting pairs and simulations of galaxies are the main method by which major mergers can be understood (Lotz et al., 2008).

Evidence suggests that major mergers are linked to massive bursts of star formation in the newly formed galaxies through condensation of gas clouds from the progenitor galaxies (Larson, 2003). As previously stated, major mergers can increase the activity of the central AGN by funnelling gas onto the accretion disks on scales of  $\sim 1$  pc (Begelman, 2003), although it is not fully understood how the gas is driven down to these scales (Alexander & Hickox, 2012, and references therein). The link between AGN activity and star formation produced via major mergers has been shown in the overlap between the peak in AGN activity and the peak of star formation rates with respect

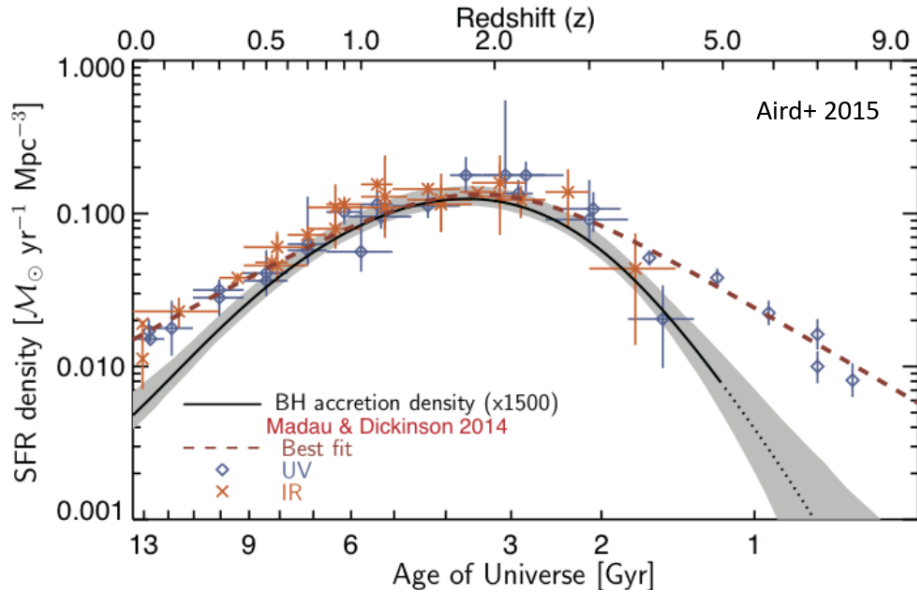


Figure 1.3: Figure from Aird et al. (2015) showing the relation between the Star Formation Rate (SFR) and SMBH accretion rate and the similar redshifts for the peak in star formation and activity of AGN ( $z \sim 2$ ), suggesting a link between the accretion modes of AGN and the SFR of the host galaxy.

to redshift, as shown in Fig. 1.3 (Silverman et al., 2008; Aird et al., 2010), wherein the peak of star formation is observed at  $z \sim 2 - 3$ , and the peak in AGN emission at  $z \sim 2 - 4$ . Thus, by understanding the growth in activity of AGN, it is possible to understand the rate at which galaxies have formed stars.

### 1.4.2 Minor Mergers and Galaxy Interactions

Minor mergers are the most common type of observed mergers, and are expected to be the most frequent type of merger at low-redshifts ( $z < 2$ ) in low-luminosity galaxies (Naab et al., 2009). Minor mergers are defined as those occurring between galaxies with luminosity ratios  $\Delta M > 1 : 3$  (as defined in Lambas et al., 2012a), where  $\Delta M$  is the difference in mass between the two merging galaxies, and it is expected that minor

mergers could be important in understanding the evolution of galaxies at  $z \lesssim 1$ . While minor mergers are more frequent, Lambas et al. (2012b) found that major mergers were more efficient at forming stars at  $z \sim 2$  and secular evolution is likely to dominate in the evolution of galaxies at low redshift (Kormendy & Kennicutt, 2004).

In this work, interactions are described as close encounters between two or more galaxies that do not produce a merger, and instead change the morphology or other quantity of the interacting galaxies. An example of these interactions would be “galaxy harassment” (Moore et al., 1996), in which high speed interactions at  $\text{km s}^{-1}$  scales can cause shocks between the interacting galaxies, disrupting the disks. Such interactions are most likely to occur within cluster and protocluster environments (see section 1.5), due to the dense nature of these regions (Dressler, 1980; Dressler et al., 1997; Treu et al., 2003; Smith et al., 2005; Postman et al., 2005; Park & Hwang, 2009). Thus, by understanding the effects of interactions between galaxies, one can statistically determine whether a galaxy resides within forming clusters (Hatch et al., 2014).

## 1.5 Clusters of Galaxies

Galaxy clusters are the largest gravitationally-bound structures in the known universe, with masses of  $M > 10^{15} M_{\odot}$  (Navarro et al., 1997, 2010; Geller et al., 2013; Hoekstra et al., 2013) and diameters of  $\lesssim 10 \text{ Mpc}^1$ . These structures were first discovered in the 18<sup>th</sup> century by Charles Messier and William Herschel (Messier, 1781). The clustering properties of galaxies were not properly understood until Hubble proved the size and scale of these structures (Hubble, 1925, 1926). The mass distribution of these galaxies was further investigated by Zwicky, who found that most of the mass did not appear to

---

<sup>1</sup>as defined by the virial radius

come from stars and other luminous objects, but from the coined term “dark matter” (Zwicky, 1933). Indeed, it is now understood that  $< 1\%$  of the mass in clusters of galaxies is constituted by stars,  $\sim 10\%$  of the mass is associated with the Intra-Cluster Medium (ICM) and  $90\%$  of the mass is from dark matter (Okabe et al., 2013). Estimates of the mass of the dark matter haloes have either come from the use of the Sunyaev-Zeldovich effect (SZ-effect; Sunyaev & Zeldovich, 1972) or weak gravitational lensing (see Smith et al., 2005; Bardeau et al., 2007), which can also be used to understand the effect of dark matter, where the dark matter is affecting the observed shape of background galaxies. Galaxy clusters can be used, therefore, to understand the nature of dark matter and how galaxies in the local universe have formed.

It is believed that clusters of galaxies are likely to have formed via gravitational collapse of the highest primordial peaks in the matter density field at high-redshifts (see Kravtsov & Borgani, 2012, and references therein), with external galaxies merging with the cluster in a state of hierarchical growth. Protoclusters are sites of forming clusters at  $z \gtrsim 1.5$  that are likely to form the clusters observed in the local universe (Venemans et al., 2007; Hatch et al., 2009, 2014), and their study can enhance the understanding of the structures observed today (e.g. Abell 2218, see Fig. 1.4). These clusters would be sites of high ICM temperatures, shown by the X-ray emission around the galaxies within these structures (see Overzier, 2016, for a review), produced by the infall of gas, heated by shocks as it enters the cluster (Gott & Gunn, 1971). Thus, understanding the environments of these extreme structures helps to understand the nature of how galaxies evolved within them to the present day.

Given that protoclusters are extremely large, filamentary structures, they can be exceedingly difficult to detect and catalogue. Large-scale simulations, therefore, have been used to understand the formation and processes within protoclusters. Kravtsov & Borgani (2012) simulate the change in the structure of the dark matter with redshift,



Figure 1.4: Figure illustrating the gravitation lensing effects by massive, foreground galaxies on more distant galaxies within the Abell cluster, producing observed skewed morphologies. (Source: NASA/Andrew Fruchter and the ERO Team [STScI])

showing that dark matter does not follow the expected spherically symmetric distribution, and appears to be filamentary in nature. Further work by Chiang et al. (2017) showed that protoclusters out to  $z = 5$  and 10 contributed to 20% and 50% of the cosmic star formation rate at these redshifts respectively, suggesting that these structures represented sites of rapid star formation in the early universe. Given the observational resolution required to determine these quantities, and the number of protoclusters required, these simulations are extremely important to understanding the star formation rate in the early universe.

It has been found that RLAGN are more likely to reside within protocluster environments (e.g. Wylezalek et al., 2013; Hatch et al., 2014) and it is suggested that the presence of a radio-jet from the RLAGN may be influenced by the protocluster in which the host galaxy resides. Given that  $\gtrsim 50\%$  of RLAGN are likely to preferentially reside within protocluster environments (Wylezalek et al., 2013; Castignani et al., 2014), these

AGN can be used to determine potential sites of protocluster environments. However, it is still not widely understood how the radio-jets are linked to the protocluster environment, and Hatch et al. (2014) suggests that the increased merger rate within these structures could be used to increase the spin of the central SMBH, previously linked to radio-jets (Pringle & King, 2003). Despite this, the power of the radio-jet does not appear to be linked to the density of the surrounding environment, suggesting that additional factors link the RLAGN to these protoclusters, and the presence of radio-loud galaxies does not specifically suggest that the galaxy resides within these structures.

## 1.6 Infra-Red Observations

IR observations cover the wavelength range  $0.75 \mu\text{m}$  to  $\sim 300 \mu\text{m}$  and, in extra-galactic astronomy, are sensitive to objects obscured by gas and dust, such as star forming regions of galaxies and obscured AGN. The Infra-Red Astronomical Satellite (IRAS; Neugebauer et al., 1984) produced the first images of the IR sky in the 1980s in four bands ( $12 \mu\text{m}$ ,  $25 \mu\text{m}$ ,  $60 \mu\text{m}$ , and  $100 \mu\text{m}$ ). The success of this mission led to the development of the IR Space Observatory, which ran between 1995 and 1998, and followed up on the findings of IRAS. In 2003, the *Spitzer* Space Telescope (henceforth *Spitzer*; Fazio et al., 2004) was launched with greater resolution and a wider field of view than previous satellites, capable of determining, with greater accuracy, large scale structures at high-redshift. *Spitzer*'s Infra-Red Array Camera (IRAC) used four bands in the near- to mid-IR ( $3.6 \mu\text{m}$ ,  $4.5 \mu\text{m}$ ,  $12 \mu\text{m}$ ,  $24 \mu\text{m}$  respectively) and, at the time of this thesis, is active with only the  $3.6 \mu\text{m}$  and  $4.5 \mu\text{m}$  (IRAC1 and IRAC2 respectively) bands still functional.

IR observations are utilised to identify dust and gas distributions that would go un-

detected in optical and UV surveys, and are sensitive to stellar populations, stellar emission and dust obscured galaxies (e.g. Dey et al., 2008; Rieke et al., 2009; Wu et al., 2014; Assef et al., 2015). Given that major galaxy mergers can drastically increase the dust obscuration of the post-merger galaxy, wide-field IR surveys (e.g. WISE; Wright et al., 2010) can reveal large populations of galaxies potentially in the stages of merging (e.g. Sanders et al., 1988a; Genzel et al., 2008). Follow-up observations in the IR can reveal more detailed information about the environments of these highly-obscured galaxies (e.g. Wu et al., 2014; Assef et al., 2015), and determine features lost in shallower surveys. K-band ( $2.2\ \mu\text{m}$ ) observations are sensitive to star formation and star forming regions (Calzetti et al., 2000), such that the stellar properties of distant galaxies can be estimated (Kodama & Bower, 2003). Using the redshifted  $1.6\ \mu\text{m}$  bump, a feature produced from the minimum opacity of the  $\text{H}^-$  ion in the atmospheres of cool stars (John, 1988), previous work has estimated minimum redshifts of distant galaxies using deep *Spitzer* observations (Papovich, 2008; Wylezalek et al., 2013; Penney et al., 2019). Using this feature available in the IR, the surface densities of distant, faint galaxy clusters and protoclusters around luminous, radio-selected galaxies could be estimated, as shown in Fig. 1.5. IR observations sensitive to stellar properties of distant galaxies can be used to understand the nature of galaxy evolution at high-redshift.

### 1.6.1 IR Selected Dust Obscured Galaxies

Previous work has shown that IR observations can be used to identify AGN (e.g. Sanders et al., 1988a; Lacy et al., 2005; Polletta et al., 2007; Stern et al., 2012), with all-sky surveys uncovering large quantities of high-redshift populations, such as the WISE mission (Wright et al., 2010). Using data from the WISE All-Sky Survey, Eisenhardt et al. (2012) selected galaxies that were bright in the W3 ( $12\ \mu\text{m}$ ) and W4 ( $22\ \mu\text{m}$ ) bands,

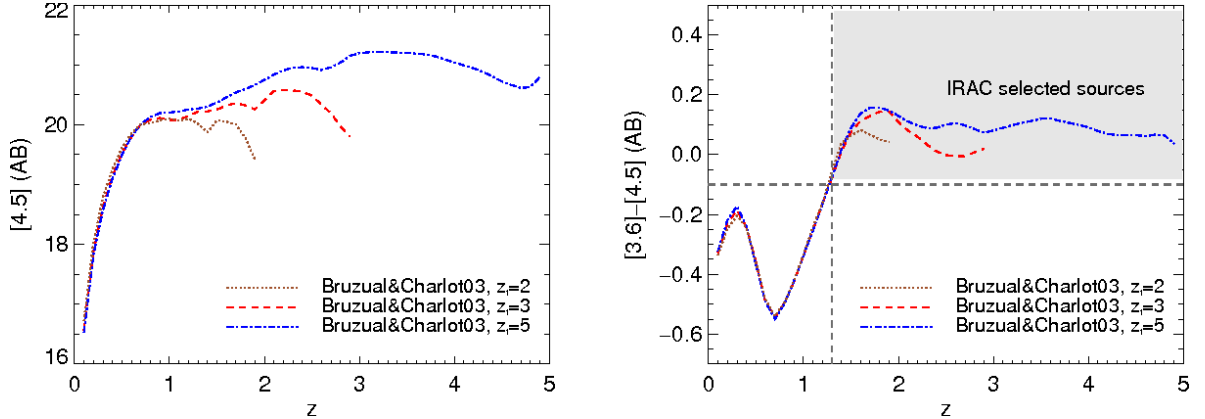


Figure 1.5: Left: IRAC2 ( $4.5 \mu\text{m}$ ) magnitude against expected redshift using models from Calzetti et al. (2000), assuming a Salpeter initial mass function, with a single decaying burst of star formation ( $\tau = 0.1 \text{ Gyr}$ ) and normalised to the observed  $m^*$  for galaxy clusters at  $z = 0.7$ . Right:  $[3.6]-[4.5]$  colour against redshift using the same models. This shows that there is a consistent redshift range of  $z > 1.5$  at  $[3.6]-[4.5] > -0.1$ , which can be used to select IRAC-selected galaxies within specific redshift ranges in the vicinity of brighter galaxies. Image taken from Wylezalek et al. (2013).

while faint/undetected in the W1 ( $3.5 \mu\text{m}$ ) and W2 ( $4.6 \mu\text{m}$ ) bands, as shown by the selection in Eqn. 1.2, with no specification on their radio activity. This selection uncovered a rare population of dust obscured galaxies, with surface densities of  $0.03 \text{ deg}^{-2}$ ,  $10^{-5}$  times less dense than the general density of WISE detected sources (Eisenhardt et al., 2012). Follow-up observations of subsets of this sample by Wu et al. (2012) showed that these galaxies had higher dust temperatures ( $60 - 120 \text{ K}$ ) than standard Dust Obscured Galaxies (DOGs; Dey et al., 2008) which used R-band and *Spitzer*  $24 \mu\text{m}$  selections ( $\frac{24 \mu\text{m}}{R} > 1000$ ), and were coined Hot Dust Obscured Galaxies (henceforth Hot DOGs). These Hot DOGs were extremely luminous in the IR, with a subset of these galaxies in Tsai et al. (2015) possessing bolometric luminosities  $> 10^{13} L_{\odot}$ , placing these galaxies in the ULIRG and HyLIRG regimes.

$$(W4 < 7.7 \cap W2 - W4 > 8.2) \cup (W3 < 10.6 \cap W2 - W3 > 5.3) \quad (1.2)$$

Follow-up work using *Spitzer* by Assef et al. (2015) found that these galaxies resided in regions with surface densities of IRAC-selected galaxies similar to Wylezalek et al. (2013) for RLAGN in potential protoclusters, using the IRAC-colour selection shown in Fig. 1.5. Further, 850  $\mu\text{m}$  observations using the Sub-millimetre Common-User Bolometer Array 2 (SCUBA-2; Holland et al., 1999) by Jones et al. (2014) for a subset of 10 Hot DOGs on 3' diameter fields found overdensities of SMGs  $\sim 3$  times greater than blank fields, suggesting that these galaxies inhabited regions significantly overdense in sub-millimeter selected galaxies. Given these overdensities and the extremely high IR-luminosities, it is likely that Hot DOGs are produced via major mergers. This has been further suggested from the multiple components determined by Eisenhardt et al. (2012) for W1814 in the  $g'$  (0.48  $\mu\text{m}$ ) and Ks (2.15  $\mu\text{m}$ ) bands. Hot DOGs could also be a link between SMGs and the optical quasar (QSO) population, seen during later evolutionary stages (Sanders et al., 1988a,b; Hopkins et al., 2006). There may be a link between these different populations related by their central AGN activity, star formation and environment (Sanders et al., 1988a,b; Bridge et al., 2013; Assef et al., 2015; Silva et al., 2015).

A sample of WISE selected galaxies with additional radio-selections was constructed by Lonsdale et al. (2015) using similar WISE selections to Hot DOGs, shown in Eqn. 1.3 with an additional radio criterion of  $-1 < \log\left(\frac{F_{22\mu\text{m}}}{F_{22\text{cm}}}\right) < 0$ , shown in Fig. 1.6. The selection ensured that these galaxies had compact radio-jets but reduced the effect of synchrotron emission on IR-sub-millimeter fluxes (Penney et al., 2019). SEDs from Lonsdale et al. (2015) showed that these galaxies had similar distributions to Hot DOGs, with near- to far-IR luminosity ratios consistent with a spectrum dominated by an obscured, luminous quasar. 870  $\mu\text{m}$  observations using the Atacama Long-baseline Millimeter/sub-millimeter Array (ALMA; Wootten & Thompson, 2009) of a sub-sample of 49 of these radio-WISE selected galaxies showed that these galaxies inhabited over-

dense regions of 870  $\mu\text{m}$ -selected SMGs,  $\sim 10$  times greater than blank fields on 10'' scales (Silva et al., 2015). Further, 850  $\mu\text{m}$  observations by Jones et al. (2015) found that these galaxies, like Hot DOGs, had bolometric luminosities of  $> 10^{13} L_{\odot}$ , with overdensities of 4 – 6 compared to blank fields on scales of 3' diameter fields. These observations were limited by the flux limits of SCUBA-2, the beam size of the detector and the size of the fields. Interestingly, no evidence was found by Jones et al. (2015) of angular clustering of SMGs on these scales, suggesting that the radio-WISE galaxies may not be interacting with the SMGs in these overdense environments.

$$(W2 - W3) + 1.25(W1 - W2) > 7 \tag{1.3}$$

## 1.7 Sub-Millimeter Observations

Sub-millimeter observations typically cover the wavelength (frequency) range of 100  $\mu\text{m}$  to 1 mm ( $\sim 300$  GHz to  $\sim 3$  THz). Ground based observations (e.g. ALMA and the Sub-millimeter Common-User Bolometer Array (SCUBA; Holland et al., 1999) on the James Clerk Maxwell Telescope (JCMT)) are affected by water vapour absorption in the air. This produces “windows” of observation for ground-based telescopes, limiting the telescopes to observe only through bandwidths less affected by absorption. To combat this, ground based telescopes are generally placed at higher altitudes, in drier climates to reduce the amount of atmospheric absorption, producing cleaner images. Recently, space-based sub-millimeter telescopes have become available (e.g. the *Herschel Space Telescope*; Pilbratt et al., 2010), which allows a deeper window into extra-galactic observations in the sub-millimeter. Sub-millimeter observations of galaxies are focused on dust and gas clouds around these distant objects, providing insight into the star

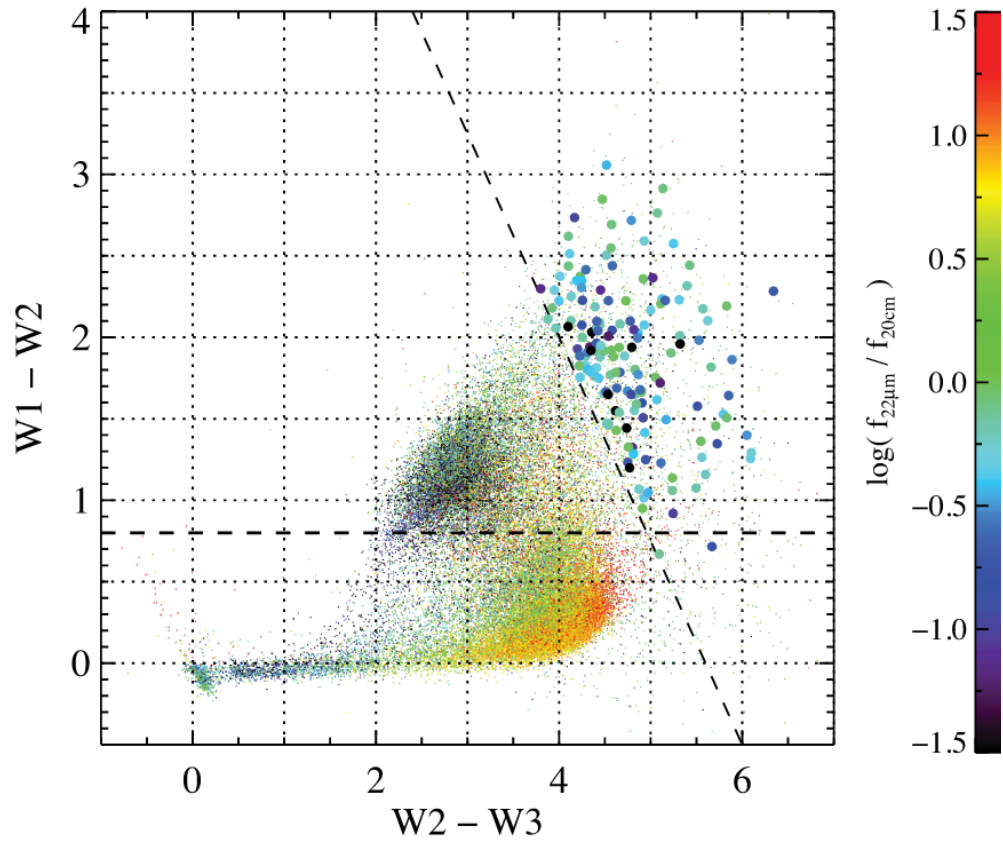


Figure 1.6: WISE colour selection for radio-WISE galaxies in Lonsdale et al. (2015). The horizontal line shows the AGN colour selection in Stern et al. (2012) for comparison with the newer selection made for the radio-WISE galaxies, shown by the diagonal-dashed line. Radio loudness is expressed by the color bar.

formation and obscured processes of galaxies.

Observations of high-redshift galaxies in the sub-millimeter have been used to understand the history of star formation with cosmic time, identifying the transitions between various phases in high-redshift galaxies. Sub-Millimeter Galaxies (SMGs) are a branch of dusty, star-forming galaxies that were luminous in the  $850\ \mu\text{m}$  that were previously undetected in optical and X-ray surveys due to their highly obscured nature (Blain et al., 2002, and references therein). These galaxies are of particular interest due to their peak density at the redshift of the height of star formation in the universe ( $z \sim 2$ ) (Chapman et al., 2002), and it has been suggested that these galaxies could contribute to half the total energy density throughout cosmic time (Casey et al., 2014, and references therein). For local galaxies, the  $850\ \mu\text{m}$  band lies on the Rayleigh-Jeans tail of the radio-sub-millimetre blackbody spectrum associated with cold dust, however for higher redshifts, the band is strongly affected by a negative K-correction (see Fig. 1.7), placing it higher up the blackbody spectrum of the galaxy. This allows  $850\ \mu\text{m}$  observations of SMGs to sample higher flux densities and are therefore perfect to observe at this rest-wavelength (Blain et al., 2002). SMGs have similar luminosities  $\gtrsim 10^{12} L_{\odot}$  to high-redshift quasars, suggesting that they are a dusty, obscured form of the high-redshift QSO, and could produce the elliptical galaxies observed at lower redshifts.

Previous sub-millimeter observations, both ground- and space-based, have been limited by the field of view and the size of the beam for measurements (Williams et al., 2011), making measurements of large- and small-scale structures around SMGs difficult. Future observations using interferometers (see Section 1.8) such as ALMA and the Sub-Millimeter Array (SMA; Ho et al., 2004) will have significantly improved beam-sizes compared to previous data, creating a unique opportunity to understand the processes within sub-millimeter selected galaxies. These facilities will be able to understand, in detail, emission from different dust clouds situated around and within merging galaxies,

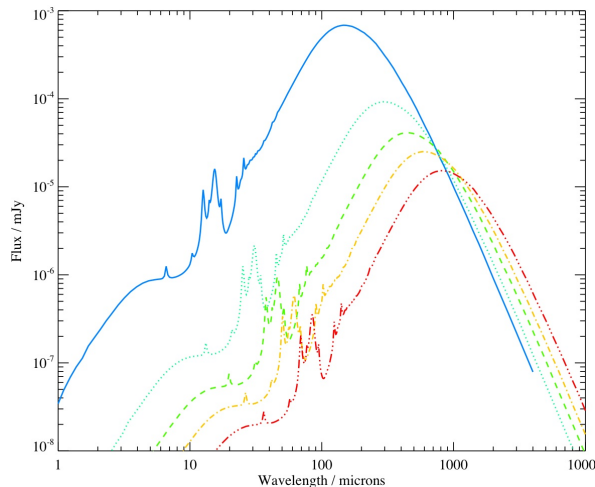


Figure 1.7: Illustration of the effect of negative K-correction, whereby higher redshift galaxies are moved to lower frequencies, which can limit the bands in which these galaxies are observed. The blue line shows a galaxy at  $z = 1$ , while the red dashed line shows a similar galaxy at  $z = 10$ . Image Credit: E. Stanway.

the effect on stellar evolution and the main components of emission.

## 1.8 Radio Observations

Radio observations typically cover the frequency range of  $\sim 1$  MHz to 100 GHz (tens of cm to several 100 m), in windows protected for the use of radio astronomy<sup>2</sup>. Ground-based radio telescopes are the main method by which radio astronomy is conducted, with the first detection of radio-waves from an astronomical object in 1932 by Karl G. Jansky, observing emission from the Milky Way (Jansky, 1933) at Bell Telephone Laboratories. Single-dish radio telescopes require extremely large radii to produce

<sup>2</sup>for more information <https://www.britastro.org/radio/spectrum.html>

similar resolutions as optical-to-IR telescopes, given the longer wavelengths observed:

$$\theta \approx \lambda/D \tag{1.4}$$

where  $\theta$  is the resolution of the telescope in radians,  $\lambda$  is the wavelength observed and  $D$  is the diameter of the aperture. This produced lower resolution for single-dish radio-telescopes for the same amount of observation time as optical-to-IR telescopes.

To combat this, a technique known as Radio Interferometry was developed in 1946 by Martin Ryle, Joseph Lade Pawsey and Ruby Payne-Scott, using multiple synchronous radio-telescopes to produce greater resolution and total signal. The signal between antennae in the interferometer is superimposed upon one another, producing interference patterns that boost/cancel the signal depending on the phase of the waves. The signal can be solved as a Fourier series, shown in Fig. 1.8, wherein the peaks and troughs can be approximated by a series of sinusoidal waves. A greater number of antennae increases the number of “baselines” (the separation between two antennae), increasing the number of waves to produce a better approximation of the signal in the system. Longer observations using interferometers ( $t \sim \text{hrs}$ ) increase the number of baselines available using the rotation of the Earth as an additional degree of freedom, whereby the rotation will change the position of the antennae relative to the observed radio-waves, and devices known as correlators are needed to take this into account. Modern interferometers include the Karl G. Jansky Very Large Array (JVLA) in Socorro, USA and ALMA in the Atacama Desert, Chile, observing at frequencies between 1 GHz and 50 GHz, and 30 GHz to 1000 GHz respectively.

While not pertinent to this thesis, for completeness, I briefly discuss Very Long Baseline Interferometry (VLBI) and space-based radio satellites. With the advent of improved radio-telescope receivers and accuracy in time measurement, data received from indi-

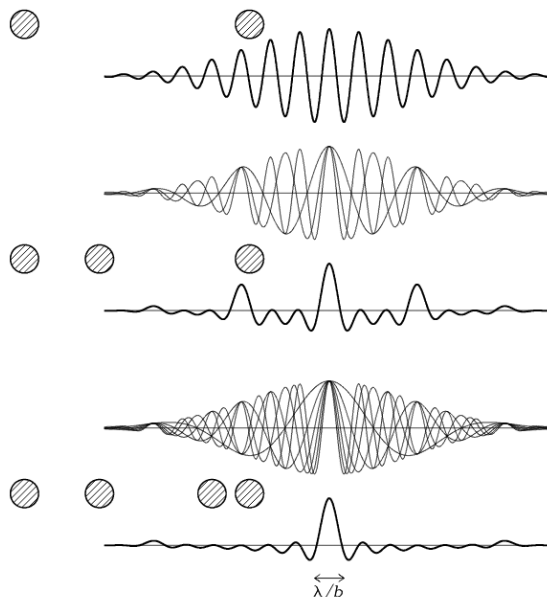


Figure 1.8: Illustration of the improved precision of determining peaks in a radio-interferometer survey using a greater number of radio-telescopes in a baseline.

vidual radio-telescopes across the globe could be correlated to produce extremely high resolution images of astronomical phenomena (e.g. imaging of an SMBH; Event Horizon Telescope Collaboration et al., 2019). There are only a few historical space-based radio satellites used for astronomy, such as the Spektr-R telescope, mainly due to the lack of atmospheric absorption of radio-waves, and space-based telescopes are mainly used to complement ground-based observatories.

### 1.8.1 Radio Continuum Observations

Radio continuum observations of high-redshift galaxies are sensitive to synchrotron and free-free emission from charged particles, depending upon the properties of the observed galaxy and the frequency of the observations. Typically, synchrotron emission is produced in astrophysical objects when charged particles are accelerated by a magnetic

field at right angles to the velocity of the particle. The acceleration of these particles causes them to produce radiation, as shown in the Larmor Formula (see Eqn. 1.5) and if the speeds of the accelerated particles are relativistic, the emitted radiation is known as synchrotron emission. Synchrotron emission is typically observed in Supernovae (henceforth SNe) and jets from AGN, wherein the charged particles interact with the contorted magnetic fields of these objects.

$$P = \frac{q^2 a^2}{6\pi\epsilon_0 c^3} \quad (1.5)$$

where  $P$  is the total power radiated by a single charged particle,  $q$  is the charge of the particle,  $a$  is the acceleration, and  $\epsilon_0$  is the vacuum permittivity.

Free-free emission is generally produced via Bremsstrahlung (“braking radiation”) processes, wherein a charge particle is decelerated as it passes near another charged particle (e.g. an electron is deflected by the presence of a nucleus). The deceleration causes a loss of kinetic energy:

$$E_k = \frac{1}{2} m_p v_p^2 \quad (1.6)$$

where  $E_k$  is the kinetic energy of the particle,  $m_p$  and  $v_p$  are the mass and velocity of the particle respectively. The kinetic energy can be equated to the energy of the radiation produced. Bremsstrahlung emission is typically observed from the ICM, observed in X-rays as electrons move through the hot plasma (e.g. Felten & Morrison, 1966; Sarazin & Kempner, 2000; Takizawa, 2002), and from emission of HII regions, where electrons are scattered from the hot plasma of the star forming clouds (Richards, 2000; Sarazin et al., 2001). Radio continuum observations therefore provide an insight into clusters

of galaxies and the star formation properties at high-redshift.

### 1.8.2 Radio Line Spectra

Emission lines can be useful tools to determine properties of distant galaxies, such as their age through redshifted line spectra, stellar mass and SMBH mass. Radio waves are less affected by the scattering of dust around galaxies, and therefore serve as a unique probe into the emission spectra of dusty molecular clouds, dust obscured galaxies and disks around AGN. While this implies that radio observations of galaxies can determine their star formation histories, the picture is complicated by the fact that the main tracer of star formation, the molecular form of HII, has strongly forbidden transitions, and can only be seen at temperatures of  $T > 100$  K.

To combat this, radio observations of the transitions of the second most abundant molecule in the universe,  $^{12}\text{CO}$  gas, have been used instead to understand the distribution, mass and velocity of star forming gas in galaxies, assuming that the  $^{12}\text{CO}$  gas traces the molecular HII gas (Solomon et al., 1997; Tacconi et al., 2008; Bolatto et al., 2013). The lowest transition of  $^{12}\text{CO}$  gas (i.e.  $\text{CO}(J=1-0)$ ) is expected to best trace the coldest molecular gas. Higher transitions (e.g.  $\text{CO}(J=2-1)$  and  $\text{CO}(J=3-2)$ ) are expected to trace warmer, more dense  $^{12}\text{CO}$  molecular gas, and therefore may not trace the bulk of the molecular HII gas. Previous work by Daddi et al. (2015), used ratios of the fluxes of higher transitions of the  $^{12}\text{CO}$  gas with respect to the lowest transitions to understand the connection between  $\text{CO}(J=5-4)$  and lower  $^{12}\text{CO}$  transitions for  $z = 1.5$  star-forming galaxies, building on previous work by Dannerbauer et al. (2009) and Aravena et al. (2014).  $^{12}\text{CO}$  transitions of high-redshift galaxies, therefore, provide a unique insight into the properties of the star forming gas within them.

## 1.9 Structure of Thesis

This thesis will examine the nature of high-redshift, luminous, dust obscured galaxies using radio and mid-IR observations. Using these observations, I attempt to understand the environments these galaxies resided in and what mechanisms might have produced these luminous IR galaxies at high-redshift. Samples from this thesis were selected using the WISE All-Sky Survey, with additional constraints from NVSS/FIRST, to select dusty objects that were luminous in the near- to mid-IR and this work uses follow-up surveys to provide further details at greater resolution or different frequencies than previously observed.

The next chapter discusses the instruments used to observe the galaxies presented in this thesis. I include information of publicly available archival data, used to build a more complete picture of the galaxies observed or to compare with other works.

Chapter 3 discusses the findings of warm-*Spitzer* follow-up observations of 33 Radio-WISE selected luminous IR, high-redshift galaxies. Chapter 4 discusses the results of 20 – 30 GHz JVLA observations of a sub-sample of 6 Hot DOGs. These chapters represent the science chapters of this thesis and are composed of the results from Penney et al. (2019) and Penney et al. (in prep). It should be noted that in Chapter 3, a cosmology of  $H_0 = 70 \text{ km s}^{-1} \text{ Mpc}^{-1}$ ,  $\Omega_m = 0.26$  and  $\Omega_\Lambda = 0.74$  is assumed. In Chapter 4, a cosmology of  $H_0 = 70 \text{ km s}^{-1} \text{ Mpc}^{-1}$ ,  $\Omega_m = 0.30$  and  $\Omega_\Lambda = 0.70$  is instead assumed.

Chapter 5 will discuss the results of the previous chapters and discuss the conclusions of this thesis.

# Chapter 2

## Instrumentation

This chapter describes the telescopes and instruments used in this thesis, including information on publicly available radio, infra-red and sub-millimeter surveys.

### 2.1 Spitzer

The Spitzer Space Telescope (henceforth *Spitzer*; Fazio et al., 2004) was launched in August 2003 and is, at the time of this thesis, still operational and follows a heliocentric, “Earth-trailing” orbit. Upon launch, *Spitzer* had three operational instruments on-board; the Infra-Red Array Camera (IRAC; Fazio et al., 2004), the Multi-band Imaging Photometer (MIPS; Rieke et al., 2004), and the Infra-Red Spectrograph (IRS; Houck et al., 2004). The bandwidths for the detectors on IRAC and MIPS can be found in Table 2.1 and the sensitivity, relative to other instruments, is shown in Fig. 2.3.

During the cryogenic mission (2003–2009) in which *Spitzer* utilized liquid helium to

## CHAPTER 2. INSTRUMENTATION

Instrument	Detector	Central Wavelength ( $\mu\text{m}$ )	Bandwidth ( $\mu\text{m}$ )
IRAC	IRAC1	3.58	0.750
	IRAC2	4.52	1.015
	IRAC3	5.72	1.425
	IRAC4	7.90	2.905
MIPS	MIPS24 $\mu\text{m}$	23.68	4.70
	MIPS70 $\mu\text{m}$	71.42	19.0
	MIPS160 $\mu\text{m}$	155.90	35.0

Table 2.1: The central wavelengths and bandwidths of the IRAC and MIPS on-board the *Spitzer* Space Telescope.

cool the detectors to  $\sim 5$  K, the IRAC modules used a  $256 \times 256$  pixel detector, with a Point Spread Function (PSF) Full-Width Half Maximum (FWHM) of  $1.66''$ ,  $1.72''$ ,  $1.88''$ ,  $1.98''$  for IRAC1, IRAC2, IRAC3 and IRAC4 respectively. These values were derived from in-flight measurements of bright stars. The IRS and MIPS detectors both utilized  $128 \times 128$  Si:As pixel detectors. The PSF of MIPS is difficult to determine given the multiple observing modes, and the types of distortion and colour terms associated with it. The IRS detectors have a PSF FWHM of  $3.8''$  and  $5.3''$  for the  $16 \mu\text{m}$  and  $22 \mu\text{m}$  detectors respectively.

Once *Spitzer* had exhausted its helium coolant, the telescope entered the “Warm Mission”, in which all of the detectors, except IRAC1 and IRAC2, were no longer operational, with the two remaining channels as functional without the cryogen as they were before the start of the Warm Mission. The new values for the PSF FWHM are  $1.95''$  and  $2.02''$  for IRAC1 and IRAC2 respectively, and were derived from a Gaussian fit of the profile of the PSF from the average of stars that were within 0.09 and 0.15 pixels from the centre in each channel. Both bands are still responsive and are currently used for scientific observations at the time of writing this thesis.

The main goal of the IRAC instrument was to study the early universe and the evolution



Figure 2.1: Left: Artist's impression of *Spitzer* Telescope, taken from <http://www.planetary.org/multimedia/space-images/charts/wise-telescope-design.html>. Right: Schematic illustrating main features of the *Spitzer* Telescope, showing the main housing and instruments. Image taken from <http://legacy.spitzer.caltech.edu/technology/overview.shtml>.

of galaxies at high redshift ( $z > 3$ ) (Fazio et al., 2004). The wavelength of IRAC1 ( $3.6 \mu\text{m}$ ) was selected to avoid water-ice absorption at  $3.1 \mu\text{m}$ . IRAC2 was initially selected at the beginning of *Spitzer*'s launch to optimize the required sensitivity and to allow for determination of photometric redshifts  $1 < z < 5$  (Simpson & Eisenhardt, 1999).

After the start of the warm *Spitzer* mission, IRAC1 and IRAC2 were useful to study galaxies within specific redshift ranges. As noted in Papovich (2008), a colour selection of  $[3.6] - [4.5] > -0.1$  can be used to select galaxies with redshifts consistent with  $z > 1.3$ . This is due to the relative placement of the  $1.6 \mu\text{m}$  bump in the emission from stellar populations (Simpson & Eisenhardt, 1999; Sawicki, 2002; van Dokkum & van der Marel, 2007), a feature which is not redshift nor galaxy-type dependent. This is further evidenced by the IRAC colour-vs.-redshift distribution in Fig. 1.5, and further work by Nyland et al. (2017), using warm-*Spitzer* observations of the SERVS field, showing the distribution of IRAC colour against photometric redshift in Fig. 2.2. This feature can

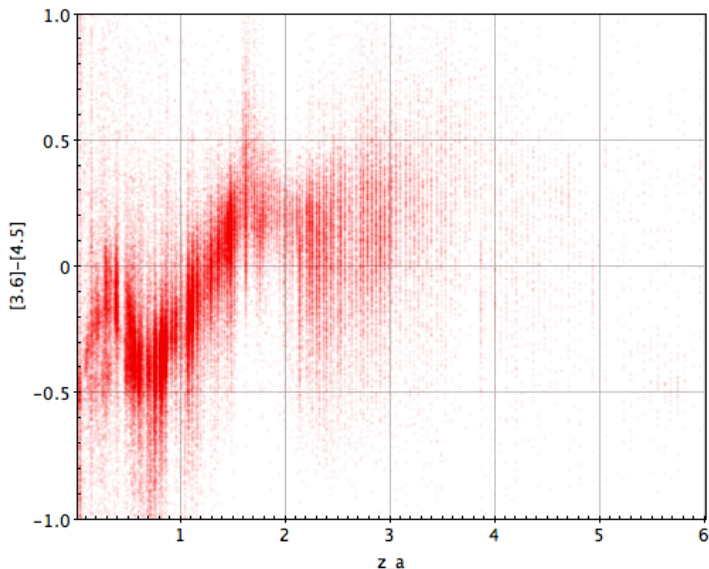


Figure 2.2: Illustrates the IRAC [3.6]-[4.5] colour against photometric redshift ( $z_a$ ) of sources selected in the SERVS field. The image shows that generally the sources selected at  $[3.6]-[4.5] > -0.1$  have redshifts  $z > 1.3$ . Image courtesy of M. Lacy.

be utilized to select populations of galaxies likely to be at consistent redshifts with the radio-WISE targets. Given *Spitzer*'s greater resolution than the Wide-Field Infrared Survey Explorer (WISE; Wright et al., 2010), deeper information can be gathered on the local environments of the radio-WISE selected galaxies in the mid-IR.

*Spitzer* public survey data is available through the Infra-Red Science Archive (IRSA) online service, which also curates public data for Herschel, Planck and other surveys. Comparison field data was taken using the IRSA service throughout the work on this thesis for S-COSMOS and SpUDS data (see Section 3.4.1), and the “basic” search in IRSA provides flux information in  $\mu\text{Jy}$ . The conversion between flux and magnitude is given by:

$$F_\nu = F_{\nu 0} \times 10^{\frac{-m_{\text{Vega}}}{2.5}}, \quad (2.1)$$

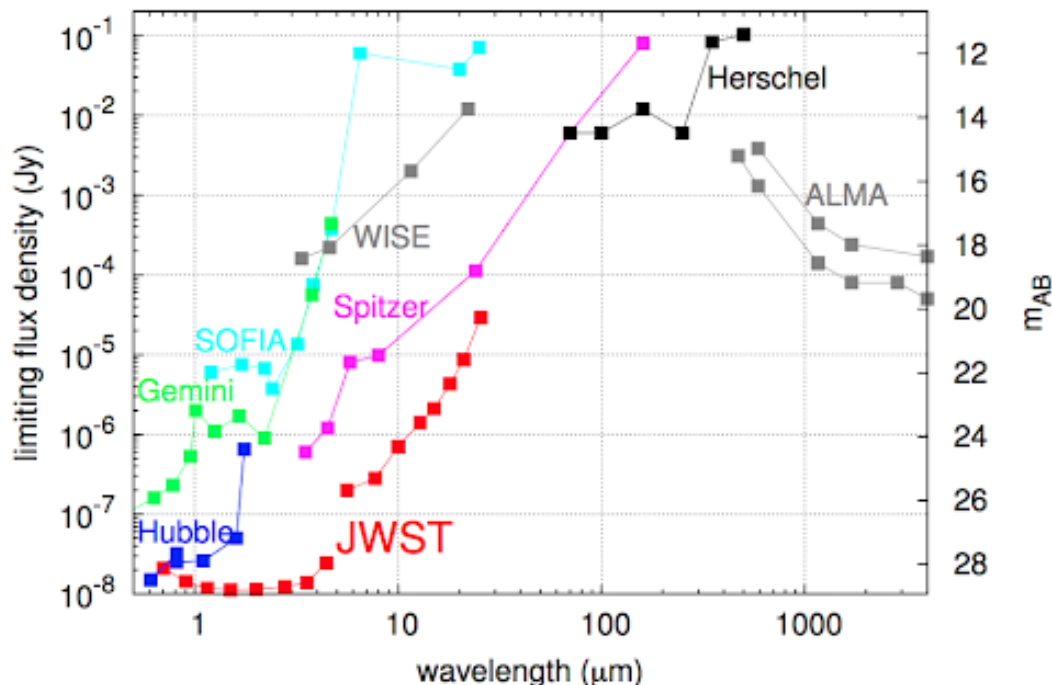


Figure 2.3: The flux limits for the *Spitzer* (magenta), WISE (grey), Herschel (black), and ALMA (grey) are shown with respect to the observed wavelength. JWST (red) and Hubble (blue) have been included for comparison. All flux densities have been computed for a  $10^4$  s observation time. Credit: NASA/STScI.

where  $F_\nu$  is the flux density in Jy,  $F_{\nu 0}$  is the zero-magnitude flux density and  $m_{\text{Vega}}$  is the Vega-system magnitude. For warm-*Spitzer* observations  $F_{\nu 0} = 280.9 \pm 4.1$  Jy for IRAC1 and  $F_{\nu 0} = 179.7 \pm 2.6$  Jy for IRAC2. The AB-to-Vega conversion factor for IRAC1 and IRAC2 are 2.79 and 3.26 respectively. Additional information regarding *Spitzer* data can be found in the IRAC Instrument Handbook<sup>1</sup>.

<sup>1</sup>[https://irsa.ipac.caltech.edu/data/SPITZER/docs/irac/iracinstrumenthandbook/IRAC\\_Instrument\\_Handbook.pdf](https://irsa.ipac.caltech.edu/data/SPITZER/docs/irac/iracinstrumenthandbook/IRAC_Instrument_Handbook.pdf)

## 2.2 WISE

The Wide-Field Infrared Survey Explorer (WISE; Wright et al., 2010) operates in four bands (W1, W2, W3, W4), which are sensitive to emission in  $3.4\ \mu\text{m}$ ,  $4.6\ \mu\text{m}$ ,  $12\ \mu\text{m}$  and  $22\ \mu\text{m}$  respectively. The telescope was launched in December 2009, before being put into hibernation in February 2011 and is placed in a Sun-synchronous orbit. It has since been re-activated as of September 2013 in the NEOWISE mission. The telescope observed the entire sky during the initial All-WISE survey, with a goal to study and uncover asteroids, brown dwarfs and the most luminous infrared galaxies in the universe.

The WISE telescope is 40 cm in diameter, with four million pixels split between each of the four detectors and a  $47' \times 47'$  field of view (FOV). The spacecraft has a length of 2.85 m, a height of 2 m, and breadth of 1.73 m, with a total payload weight of 347 kg. The reflected light from the mirrors which form the image inside of the telescope is passed through dichroic filters before reaching the four detectors, allowing the telescope to select wavelengths at  $3.4\ \mu\text{m}$ ,  $4.6\ \mu\text{m}$ ,  $12\ \mu\text{m}$  and  $22\ \mu\text{m}$ . For the W1, W2 and W3 bands, the angular resolution of the detectors is  $6''$ , while the W4 band has an angular resolution of  $12''$ . The entire telescope was cooled by a cryostat of frozen Hydrogen, cooling the main telescope to 8 K, the W3 and W4 detectors to 12 K and the W1 and W2 detectors to 32 K (Wright et al., 2010). To facilitate the different temperatures, the detectors are housed in two separate tanks, with the smallest housing the W3 and W4 detector arrays. The expected lifetime of this coolant was 10 months, and lasted between December 2009 and October 2010.

The detector response for each of the bands were determined in three ways (Wright et al., 2010); using a Fourier Transform Spectrometer (FTS) to measure the response of the entire system; using an FTS to measure the product of component data to estimate

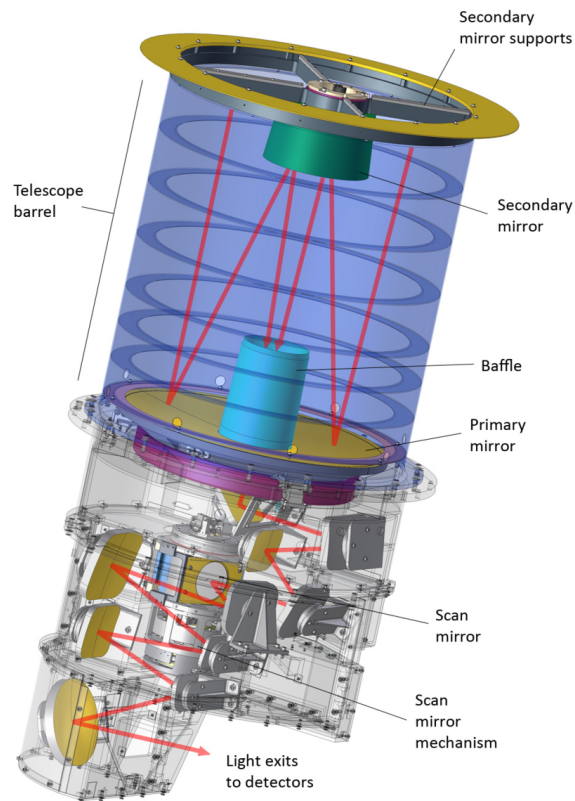


Figure 2.4: Schematic of the WISE telescope, illustrating the main setup of the telescope, the housing of the main instruments and the 40 cm diameter main mirror. See <http://www.planetary.org/multimedia/space-images/charts/wise-telescope-design.html> for further information.

the system response; and calculated from the designs of each component. For each detector array, the bandwidth and pixel Full-Width Half Maximum (FWHM) is shown in Table 2.2. The sensitivity for each of the WISE bands is shown in Fig. 2.3, showing that for all wavelengths WISE is less sensitive than *Spitzer*.

Instrument	Central Wavelength ( $\mu\text{m}$ )	Bandwidth ( $\mu\text{m}$ )
W1	3.35	0.66
W2	4.60	1.04
W3	11.56	5.51
W4	22.09	4.10

Table 2.2: The central wavelengths and bandwidths of the detectors on board the Wide-Field Infra-Red Survey Explorer Telescope.

The four WISE bands are sensitive to specific emission from various objects (Wright et al., 2010) and their wavelengths and bandwidths are shown in Fig. 2.5 alongside cold-*Spitzer* bands for reference. W1 is sensitive to stars and galaxies, W2 is sensitive to thermal radiation from internal processes of sub-stellar objects such as Brown Dwarfs, W3 is sensitive to thermal radiation from asteroids, and W4 is sensitive to dust in star forming galaxies, with temperatures between 70 – 100 K.

During its main observation run, WISE made several key discoveries about the Universe in the IR spectrum, such as discovering the most luminous galaxy in the universe (Tsai et al., 2015), determining the coolest classes of brown dwarfs (Kirkpatrick et al., 2012) and providing evidence for extremely luminous IR galaxies (ELIRGs) at a multitude of redshifts (Stern et al., 2012; Eisenhardt et al., 2012; Wu et al., 2012). WISE selections in the W2 and W3 bands were used to select Hot DOGs (see Chapter 4) based on their bright near-to-mid-IR emission. WISE selections in W1, W2 and W3 were utilized to select objects with significantly red IR colours for the radio-WISE selected galaxies (Lonsdale et al., 2015), shown in Chapter 3.

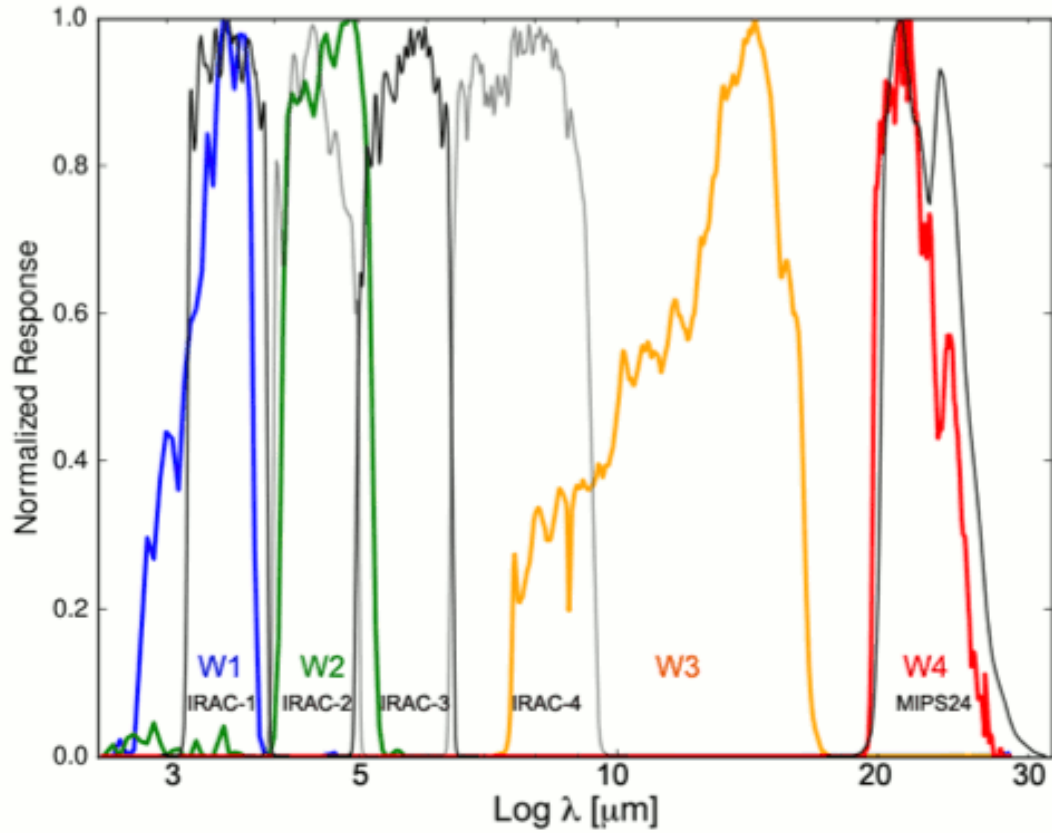


Figure 2.5: WISE bands, with W1 in blue, W2 in green, W3 in yellow and W4 in red. In grey for reference are the cold-*Spitzer* IRAC and initial MIPS bands. Image courtesy of the WISE All-Sky release (see: [http://wise2.ipac.caltech.edu/docs/release/allsky/expsup/sec4\\_4h.html](http://wise2.ipac.caltech.edu/docs/release/allsky/expsup/sec4_4h.html))

WISE Band	$F_{\nu 0}$	$C_{\text{AB-Vega}}$
W1	309.540	2.699
W2	171.787	3.339
W3	31.674	5.174
W4	8.363	6.620

Table 2.3: List of conversion factors for WISE bands.  $F_{\nu 0}$  shows the zero-magnitude flux and  $C_{\text{AB-Vega}}$  gives the conversion between AB and Vega magnitudes (where  $m_{\text{AB}} = m_{\text{Vega}} + C_{\text{AB-Vega}}$ ).

Similar to *Spitzer* public data, the All-Sky and other WISE data can be located on the IRSA website. The standard WISE search in IRSA will return fluxes in magnitudes in the Vega system, given by w1mpro, w2mpro, w3mpro and w4mpro for W1, W2, W3 and W4 respectively. Flux/magnitude conversions can be made using Eqn 2.1, where the zero-magnitude flux density and AB-to-Vega conversion factors ( $C_{\text{AB-Vega}}$ ) for each band is given in Table 2.3. Magnitudes and fluxes determined using w1mpro, w2mpro, etc. are calculated using a profile fit designed to determine the flux of the source based on the morphology on the detector. Fluxes can also be determined using the “Long Form” search in the IRSA website within several different aperture radii (5.5”, 8.25”, 11”, 13.75”, 16.5”, 19.25”, 22” and 24.75”) for W1, W2 and W3, and double each radius for W4.

## 2.3 JWST

Future IR observations will make use of the unprecedented resolution of the James Webb Space Telescope (JWST; Gardner et al., 2006), expected to launch in March 2021. The JWST will possess four instruments: the Near-IR Camera (NIRCam), the Near-IR Spectrograph (NIRSpec), the mid-IR Instrument (MIRI), and the Near IR Imager and Slitless Spectrograph (NIRISS). NIRCam will feature a  $2.2' \times 2.2'$  field of

view and will observe between  $0.6\ \mu\text{m}$  and  $5\ \mu\text{m}$ , looking from the edge of the optical spectrum to the near-IR. NIRSpec will operate at the same wavelengths as NIRCам, with a set of slits and an aperture to make spectroscopic measurements of distant galaxies within a  $3' \times 3'$  field of view. MIRI will function as a spectrograph and imager at wavelengths of  $4.6\ \mu\text{m}$  to  $28.6\ \mu\text{m}$  within fields of view of  $3.5'' \times 3.5''$  and  $74'' \times 116''$  for the spectrograph and imager respectively (McMurtry et al., 2005). NIRISS is a spectrograph that will operate between  $0.8\ \mu\text{m}$  and  $5.0\ \mu\text{m}$  within a  $2.2' \times 2.2'$  field of view. As shown in Fig. 2.3, JWST is more sensitive than both *Spitzer* and WISE for the observed wavelengths. The main goals of the JWST are to: search for the first light from stars and galaxies, study the formation and evolution of galaxies, studying the formation and evolution of the stars and other planetary systems, and the origins of life. With findings from the JWST, it is likely that further observations will be able to expand on the findings of this thesis.

## 2.4 Herschel

The Herschel Space Observatory (Herschel) was launched in 2009, and observed the far-IR and sub-millimeter between 2009 and April of 2013. Herschel was placed into an Earth-Sun orbit at the second Lagrangian point throughout its active lifespan. During its observation run, Herschel had four goals:

- Observing and understanding galaxy formation and evolution in the early universe.
- Investigating the impact of the ISM with star formation.
- Determining molecular chemistry across the universe.

Instrument	Central Wavelength ( $\mu\text{m}$ )	Wavelength Range ( $\mu\text{m}$ )
PACS	70/100	60–85/85–125
	160	125–210
SPIRE	250	210–290
	350	290–410
	500	410–590

Table 2.4: Instruments and bands on the Herschel Space Telescope. The table includes the two photometers on board the spacecraft, and the spectrometer, HIFI, has been excluded. The PACS lowest band runs simultaneously with the 160  $\mu\text{m}$  band, and the observed wavelength used in the lowest band is selected using a filter wheel.

- Investigating the chemical atmospheres of Solar System bodies, such as planets, moons and comets.

At the time of launch, Herschel had the largest single mirror used in a space telescope, with a diameter of 3.5 m, and the light from the mirror was directed onto three instruments with wavelengths observed between 55  $\mu\text{m}$  and 672  $\mu\text{m}$ . The Photo-detecting Array Camera and Spectrometer (PACS; Poglitsch et al., 2010), and Spectral and Photometric Imaging Receiver (SPIRE; Griffin et al., 2010), Heterodyne Instrument for the Far IR (HIFI; de Graauw et al., 2010) were cooled to  $T < 2\text{ K}$ . The only limit on the lifespan of the spacecraft was the temperature of the coolant. The wavelengths of the detectors on each of the instruments is shown in Table 2.4. The PACS photometer allows simultaneous observation in two bands, either at 70  $\mu\text{m}$  and 160  $\mu\text{m}$  or 100  $\mu\text{m}$  and 160  $\mu\text{m}$ , where the 70  $\mu\text{m}$  or 100  $\mu\text{m}$  bands are selected via a filter wheel (see Nielbock et al., 2013, for further information). The sensitivity for the instruments can be seen in Fig. 2.3.

Herschel PACS and SPIRE observations were made on subsets of Hot DOGs in Wu et al. (2012) and Tsai et al. (2015), and a small number of radio-WISE selected galaxies were observed in Lonsdale et al. (2015) to determine their photometric redshifts and sub-

millimeter properties. The observed fluxes can be used alongside other archive data to produce SEDs of Hot DOGs in conjunction with observations from work in this thesis to understand the nature of dust in obscured, high redshift galaxies.

## 2.5 JCMT SCUBA-2

SCUBA-2 is a ground-based, bolometer camera operating as part of the James Clerk Maxwell Telescope in Mauna Kea, Hawaii. SCUBA-2 was commissioned in 2011, replacing the previous SCUBA instrument, and is still operational at the time of writing this thesis. The detector consists of two bands operating at  $450\ \mu\text{m}$  and  $850\ \mu\text{m}$ , with an array of more than 10,000 pixels. The main beam size of the arrays are  $7.9''$  and  $13.0''$  at  $450\ \mu\text{m}$  and  $850\ \mu\text{m}$  respectively, and including extended emission the effective beam is  $9.8''$  and  $14.6''$  for  $450\ \mu\text{m}$  and  $850\ \mu\text{m}$  respectively (Dempsey et al., 2013).

Given the operating wavelengths, SCUBA-2 is most sensitive to cold gas and dust in the universe, and can therefore be used to trace clouds of star-forming gas in galaxies and detect highly obscured AGN. Observations of objects at high-redshift benefit from the negative K-correction, moving observed emission at these wavelengths to the peak of the SED, as shown in Fig. 1.7. Jones et al. (2014) observed a sample of 10 Hot DOGs using SCUBA-2  $850\ \mu\text{m}$  observations to determine the level of overdensity of SMGs within a radius of  $1.5'$  from the central Hot DOG, finding that, compared to blank fields, Hot DOGs inhabited environments  $\sim 3\times$  more dense. Work by Jones et al. (2015) using similar SCUBA-2  $850\ \mu\text{m}$  observations on a sample of 30 radio-WISE selected galaxies found that these galaxies inhabited fields of SMGs 4 – 6 times more dense than blank fields. In this thesis, I will be comparing to these findings.

## 2.6 VLA

The Very Large Array (VLA) is a ground-based interferometer consisting of twenty-seven 25 m wide radio telescopes arranged in a Y-shaped pattern. Each telescope is fixed to a railroad track, allowing the dishes to be moved into different arrays to allow for measurements at different frequencies and resolutions.

### 2.6.1 JVLA

Initially, the VLA started operations in 1972 and is located in New Mexico,  $\sim 80$  km West of Socorro. In 2011, after several years of upgrades, the VLA was upgraded to the Karl G. Jansky Very Large Array, or the Expanded Very Large Array (JVLA; Perley et al., 2011). With this upgrade, the JVLA is able to reach to greater sensitivities than the VLA, with  $1\sigma$  continuum sensitivities of  $1 \mu\text{Jy}$  compared to  $10 \mu\text{Jy}$  for a 12 hr observation time in the K (18 – 26.5 GHz) and Ka (26.5 – 40 GHz) bands using the VLA (see Napier, 2006). Further, the maximum bandwidth at each polarization was increased from 0.1 GHz to 8 GHz, with the number of frequency channels at maximum bandwidth increased between the VLA and JVLA by a factor of over 1000 times. The sensitivity of the JVLA at its observation frequencies is shown with respect to the Square Kilometer Array (SKA), the Atacama Large Millimeter Array (ALMA) and Spitzer in Fig. 2.6.

The JVLA uses four different antenna configurations (A, B, C and D) to observe at different resolutions and sensitivity (Perley et al., 2011). These configurations have baseline lengths of 36, 11, 3.4 and 1 km respectively. The JVLA cycles through these different baseline configurations on a cycle of 3–4 months per configuration, allowing

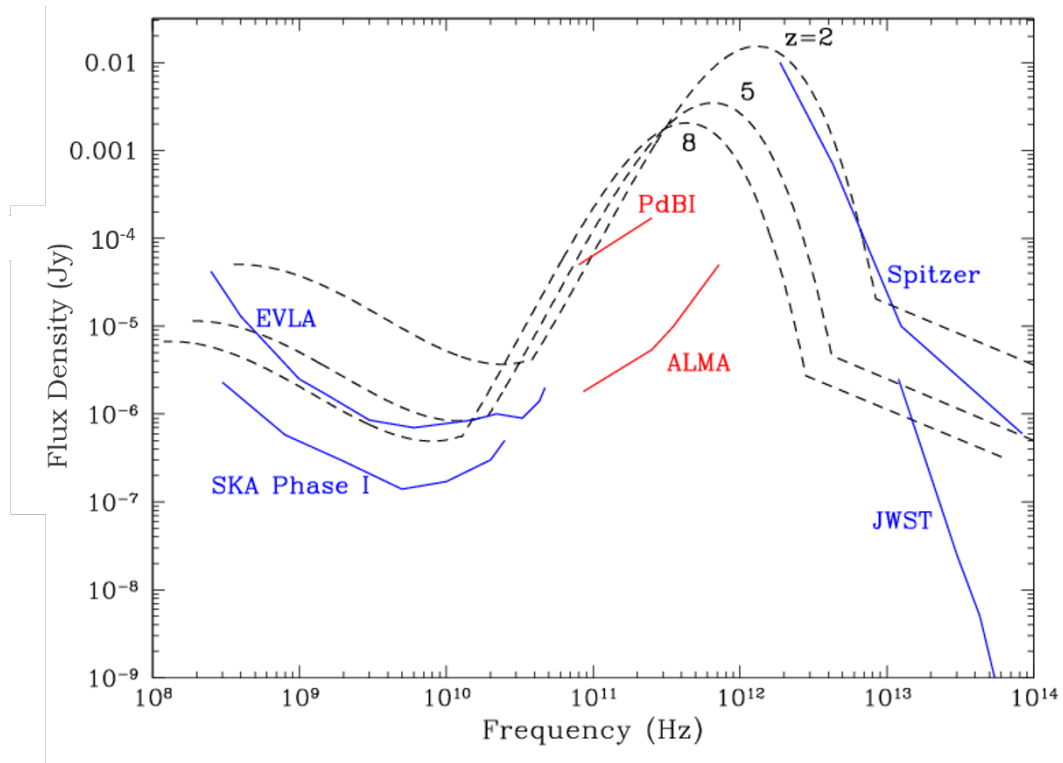


Figure 2.6: The flux limits for the JVLA, SKA, ALMA and *Spitzer* are shown with respect to the expected fluxes for the Arp 220 galaxy (black dashed line). The different dashed lines show the simulated values for Arp 220 at different redshifts, showing the sensitivity of the arrays with respect to continuum values of galaxies at various redshifts. Taken from Carilli (2008).



Figure 2.7: Image, taken from Perley et al. (2011), illustrates layout of the array of antennae, showing the Y-distribution used to produce the baselines.

for flexibility in operations.

The JVLA is sensitive between the frequency 1 GHz and 50 GHz, with 8 bands, listed in Table 2.5. Four main goals for astronomical observations for the JVLA were set in Perley et al. (2011):

- Measuring the topology of magnetic fields in astrophysical objects.
- Measuring the obscured universe, allowing for unbiased surveys of dust-enshrouded objects, obscured at other wavelengths.
- Enable rapid response to transient sources that can rapidly evolve.
- Track the formation and evolution of astrophysical objects; from stars to galactic nuclei.

Data products of the JVLA can be calibrated, constructed and analysed via several different packages, written specifically for radio interferometric data (e.g. CASA, Myriad, AIPS). Spectral and continuum images can be constructed from JVLA data products, which can then be used to produce image moment files to analyse specific characteristics of astronomical objects, such as the velocity at specific positions (known as “velocity fields”) and the velocity dispersion at different positions.

The JVLA is therefore a useful tool to understanding obscured galaxies and their environments at centimeter (cm) and millimeter (mm) wavelengths. In this thesis, JVLA data will be used to infer cold gas distributions around Hot Dust Obscured Galaxies (Hot DOGs; Wu et al., 2012), determining the CO(J=1–0) emission of gas associated with these galaxies. These data can also infer the position and velocity of the galaxies, define the redshift of the object from the emission spectra, and determine the gas mass and luminosity.

Band	Band range (GHz)
L	1.0–2.0
S	2.0–4.0
C	4.0–8.0
X	8.0–12.0
Ku	12.0–18.0
K	18.0–26.5
Ka	26.5–40.0
Q	40.0–50.0

Table 2.5: The bands and frequency ranges for the Extended Very Large Array (JVLA) (Perley et al., 2011).

### 2.6.2 NVSS

The National Radio Astronomy Observatory (NVSS) 1.4 GHz VLA Sky Survey (NVSS; Condon et al., 1998) is a continuum survey of the entire sky north of  $-40$  deg declination. The NVSS map is formed from 2326,  $4 \times 4$  deg image cubes in the Stokes I, Q and U planes. The restoring beam of these images has a FWHM of  $45''$ , chosen in consideration of the high surface-brightness sensitivity needed for photometry. The root mean square (rms) fluctuations for brightness are  $0.45$  mJy/beam and the completeness limit for sources is  $2.5$  mJy. NVSS catalogued  $1.8 \times 10^6$  objects in its run between 1993 to 1997, and was used to define radio characteristics of WISE-selected sources in Lonsdale et al. (2015).

### 2.6.3 FIRST

The Faint Images of the Radio Sky at Twenty-cm (FIRST) is a VLA sky survey producing radio images at greater depths than NVSS using the VLA. Most of the FIRST catalogue was obtained between 1993 and 2004, with additional data of the southern galactic cap obtained between 2004 and 2011. FIRST used the VLA in its B-configuration for imaging, taking 180 s (60 s after 2011) exposures in a hexagonal grid chosen to coincide with the Sloan Digital Sky Survey (SDSS), using  $2 \times 7$  3 MHz channels, centred at 1365 and 1435 MHz (1335 and 1730 MHz after 2011) respectively. Images produced in FIRST have a pixel size of  $1.8''$ , an rms of  $\sim 0.15$  mJy, and a resolution of  $5''$ . The publicly available online FIRST catalogue has a source detection threshold of 1 mJy. Given the higher resolution and fainter limits of the FIRST survey, this work uses positions of the radio-WISE selected galaxies where available.

## 2.7 ALMA

ALMA is a radio-interferometer consisting of 66 radio telescopes in the Atacama Desert, Chile, operating since 2011 and at the time of writing this thesis is still operational. ALMA consists of 50 antennae of diameter 12 m. Two additional arrays of four 12 m and twelve 7 m antennae form the Atacama Compact Array (ACA; Iguchi et al., 2009). All of the antennae in ALMA are moved via specialised transporters, which relocate the antennae into larger/smaller configurations. The diameter of the configuration can change between 150 m to a maximum diameter of 16 km, and allows the telescope to increase the resolution through increasing the diameter of the configuration.

The observed bands of ALMA are shown in Table 2.6, and shows that ALMA covers the sub-millimeter to millimeter wavelength range, and the sensitivity for this range is shown in Fig. 2.6. The number of bands within this wavelength range allow for detailed information on emission lines at these wavelengths, helping to determine redshifts, line luminosities, and provide detailed maps of the motion of cold dust within a variety of astronomical objects. ALMA is expected to also provide information on star formation in the early universe, and produce detailed imaging of planet/star formation in the local universe.

ALMA 870  $\mu\text{m}$  observations were made on a sample of radio-WISE selected galaxies by Silva et al. (2015), which determined an overdensity of SMGs within  $\sim 150$  kpc,  $\sim 10\times$  that seen in blank fields, suggesting that these galaxies were interacting with nearby companions on relatively small scales. In Chapter 3, I compare the overdensities observed using ALMA to overdensities of similar objects using *Spitzer* observations. Further work by Gonzales et al. (in prep), using ALMA Band-3 and Band-5 observations of a sample of Hot DOGs identified CO(J=4–3) and CO(J=6–5) emission lines

## CHAPTER 2. INSTRUMENTATION

---

ALMA Band	Wavelength Range (mm)	Frequency Range (GHz)
1	6.0–8.5	35–50
2	3.3–4.5	65–90
3	2.6–3.6	84–116
4	1.8–2.4	125–163
5	1.4–1.8	163–211
6	1.1–1.4	211–275
7	0.8–1.1	275–373
8	0.6–0.8	385–500
9	0.4–0.5	602–720
10	0.3–0.4	787–950

Table 2.6: Table showing the ALMA bands and the associated wavelengths/frequencies.

from the sample, and were able to determine continuum fluxes for all of the galaxies in their sample. I use the Hot DOG detections from this work in addition to JVLA observations of the same Hot DOGs to produce SEDs of each of the galaxies in Chapter 4.

## Chapter 3

# The Environments of Luminous Radio-WISE selected Infrared Galaxies

This chapter presents follow-up observations of 33 NVSS/FIRST radio-WISE selected galaxies using the *Spitzer* telescope at  $3.6\ \mu\text{m}$  and  $4.5\ \mu\text{m}$  (Penney et al., 2019). These galaxies are selected to be radio-intermediate, such that the  $22\ \mu\text{m}$ -to- $22\ \text{cm}$  flux ratio is  $-1 < \log(F_{22\ \mu\text{m}}/F_{22\ \text{cm}}) < 0.1$ , with additional WISE selection criteria to select for dust obscured galaxies:  $(W2 - W3) + 1.25(W1 - W2) > 7$ .

### 3.1 Introduction

High-redshift galaxy protoclusters are the largest known structures, with 90% of their  $\sim 10^{15} M_{\odot}$  expected to be confined within regions spanning  $\sim 35 h^{-1} \text{ Mpc}$  (Chiang et al., 2013; Muldrew et al., 2015)<sup>1</sup>. Simulations of protoclusters by (Chiang et al., 2017) predict a significant excess of star-forming galaxies within the central 10 – 20 Mpc of the simulated protocluster, suggesting that these structures are sites of massive star formation in the early universe (Steidel et al., 1998, 2005). However, given their extended nature, it is observationally difficult to confirm sightings of these structures (Muldrew et al., 2015). Observations of protoclusters have utilised detections of luminous IR and radio galaxies to indicate potential sites of protoclusters (e.g. Le Fevre et al., 1996; Best et al., 2003; Wylezalek et al., 2013; Hatch et al., 2014).

Radio-loud galaxies have been observed to typically reside within overdense environments (Dunlop & Peacock, 1990; Donoso et al., 2010; Wylezalek et al., 2013), with simulations of galaxy mergers suggesting that radio-loud galaxies could be produced from intense mergers (see Chiaberge et al., 2015, for a review). Given the increased likelihood of mergers within protocluster sites, it is likely that these galaxies trace forming galaxy clusters (Hatch et al., 2014), and therefore by selecting radio-loud sources, one can attempt to understand the nature of protocluster sites by observing the surrounding environment.

Studies of powerful Active Galactic Nuclei (AGN) at similar redshifts to Sub-millimeter Galaxies (SMGs) have revealed significant overdensities of near- and far-IR galaxies (Best et al., 2003; Stern et al., 2003; Stevens et al., 2003; De Breuck et al., 2004; Greve et al., 2007; Venemans et al., 2007). An example of this is the radio-loud galaxy

---

<sup>1</sup>where  $h^{-1}$  is linked to the Hubble parameter,  $H_0$ , by  $h = H_0/100 \text{ km s}^{-1} \text{ Mpc}^{-1}$

### CHAPTER 3. THE ENVIRONMENTS OF LUMINOUS RADIO-WISE SELECTED INFRARED GALAXIES

---

MRC1138–262 (the Spiderweb galaxy; Miley et al., 2006), one of the most massive and intensely studied galaxies (Kurk et al., 2000; Pentericci et al., 2000). Observations of the local environment have been made at a wide range of wavelengths to understand the protocluster associated with the HzRG, with initial observations by Kurk et al. (2000) and Pentericci et al. (2000) finding an excess of Ly $\alpha$  and H $\alpha$  emitting galaxies in the vicinity of the Spiderweb galaxy compared with blank fields. Further sub-millimeter observations using Herschel’s SPIRE by Rigby et al. (2014) found an overdensity of 500  $\mu\text{m}$  selected sources within a  $\sim 400 \text{ arcmin}^2$  field centred on the Spiderweb galaxy and Dannerbauer et al. (2014) found a local density of 870  $\mu\text{m}$  selected SMGs four times greater than blank fields. Thus, FIR data, including data from the *Herschel* PACS and SPIRE instruments, and *Spitzer*’s Multi-band Imaging Photometer (MIPS; Rieke et al., 2004), suggest that the Spiderweb galaxy inhabits a region of intense star formation and potential mergers around a central massive galaxy.

Studies using IR measurements centred on Radio-Loud AGN (RLAGN), motivated by the observations of the Spiderweb galaxy, were made to understand the nature of these galaxies and their local environment. The Clusters Around Radio-Loud AGN (CARLA) survey (Wylezalek et al., 2013, 2014; Hatch et al., 2014) used *Spitzer* IRAC observations of 420 fields containing RLAGN, comparing the surface density of galaxies with specific colour selection criteria to blank fields in the *Spitzer* UKIDSS Ultra-Deep Survey (SpUDS; Dunlop et al., 2007) within several hundred kilo-parsecs of the central RLAGN (Wylezalek et al., 2013, 2014). Significant overdensities of IRAC colour-selected galaxies around RLAGN were uncovered, with 10% of the CARLA fields containing densities  $> 5\sigma$  level with respect to comparison fields within a 2.5 arcmin radius of the RLAGN.

As previously discussed, Hot DOGs are a group of heavily dust obscured galaxies, luminous in the IR and generally observed at  $z > 2$ . These galaxies were selected for the red WISE colours, luminous in the W3 and W4 bands, and faint/undetected in the

### CHAPTER 3. THE ENVIRONMENTS OF LUMINOUS RADIO-WISE SELECTED INFRARED GALAXIES

---

W1 and W2 bands (Eisenhardt et al., 2012) and the selection criteria for these galaxies was radio-blind. Observations by Assef et al. (2015) using warm-*Spitzer* observations show that these galaxies inhabit regions of IRAC colour-selected galaxies as overdense as RLAGN in the CARLA sample. As discussed in Chapter 1, these high-redshift, dust obscured, luminous IR galaxies could be radio-quiet analogues of the RLAGN in CARLA. Lonsdale et al. (2015) used additional radio selection criteria using NVSS and WISE to select for radio-intermediate galaxies and the WISE selection criteria is shown below for the reader (Eqn. 3.1). These radio-WISE galaxies are selected for their compact radio emission to reduce the effect of synchrotron emission on IR and sub-millimetre fluxes, and it is likely that these galaxies harbour radio jets from the core regions (Lonsdale et al., 2016). The sample could represent the early stages of luminous quasars, which include compact, young radio emission and powerful IR emission, consistent with dust enshrouded AGN (Lonsdale et al., 2015). It should be noted that the RLAGN in CARLA have much greater radio power than these galaxies, but radio-WISE selected galaxies are typically more radio-loud than Hot DOGs (Assef et al., 2015; Tsai et al., 2015).

$$(W2 - W3) + 1.25(W1 - W2) > 7 \quad (3.1)$$

SEDs of a sample of 49 radio-WISE selected galaxies using ALMA at  $870 \mu\text{m}$  by Lonsdale et al. (2015) found 26 had detections at  $870 \mu\text{m}$ , with fluxes placing them in the ULIRG and HyLIRG regimes, similar to Hot DOGs (Eisenhardt et al., 2012; Wu et al., 2012; Bridge et al., 2013; Jones et al., 2014), with dust temperatures  $\gtrsim 30 \text{ K}$ . Throughout this work, the targets are referred to as radio-WISE galaxies. The subset in this work, shown in Table B.1, were selected from the main catalogue (Lonsdale et al., 2015) for spectroscopic redshifts  $z > 1.3$ , with a maximum redshift of  $z = 2.72$ . Radio-WISE

### CHAPTER 3. THE ENVIRONMENTS OF LUMINOUS RADIO-WISE SELECTED INFRARED GALAXIES

---

galaxies have a significant overdensity of SMGs found at longer  $850\ \mu\text{m}$  wavelengths in the surrounding  $\sim 1.5'$  radius (Jones et al., 2015) with overdensities of 4–6 times that of the field. These overdensities were greater than that observed for fields containing Hot DOGs (Jones et al., 2014), with no evidence of angular clustering on scales out to  $1.5'$  from the target, and are expected to be radio-loud counterparts to Hot DOGs (Lonsdale et al., 2015). Furthermore, ALMA found overdensities of SMGs 10 times that of blank fields for 17 of the 49 galaxies within scales of  $\sim 150\ \text{kpc}$  ( $17''$ ) (Silva et al., 2015). The findings suggests that many of these HyLIRGs could inhabit dense, unvirialised regions, given the levels of overdensity extending over large scales. Findings around these galaxies are consistent with simulations of large scale structure by Chiang et al. (2013) and Muldrew et al. (2015), which predict pre-virialised objects can be signposted by significant overdensities of dusty, star-forming galaxies.

It is of interest to understand how these extremely luminous and powerful radio-WISE selected galaxies interact with and affect their surrounding environment. IRAC colours are used to select galaxies at consistent redshifts and the surface densities of galaxies in the environment of radio-WISE galaxies. In this work, the nature of these fields are characterised using IRAC to greater than 10 times the depth of WISE observations. Section 3.2 describes the sample and the methods used to reduce the data and Section 3.5 discusses the findings. All colours and magnitudes are displayed in AB-magnitudes, and IRAC1 and IRAC2 magnitudes are expressed as [3.6] and [4.5] respectively<sup>2</sup>.

---

<sup>2</sup>As discussed in Chapter 1, a cosmology of  $H_0 = 70\ \text{km s}^{-1}\ \text{Mpc}^{-1}$ ,  $\Omega_m = 0.26$  and  $\Omega_\Lambda = 0.74$  is assumed.

## 3.2 *Spitzer* Observations

During the observations, 33 specific fields were targeted containing radio-WISE galaxies with redshifts  $z > 1.3$  using *Spitzer*'s IRAC camera (PI: Carol Lonsdale, PID: 11013). Given the rarity of these galaxies, with sky-densities of  $0.025 \text{ deg}^{-2}$ , these targets do not lie within existing publicly available deep fields. Given their red colours and obscured nature, warm *Spitzer* observations are the most sensitive to galaxies in the surrounding environment. The observations follow a dithered pattern centred on the radio-WISE galaxy. Fourteen  $5.2' \times 5.2'$  frames per field are imaged for  $\sim 100$  s each and mosaicked to produce a deeper image of the field. This produces a square  $\sim 30.8 \text{ arcmin}^2$  ( $5.55' \times 5.55'$ ) two band image centred on the radio-WISE selected galaxy with a Point Spread Function (PSF) of the images of  $\sim 1.95''$  for IRAC1 and  $\sim 2.02''$  for IRAC2, found in the IRAC Instrument Handbook. The central  $5.12' \times 5.12'$  region of the field was measured for  $\sim 700$  s for IRAC1 and  $\sim 1000$  s for IRAC2.

### 3.2.1 Data Reduction

The frames for each field were stacked and reduced using the MOPEX package (Makovoz & Marleau, 2005), specifically designed for manipulating *Spitzer* images. The pixel scale was set to  $0.6''$  in MOPEX and optimized parameters for deep IRAC images were used (Lacy et al., 2005). During the image interpolation stage of image reduction, the drizzle method was utilised to reduce artefacts in the image. The drizzle algorithm changes the size of each input pixel by the specified drizzle factor along each axis. The new pixels are then projected onto the image, with values within the pixels orientated according to the drizzle factor, as shown in Fig. 3.1. A drizzling factor of 1.2 was added

### CHAPTER 3. THE ENVIRONMENTS OF LUMINOUS RADIO-WISE SELECTED INFRARED GALAXIES

---

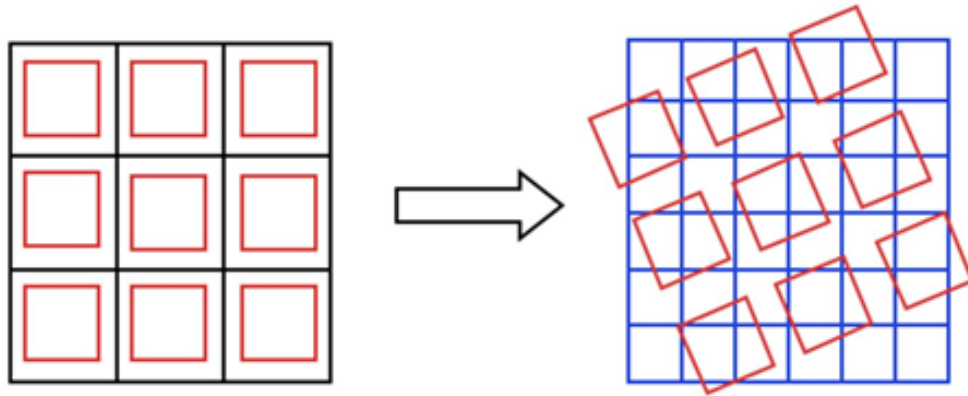


Figure 3.1: Illustration of the Drizzle algorithm in MOPEX, changes the size of the input pixels by a factor, rearranging the flux values using the input factor to determine the position of the new pixels. Black squares show the initial input pixels, red squares show the shrunken pixels, and blue squares show the array of flux values that are input into the newly formed pixels. See <https://irsa.ipac.caltech.edu/data/SPITZER/docs/dataanalysisistools/tools/mopex/mopexusersguide/86/> for more information.

in the image interpolation stage to reduce cosmic-ray and bad-pixel effects. Initially, upon adding this drizzle factor, improved image quality was seen in the test field, however upon producing additional fields, several artefacts were seen in the image not cleaned by the processes used in Lacy et al. (2005) or the drizzle algorithm. After tests on additional fields, including the Overlap Module was seen to significantly increase the image quality across all fields, reducing bad pixels and other artefacts. For all fields, higher levels of noise were observed in the first two frames, so these frames were removed from the image mosaicking process, reducing the time imaged for each radio-WISE field to  $\sim 500$  s for IRAC1.

### 3.2.2 Source Extraction

Two different source extraction methods were initially considered; the APEX module in MOPEX (Makovoz & Marleau, 2005) is specifically designed to extract sources from *Spitzer* IRAC and MIPS images, and Source Extractor (henceforth SExtractor; Bertin & Arnouts, 1996), which is a general source extraction package used for a variety of images. Using standard extraction methods, the number of sources extracted is compared, as well as the depth of the extracted sources. It was found that, for most radio-WISE selected fields, SExtractor extracted the most sources in the field to greater depths than APEX. Therefore, SExtractor was used for all of the IRAC images in single-image mode. Optimized SExtractor parameters for IRAC were taken from Lacy et al. (2005) with a flux aperture diameter of 4'' ( $\sim 2$  times the PSF of *Spitzer*). The native MJy sr<sup>-1</sup> units of the image are converted to  $\mu\text{Jy pixel}^{-1}$ , using the conversion factor of  $8.4619 \mu\text{Jy pixel}^{-1}/\text{MJy sr}^{-1}$  for the 0.6'' pixel scale. Additionally, coverage maps produced by MOPEX were used for weighting images when extracting sources, thereby accounting for regions of higher noise in individual images, and increasing the depth for other portions of the images. Using these coverage maps increased the number of sources extracted by 40% compared to no weighting. Empirical aperture corrections were confirmed by comparing the flux densities derived from SExtractor in the SpUDS field to those from the SpUDS catalogue (Dunlop et al., 2007). These conversion factors were found to be 1.42 and 1.45 for [3.6] and [4.5] respectively, in agreement with Wylezalek et al. (2013).

To determine [3.6] – [4.5] IRAC colours of the sources in the final catalogue, sources needed to be matched to their counterparts in the separate bands. Therefore, the maximum matching radius was determined between the two bands, ensuring the completeness of the sample while excluding galaxies that appeared at similar positions

### CHAPTER 3. THE ENVIRONMENTS OF LUMINOUS RADIO-WISE SELECTED INFRARED GALAXIES

---

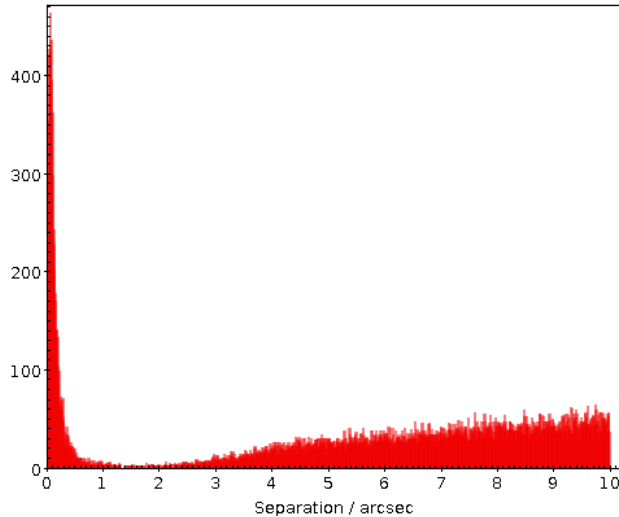


Figure 3.2: Histogram of the matching separations of sources between IRAC1 and IRAC2 of all sources extracted by SExtractor in the radio-WISE selected fields. The minimum of  $2''$  is used as a matching radius between IRAC bands for the rest of this work to determine counterparts between bands.

between the bands. Using the TOPCAT package (Taylor, 2005), sources were matched within the stacked catalogue of the 33 radio-WISE fields within  $10''$  of each source, using no selection bias for colour or depth. During the matching process, the MATCH SELECTION parameter was set to “All Matches”, and a histogram of the separations of the matches was constructed, shown in Fig. 3.2. In Fig. 3.2 a peak is observed at the lowest separations, declining rapidly before rising again at  $\sim 2''$ . To increase the completeness of the catalogue, the minima of the distribution is chosen as the maximum matching radius, and the value agrees with the PSF of warm-*Spitzer* ( $\approx 2''$ ).

Finally, the number of galaxies from the source extraction process that could be artefacts of either bright sources in the field or fluctuations in the background intensity were determined. Bright sources can create diffraction effects, producing areas around the galaxy with greater levels of background intensity, which could create spurious galaxies within the fields. In general,  $\sim 2$  objects are observed per field that could be caused

## CHAPTER 3. THE ENVIRONMENTS OF LUMINOUS RADIO-WISE SELECTED INFRARED GALAXIES

---

by these bright sources, representing  $< 2\%$  of the galaxies in the radio-WISE selected fields. Galaxies at the edge of the field could be affected by the dithering pattern, which produces portions of the field imaged for less time. This could result in galaxies which may appear unrealistically blue/red in the catalogue. Therefore only the uniformly covered central  $5.12' \times 5.12'$  square ( $\sim 7.15 \text{ Mpc}^2$  at  $z = 1.93$ ) is analysed, centred on the radio-WISE galaxy to mask out these objects.

### 3.2.3 Completeness Limits

To determine the extent to which the survey could identify potential companion galaxies, the depth at which source detection was 95% complete was investigated. Initially, using packages available on IRAF<sup>3</sup>, sources from IRAC1 and IRAC2 with known fluxes roughly the size of the PSF were taken for both bands. 400 of these sources were then distributed in a grid of known positions onto a randomly selected radio-WISE selected field. The sources were then extracted using SExtractor without the coverage maps and the process was repeated, increasing/decreasing the brightness of the simulated sources on the field. To ensure that the positions of the simulated sources in the grid were not affected by bright sources nearby, the grid was translated by half a separation in the x- and y-axes, and the process was repeated once more. The results for this investigation are shown in Fig. 3.3 for an example field. The completeness limits differ between the fields that were tested, potentially due to changes in the background between the two fields, or due to the number of bright objects.

Due to the above discrepancy between the fields using simulated galaxies to determine the completeness limits of the IRAC images, the 95% completeness limit was calculated by analysing the number of sources detected in all of the radio-WISE selected fields, and

---

<sup>3</sup><http://ast.noao.edu/data/software>

## CHAPTER 3. THE ENVIRONMENTS OF LUMINOUS RADIO-WISE SELECTED INFRARED GALAXIES

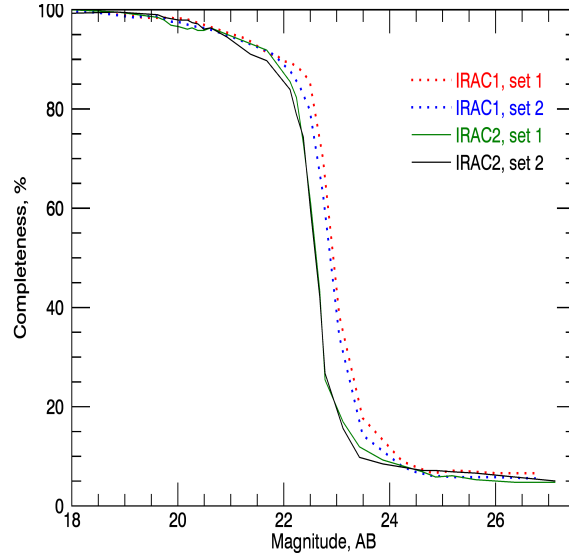


Figure 3.3: Curves of completeness with respect to IRAC magnitude for two fields using simulated sources of varying brightness to determine the completeness limits of the individual fields. Two grids of 400 simulated sources were used to determine the completeness limits of the fields to ensure bright background sources did not contaminate the completeness estimate. IRAC1 is shown by green and blue lines, IRAC2 is shown by red and black lines.

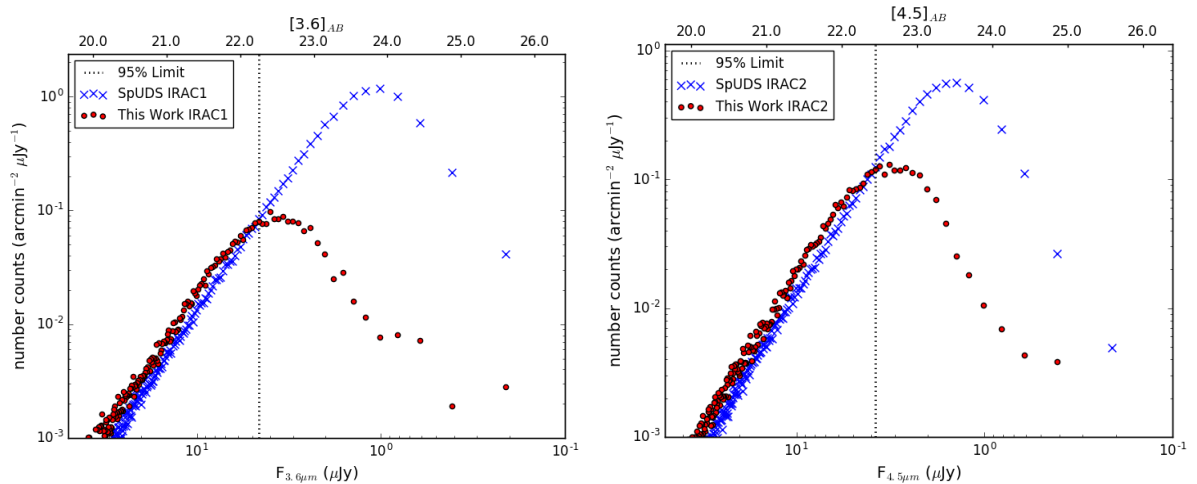


Figure 3.4: The completeness limits for IRAC1 (left) and IRAC2 (right). The blue crosses indicate the SpUDS data and the red points correspond to 33 stacked radio-WISE selected fields. A black dashed line has been included to indicate the 95% completeness limit of this work.

## CHAPTER 3. THE ENVIRONMENTS OF LUMINOUS RADIO-WISE SELECTED INFRARED GALAXIES

---

comparing them with the number of galaxies detected in SpUDS. Given that the SpUDS catalogue was created in a different manner to the source extraction method detailed above, the images of the SpUDS field were run through the same SExtractor method as the radio-WISE selected fields for comparison. The results are shown in Fig. 3.4, and a small increase in the density of sources in the radio-WISE selected fields can be seen. This is unexpected, given that there should not be any significant overdensity in the catalogue without selection criteria. This is not caused by the method of source extraction, as both samples used the same source extraction method (SExtractor). It is most likely due to the drizzle method used in this work to create the images, affecting the estimation of the background noise, although it is unclear why there is such a distinct excess. As shown in Section 3.5, it does not appear to have made a significant effect on the overdensity of these fields with respect to comparison fields.

From this investigation, the 95% completeness limits determined were  $[3.6]=22.23$  and  $[4.5]=22.44$  (see Fig. 3.4), corresponding to source flux limits of  $4.71 \mu\text{Jy}$  and  $3.82 \mu\text{Jy}$ . The noise level was  $0.06 \mu\text{Jy}$  ( $[3.6]=23.95$ ) in IRAC1 and  $0.04 \mu\text{Jy}$  ( $[4.5]=23.70$ ) in IRAC2 in a  $4''$  diameter aperture. This level shows a 95% confidence limit on any galaxies detected within these limits, and it cannot be ascertained whether objects fainter than these limits are produced from random background fluctuations in the images.

### 3.3 Properties of Radio-WISE Galaxies

The *Spitzer* properties of the central radio-WISE selected galaxies, listed in Table B.1, are compared with those of Hot DOGs (Wu et al., 2012), shown in Fig. 3.5. From Table B.1, the IRAC  $[3.6]$  and  $[4.5]$  magnitudes of the radio-WISE selected galax-

### CHAPTER 3. THE ENVIRONMENTS OF LUMINOUS RADIO-WISE SELECTED INFRARED GALAXIES

---

ies are significantly brighter than the average magnitudes of red galaxies in the fields ( $\langle [3.6]_{\text{AB}} \rangle = 21.34 \pm 0.97$  and  $\langle [4.5]_{\text{AB}} \rangle = 21.17 \pm 0.94$ ): these galaxies are well measured in the rest-frame near-IR. They also possess redder IRAC [3.6] – [4.5] colours than average galaxies in the field, consistent with obscured galaxies. Comparing the IRAC [3.6] – [4.5] colours of the 33 radio-WISE galaxies in this work with the 25 Hot DOGs in Wu et al. (2012), there are slightly redder IRAC colours in the radio-WISE selected population using the same apertures and corrections, with a median colour of  $1.02 \pm 0.17$  for the radio-WISE galaxies, compared with  $0.73 \pm 0.33$  for the Hot DOGs. The radio-WISE selected galaxies are typically brighter and redder than the Hot DOG population. There is significant scatter in Fig. 3.5 for the radio-WISE selected galaxies, with a Pearson correlation coefficient of 0.11 and -0.14 for IRAC1 and IRAC2 respectively, suggesting that there is little correlation between their flux densities in the mid-IR and their [3.6] – [4.5] colour. There is slightly less scatter for the Hot DOG population, where the Pearson correlation coefficient is 0.38 and -0.24 for IRAC1 and IRAC2 respectively, although there is no significant correlation between mid-IR flux density and [3.6] – [4.5] colour.

Using the WISE W3 ( $12 \mu\text{m}$ ) and W4 ( $22 \mu\text{m}$ ) data, the median W3 – W4 colour for the radio-WISE galaxies and Hot DOGs are  $1.05 \pm 0.34$  and  $1.72 \pm 0.27$  respectively, as shown in Fig. 3.6. This suggests that the radio-WISE galaxies possess generally bluer mid-IR colours than the Hot DOGs in Wu et al. (2012). Hot DOGs were also selected based on their W2 – W3 colour, and there is a redder median W2 – W3 colour for the Hot DOGs compared with the radio-WISE galaxies in this sample, with  $4.44 \pm 0.86$  and  $2.77 \pm 0.55$  for the Hot DOGs and radio-WISE galaxies respectively (see Fig. 3.6). There is a stronger correlation between the W3 and W4 bands and the W3 – W4 colour for both classes of galaxy. For the radio-WISE galaxies, a correlation coefficient of 0.46 and -0.11 is found for W3 and W4 respectively. For the Hot DOGs in Wu et al. (2012),

## CHAPTER 3. THE ENVIRONMENTS OF LUMINOUS RADIO-WISE SELECTED INFRARED GALAXIES

---

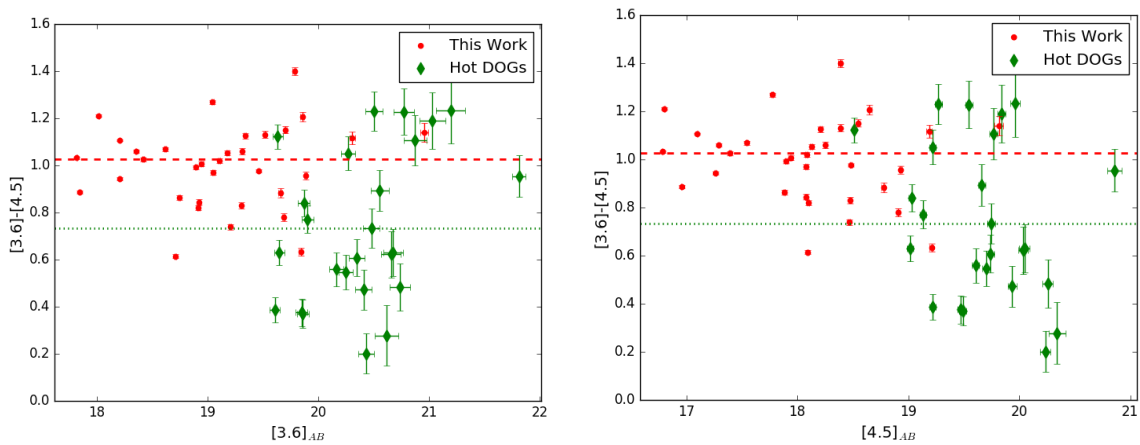


Figure 3.5: Comparison of *Spitzer* properties of the 33 central radio-WISE selected galaxies in this work, and 25 Hot DOGs (Wu et al., 2012) comparing the IRAC colour with  $[3.6]$  (left) and  $[4.5]$  (right). A red dashed and green dotted line represent the median  $[3.6] - [4.5]$  IRAC colours for the radio-WISE galaxies and Hot DOGs respectively. The radio-WISE selected galaxies in this work (red points), appear to have brighter IRAC magnitudes than the Hot DOGs (green diamonds). The radio-WISE galaxies have been imaged to a greater depth than these Hot DOGs, with *Spitzer* observation times of  $\sim 1000$ s and  $\sim 150$ s respectively (see Section 3.2.2).

### CHAPTER 3. THE ENVIRONMENTS OF LUMINOUS RADIO-WISE SELECTED INFRARED GALAXIES

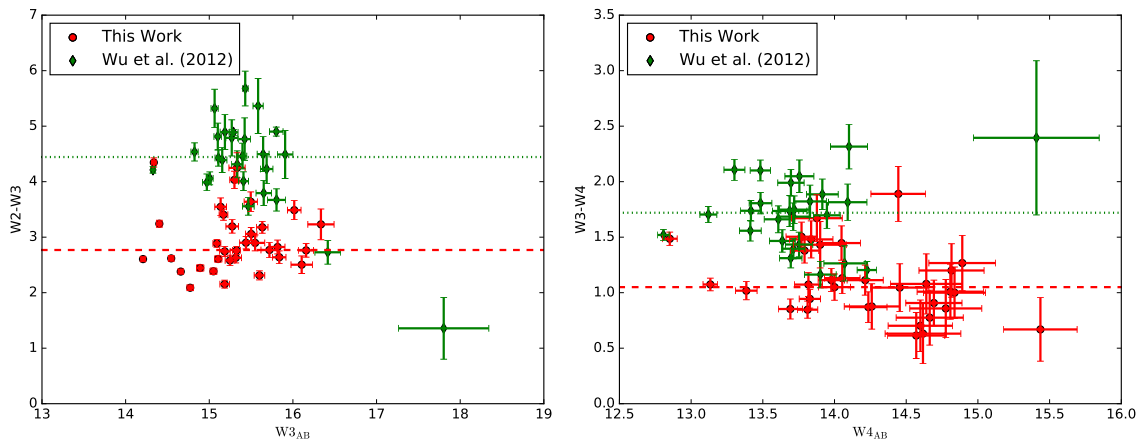


Figure 3.6: Comparison of the WISE properties of the 33 central radio-WISE selected galaxies in this work, and 25 Hot DOGs from Wu et al. (2012) comparing the W2-W3 colour (left) and the W3-W4 colour (right). A red dashed and green dotted line represent the median  $[3.6] - [4.5]$  IRAC colours for the radio-WISE galaxies and Hot DOGs respectively. The radio-WISE selected galaxies in this work (red points), appear to have fainter WISE W3 ( $12\ \mu\text{m}$ ) and W4 ( $22\ \mu\text{m}$ ) magnitudes than the Hot DOGs (green diamonds), and generally possess bluer W2-W3 and W3-W4 colours, in contrast to the *Spitzer* colours shown in Fig. 3.5.

a correlation coefficient of 0.55 and -0.22 is found for W3 and W4 respectively. This suggests that, generally, the WISE colours are more correlated with their  $12\ \mu\text{m}$  and  $22\ \mu\text{m}$  flux densities than the IRAC flux densities for both galaxy classes.

Comparing the luminosity of the 30 radio-WISE galaxies in common with Lonsdale et al. (2015) with the luminosity estimates for the Hot DOGs in Wu et al. (2012), there is an average luminosity of  $2.7 \times 10^{13} L_{\odot}$  for the radio-WISE galaxies compared with  $6.1 \times 10^{13} L_{\odot}$  for the Hot DOGs. Comparing the correlation of the colour of the radio-WISE selected galaxies with the mid-IR luminosities listed in Lonsdale et al. (2015), there is a correlation coefficient of 0.31 for  $[3.6] - [4.5]$  and 0.42 for W3-W4 colours, suggesting the redder IRAC and WISE colours are associated with brighter mid-IR luminosities. For the nine Hot DOGs in Wu et al. (2012) with sub-millimeter data, there is a correlation coefficient of 0.42 and -0.42 for IRAC and WISE colours

## CHAPTER 3. THE ENVIRONMENTS OF LUMINOUS RADIO-WISE SELECTED INFRARED GALAXIES

---

respectively, suggesting a correlation between the total luminosities of these galaxies and their mid-IR colours.

### 3.4 Object Selection Criteria

Colour selection is used to isolate *Spitzer* galaxies likely to be at  $z > 1.3$ , matching the redshift range of the radio-WISE selected galaxies. As discussed in Chapter 1, Papovich (2008) demonstrated that, regardless of age or galaxy type, galaxies at  $z > 1.3$  can be selected by IRAC colour  $[3.6] - [4.5] > -0.1$  (or a flux density ratio of IRAC2 ( $F_{\text{IRAC}2}$ ) to IRAC1 ( $F_{\text{IRAC}1}$ ) of  $\frac{F_{\text{IRAC}2}}{F_{\text{IRAC}1}} > 0.88$ ), based on models by Bruzual & Charlot (2003). This colour selection uses the  $1.6 \mu\text{m}$  bump, a feature apparent in almost all galaxies, produced by the minimum opacity of the  $\text{H}^-$  ion in the atmospheres of cool stars (John, 1988). Due to the relative placement of this bump and the IRAC channels, this colour selection method should be efficient at finding  $z > 1.3$  galaxies in the vicinity of radio-WISE selected galaxies (see also Simpson & Eisenhardt, 1999; Wylezalek et al., 2013; Assef et al., 2015).

Galaxies are selected above the completeness limits determined in Section 3.2.3 with these IRAC colours. Candidate galaxies with IRAC2 magnitudes within the completeness limits, but fainter for IRAC1, were also accepted within the colour limit  $[3.6] - [4.5] > -0.1$  to ensure a complete list of redder galaxies. Galaxies selected using  $[3.6] - [4.5] > -0.1$  (henceforth Group-I galaxies) appear to be distributed fairly uniformly across the central  $5.12' \times 5.12'$  field (instead of the full image extent of  $5.25' \times 5.25'$ ), with no obvious clustering around the central radio-WISE selected galaxy, as shown for a typical example in Fig. 3.7(a). Spectroscopic redshifts would be needed to reveal the three dimensional distribution of galaxies across the field, given the colour

## CHAPTER 3. THE ENVIRONMENTS OF LUMINOUS RADIO-WISE SELECTED INFRARED GALAXIES

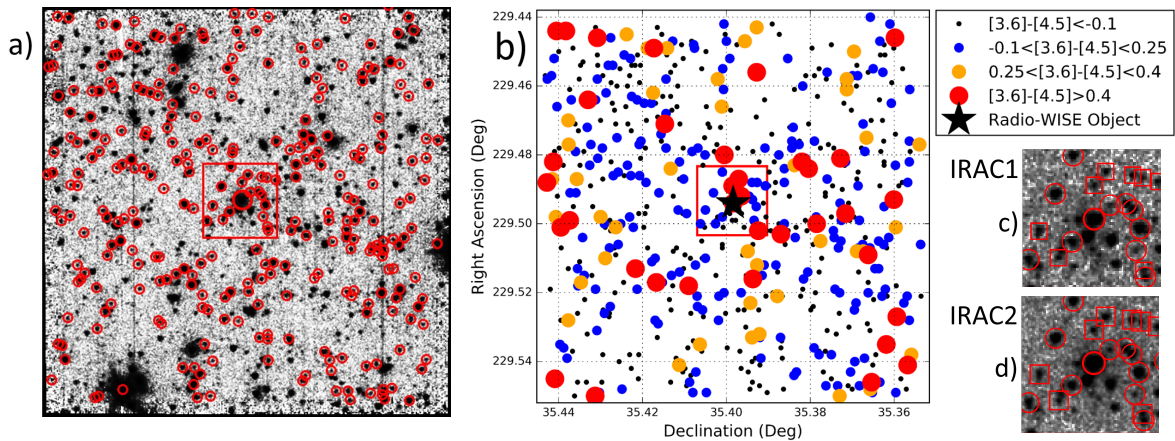


Figure 3.7: (a) A typical IRAC2  $5.55' \times 5.55'$  field, centred on W1517 indicated by a large bold circle. Catalogued galaxies whose IRAC colours  $[3.6] - [4.5] > -0.1$ , above the completeness limits discussed in Section 3.2.3 are marked by red circles. (b) Map of the same field with positions marked by the IRAC colours of the galaxies. (c) Central  $1' \times 1'$  ( $\sim 500 \text{ kpc} \times 500 \text{ kpc}$ ) region centred on the radio-WISE selected galaxy for IRAC1. (d) Central  $1' \times 1'$  region centred on the radio-WISE selected galaxy for IRAC2. For the inset regions, galaxies with IRAC1 magnitudes  $21 < [3.6] < 22$  and IRAC colours  $[3.6] - [4.5] > -0.1$  are boxed, objects within the completeness limits and IRAC colours  $[3.6] - [4.5] > -0.1$  are circled and the central radio-WISE selected galaxy is shown by a large, bold ring. The inset regions are highlighted by the box in (a) and (b).

selection is consistent only with the detections having a redshift  $z > 1.3$ . Galaxies in this catalogue will not all be at the same redshift as the radio-WISE selected galaxies.

In Section 3.5, I compare the surface density, radial distribution and other features of these galaxies with large comparison fields. In the 33 radio-WISE selected fields,  $\sim 7400$  Group-I galaxies are detected within the 95% completeness limits ( $\sim 225$  galaxies per field).

### 3.4.1 SpUDS and S-COSMOS Comparison Fields

SpUDS (PI: J. Dunlop) is a *Spitzer* Cycle-4 legacy program, observing  $\sim 1 \text{ deg}^2$  in the UKIDSS UDS field using IRAC and MIPS. SpUDS has a  $3\sigma$  depth of  $1 \mu\text{Jy}$  ( $m_{\text{AB}} = 24$ , Caputi et al., 2011). S-COSMOS (PI: D. Sanders) is a *Spitzer* Cycle-2 legacy program, covering the  $2 \text{ deg}^2$  of the Cosmic Evolution Survey (COSMOS) field, reaching to  $5\sigma$  depths of  $1 \mu\text{Jy}$  ( $m_{\text{AB}}=24$ , Scoville et al., 2007). These comparison fields are 3–5 times deeper than the survey in this work and are complete at the 95% flux density limits for this work, making them ideal for comparison with densities of galaxies in the radio-WISE selected fields.

To compare with the fields centred on radio-WISE galaxies, fields centred on galaxies with IRAC colours  $[3.6] - [4.5] > 0.58$ ,  $16 < [3.6] < 20.97$  and  $[4.5] < 19.85$  were cut out from the SpUDS and S-COSMOS fields, as shown in Fig. 3.8. Using the same IRAF package as Section 3.2.3, SpUDS and S-COSMOS fields were selected to have the same  $5.12' \times 5.12'$  ( $\sim 26.2 \text{ arcmin}^2$ ) dimensions as the radio-WISE selected fields. This produced 15 and 51 fields in SpUDS and S-COSMOS respectively, which were combined in all investigations as expected levels of variance were seen between these blank fields. No radio-WISE selected galaxies are found in either of these comparison fields. As shown in Fig. 3.8, the median  $[3.6]$  magnitude and  $[3.6] - [4.5]$  IRAC colour for this control sample is 19.67 and 0.68 respectively, whereas the median values for the radio-WISE selected targets are 19.18 and 1.03 respectively. This suggests that the comparison sample is much bluer and fainter than the radio-WISE targets, showing that objects with similar IRAC properties to these rare, luminous radio-WISE selected galaxies are not observed in deep, wide-area, blank fields.

Given the lack of comparison fields unlike the non-overlapping, randomly-centred SpUDS

CHAPTER 3. THE ENVIRONMENTS OF LUMINOUS RADIO-WISE  
SELECTED INFRARED GALAXIES

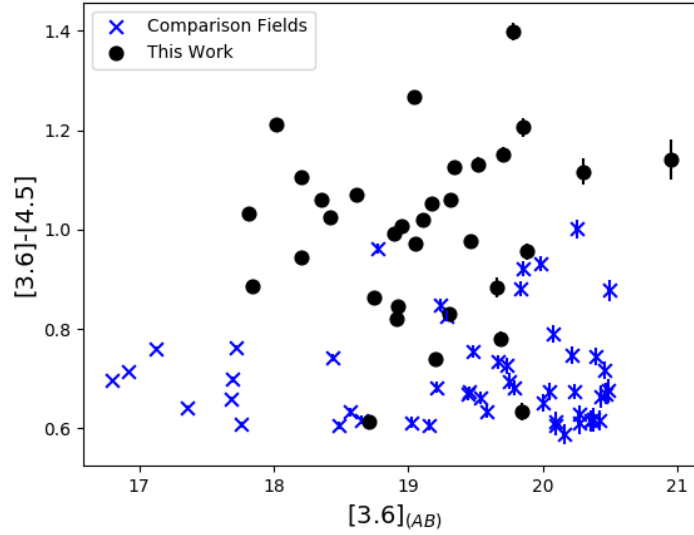


Figure 3.8: Comparison of the *Spitzer* IRAC properties between the radio-WISE selected galaxies and the central galaxies in the comparison fields (Section 3.4.1). Radio-WISE selected galaxies are represented by black points, and centred galaxies from the SpUDS and S-COSMOS fields are represented by blue crosses.

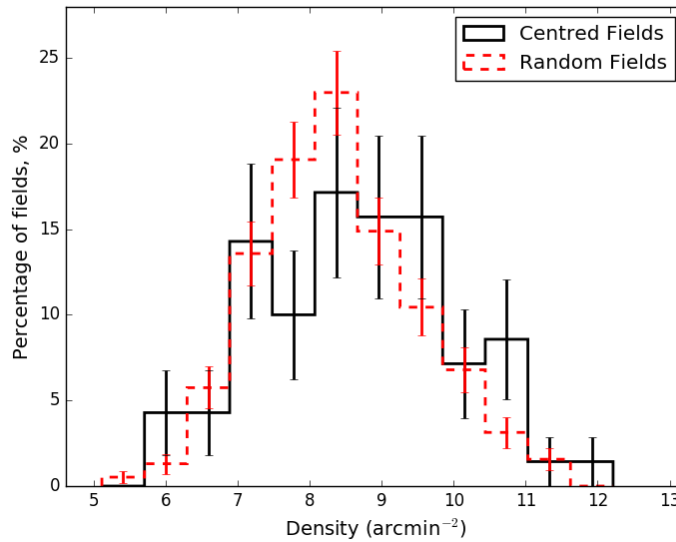


Figure 3.9: Density of the comparison fields with color selection  $[3.6] - [4.5] > -0.1$ . Fields centred randomly are shown in dashed red and those centred on galaxies with similar IRAC properties to the radio-WISE selected galaxies are shown in black.

## CHAPTER 3. THE ENVIRONMENTS OF LUMINOUS RADIO-WISE SELECTED INFRARED GALAXIES

---

fields in Wylezalek et al. (2013), the density of Group-I galaxies in the radio-WISE selected fields is compared with randomly-placed, independent pointings in the SpUDS and S-COSMOS fields of the same  $5.12' \times 5.12'$  area, which produced 96 and 288 independent  $5.12' \times 5.12'$  fields respectively. Fig. 3.9 compares the difference in density between the fields centred on galaxies with similar colours to the radio-WISE galaxies and to randomly placed fields. Using a Kolmogorov-Smirnov test (K-S test) a K-S statistic of 0.17 is found, with a  $p$ -value of 0.06 for the two subsets of the comparison fields. A result with a  $p$ -value  $> 0.05$  suggests that one cannot rule out that the two samples are drawn from the same underlying distribution and thus do not possess a significant excess. There appears to be little difference when using the fields centred on galaxies with similar IRAC properties to the radio-WISE galaxies to randomly selected fields, although the possibility that these subsets are drawn from a different underlying distribution cannot be ruled out. The more numerous randomly-centred fields are chosen to compare with the radio-WISE selected fields to increase the number of comparison fields.

### 3.4.2 Photometric Redshifts

To determine whether the two IRAC bands were significant enough to provide photometric redshifts of potential companion sources to the radio-WISE selected galaxies, the EAZY redshift code (Brammer et al., 2008) was utilised. To understand whether the code would accurately determine the redshifts from these two bands, the method was first tested on data from the z-COSMOS survey (Lilly et al., 2009), a spectroscopic survey of the COSMOS field. Using the two IRAC bands, the photometric redshifts were determined for  $\sim 520$  galaxies in the z-COSMOS survey, and compared to the spectroscopic redshifts, as shown in Fig. 3.10. A distinct lack of correlation is seen be-

### CHAPTER 3. THE ENVIRONMENTS OF LUMINOUS RADIO-WISE SELECTED INFRARED GALAXIES

---

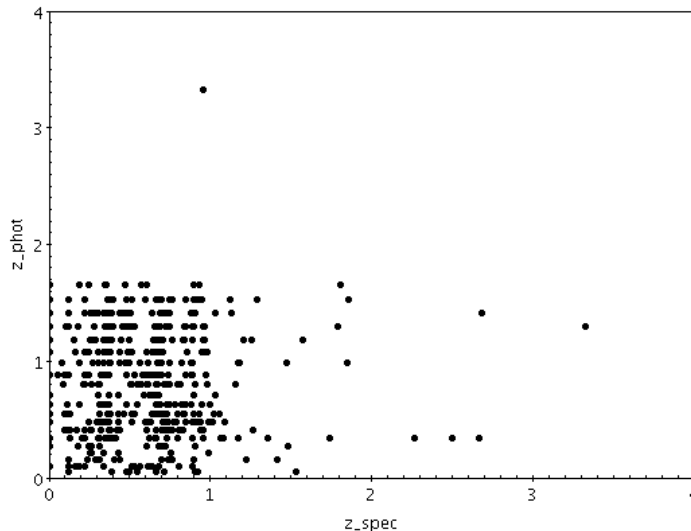


Figure 3.10: Figure showing the lack of correlation between the spectroscopic redshifts from the *z*-COSMOS survey and EAZY photometric redshifts using only  $3.6\ \mu\text{m}$  and  $4.5\ \mu\text{m}$  bands from IRAC.

tween the values in Fig. 3.10, suggesting that the two IRAC bands are not substantial enough to determine photometric redshifts for the radio-WISE selected sample.

To improve the number of bands accessible in the radio-WISE selected fields, archive data from the IR Spectrometer And Array Camera (ISAAC; Moorwood et al., 1998) was used, which provided J-band ( $1.25\ \mu\text{m}$ ) and/or Ks-band ( $2.16\ \mu\text{m}$ ) data for 21 radio-WISE selected fields, listed in Table 3.1. The same source extraction method discussed in Section 3.2.2 was used for the ISAAC fields, varying the minimum pixel number above the background to account for the smaller pixel size of the ISAAC telescope ( $0.148''/\text{pixel}$ ) and matched the extracted sources to the catalogue of the *Spitzer* radio-WISE selected fields within a  $2''$  radius ( $\sim$  PSF of *Spitzer*). The number of sources uncovered is included in Table 3.1, and shows that the number of matched sources is  $\sim 4 - 18\%$  of the total sources per field in IRAC. Using these bands, I attempted to determine the photometric redshifts of the fields with both Ks- and J-band data, using the spectroscopic redshift of the central radio-WISE target as the prior for the redshift.

### CHAPTER 3. THE ENVIRONMENTS OF LUMINOUS RADIO-WISE SELECTED INFRARED GALAXIES

---

Initially, the photometric redshifts appeared to agree with the spectroscopic redshift of the central radio-WISE selected galaxy in the field. To test whether this was due to a skew in the EAZY-code, the prior redshift was changed to  $z = 1$ , drastically different from any of the spectroscopic redshifts of the radio-WISE selected galaxies. Using this method, it was found that the photometric redshifts appeared to agree with the new prior redshift, suggesting that the photometric redshift could not be trusted. It was, therefore, decided that the photometric redshift would not be used for the rest of the investigation, and instead I would rely upon the redshift range achieved using the IRAC colours.

WISE Designation	Matched Sources (IRAC and J-band)	Matched Sources (IRAC and Ks-band)	Matched Sources (IRAC and J- and Ks-band)
W0719	...	11	...
W0823	...	21	...
W1308	16	24	11
W1343	...	15	...
W1400	...	25	...
W1412	35	36	32
W1434	...	13	...
W1500	25	39	17
W1513	12	19	10
W1541	...	13	...
W1634	8	...	...
W1641	...	21	...
W1653	...	19	...
W1702	...	15	...
W1703	27	38	19
W1936	17	16	5
W1951	...	24	...
W1958	15	11	5
W2000	...	5	...
W2021	14	17	7
W2059	...	38	...

Table 3.1: Number of galaxies matched between the ISAAC J-band ( $1.25\ \mu\text{m}$ ) and/or Ks-band ( $2.16\ \mu\text{m}$ ) with *Spitzer* observations of radio-WISE selected fields. ISAAC observations were made on several fields containing radio-WISE selected galaxies, 20 of which matching the radio-WISE selected galaxies in this work. I use a similar source extraction method detailed in Section 3.2.2 to determine whether galaxies found in warm-*Spitzer* observations are also found in ISAAC J- and/or Ks-band.

## 3.5 Results

In this section, the results of the imaging and source extraction on warm-*Spitzer* IRAC observations of the 33 fields containing radio-WISE selected galaxies are discussed. Galaxies within specific redshift ranges are selected using the IRAC-colour selection criteria discussed in Section 3.4.

### 3.5.1 Group-I Selected *Spitzer* Galaxies

The relative density of Group-I, IRAC-selected galaxies in  $5.12' \times 5.12'$  fields in the radio-WISE, SpUDS and S-COSMOS fields as a function of IRAC colour  $[3.6] - [4.5] > -0.1$  is shown in Fig. 3.11.

A modest overdensity of 10% and 12% for  $[3.6]$  and  $[4.5]$  respectively is observed across the magnitude range within the completeness limits of this work in the radio-WISE selected fields. Removing the radio-WISE galaxies, the largest excess (28% and 33% for  $[3.6]$  and  $[4.5]$  respectively) is observed in the magnitude range of  $18.5 < m_{AB} < 20.5$  for both  $[3.6]$  and  $[4.5]$ . Cosmic variance is a significant factor in the comparison fields, expected to scatter the density of galaxies found in  $5.12' \times 5.12'$  fields by  $\sim 30\%$  (Trenti & Stiavelli, 2008), greater than the observed excess in the radio-WISE selected fields. Given that the radio-WISE selected fields have been averaged, this suggests that the observed overdensity is unlikely to be caused by cosmic variance; these radio-WISE selected fields are modestly overdense. A reduced density of galaxies at fainter magnitudes in IRAC2 ( $[4.5] \gtrsim 21.7$ ) is seen, likely due to the completeness limits (see Fig. 3.4).

## CHAPTER 3. THE ENVIRONMENTS OF LUMINOUS RADIO-WISE SELECTED INFRARED GALAXIES

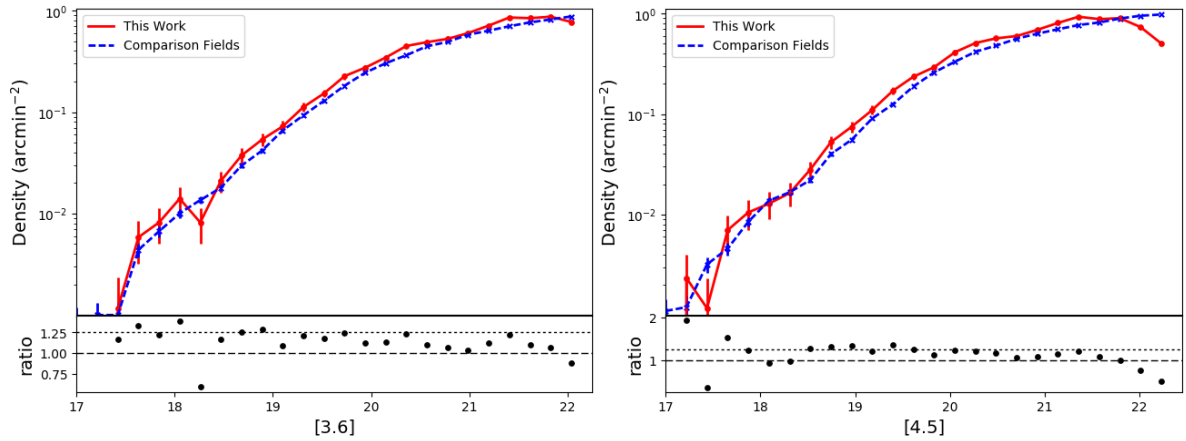


Figure 3.11: Comparison of the density of IRAC-selected galaxies in the  $33\ 5.12' \times 5.12'$  radio-WISE selected fields (solid red) in  $\text{arcmin}^{-2}\ \text{mag}^{-1}$  with respect to their magnitudes in [3.6] (left) and in [4.5] (right), with comparison fields indicated in dashed blue. Below each figure is a density ratio of the radio-WISE fields against the comparison fields. A dashed and dotted line denote a  $1\times$  and  $1.25\times$  overdensity.

The excess of  $[3.6] - [4.5] > -0.1$  galaxies is much less than found using the same IRAC colour selection around radio-loud galaxies (Wylezalek et al., 2013), suggesting that the environments of the radio-WISE galaxies are less significantly overdense in the IRAC bands than galaxies with bright radio emission. It is unlikely that this lack of excess density is due to the depth of observations in this work, given the relatively uniform overdensity across most magnitudes of this study, as shown in Fig. 3.11. The lack of a large excess relative to the comparison fields (10–25% in comparison to the  $\sim 4$ – $6\times$  overdensity seen in Jones et al. (2015) for SMGs) applies across a wide magnitude range in this study, suggesting there is no specific magnitude range associated with the radio-WISE target galaxy.

To investigate the significance of the modest  $\sim 10\%$  overdensity compared to previous work on active galaxies, the density is determined field by field. The distribution of galaxies is compared per field to the number of similar galaxies in the comparison fields, in Fig. 3.12. A Gaussian distribution was fitted to the comparison fields, giving

### CHAPTER 3. THE ENVIRONMENTS OF LUMINOUS RADIO-WISE SELECTED INFRARED GALAXIES

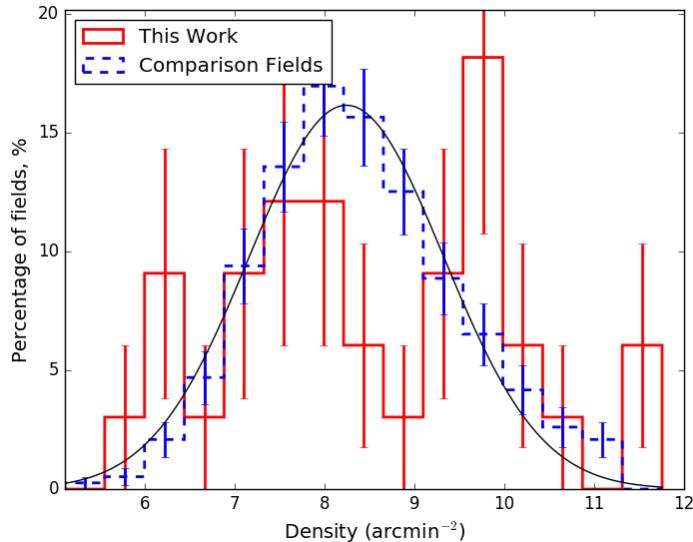


Figure 3.12: Density of galaxies across the 33  $5.12' \times 5.12'$  fields compared to 383 comparison fields with the same dimensions. Radio-WISE selected fields are indicated in solid/red and comparison fields in dashed/blue. A Gaussian distribution has been fitted to the comparison fields in black.

$8.31 \pm 1.10 \text{ arcmin}^{-2}$ . 55% of the radio-WISE selected fields exceed the mean density and 36% are denser than the mean plus  $1\sigma$  density of the SpUDS fields. In comparison, Wylezalek et al. (2013) found a greater overdensity across a sample of 420 fields centred on RLAGN, with 92% of fields denser than the comparison sample mean, significantly greater than the excess around the radio-WISE galaxies. Using a K–S test to determine whether the density of Group-I sources per field in the radio-WISE selected fields are drawn from the same sample as the comparison fields, a K–S statistic of 0.22 is found with a  $p$ -value of 0.08. The radio-WISE selected fields are not significantly denser in IRAC-selected galaxies than the comparison fields.

The radial distribution of these Group-I galaxies is compared with respect to the central radio-WISE selected galaxies to determine if there is any spatial correlation between these galaxies and the central galaxy. All 33 fields were combined to provide a distribution of Group-I galaxies away from the central radio-WISE galaxy position, which

## CHAPTER 3. THE ENVIRONMENTS OF LUMINOUS RADIO-WISE SELECTED INFRARED GALAXIES

---

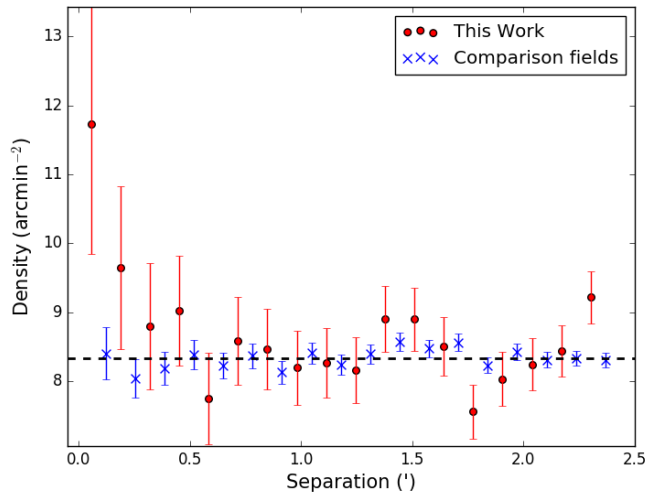


Figure 3.13: The radial distribution of IRAC-selected galaxies away from the radio-WISE selected galaxy using the entire magnitude range of this work ( $[4.5] < 22.45$ ). Galaxies have IRAC colour  $[3.6] - [4.5] > -0.1$ , out to a  $2.5'$  radius from the centre of the field. Radio-WISE selected fields are represented by red circles and the comparison fields are indicated by blue crosses. The dashed line denotes the average density of the comparison fields for reference.

was excluded from this investigation. The same distribution was constructed around the random positions for the comparison fields. As shown in Fig. 3.13, there is no overdensity beyond  $\sim 0.25'$  ( $130 \text{ Mpc}$  at  $z = 1.93$ ) from the central galaxy. To test whether this peak is produced from specific fields, random fields are omitted from the investigation, and the process repeated, with no dramatic change in the average overdensity. This suggests that this peak is seen across most of the radio-WISE selected fields. Towards the centre of the field, however, a rise in the number of Group-I galaxies is seen,  $\sim 1.33 \pm 0.20$  times the level of the comparison fields. This implies possible clustering between these Group-I galaxies and the central galaxy on small scales of  $\lesssim 0.25'$ . This overdensity towards the centre of the field could be linked to the  $\sim 10\%$  overdensity seen in Fig. 3.11. It should be noted that the result in Fig. 3.13 is obtained statistically over all 33 fields and does not represent the radial distribution of Group-I galaxies in each individual field. The peak in the figure corresponds to an average excess of  $\sim 2-3$

### CHAPTER 3. THE ENVIRONMENTS OF LUMINOUS RADIO-WISE SELECTED INFRARED GALAXIES

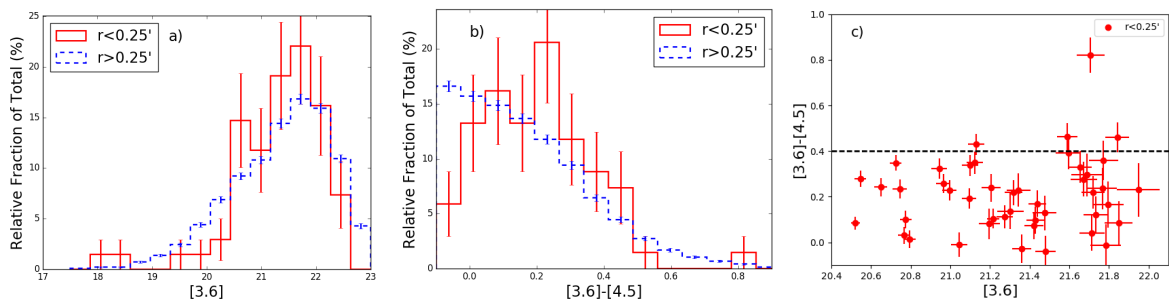


Figure 3.14: Comparison of the properties of all IRAC selected galaxies summed across all 33 radio-WISE selected fields within  $0.25'$  of the central radio-WISE galaxy to the rest of the field: (a) compares the relative fraction of galaxies in the inner  $0.25'$  radius from the radio-WISE galaxy (red line) to the relative fraction of galaxies at radii  $> 0.25'$  (blue dashed) as a function of  $[3.6]$ . (b) compares the  $[3.6] - [4.5]$  colours of the galaxies in the peak to the  $[3.6]$  (red line) to the galaxies beyond  $0.25'$  separation from the radio-WISE galaxy (blue dashed). (c) shows the colors of galaxies in the inner  $0.25'$  radius from the radio-WISE galaxy against their colour. A black line has been added to denote the minimum  $[3.6]-[4.5]$  colour observed in the radio-WISE selected galaxies.

galaxies per field within  $0.25'$  of the radio-WISE galaxy.

To determine whether this peak is produced by galaxies in a specific range of magnitudes or IRAC colours, the distribution of the  $[3.6]$  and the  $[3.6] - [4.5]$  colours of the galaxies in the inner  $0.25'$  is shown in Fig. 3.14a. The figure shows a potential modest excess of galaxies within the magnitude range of  $20.5 < [3.6] < 22$ . This excess is not significantly greater than the density for galaxies at separations  $> 0.25'$  from the radio-WISE galaxies for most values of  $[3.6]$ . Comparing the two subsets, a K-S statistic of 0.12 is found, with a  $p$ -value of 0.29 suggesting that these subsets are likely drawn from the same distribution. Comparing the IRAC colours (see Fig. 3.14b), no significant excess of galaxies within any colour range is seen, except at  $[3.6] - [4.5] \sim 0.2$ . The distribution of these subsets are different, the density of galaxies in each colour bin rising between  $-0.1 < [3.6] - [4.5] < 0.2$  within  $0.25'$ , in contrast to the rest of the field which shows a reduction in density with redder IRAC colour. Using a K-S test

### CHAPTER 3. THE ENVIRONMENTS OF LUMINOUS RADIO-WISE SELECTED INFRARED GALAXIES

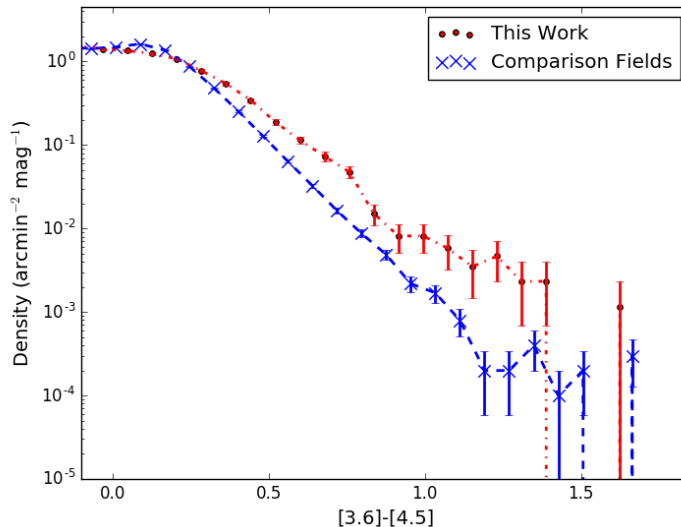


Figure 3.15: Number of galaxies ( $\text{arcmin}^{-2}$ ) as a function of IRAC ( $[3.6] - [4.5]$ ) colours. Red circular points indicate radio-WISE selected fields, excluding the central radio-WISE galaxy, blue crosses indicate the comparison fields.

for these subsets, a K-S statistic of 0.17 is found with a  $p$ -value of 0.03, suggesting that the null hypothesis that these samples are drawn from the same distribution cannot be accepted. From Fig. 3.14c, only  $\sim 10\%$  of the galaxies in the inner  $0.25'$  exhibit  $[3.6] - [4.5] > 0.4$ , in a similar colour range to the radio-WISE galaxies, suggesting that the peak in Fig. 3.13 is not composed of galaxies with similar IRAC colours to the radio-WISE galaxies. These results show that the excess of galaxies in the local  $0.25'$  environment of the radio-WISE galaxies are faint but not exceptionally red.

To investigate whether the modest overdensity shown in Fig. 3.11 can be linked to bluer or redder IRAC-selected galaxies, the density of galaxies is compared to their  $[3.6] - [4.5]$  colour, excluding the central radio-WISE selected galaxies. A distribution of the density of red galaxies is shown in Fig. 3.15. The density of redder galaxies drops off more steeply at  $[3.6] - [4.5] > 0.4$  for the SpUDS and S-COSMOS fields than in the radio-WISE fields. This is similar to the findings from CARLA (Cooke et al.,

## CHAPTER 3. THE ENVIRONMENTS OF LUMINOUS RADIO-WISE SELECTED INFRARED GALAXIES

---

2016), that there was an increasing fraction of redder galaxies around their target than in blank fields. The radio-WISE selected fields contain a greater density of increasingly red IRAC galaxies in their fields. This suggests that these radio-WISE selected galaxies reside in fields containing an excess of redder IRAC galaxies on  $5.12' \times 5.12'$  scales.

### 3.5.2 Group-II *Spitzer*-Selected Galaxies

I attempt to model the SEDs of these galaxies to probe the nature of the redder IRAC colours associated with them. Modelling galaxies within different starting conditions using EzGal, I attempted to understand what extinction level ( $A_v$ ) and formation redshift ( $z_f$ ) would produce the Group-II galaxies observed in Fig. 3.15. For galaxies consistent with the same redshift as the targets, the excess galaxies are expected to be even redder than the models for extinctions as high as  $A_v = 5$ . Given a general extinction for galaxies of  $A_v \sim 1.1$  (Sklias et al., 2014), these redder-IRAC galaxies are significantly more dusty than typical galaxies. As Fig. 3.16 shows, these colours would be consistent across the redshift range of the targets, such that the redder-IRAC colours are unlikely to be caused by redshift alone.

These redder-selected galaxies (henceforth Group-II galaxies) have similar IRAC [3.6] – [4.5] colours to the radio-WISE selected galaxies, indicating greater hot dust emission or higher levels of obscuration than field galaxies at  $z > 1.3$ . The same set of results as Section 3.5.1 are derived for these Group-II galaxies to investigate their overdensity, using a colour selection of  $[3.6] - [4.5] > 0.4$  (or a flux density ratio of  $\frac{F_{\text{IRAC}2}}{F_{\text{IRAC}1}} > \frac{7}{5}$ ). This colour cut was chosen to include the range of IRAC colours where there is an excess density of redder galaxies in the radio-WISE fields, highlighted in Fig. 3.15. It should be noted that Group-II galaxies are a subset of Group-I galaxies, and as shown in Fig. 3.14c, the peak in Fig. 3.13 is not composed of the Group-II galaxies.

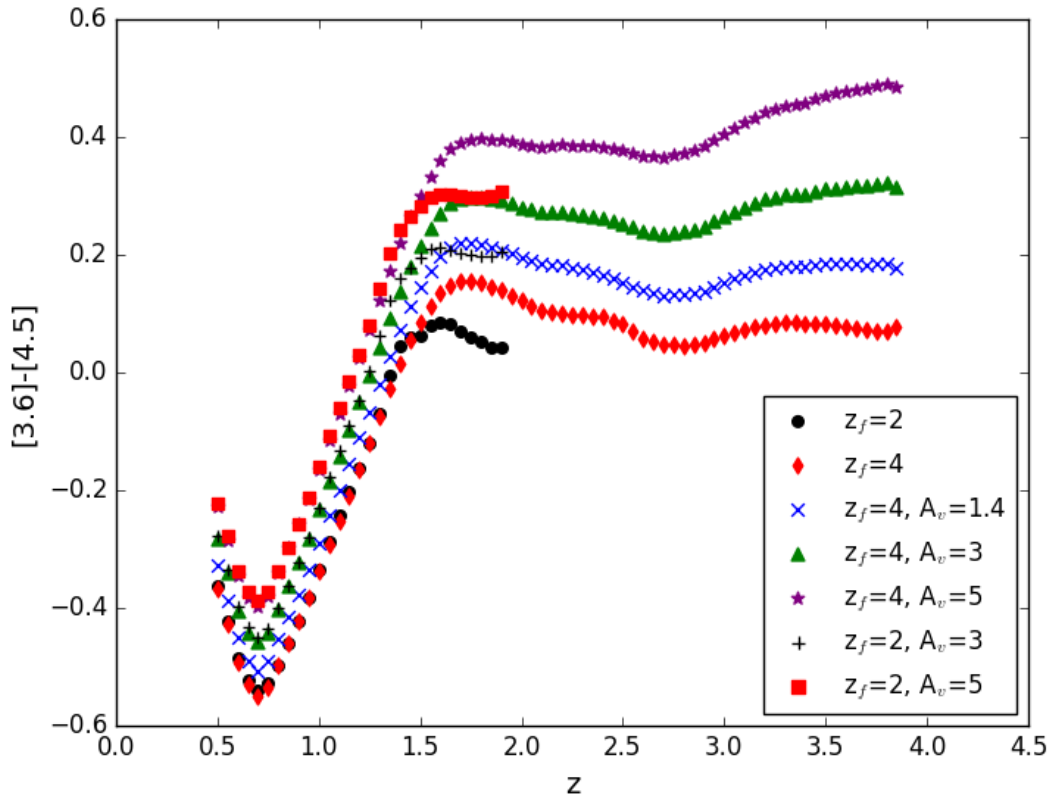


Figure 3.16: Illustration of the dependence of colour with redshift for different galaxy models at different formation redshifts,  $z_f$ . Stellar libraries are used to model these galaxies (Bruzual & Charlot, 2003), assuming a Salpeter initial mass function and a single exponentially decaying burst of star formation at  $\tau=0.1$  Gyr. The models were generated using *EzGal* (Mancone & Gonzalez, 2012) with additional dust extinction using a Calzetti law (Calzetti et al., 2000) for values of  $A_v$  to model the  $[3.6] - [4.5]$  colour for different extinction levels.

### CHAPTER 3. THE ENVIRONMENTS OF LUMINOUS RADIO-WISE SELECTED INFRARED GALAXIES

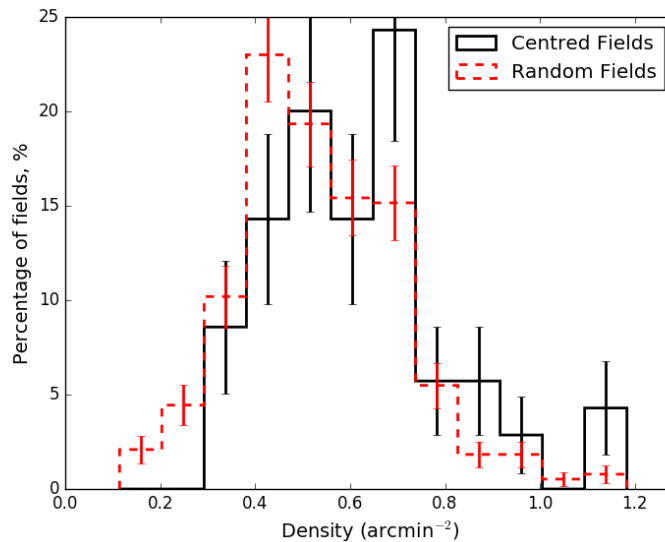


Figure 3.17: Comparison of the density of SpUDS and S-COSMOS fields with color selection  $[3.6] - [4.5] > 0.4$  between fields centred randomly and those centred on galaxies with similar IRAC properties to the radio-WISE selected galaxies. Randomly centred fields are shown in dashed red, while fields centred on galaxies are in black.

First, I determined whether the distribution of Group-II galaxies was different in the radio-WISE selected fields compared with fields centred on galaxies with similar IRAC properties to the radio-WISE galaxies and with randomly-centred fields in the SpUDS and S-COSMOS fields. The density is compared field-to-field, as shown in Fig. 3.17, after the central galaxies in these fields were removed. There does not appear to be a significant difference in the density of these Group-II galaxies between the two comparison fields. A K-S test gives a K-S statistic of 0.17 with a  $p$ -value of 0.07, suggesting that these subsets are drawn from the same underlying distribution. To increase the number of comparison fields, the randomly-centred SpUDS and S-COSMOS fields are used to compare with the radio-WISE selected fields for the Group-II galaxies.

The analysis in Section 3.5.1 is repeated for these redder-IRAC galaxies (see Fig. 3.18). The results contrast drastically to the earlier results, suggesting that the radio-WISE selected galaxies inhabit significantly overdense regions of Group-II galaxies. The mean

### CHAPTER 3. THE ENVIRONMENTS OF LUMINOUS RADIO-WISE SELECTED INFRARED GALAXIES

---

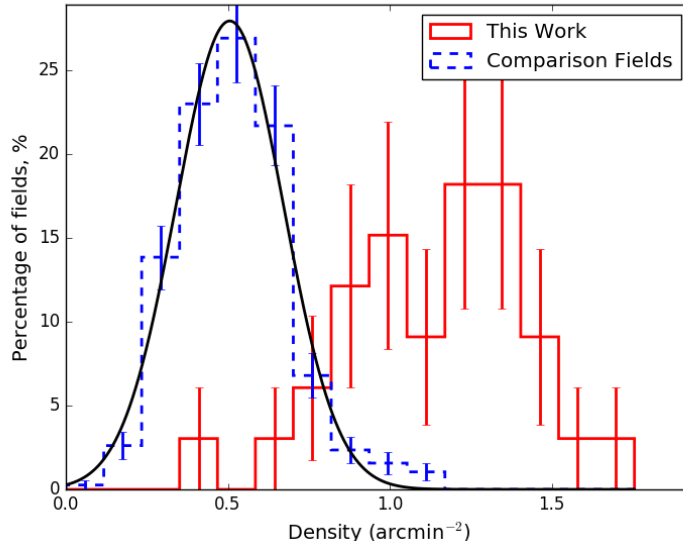


Figure 3.18: Distribution of the number of galaxies with IRAC colour  $[3.6] - [4.5] > 0.40$  per  $\sim 26.2$  arcmin<sup>2</sup> field. Radio-WISE selected fields are shown in red, comparison fields are indicated by dashed blue. A Gaussian fit has been added to the comparison fields to determine the level of overdensity for the radio-WISE selected fields, where the typical number of galaxies is  $0.47 \pm 0.16$ .

density in the comparison fields for the Group-II galaxies is  $0.47 \pm 0.16$  arcmin<sup>-2</sup> (versus  $8.31 \pm 1.1$  arcmin<sup>-2</sup> for Group-I in the comparison fields): 97% of the radio-WISE selected fields exhibit densities greater than the mean for the comparison fields and at the  $> 1\sigma$  level;  $\sim 76\%$  of fields are overdense by  $> 3\sigma$  and 33% by  $> 5\sigma$ . Since a large number of these fields exhibit significant overdensities with respect to the comparison fields, it is likely that the observed overdensity of Group-II galaxies is associated with the radio-WISE galaxy. These results suggest that the overdensity of Group-II galaxies, shown in Fig. 3.18, is significant over all of the radio-WISE selected fields. Further, by repeating the K-S test for this distribution and comparing to the SpUDS and S-COSMOS fields gives a K-S statistic of 0.83 with a  $p$ -value of  $1.68 \times 10^{-19}$ , and thus the samples are not drawn from the same underlying distribution.

To investigate the spatial distribution of the Group-II galaxies relative to the central

### CHAPTER 3. THE ENVIRONMENTS OF LUMINOUS RADIO-WISE SELECTED INFRARED GALAXIES

---

radio-WISE galaxy, the 33 fields are stacked to determine the radial distribution of these galaxies. As shown in Fig. 3.19, the overdensity of Group-II galaxies is fairly uniform across most of the field ( $\sim 1.15 \text{ arcmin}^{-2}$ ), generally  $\sim 2$  times the average density found in the comparison fields, and less than the overdensity of  $\sim 5\text{--}6$  found in Jones et al. (2015) ( $\sim 0.38 \text{ arcmin}^{-2}$ ) for rare SMGs around radio-WISE galaxies. Previous findings with ALMA around similar radio-WISE selected galaxies (Silva et al., 2015) found a surface density of  $\sim 19 \text{ arcmin}^{-2}$  in the environment detected at  $870 \mu\text{m}$ , 10 times that of blank fields within  $10''$  of the central galaxy. Further, only a single match is found using the SMG positions presented in Silva et al. (2015), albeit for a Group-I selected galaxy, suggesting that the Group-II galaxies are not IRAC counterparts to the SMGs in Silva et al. (2015). This suggests that the SMGs detected in Silva et al. (2015) are more obscured than the IRAC-selected galaxies in this work, with SEDs that peak at greater wavelengths. These SMGs are likely to be fainter at  $3.6 \mu\text{m}$  and  $4.5 \mu\text{m}$ , implied by a lack of detection in this work. Similarly, the Group-I selected galaxies may not have bright  $870 \mu\text{m}$  emission, suggested by their lack of detection in Silva et al. (2015), and could suggest that their SEDs peak at lower wavelengths. The significance of the overdensity in Fig. 3.19 is discussed further in Section 3.7.2.

An increased density of Group-II galaxies is found within  $0.5'$  of the radio-WISE galaxies with respect to comparison fields, suggesting angular clustering around the central galaxy on sub-arcmin scales, an effect that is not seen for brighter SMGs (Jones et al., 2015), which show no central concentration. This could be influenced by the large  $15''$  beam size and the low density of detections per field in Jones et al. (2015), however the overdensity of  $4\text{--}6$  in Jones et al. (2015) is greater than the  $1.95\times$  overdensity shown in Fig. 3.19, where the S/N of the overdensity of Group-II galaxies is greater than 3. The Group-II galaxies in the  $0.5'$  peak are thus not IRAC counterparts of SMGs detected at  $850 \mu\text{m}$ . Furthermore, using the positions of the SMGs in Jones et al. (2017),

### CHAPTER 3. THE ENVIRONMENTS OF LUMINOUS RADIO-WISE SELECTED INFRARED GALAXIES

---

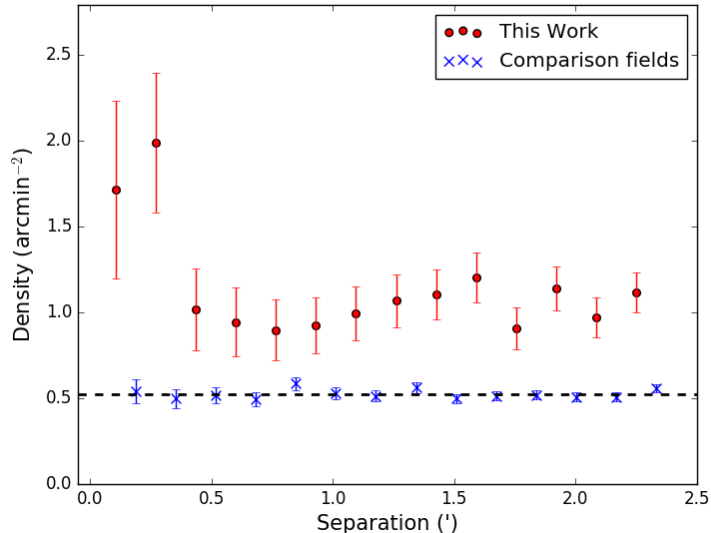


Figure 3.19: The radial distribution of Group-II galaxies with IRAC colour  $[3.6] - [4.5] > 0.4$  to a  $2.5'$  radius from the central radio-WISE galaxy. Radio-WISE selected fields are represented by red circles and comparison fields are indicated by blue crosses. The dashed line denotes the average density of the comparison fields for reference. See Fig. 3.13 for the radial distribution of Group-I galaxies for comparison.

only one galaxy matches the positions of the SMGs around the radio-WISE selected galaxies, a Group-I galaxy, confirming that these Group-II galaxies are not counterparts to the SMGs. The SMGs in Jones et al. (2015) & Silva et al. (2015) are likely to be a different subset of galaxies with low mid-IR fluxes, associated with the radio-WISE selected galaxies than the IRAC selected Group-I and Group-II galaxies in this work.

The Group-II galaxies are likely to have similar redshifts to the radio-WISE galaxies. However, little evidence of angular clustering of galaxies is observed in each individual radio-WISE selected field within  $0.5'$ , implying that this is a statistical peak from the stacking of all 33 radio-WISE selected fields in Fig. 3.19. The result is expected, however, from the distribution of faint, redder  $[3.6]$  galaxies in the local environment (see Fig. 3.14b). The statistical peak in Fig. 3.19 could be composed of mainly fainter IRAC1 objects.

### CHAPTER 3. THE ENVIRONMENTS OF LUMINOUS RADIO-WISE SELECTED INFRARED GALAXIES

---

I now compare the density of the Group-I and Group-II galaxies in each field to determine if the density of galaxies in each subset is correlated. Using a Pearson correlation test, the correlation coefficient is 0.65 with a  $p$ -value of  $4.17 \times 10^{-5}$ , suggesting that the null hypothesis that these two datasets are correlated cannot be accepted. Comparing the five densest and five sparsest fields in each subset, only one field out of the five is in common between the densest fields and three out of the five are in common between the sparsest fields for both IRAC colour selections. This also suggests that there is little correlation between the density of the Group-I and Group-II galaxies, potentially owing to the Group-II galaxies having significantly higher redshifts or residing within a protocluster compared to the Group-I galaxies, given that galaxies become progressively redder with increasing redshift (Stern et al., 2005).

I now compare the density of IRAC-selected galaxies expected to be at  $z > 1.3$  in the environment of the radio-WISE selected galaxies to the properties of the central target (Table B.1) in Fig. 3.20. Using the Pearson's correlation test, there is little correlation between the density of Group-I galaxies and the redshift of the central radio-WISE galaxy, where the correlation coefficient is  $-0.05$  with a  $p$ -value of 0.79. The correlation between the mid-IR magnitudes of the targets and the density of the Group-I galaxies is  $-0.34$  and  $-0.33$  ( $p$ -value= $0.05$  and  $0.06$ ) for IRAC1 and IRAC2 respectively. This suggests a weak anti-correlation between the density of Group-I galaxies and the mid-IR magnitudes of the central radio-WISE selected galaxies.

I also compare the density of the  $[3.6] - [4.5] > 0.4$  galaxies in each field with the properties of the central radio-WISE galaxy. Using the Pearson correlation test of the density and the redshift of the central radio-WISE galaxy, there is a coefficient of  $-0.29$  with a  $p$ -value of 0.11. This suggests one cannot rule out a weak anti-correlation between the density of Group-II galaxies and the redshift of the target. Comparing the magnitude of the central radio-WISE galaxy with density, there is a correlation coefficient of

## CHAPTER 3. THE ENVIRONMENTS OF LUMINOUS RADIO-WISE SELECTED INFRARED GALAXIES

---

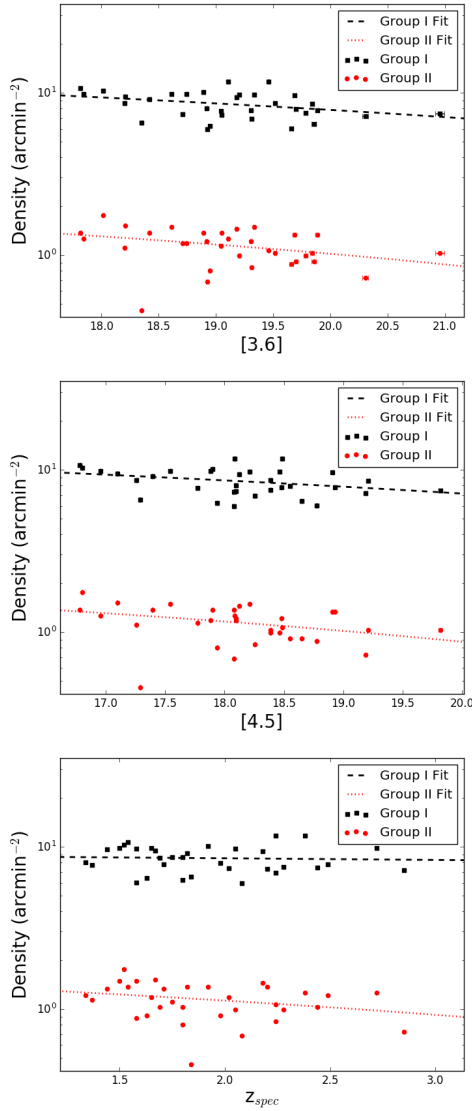


Figure 3.20: Comparison of the density of galaxies in the surrounding field, as a function of the features of the central radio-WISE selected galaxy, using the completeness limits in Section 3.2.3. (a) illustrates the distribution of [3.6] magnitude of the central radio-WISE selected galaxy against the density of the surrounding field. (b) illustrates the distribution of [4.5] magnitude of the central radio-WISE selected galaxy against the density of the surrounding field. (c) illustrates the distribution of redshift of the central galaxy with the density of the surrounding  $5.12' \times 5.12'$  field. In each, black squares show the density of Group-I galaxies and red points illustrate the density of Group-II galaxies.

### CHAPTER 3. THE ENVIRONMENTS OF LUMINOUS RADIO-WISE SELECTED INFRARED GALAXIES

---

$-0.36$  and  $-0.37$  ( $p$ -value= $0.04$  and  $0.03$ ) for IRAC1 and IRAC2 respectively. Given the  $p$ -values of this result, it is unlikely that the mid-IR flux densities of the radio-WISE galaxies are correlated with the density of their environment due to scatter. Overall, there is no correlation between the environment of the radio-WISE selected galaxies and the properties of the central radio-WISE galaxy, similar to findings by Jones et al. (2015), although a correlation between the redshift of the central target and the density of the field cannot be ruled out.

## 3.6 Angular Auto-Correlation Function

To further investigate the distribution of the two samples of IRAC-selected galaxies, the two-point angular correlation function is determined to understand whether they are clustered. On relevant scales, this excess density usually takes the form of a power-law angular function.

$$\omega(\theta) = \left(\frac{\theta}{\theta_0}\right)^{1-\gamma} \quad (3.2)$$

Using the Landy-Szalay estimator:

$$\omega(\theta) = 1 + \left(\frac{N_r}{N_d}\right)^2 \frac{DD(\theta)}{RR(\theta)} - 2 \left(\frac{N_r}{N_d}\right) \frac{DR(\theta)}{RR(\theta)} \quad (3.3)$$

(Landy & Szalay, 1993) to determine the correlation function for galaxies in the catalogue in this work, and for similar populations in SpUDS and S-COSMOS.  $N_d$  is the number of data points,  $N_r$  is the number of random comparison points randomly projected onto the same area and used as a comparison to determine whether the real

### CHAPTER 3. THE ENVIRONMENTS OF LUMINOUS RADIO-WISE SELECTED INFRARED GALAXIES

---

galaxies in the field are correlated.  $DD(\theta)$  is the number of pairs of data points with separation  $\theta$ ,  $RR(\theta)$  is the corresponding number of random pairs and  $DR(\theta)$  is the number of data-random pairs. An unclustered sample should have  $\omega(\theta) \sim 0$ .

To avoid blended sources, the smallest separation used is  $0.06'$  ( $3.6''$ ,  $\sim 2 \times \text{PSF}$ ), and also greater than the  $1.8''$  matching radius for galaxies between IRAC1 and IRAC2 in this survey. To further reduce the uncertainty, the full SpUDS and S-COSMOS fields are used, increasing the number of data pairs available for comparison. Around 14000 galaxies were used in the Group-I magnitude and colour selection for the SpUDS field and the full S-COSMOS field. An additional source of uncertainty arises in the number of random objects used to compare to a randomly distributed sample. To reduce this uncertainty, a bootstrap method (Vanderplas et al., 2012) is chosen, using 100 bootstraps for each field. The bootstrap method estimates a distribution of points by re-sampling the data, using estimates from a number of subsets to build an estimate of the total standard deviation and mean. The main advantage of the bootstrap method is that it increases the rate at which the properties of a sample can be estimated. Beyond 100 repetitions (bootstraps), little improvement in the measurement error for the correlation is observed for each radio-WISE field. Errors for each bin are calculated using the standard deviation of the correlation function for each bootstrap.

When using the AstroML method to estimate the auto-correlation function for the *Spitzer* fields containing the radio-WISE selected objects, corrections were made to the code to ensure accuracy of the results. The original AstroML code assumes that the data points ( $DD(\theta)$ ) are distributed in alignment with the line of longitude, such that there is no angle of the field with respect to the equatorial line. The AstroML code then produces a field of random data points ( $RR(\theta)$ ) between the maximum and minimum RA and DEC values assigned by the data. For fields in alignment with the equatorial line, this would produce a random field overlapping the data field, and thus  $DR(\theta)$

## CHAPTER 3. THE ENVIRONMENTS OF LUMINOUS RADIO-WISE SELECTED INFRARED GALAXIES

---

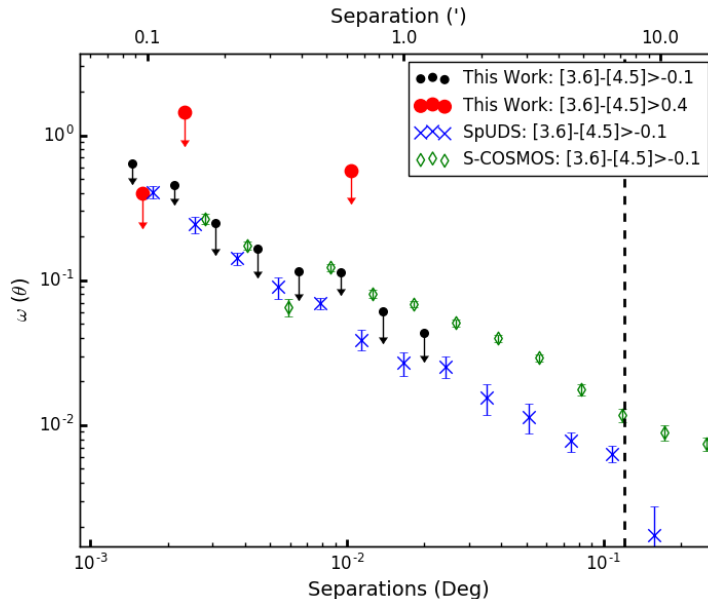


Figure 3.21: Angular two-point correlation function for both colour selections in this work.  $2\sigma$  upper limits for the Group-I galaxies in the radio-WISE selected fields are shown by black circles,  $2\sigma$  upper limits for the Group-II galaxies in the radio-WISE selected fields given by red circles. The mean for the two comparison fields have been shown separately; the full  $1 \text{ deg}^2$  SpUDS field is indicated by blue crosses, while the full  $2 \text{ deg}^2$  S-COSMOS field is indicated by green diamonds.

is always representative of  $DD(\theta)$  and  $RR(\theta)$ . However, the *Spitzer* fields containing the radio-WISE selected galaxies and the SpUDS field have random orientations with respect to the equatorial line, thus producing random fields far larger and misaligned to the data field. To solve this, the AstroML code was corrected to produce a random comparison sample in alignment with the target field.

Previous angular two-point correlation functions for IRAC galaxies have found  $\theta_0 \sim 0.03'$  and  $\gamma \sim 1.8$  (e.g. Oliver et al., 2004; Waddington et al., 2007; Papovich, 2008). Typically, Oliver et al. (2004) and Waddington et al. (2007) observe the clustering of galaxies at  $z \sim 0.75$  using SWIRE, with IRAC1  $5\sigma$  flux density limits of  $3.7 \mu\text{Jy}$  and 50% completeness in IRAC1 at  $4 \mu\text{Jy}$  for Oliver et al. (2004) and Waddington et al.

### CHAPTER 3. THE ENVIRONMENTS OF LUMINOUS RADIO-WISE SELECTED INFRARED GALAXIES

---

(2007) respectively. Papovich (2008), who introduced the selection technique in this work, selected  $z > 1.3$  galaxies using  $[3.6] - [4.5] > -0.1$ , with  $5\sigma$  flux limits of 3.7 and  $5.4\mu\text{Jy}$  for IRAC1 and IRAC2 respectively. It should be noted that, due to the size of the fields here, the angular correlation function for the radio-WISE selected fields is only probed on small scales of  $\lesssim 5'$ .

The results of the two-point angular auto-correlation function for the radio-WISE selected fields are shown in Fig. 3.21. For the Group-I galaxies,  $\theta_0 = 0.026' \pm 0.013'$  and  $\gamma = 2.26 \pm 0.42$  ( $\chi^2 = 0.22$  with 6 degrees of freedom). The value of  $\gamma$  for the radio-WISE selected fields is much larger than previous values observed in SWIRE (Oliver et al., 2004; Waddington et al., 2007), suggesting that the clustering of galaxies decreases quicker than other fields. The value of  $\theta_0$  is roughly equal to the accepted value, and suggests that the Group-I galaxies in the radio-WISE selected fields are no more clustered than in blank fields. This is unusual, given that the galaxies selected in the SWIRE fields are generally at lower redshifts than this work and could be due to the large range of potential redshifts that the Group-I IRAC colour selection encompasses, such that galaxies at significantly different redshifts could be paired in this investigation. However, without deep coverage of these fields in other bands, as shown in Section 3.4.2, determining photometric redshifts of these galaxies is unfeasible.

There is a slight difference in the two-point angular auto-correlation function between the SpUDS and S-COSMOS fields. This could be due to cosmic variance or the wide range of redshifts in the Group-I and Group-II colour selection. Using a Pearson correlation test for the comparison fields gives a correlation coefficient of 0.96 with a  $p$ -value of  $3.27 \times 10^{-27}$ , suggesting that the null hypothesis that the two comparison samples are drawn from the same distribution is not valid, and suggests that there is significant deviation at larger separations between the two comparison fields. For the SpUDS field, using Group-I colour limits,  $\theta_0 = 0.056' \pm 0.002'$  and  $\gamma = 2.38 \pm 0.05$  ( $\chi^2 = 15.8$

### CHAPTER 3. THE ENVIRONMENTS OF LUMINOUS RADIO-WISE SELECTED INFRARED GALAXIES

---

with 11 degrees of freedom). For the S-COSMOS field, using the same colour selection,  $\theta_0 = 0.029' \pm 0.009'$  and  $\gamma = 1.80 \pm 0.11$  ( $\chi^2 = 44.6$ ), in agreement with previous values for the two-point angular auto-correlation function. The value of  $\gamma$  for the SpUDS field agrees with the value for the radio-WISE selected fields for the Group-I colour selection, while the value of  $\gamma$  for the S-COSMOS field is smaller than the value for the radio-WISE selected fields, suggesting that the clustering of the Group-I galaxies in the radio-WISE selected fields decreases at the same rate or greater compared to blank fields for this colour selection. The value of  $\theta_0$  for the SpUDS field is greater than the radio-WISE selected fields for the Group-I selection, suggesting that the radio-WISE selected fields are no more clustered than blank fields for this IRAC colour selection.

A K-S test is used to determine whether there is a significant difference in the correlation function between the comparison fields and the radio-WISE selected fields. For the SpUDS field, a K-S statistic of 0.31 is found, with a  $p$ -value of 0.65. Similarly, for the S-COSMOS field, a K-S statistic of 0.29 is found, with a  $p$ -value of 0.73, suggesting that it is likely that the comparison fields and the radio-WISE selected fields are drawn from the same distribution. From these results, it is unlikely that many of the Group-I galaxies in the radio-WISE selected fields are associated with one another, although they may be related to the radio-WISE selected galaxy, given the peak in Fig. 3.13. This lack of correlation is expected, given that the Group-I colour selection should only indicate the galaxies have a redshift  $z > 1.3$ , giving them a large range of potential redshifts.

For the Group-II galaxies, the auto-correlation function finds a value of  $\theta_0 = 0.072' \pm 0.013'$  and  $\gamma = 3.10 \pm 0.20$  ( $\chi^2 = 4.23$  with 2 degrees of freedom), shown by the red-distribution in Fig. 3.21. The value of  $\gamma$  is significantly larger than the values for the Group-I selection suggesting that there is a significant decrease in clustering for these galaxies, although this is likely due to the lack of positive  $\omega(\theta)$  values. Given the lack

## CHAPTER 3. THE ENVIRONMENTS OF LUMINOUS RADIO-WISE SELECTED INFRARED GALAXIES

---

of correlation at radii  $\lesssim 0.5'$  for the Group-II galaxies in the radio-WISE fields, due to the small densities of galaxies at these scales, it is impossible to comment on the correlation of the  $0.5'$  peak in Fig. 3.19. Due to the small densities of Group-II galaxies in the comparison fields, (see Fig. 3.18), the entire SpUDS and S-COSMOS fields are combined. Using this method,  $\theta_0 = 0.11' \pm 0.04'$  and  $\gamma = 2.27 \pm 0.22$  ( $\chi^2 = 1.19$  with 6 degrees of freedom). The values for the comparison fields are close to the values found in previous work (Oliver et al., 2004; Waddington et al., 2007), suggesting that the Group-II selected galaxies in the comparison fields are more correlated than those in the radio-WISE selected fields. However, given the uncertainties associated with counting galaxies in the  $5.12' \times 5.12'$  fields compared to the significantly reduced errors on larger scales, observations on larger fields around the radio-WISE galaxies would be needed to better understand the correlation for this IRAC colour selection.

### 3.7 Discussion

In this section, I discuss the results of the radio-WISE selected fields with respect to the comparison fields and previous work on other dust obscured galaxies selected using WISE. It should be noted that the overdensities of SMGs to IRAC-selected overdensities around radio-WISE galaxies are compared but without additional information it cannot be determined if galaxies in this work are IRAC counterparts of SMGs.

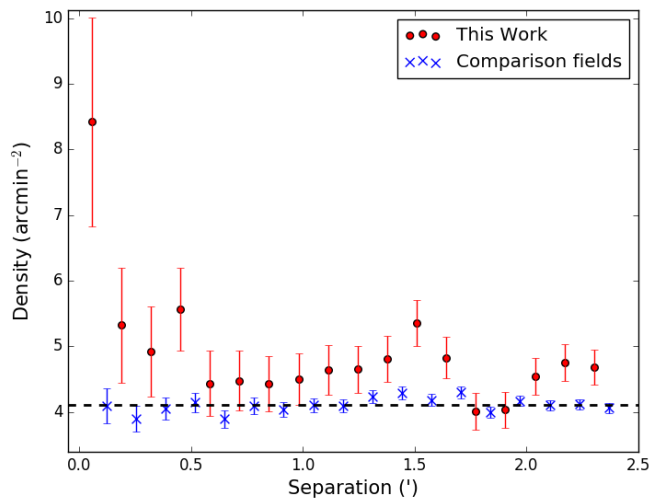


Figure 3.22: Radial distribution of Group-I galaxies for the radio-WISE selected fields (red points) cut at the limits used in Assef et al. (2015) ( $[4.5] = 10 \mu\text{m}$ ). The density of the comparison fields (blue crosses) are included to show the expectation from blank fields.

### 3.7.1 Overdensity of Galaxies in Radio-WISE Selected Fields

Targeted *Spitzer* observations of fields containing radio-WISE galaxies suggest that these galaxies do not inhabit significantly overdense regions of Group-I ( $[3.6] - [4.5] > -0.1$ ) galaxies on scales extending over  $2.5'$ . There is also no significant excess variance in the distribution of density of such galaxies in the radio-WISE selected fields.

Shallower observations ( $\sim 150$  s per field, giving a completeness limit of  $10 \mu\text{Jy}$ ) of 90 Hot DOGs by Assef et al. (2015) using *Spitzer* with the same IRAC colour selection find a density of Group-I galaxies of  $\sim 5\text{--}6 \text{ arcmin}^{-2}$  within a 95% completeness limit of  $10 \mu\text{Jy}$  in IRAC2. Similar to findings by Jones et al. (2014) for 10 Hot DOGs at  $850 \mu\text{m}$ , Assef et al. (2015) see no signs of angular clustering around the central Hot

## CHAPTER 3. THE ENVIRONMENTS OF LUMINOUS RADIO-WISE SELECTED INFRARED GALAXIES

---

DOG within  $2'$  radius. To compare the density of Group-I galaxies in the radio-WISE selected fields to the *Spitzer* fields containing Hot DOGs in Assef et al. (2015), the data for the radio-WISE selected fields is cut to the same  $10 \mu\text{Jy}$  completeness limit in IRAC2. A density of  $4.77 \pm 0.75 \text{ arcmin}^{-2}$  is found using this method, similar to the findings by Assef et al. (2015), albeit still with a central, statistical peak within  $\sim 0.25'$  of the radio-WISE selected galaxy, shown in Fig. 3.22. This suggests that the density of Group-I galaxies in the radio-WISE selected fields is consistent with fields containing Hot DOGs, although there is an additional peak in the density towards the radio-WISE galaxies.

### 3.7.2 Radial Distribution

There is a  $> 2\sigma$  peak ( $\sim 1.85 \text{ arcmin}^{-2}$ ) in the density of Group-I galaxies within  $0.25'$  ( $\sim 130 \text{ kpc}$ ) of 33 radio-WISE galaxies (Fig. 3.13), a statistical finding. This peak implies an excess of associated galaxies on relatively small scales, consistent with findings for galaxies selected at longer wavelengths with ALMA (Silva et al., 2015). Beyond  $0.25'$ , there is no observed excess density of Group-I galaxies out to  $2.5'$ , showing that the central  $0.25'$  peak is responsible for the  $\sim 10\%$  overdensity observed in Fig. 3.11. The central peak in density of Group-I galaxies ( $\sim 10.7 \text{ arcmin}^{-2}$ ) is composed of fainter IRAC1 galaxies than the radio-WISE selected galaxies, in the magnitude range of  $20.5 < [3.6] < 22$ , which do not generally exhibit redder-IRAC colours, as shown in Fig. 3.14c. These faint galaxies are unlikely to be artefacts of the image, as shown in Fig. 3.7d the galaxies in this magnitude range are visibly discernible from the background of the image. These galaxies could be influenced by the central radio-WISE galaxy, although it is unclear what mechanisms in the environment or from the target galaxy would account for them. The lack of redder-IRAC colours suggests

### CHAPTER 3. THE ENVIRONMENTS OF LUMINOUS RADIO-WISE SELECTED INFRARED GALAXIES

---

that the galaxies within  $0.25'$  of the central target are not heavily dust obscured and are unlikely to possess populations of older, redder stellar populations.

Jones et al. (2015) find an extended overdensity of very luminous sub-millimeter galaxies on  $1.5'$  radius scales,  $\sim 4$ – $6$  times that of blank fields. The very luminous SMGs in the environment of radio-WISE galaxies seen in Jones et al. (2015) are a different population to the Group-I galaxies in this work, given the different excess densities and lack of corresponding positions, where the overdensity in this work is  $\sim 1.3$  compared to  $\sim 4$ – $6$  in Jones et al. (2015). Despite the lower density of Group-I galaxies in this work, there is significantly greater angular clustering within  $0.25'$  of the radio-WISE selected galaxy (see Fig. 3.13) than in the field. This could suggest that the Group-I galaxies are influenced by the central radio-WISE galaxy. A lack of star-forming galaxies within  $0.25'$  of the radio-WISE galaxy is observed in ALMA (Silva et al., 2015), which saw a reduced density in SMGs in close proximity to the radio-WISE galaxies in their sample. However, it is unlikely that they are IRAC counterparts to the SMGs in Silva et al. (2015), given the lack of corresponding positions and the difference in the observed excess between these works. Without further information on the galaxies in this peak, it cannot be determined whether this is just a statistical fluctuation and how the radio-WISE galaxy could be influencing the galaxies within  $0.25'$  radius.

The peak in Fig. 3.13 is similar in spatial extent to the findings for HzRGs in Wylezalek et al. (2013), who suggested an association between these central HzRGs and the Group-I galaxies. The radio luminosities of the radio-WISE galaxies in this work are substantially lower than the HzRGS in CARLA, and have been selected for their less extended radio emission. The density in the peak is significantly less than that seen in CARLA, where  $\sim 20$  detections  $\text{arcmin}^{-2}$  are found in the central  $0.25'$ . From the luminosity functions in Wylezalek et al. (2014), the additional  $\sim 0.5$  magnitude depth

### CHAPTER 3. THE ENVIRONMENTS OF LUMINOUS RADIO-WISE SELECTED INFRARED GALAXIES

---

in CARLA does not double the expected density, so the radio-WISE selected fields are not as overdense in Group-I galaxies as the radio-loud galaxies in CARLA.

Unlike the Group-I galaxies, the Group-II galaxies in the radio-WISE selected fields show a significant spatially-uniform overdensity of 1.95 between  $0.5' - 2.5'$  from the targets. This overdensity is roughly half the overdensity of SMGs in the environment of ultra-luminous, dusty galaxies in Jones et al. (2015), which found overdensities of 4–6 for SMGs within  $1.5'$  of the radio-WISE galaxy compared to blank fields. These Group-II galaxies could be star-forming galaxies (Casey, 2016), however IRAC is not sensitive to star formation at these redshifts, and any speculation is inconclusive without further information. Deeper, multi-wavelength observations are necessary to determine whether these Group-II galaxies are at the same redshift as the radio-WISE galaxy.

There is an additional peak in the distribution of the Group-II galaxies within  $0.5'$  from the central radio-WISE galaxy (Fig. 3.19). This peak represents an overdensity  $\sim 2\sigma$  greater than the field, reaching 3–4 times the average density of the comparison fields, similar to the overdensity of Group-I galaxies in Wylezalek et al. (2013) using similar completeness limits and for SMGs in Jones et al. (2015). The overdensity of Group-II galaxies in this peak (3.53 times that of blank fields) is similar to the overdensity of 4–6 observed by Jones et al. (2015) on  $3'$  diameter fields, using shallower data than Silva et al. (2015). This suggests that these Group-II galaxies are dust obscured, similar to the SMGs in Jones et al. (2015), although they are not IRAC counterparts. Given the smaller overdensities of these galaxies with respect to blank fields within  $0.5'$  of the central target, compared to the overdensities observed in Silva et al. (2015) ( $\sim 10$  times the density observed in blank fields), these Group-II galaxies are not IRAC counterparts to the ALMA detected SMGs around the same class of galaxy. The excess of Group-II galaxies is likely to be linked to the presence of the radio-WISE selected galaxy, given the  $> 2\sigma$  statistical overdensities observed in the peak in Fig. 3.19.

## CHAPTER 3. THE ENVIRONMENTS OF LUMINOUS RADIO-WISE SELECTED INFRARED GALAXIES

---

I speculate that the excess of Group-II galaxies could be caused from infall into the cluster, producing bursts of star formation as the galaxies interact with gas from the Intra-Cluster Medium (ICM). Gas from the Inter-Stellar Medium (ISM) in these galaxies would be compressed by interactions with the ICM, and this dust-enshrouded star formation could produce the observed redder-IRAC colours. The Group-II galaxies in the  $0.5'$  peak are also likely to be dust obscured, star-forming galaxies similar to the redder galaxies in the Spiderweb field (Kurk et al., 2004). If Group-II galaxies  $\lesssim 0.5'$  from the radio-WISE galaxy interacted with one another and/or the central radio-WISE galaxy in a potentially forming cluster, this could also stir up a dusty envelope to produce the observed redder IRAC colours (Dannerbauer et al., 2014). Further work is necessary to understand the  $> 2\sigma$  peak in the distribution of these red IRAC galaxies around the radio-WISE selected galaxy, and the spatially uniform excess density between  $0.5' - 2.5'$  from the targets.

### 3.8 Summary

The results of *Spitzer* IRAC imaging on  $5.12' \times 5.12'$  fields centred on radio-WISE selected galaxies are:

- The radio-WISE selected fields are found to have a similar density of IRAC selected galaxies with colour  $[3.6] - [4.5] > -0.1$  to blank fields, with only a modest 10% overdensity of Group-I selected galaxies. Using a K-S test for the density of Group-I galaxies in each  $5.12' \times 5.12'$  field, a K-S statistic of 0.22 is found, with a  $p$ -value of 0.08, suggesting that these fields are drawn from the same distribution and thus there is no significant overdensity of galaxies with IRAC colours indicating  $z > 1.3$  in the radio-WISE selected fields.

### CHAPTER 3. THE ENVIRONMENTS OF LUMINOUS RADIO-WISE SELECTED INFRARED GALAXIES

---

- Using a redder IRAC colour selection of  $[3.6] - [4.5] > 0.4$ , there is a significant overdensity of Group-II galaxies by a factor of 1.95 on average with respect to blank fields within a radius of  $2.5'$  of the central radio-WISE galaxy. A significant overdensity of  $> 3\sigma$  is seen compared with blank fields in 76% of the radio-WISE selected fields, suggesting that these galaxies inhabit dense regions of redder-IRAC galaxies.
- Smaller overdensities are observed compared with Jones et al. (2015) and Silva et al. (2015) findings for SMGs around galaxies also selected from WISE and radio surveys.
- However, unlike the SMGs in Jones et al. (2015), there is a statistical peak in density on scales  $< 0.25'$  from the central radio-WISE galaxy for both colour selections. Many of these galaxies could have similar redshifts to the central radio-WISE galaxy.
- The radio-WISE galaxies appear to be signposts for overdense regions of red galaxies (Silva et al., 2015) and as such could be used to help understand the nature of galaxy and cluster formation during the epoch of peak star formation ( $z \sim 2$ ) (Eisenhardt et al., 2012; Jones et al., 2015).

With the launch of the James Webb Space Telescope (JWST)<sup>4</sup> in 2021, very deep multi-band searches could be made to investigate the central peak of the Group-II galaxies in these fields, highlighted in Fig. 3.19. With the much improved depth of JWST observations, the peak from the faint galaxies can be further investigated to better understand the distribution and nature of these faint galaxies and uncover potentially further fainter counterparts. Deep multi-band searches would also be able to determine

---

<sup>4</sup><https://www.jwst.nasa.gov/>

### CHAPTER 3. THE ENVIRONMENTS OF LUMINOUS RADIO-WISE SELECTED INFRARED GALAXIES

---

the extent to which foreground and background galaxies contribute to the peaks observed in the radial distribution of these fields with respect to the central radio-WISE galaxy.

# Chapter 4

## JVLA Observations of Cold Gas around Hot DOGs

This chapter presents  $\sim 30$  GHz JVLA observations of six Hot Dust Obscured Galaxies (Hot DOGs; Penney et al., in prep.) that were previously presented in Tsai et al. (2015). These Hot DOGs were selected using the WISE All-Sky Survey for bright detections at  $12\ \mu\text{m}$  (W3) and/or  $22\ \mu\text{m}$  (W4) and faint detections at  $3.4\ \mu\text{m}$  (W1) and  $4.5\ \mu\text{m}$  (W2), using a selection of:  $W4 < 7.7 \cap (W2 - W4) > 8.2$ , or  $W3 < 10.6 \cap (W2 - W3) > 5.3$  (Eisenhardt et al., 2012).

### 4.1 Introduction

Galaxy evolution models currently predict that the majority of massive galaxies ( $M_* \gtrsim 10^{12} M_\odot$ ) evolve via major mergers at high redshift (see Conselice, 2014, and

## CHAPTER 4. JVLA OBSERVATIONS OF COLD GAS AROUND HOT DOGS

---

references therein). This major-merger theory could be key to understanding how elliptical and Ultra-Luminous Infrared Galaxies (ULIRGs) at low redshifts form (Toomre, 1977; Barnes & Hernquist, 1998; Kormendy & Bender, 2012). It is now understood that these mergers cause large quantities of gas and dust to be forced into the central regions of the galaxies, with some accreting onto a central Supermassive Black Hole (SMBH) and some producing a burst of high-mass star formation (Sanders et al., 1988a; Barnes & Hernquist, 1992; Schweizer & Seitzer, 1998) as cold gas condenses in giant molecular clouds.

Radio observations are critical to understanding the star formation histories of galaxies at high redshift, providing estimates on the dynamics of the cold star-forming gas within the host galaxy. Molecular Hydrogen (henceforth H II) gas best traces regions of star formation, however the H II gas has strongly forbidden transitions and can only be observed at high temperatures ( $T > 100$  K). The second most abundant molecular gas in the universe however,  $^{12}\text{CO}$ , is readily excited. The lowest  $^{12}\text{CO}$  transition,  $^{12}\text{CO}(J=1-0)$  (henceforth CO(1-0)), best traces the coldest molecular gas (Greve et al., 2003; Ivison et al., 2011; Riechers et al., 2011). CO(1-0) transitions are generally fainter than higher transitions (Riechers et al., 2011), but should more accurately estimate the star formation rates in galaxies, depending on the activity of the galaxy. By assuming  $^{12}\text{CO}$  and H II are linked (Solomon et al., 1997; Tacconi et al., 2008; Bolatto et al., 2013), the mass of the H II regions can be estimated. Further, detections of the lowest  $^{12}\text{CO}$  transitions can be used in tandem with higher transitions (e.g. J=4-3) to understand properties such as local density, the star formation rate and temperature of the star-forming gas in the galaxies (e.g. Peñaloza et al., 2017). Thus, using low-J  $^{12}\text{CO}$  observations, one can understand the rates of star formation occurring in high redshift galaxies, including high- $z$ , powerful Active Galactic Nuclei (AGN).

As discussed in Chapter 1, Hot DOGs are Hyper-luminous Infra-Red (IR) Galaxies

## CHAPTER 4. JVLA OBSERVATIONS OF COLD GAS AROUND HOT DOGS

---

(HyLIRGs); initially discovered using the Wide-field IR Survey Explorer (WISE; Wright et al., 2010) All-Sky Survey. They were selected to have faint or no detections in the W1 ( $3.5\ \mu\text{m}$ ) and W2 ( $4.6\ \mu\text{m}$ ) bands, and bright detections in the W3 ( $12\ \mu\text{m}$ ) and W4 ( $22\ \mu\text{m}$ ) bands (Eisenhardt et al., 2012). Follow-up observations to determine more complete SEDs (Wu et al., 2012) suggest significantly higher dust temperatures ( $\gtrsim 60\ \text{K}$ ) than most dusty galaxies, with a peak in their SED at  $\sim 22\ \mu\text{m}$ .

Far-IR (henceforth FIR) observations of a sub-sample of Hot DOGs have confirmed significantly high IR luminosities ( $> 10^{13}\ L_{\odot}$ ; Jones et al., 2014; Tsai et al., 2015). Optical spectroscopy of the most luminous of these galaxies revealed evidence of emission lines from obscured AGN, needed to explain their significantly high luminosities and dust temperatures (Tsai et al., 2015). Follow-up observations using *Spitzer* show mid-IR SEDs that appear to be dominated by obscured AGN emission (Assef et al., 2015). 850- $\mu\text{m}$  SCUBA-2 observations by Jones et al. (2014) show these galaxies inhabit overdense environments of Sub-millimeter Galaxies (SMGs),  $\sim 3$  times overdense compared to blank fields within  $1.5''$  of the galaxies. Assef et al. (2015) used warm-*Spitzer* observations to show these galaxies reside within regions with surface densities of IRAC colour-selected galaxies consistent with fields containing radio-loud AGN (Wylezalek et al., 2013) on  $1'$  radius scales, as discussed in Chapter 3.

In this chapter, I present CO(1–0) (rest frequency: 115.3 GHz) observations of a sub-sample of six ultra-luminous Hot DOGs from Tsai et al. (2015) using the lowest-resolution configuration of the JVLA, see Table 4.1. These galaxies were selected for their extremely high luminosities ( $L_{\text{bol}} \geq 10^{14}\ L_{\odot}$ ) and redshifts  $z \gtrsim 3$ . This work uses observations from the JVLA to infer the masses of the H II regions, CO(1–0) luminosities and rest frame 115.3 GHz continuum fluxes of these galaxies to understand the processes in these highly obscured galaxies at the redshift of major mergers, starbursts and AGN activity.

WISE Designation	RA (J2000)	DEC (J2000)	$z$	Major (arcsec)	Minor (arcsec)	PA (Deg)
W0116-0505	01:16:01.49	-05:05:05.1	3.173	4.00	2.62	-30.96
W0126-0529	01:26:11.95	-05:29:09.1	2.937	4.17	2.44	-36.48
W0410-0913	04:10:10.62	-09:13:05.8	3.630*	4.08	2.92	-9.59
W0831+0140	08:31:53.25	01:40:10.3	3.912	3.78	3.06	-2.69
W1322-0328	13:22:32.55	-03:28:42.7	3.043	3.37	2.52	6.28
W2305-0039	23:05:25.93	-00:39:25.3	3.106	3.61	2.64	-29.03

Table 4.1: Properties of the sample in this paper, showing the position, redshift, major and minor axis of the synthesized beam in the images, and the position angle of the synthesized beam. Redshifts have been taken from Tsai et al. (2015) using multi-wavelength spectroscopy, although W0126 has an ambiguous redshift detection, which will be discussed in Section 4.3. Here, (\*) shows a redshift identification from CO(J=6-5) emission.

## 4.2 Observations and Data Reduction

Observations of six Hot DOGs presented in Table 4.1 were carried out in 1 – 2 hr blocks during generally excellent weather conditions between February and April 2017. The most compact baseline for detection, D-configuration, was used for the observations due to its greater surface brightness sensitivity, at the cost of a reduced angular resolution. Two observation blocks were used for each galaxy in this sample, except for W0126, which had a single  $\sim 2$  hr observation. K-Band ( $\nu=18.0\text{--}26.5$  GHz) observations were made for W0410 and W0831, and Ka-Band ( $\nu=26.5\text{--}40.0$  GHz) observations were made for W0116, W0126, W1322 and W2305. A single polarization was used, and the flux calibrators for each field were 3C48 (W0116, W0126 and W2305), 3C138 (W0410 and W0831), and 3C286 (W1322). The observations produced  $\sim 1$  GHz bandwidth spectra centred on the expected CO(1–0) emission peak ( $\nu_{\text{rest}} = 115.3$  GHz; Morton & Noreau, 1994) indicated by optical/IR spectra in Tsai et al. (2015).

Calibration and imaging were carried out using the Common Astronomy Software Application (CASA; McMullin et al., 2007)<sup>1</sup>. Calibrations were made using the publicly available calibration pipeline<sup>2</sup> for all fields except W1322, in which the calibration method detailed in the online calibration cookbook<sup>3</sup> was used for one of the two observation blocks on this field. This was due to features affecting the final imaging from a bad reference antenna used in the pipeline. The pattern produced by using the bad antenna is shown in Fig. 4.1, and from the striped pattern present in the image, it is clear that a bad antenna was being used as a reference antenna during the calibration stage, producing a degraded image. This issue is not the first instance, with previous

---

<sup>1</sup><http://casa.nrao.edu>

<sup>2</sup>[science.nrao.edu/facilities/vla/data-processing/pipeline/scripted-pipeline](http://science.nrao.edu/facilities/vla/data-processing/pipeline/scripted-pipeline)

<sup>3</sup>[casaguides.nrao.edu/index.php/TWHydraBand7\\_Imaging\\_4.3](http://casaguides.nrao.edu/index.php/TWHydraBand7_Imaging_4.3)

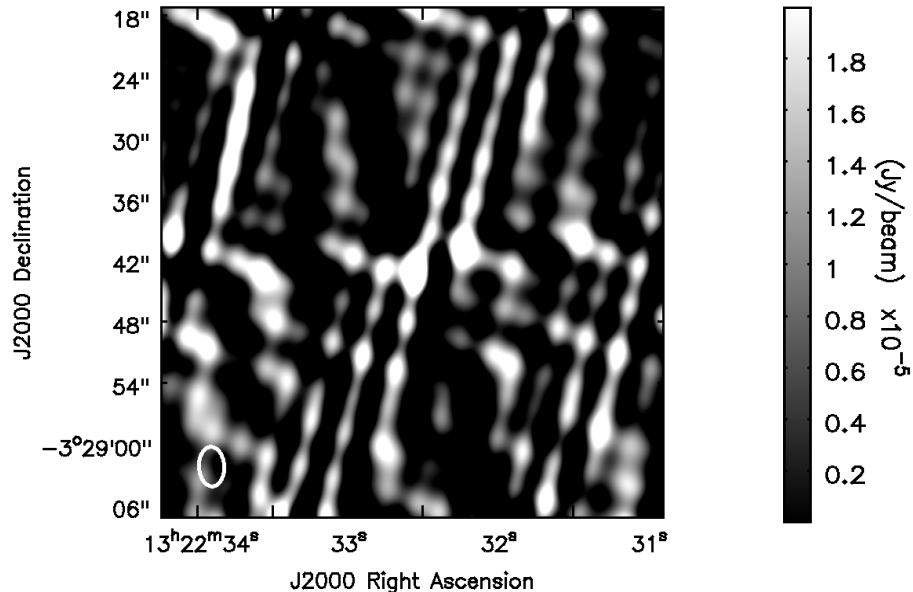


Figure 4.1: Image of one of the scans of the W1322 field after pipeline calibrations. Striped emission can be seen across the image, caused by a bad baseline in the calibration. Online calibrations were instead used for this scan.

work (e.g. Sharon et al., 2016) using online cookbooks to calibrate individual fields. For the other five fields, no additional calibrations were required following the initial pipeline calibrations.

Imaging of the six fields containing the Hot DOGs were made using CASA’s TCLEAN package. Initial dirty spectral maps without masking of the Hot DOGs were taken to estimate the positions of the galaxies and the frequency of emission. Continuum subtraction was then carried out using the UVCONTSUB package. Cleaning and imaging of all fields was made using HOGBOM deconvolution, with BRIGGS weighting and ROBUST= 2.0 to produce a natural weighting. All spectral cubes were constructed using 6 MHz ( $50 \text{ km s}^{-1}$ ) resolution to boost the signal-to-noise (SNR) ratio. Spectra were extracted in  $4''$  diameter apertures, roughly the size of the synthesized beam (see Table 4.1).

### 4.3 Observational Results

The spectra for the six Hot DOGs in this sample are shown in Fig. 4.2. W0410 has the strongest emission line in the sample, with a redshift of  $z = 3.633 \pm 0.005$ , (compared with an optical redshift of  $z = 3.592 \pm 0.002$  from Tsai et al. (2015)), in close agreement with CO(J=6–5) line detection using ALMA (Lopez et al. in prep). These results suggest that the gas associated with the lower, optical redshift could be emitted from outflows with velocities of  $\sim 3000 \text{ km s}^{-1}$  projected towards the observer. Every other galaxy in this sample shows evidence of CO(1–0) emission, with the exception of W0126, which has the least confident redshift identification in Tsai et al. (2015), from a single Ly $\alpha$  emission line. Vito et al. (2018) suggest a lower redshift for this galaxy using X-ray data:  $z = 0.8$ . From the JVLA observations, it can be confirmed that there is no CO(1–0) emission line at a redshift of  $z = 2.937$  as strong as in the other targets. The emission line from W0116 is also at a lower frequency than expected by  $\delta\nu=0.09 \text{ GHz}$ , giving an associated redshift of  $z = 3.187 \pm 0.005$ , compared with  $z=3.173 \pm 0.002$  in Tsai et al. (2015), a velocity difference of  $\sim 1400 \text{ km s}^{-1}$ , which could possibly suggest that the CO(1–0) gas in W0116 is associated with out-flowing material from the central source. The associated redshifts for W0831, W1322 and W2305 from the CO(1–0) are in agreement with Tsai et al. (2015), within  $\delta V \sim 500 \text{ km s}^{-1}$ .

The positions of the CO(1–0) emission are shown in Fig. 4.3. All images use the spectral window (henceforth *spw*) centred on the detected emission line. The window centred on the frequency range associated with the redshift from Tsai et al. (2015) is used for W0126. All images, except for W0126, show emission centred on the position of the target source, suggesting that the cold CO molecular gas is associated with the target galaxy. All fields, except W0126, have a SNR  $\gtrsim 3$ , showing that the position of the

# CHAPTER 4. JVLA OBSERVATIONS OF COLD GAS AROUND HOT DOGS

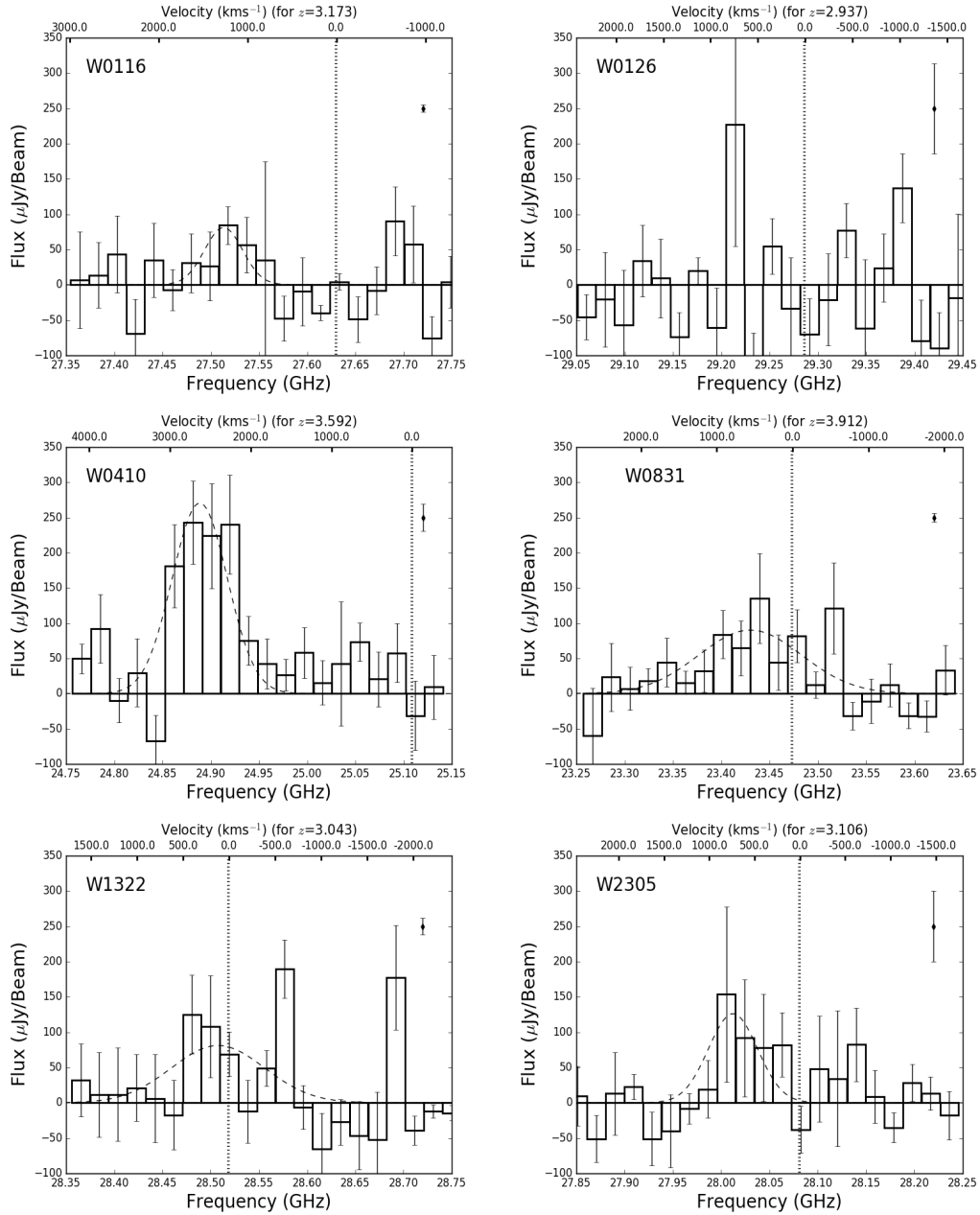


Figure 4.2: Spectra of the six sources in this sample. A Gaussian has been added to illustrate the CO(1-0) line. An additional error bar in the upper right-hand corner has been included to show the continuum level for each field. A dotted line has been given for the optical/IR redshift from Tsai et al. (2015). Frequency limits in these figures have been chosen to show the line emission of the galaxies.

## CHAPTER 4. JVLA OBSERVATIONS OF COLD GAS AROUND HOT DOGS

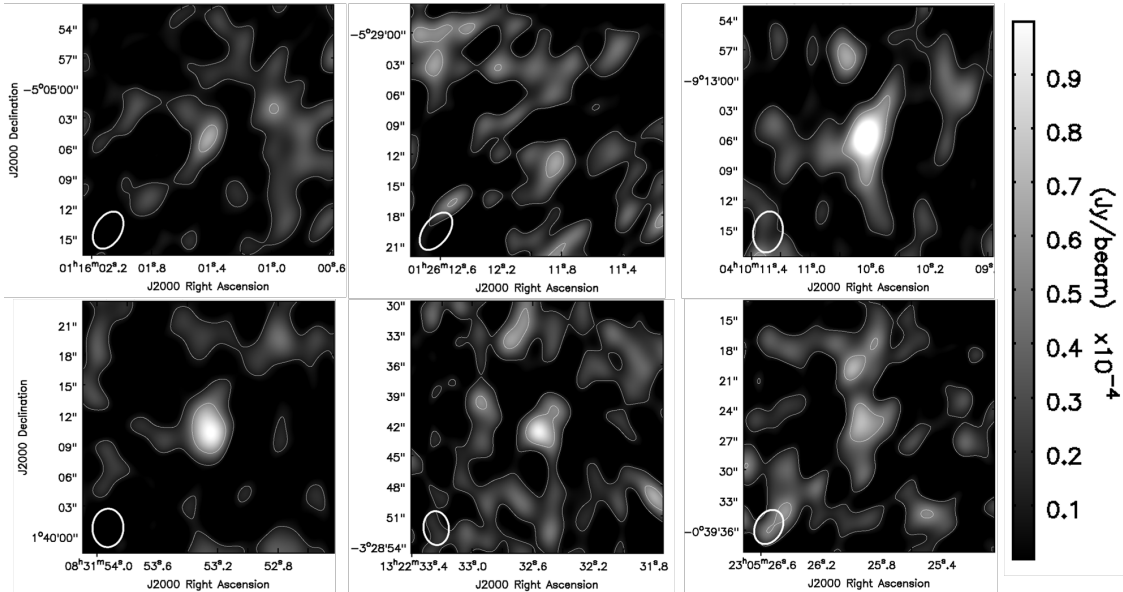


Figure 4.3: Emission centred images for (left to right, top to bottom) W0116, W0126, W0410, W0831, W1322 and W2305. Contours show the  $0.1 \mu\text{Jy}$ ,  $0.5 \mu\text{Jy}$  and  $1 \mu\text{Jy}$  levels. An ellipse in the bottom left-hand corner of each image illustrates the synthesized beam for each image.

emission lines are unlikely to be significantly affected by background noise.

Using the IMMOMENTS package available in CASA, the velocity fields of the six galaxies (moments=1) were constructed to investigate any motion of cold molecular gas in the galaxies, and the velocity maps are shown in Fig. 4.4. From the *spw* associated with the emission line, there is no sign of rotational motion of the gas. This is expected, given the resolution of these observations, and unsurprisingly there is no large-scale bulk motion of cold molecular gas around these galaxies on 20 – 50 kpc scales. Star-formation could still be present within these galaxies and the cold molecular gas is not affected by outflows from the central AGN. Greater resolution and sensitivity is needed to understand whether there is an outflow of cold molecular CO gas responsible for the emission from W0116.

CHAPTER 4. JVLA OBSERVATIONS OF COLD GAS AROUND HOT DOGS

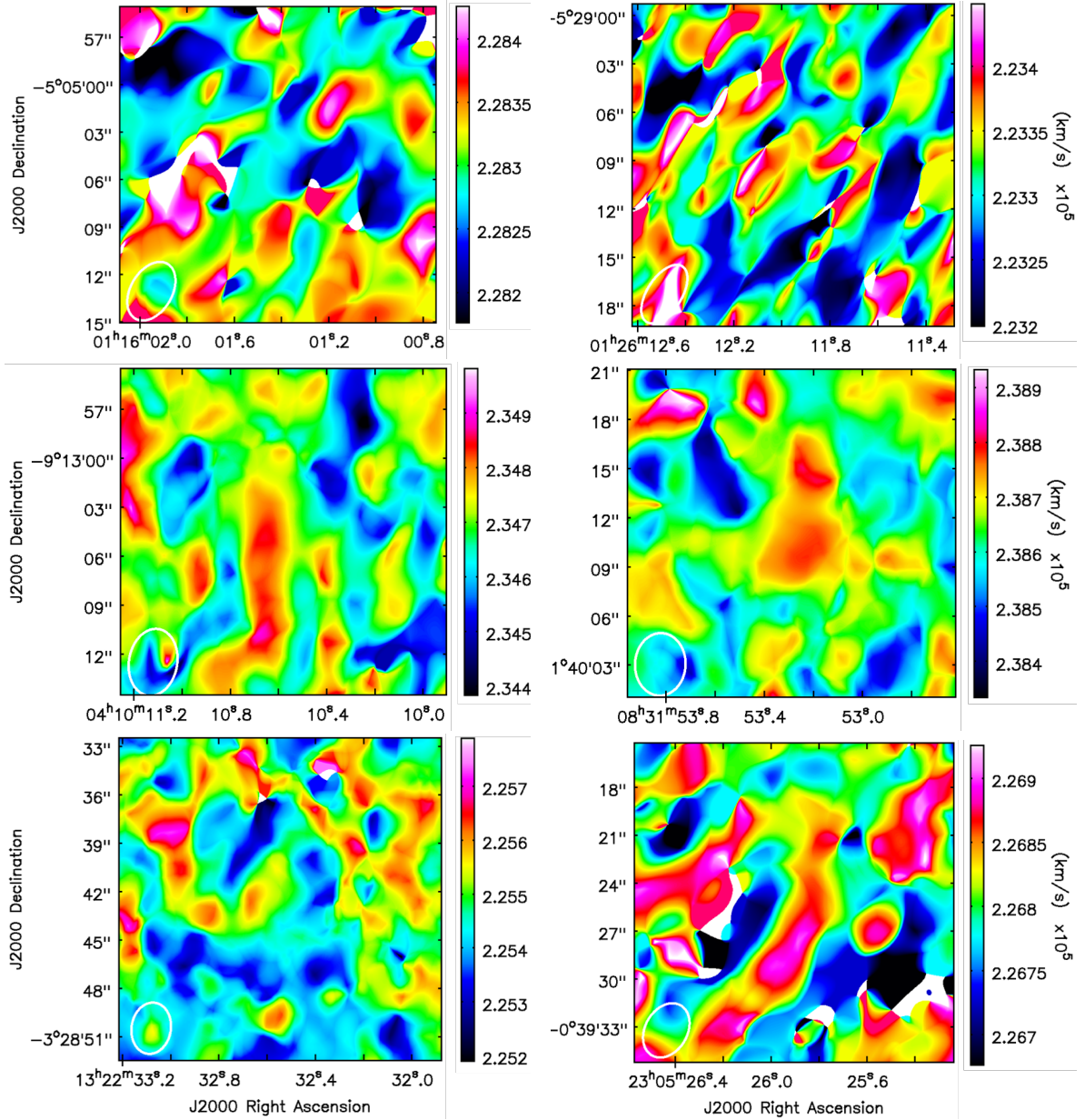


Figure 4.4: Images of the velocity fields of each of the Hot DOGs in the sample (left to right, top to bottom: W0116, W0126, W0410, W0831, W1322 and W2305). Each field has an independent colourbar, showing the different velocities in units of  $\text{km s}^{-1}$ . Rest frame velocities for each of the galaxies in the sample are:  $2.283 \times 10^5 \text{ km s}^{-1}$ ,  $2.233 \times 10^5 \text{ km s}^{-1}$ ,  $2.347 \times 10^5 \text{ km s}^{-1}$ ,  $2.386 \times 10^5 \text{ km s}^{-1}$ ,  $2.255 \times 10^5 \text{ km s}^{-1}$  and  $2.268 \times 10^5 \text{ km s}^{-1}$  for W0116, W0126, W0410, W0831, W1322 and W2305 respectively.

## CHAPTER 4. JVLA OBSERVATIONS OF COLD GAS AROUND HOT DOGS

---

I now compare the JVLA observations with independent observations using ALMA (Lopez et al. in prep). Observations of W0116, W0831, W1322 and W2305 were made using ALMA's Band-3 (2.6 – 3.6 mm) to image CO(J=4–3) emission, while additional ALMA observations were made for W0410 using Band-5 (1.4 – 1.8 mm) to image the CO(J=5–4) emission line. CII observations were also made for W0831 using Band-8 (0.6–0.8 mm). Fig. 4.3 shows that there is a potential companion to W2305 within  $\sim 1''$  of the Hot DOG (RA=23:05:26.00, DEC=–00:39:19.91). Inspecting the JVLA spectra at the position of this additional source, there is a peak in the spectra at a frequency corresponding to the same redshift of CO(1–0) emission as W2305 ( $L'_{\text{CO}(J=1-0)} = 0.62 \times 10^{10} L_{\odot}$ ). Comparing with ALMA observations of CO(J=4–3) gas, which should trace warmer molecular gas, at this position to understand the nature of the companion shows a lack of a peak in the spectra. This suggests that the companion is not composed of warmer CO gas, such that this is unlikely to be a merging companion. The W2305 companion is likely to either be a site of additional star forming matter within the Hot DOG, or associated with the synchrotron emission seen in the FIRST survey (see Section 4.4.1). There is a similar feature for W0126,  $\sim 5''$  below the expected position, however there is no emission spectra at this position consistent with the redshift in Tsai et al. (2015) and this is likely to be noise. I discuss the luminosity of these sources with respect to previous observations in Section 4.3.1.

### 4.3.1 CO(1–0) Luminosity

Using the emission spectra in Fig. 4.2, the CO(1–0) line luminosities can be determined. Using the same method as Solomon et al. (1997), the luminosity is derived from the integrated flux of the emission line using Eqn. 4.1:

$$L'_{\text{CO}(J=1-0)} = 3.25 \times 10^7 \times S_{\text{CO}} \delta V \times \frac{D_L^2}{\nu_{\text{obs}}^2 (1+z)^3}, \quad (4.1)$$

where  $S_{\text{CO}}$  is the integrated flux density of the line (Jy),  $\delta V$  is the change in velocity ( $\text{km s}^{-1}$ ) and  $D_L$  is the luminosity distance to the galaxy (Mpc).  $L'_{\text{CO}(J=1-0)}$  is in units of  $L_\odot$ . Assuming that the CO gas and H II gas originate from the same reservoir (Ivison et al., 2010), such that the CO gas trace the H II gas, the luminosity of the CO(1–0) gas can be converted to the H II mass using:

$$M(\text{H II}) = \alpha L'_{\text{CO}}, \quad (4.2)$$

where  $M(\text{H II})$  is the mass of the H II region in  $M_\odot$ ,  $L'_{\text{CO}}$  is the luminosity of the emission line in  $L_\odot$  and  $\alpha \sim 0.8$  is the conversion factor, derived empirically for ULIRGs and mergers (Downes & Solomon, 1998; Bolatto et al., 2013). The results are shown in Table 4.2 for the six Hot DOGs in the sample. CO(1–0) luminosities of  $> 1 \times 10^{10} \text{ K km s}^{-1} \text{ pc}^2$  are found, similar to findings by Ivison et al. (2010) and Riechers et al. (2011) for ULIRGs at similar redshifts. I compare the properties of the CO(1–0) luminosity with galaxies at similar redshifts in Fig. 4.5. These galaxies generally follow a similar trend to other galaxies with respect to their  $L'_{\text{CO}(1-0)}$  and  $L_{\text{IR}}$  properties, suggesting that these galaxies have typical cold gas reserves compared to other galaxies. This trend continues with the width of the CO(1–0) emission with respect to the luminosity compared with the comparison samples, suggesting that the increased width of the emission of the Hot DOGs in this sample compared to other galaxies does not substantially deviate from expectation. As expected, the  $L'_{\text{CO}(1-0)}$  emission from these Hot DOGs is fainter than dusty star forming galaxies (DSFGs) in Aravena et al. (2016) at  $z \sim 2.7 - 2.8$ . Comparing the  $\frac{L'_{\text{CO}(1-0)}}{D_L}$  ratio to  $\frac{L_{\text{IR}}}{D_L}$  value, the

## CHAPTER 4. JVLA OBSERVATIONS OF COLD GAS AROUND HOT DOGS

---

Hot DOGs in this work have similar values to DSFGs in Aravena et al. (2016), and values twice that of SMGs in Ivison et al. (2011), suggesting that the star-forming gas in the Hot DOGs is more luminous than other SMGs relative to their redshift.

Follow-up observations by Wu et al. (2014) attempted to determine the cold molecular gas content of three Hot DOGs using the Sub-Millimetre Array (SMA) and the Combined Array for Research in Millimeter-wave Astronomy (CARMA), using CO(3–2) and CO(4–3) transitions. Wu et al. (2014) found masses of  $< 3.3 \times 10^{10} M_{\odot}$  and  $< 2.3 \times 10^{10} M_{\odot}$  for W0149+2350 and W1814+3412 respectively. Comparing these results with the CO(1–0) masses in Table 4.2, in general agreement for W0116 and W0126, although the other galaxies in this sample are significantly more massive, suggesting Hot DOGs do not have similar cold molecular gas contents. ALMA observations by Fan et al. (2018) for three Hot DOGs using CO(4–3) emission (including W0410) suggest  $L'_{\text{CO}(4-3)}$  in the range of  $10^{10} - 10^{11} L_{\odot}$ . Using a  $L'_{\text{CO}(4-3)}$  to  $L'_{\text{CO}(1-0)}$  conversion factor of 0.87 (e.g. Aravena et al., 2016), in agreement with this work, suggesting that these galaxies are gas-rich for cold molecular CO gas.

# CHAPTER 4. JVLA OBSERVATIONS OF COLD GAS AROUND HOT DOGS

---

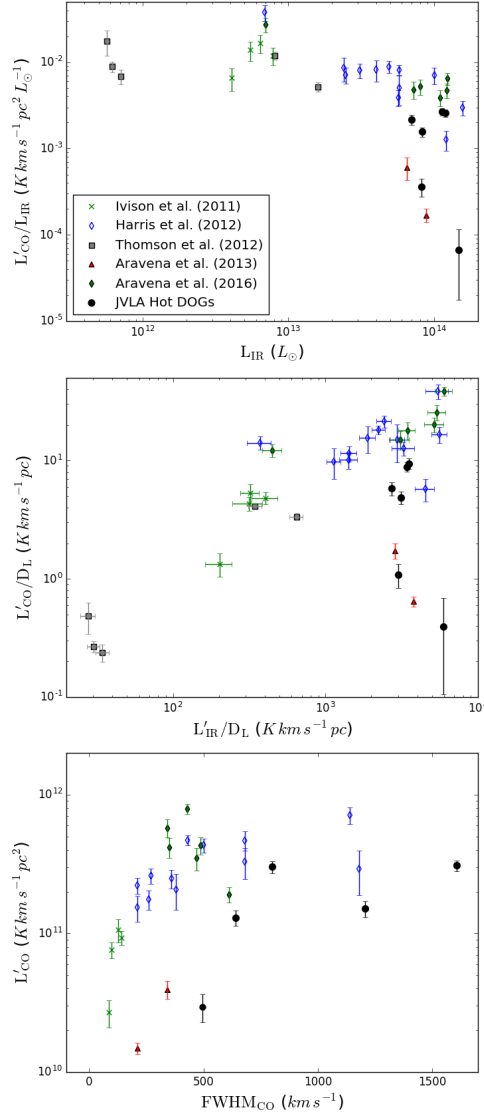


Figure 4.5: Comparison of the  $L'_{\text{CO}(1-0)}$  properties of the galaxies in this sample with other galaxies at high redshift. Left: The  $L'_{\text{CO}(1-0)}/L_{\text{IR}}$  ratio ( $\text{K km s}^{-1} \text{pc}^{-1} L_{\odot}^{-1}$ ) against  $L_{\text{IR}}$ . Middle: Comparison of the  $L'_{\text{CO}(1-0)}$  against  $L_{\text{IR}}$  with respect to the luminosity distance ( $D_L$ ). Right:  $L'_{\text{CO}(1-0)}$  against the FWHM of the CO(1–0) emission line. In each, I compare against ALMA-selected SMGs (Ivison et al., 2011) (green crosses), unlensed DSFGs (Harris et al., 2012) (blue empty diamonds), strongly lensed SMGs (Thomson et al., 2012) (grey squares), lensed SPT-galaxies (Aravena et al., 2013) (red triangles) and ALMA selected lensed SPT-galaxies (Aravena et al., 2016) (green filled diamonds). All VLA observed Hot DOGs are illustrated by black filled circles.

ID	$L_{\text{bol}}$ ( $10^{13}L_{\odot}$ )	$L'_{\text{CO}(1-0)}$ ( $10^{10}\text{K km s}^{-1}\text{pc}^2$ )	$M(\text{H II})^{\alpha}$ ( $10^{10}M_{\odot}$ )	ALMA ( $\mu\text{Jy}$ )	JVLA ( $\mu\text{Jy}$ )	$F_{\text{CO}(J=1-0)} / F_{\text{JVLA}}$
W0116	11.7	$2.96 \pm 0.68$	$2.36 \pm 0.54$	$278 \pm 55$	$5.4 \pm 7.1$	$31.4 \pm 1.3$
W0126	14.7	$0.98 \pm 1.54$	$0.78 \pm 1.23$	...	$63.6 \pm 9.5$	$1.0 \pm 1.6$
W0410	16.8	$30.15 \pm 3.00$	$24.12 \pm 2.39$	$1040 \pm 100$	$19.2 \pm 7.5$	$54.4 \pm 0.4$
W0831	18.0	$30.86 \pm 2.74$	$24.69 \pm 2.20$	$517 \pm 70$	$6.1 \pm 5.4$	$92.7 \pm 0.9$
W1322	10.1	$15.05 \pm 1.94$	$12.03 \pm 1.55$	$143 \pm 25$	$11.9 \pm 7.4$	$41.7 \pm 0.6$
W2305	13.9	$12.95 \pm 1.59$	$10.36 \pm 1.27$	$381 \pm 43$	$50.3 \pm 7.6$	$9.4 \pm 0.2$

Table 4.2: Total IR luminosity (Tsai et al., 2015), CO(1–0) luminosity, estimated H II masses and continuum values for all six Hot DOGs in this sample for ALMA (Lopez et al. in prep) and the JVLA respectively. The final column gives the flux ratio of the line to continuum for each Hot DOG. The luminosity and H II mass for W0126 have been estimated assuming  $z = 2.947$  from measurements by Tsai et al. (2015).

<sup>$\alpha$</sup>  see Section 4.3.1 for calculation.

### 4.3.2 30-GHz Continuum

The continuum flux for the six Hot DOGs in the sample is calculated using the *spws* not associated with the emission line. The same 4'' diameter aperture is used and a  $\sim 0.83$  GHz bandwidth after excluding the channels associated with the emission line. The *spw* centred on the expected emission frequency is not excluded for W0126, given the lack of CO(1–0) line and the distribution of the continuum is shown in Fig. 4.6. Generally, the net positive continuum appears to be centred on the position of the Hot DOGs and the continuum values are listed in Table 4.2. W0126 and W2305 have the highest  $\sim 30$  GHz continuum emission of the Hot DOGs in the sample. The other Hot DOGs in this sample have similar but lower 30 GHz observed-frame continuum flux. The significantly greater continuum values for W0126 and W2305 could suggest that additional dust processes around  $\nu \sim 30$  GHz or synchrotron/free-free emission have boosted the continuum flux. This is discussed further in Section 4.4.1.

K- and Ka-band radio observations for high-redshift galaxies are rare, and so a comparison with related observations is difficult. The fluxes of the six Hot DOGs are 10 – 50% of those obtained by Aravena et al. (2016) and Aravena et al. (2013) for six DSFGs selected using CO(1–0) emission and two lensed DSFGs within a redshift range of  $z = 2 - 3$ . A mean continuum flux is computed for the Hot DOGs (excluding W0126) of  $18.6 \pm 7.0 \mu\text{Jy}$ , indicated in Fig. 4.11, compared with  $144 \pm 57 \mu\text{Jy}$  for the DSFGs in Aravena et al. (2013) and Aravena et al. (2016). A similar result is observed when comparing two SMGs ( $z = 2.5 - 3$ ) from Thomson et al. (2012) with values of  $42 \pm 20 \mu\text{Jy}$  and  $57 \pm 25 \mu\text{Jy}$ . This suggests that the star formation in these Hot DOGs is significantly lower than DSFGs and SMGs. This is surprising, given the very different nature of the cold gas in galaxies in this sample of Hot DOGs compared to typical SMGs and DSFGs at their respective redshifts. Similar results are found when comparing to ULIRGs

## CHAPTER 4. JVLA OBSERVATIONS OF COLD GAS AROUND HOT DOGS

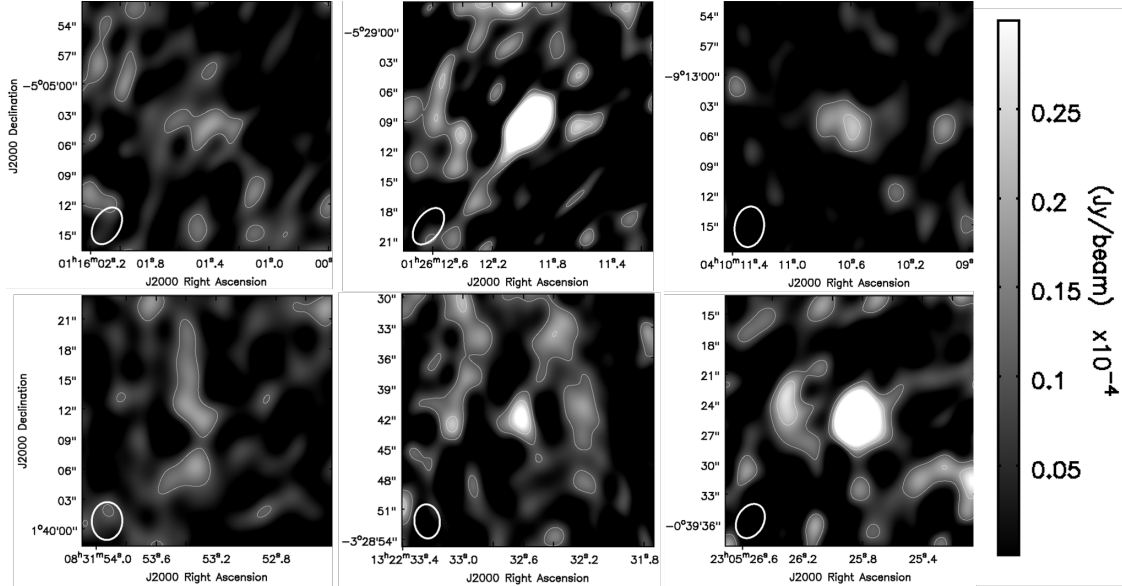


Figure 4.6: Continuum images for (left to right, top to bottom) W0116, W0126, W0410, W0831, W1322 and W2305. Contours show the  $0.1 \mu\text{Jy}$ ,  $0.2 \mu\text{Jy}$  and  $0.3 \mu\text{Jy}$  levels. An ellipse in the bottom left-hand corner of each image illustrates the synthesized beam for each image.

at  $0.2 < z < 0.6$  from Combes et al. (2011), in which the mean of the 15 detected CO(1–0) fluxes is  $4.88 \text{ Jy km s}^{-1}$  compared to  $0.31 \text{ Jy km s}^{-1}$  for the six Hot DOGs in the sample. In Fig. 4.2 most of the Hot DOGs in the sample have CO(1–0) line widths  $\gtrsim 1500 \text{ km s}^{-1}$ . The full width at zero intensity (FWZI) values reported in Thomson et al. (2012),  $\sim 500 - 1000 \text{ km s}^{-1}$ , are significantly lower, although the Hot DOGs are much fainter, showing that the CO(1–0) lines are less luminous than in typical SMGs. Using the IR and CO(1–0) luminosities of the JVLA-observed Hot DOGs with respect to two SMGs in Thomson et al. (2012), a mean value of  $\frac{L_{\text{IR}}}{L'_{\text{CO}(1-0)}} = 770 L_{\odot} \text{K}^{-1} \text{km}^{-1} \text{pc}^{-2} \text{s}$  is found for the Hot DOGs in this work (using  $L_{\text{IR}}$  from Tsai et al. (2015) and excluding W0126) compared with a value of  $140 L_{\odot} \text{K}^{-1} \text{km}^{-1} \text{pc}^{-2} \text{s}$  for the two SMGs. This suggests that the Hot DOGs are significantly more luminous in the IR than would be expected for galaxies at this redshift for a given  $L'_{\text{CO}(1-0)}$ . Comparing to VLA observations of lensed galaxies by Riechers et al. (2011), which report line widths of  $\gtrsim 1300 \text{ km s}^{-1}$

and peak flux densities of  $\sim 0.5$  mJy, two orders of magnitude greater than shown in Fig. 4.2, the CO(1–0) emission lines from Hot DOGs are much fainter than optically selected QSOs.

### 4.3.3 Spectral Energy Distributions

Using archival data in addition to the JVLA observations, SEDs of the six Hot DOGs can be produced. Included in these SEDs are continuum data from ALMA (Lopez et al. in prep) (see Table 4.2), and Herschel PACS and SPIRE ( $70\ \mu\text{m}$ ,  $160\ \mu\text{m}$ ,  $250\ \mu\text{m}$ ,  $350\ \mu\text{m}$ ,  $500\ \mu\text{m}$ ) from Tsai et al. (2015). From archival data, Sloan Digital Sky Survey (SDSS; Alam et al., 2015), Warm-*Spitzer* IRAC1 ( $3.6\ \mu\text{m}$ ) and IRAC2 ( $4, 5\ \mu\text{m}$ ), WISE ( $3.5\ \mu\text{m}$ ,  $4.6\ \mu\text{m}$ ,  $12\ \mu\text{m}$  and  $22\ \mu\text{m}$ ), Bolocam 1 mm observations (Wu et al., 2012) and data from the Faint Images of the Radio Sky at Twenty-Centimeters (FIRST; White et al., 1997) have also been added. For W0831, continuum data from SCUBA-2 ( $850\ \mu\text{m}$ ) from Jones et al. (2014) and ALMA CII observations (Lopez et al. in prep) have been included. For W0410, SHARC-II  $850\ \mu\text{m}$  observations have been added (see Wu et al. (2012) for details of the observations). Using these data, with the JVLA data from this work, the full SEDs are presented in Fig. 4.7 for the six Hot DOGs. It should be noted that it is assumed that the observed frame 1.4 GHz and 30 GHz radio-fluxes do not vary significantly on the timescales between the observations used to construct the SEDs.

For each SED, I initially attempted to fit two broken power-laws using a standard Monte-Carlo Markov Chain (MCMC) routine (Metropolis et al., 1953), with a single broken power-law fitting the data between 600 GHz–850 THz ( $350\ \text{nm}$ – $450\ \mu\text{m}$ ) and another single broken power-law fitting the data between 1.4 GHz–600 GHz ( $22\ \text{cm}$ – $450\ \mu\text{m}$ ). The results are shown in Fig. 4.7, and the  $\chi^2$  values for each of the fits are

# CHAPTER 4. JVLA OBSERVATIONS OF COLD GAS AROUND HOT DOGS

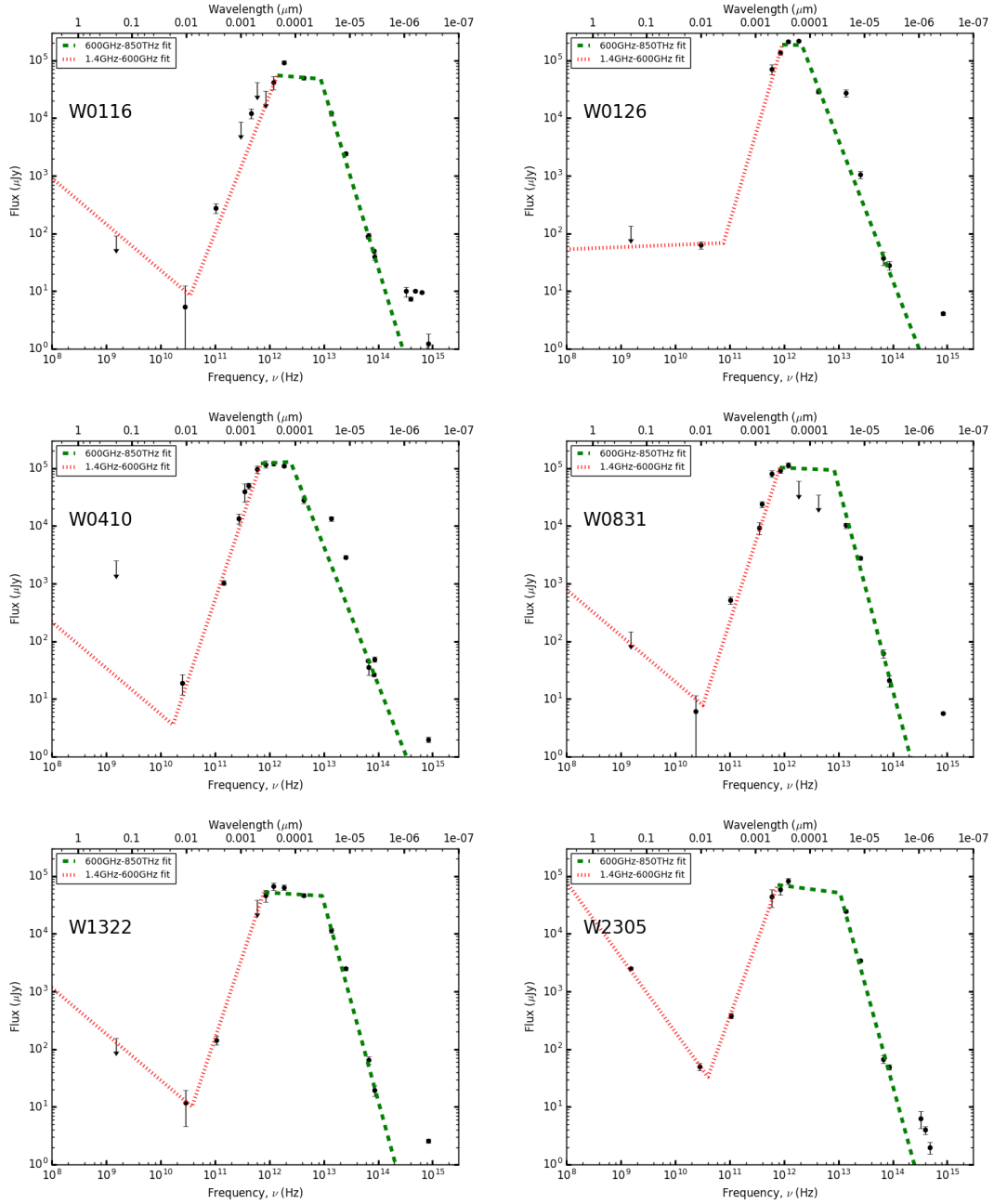


Figure 4.7: SEDs of the six Hot DOGs (left to right, top to bottom: W0116, W0126, W0410, W0831, W1322 and W2305). Broken power-law fits have been used to fit the optical-to-FIR data (green dashed line) and the FIR-to-radio data (red dotted line) for each galaxy.

## CHAPTER 4. JVLA OBSERVATIONS OF COLD GAS AROUND HOT DOGS

---

shown in Table 4.3. Upper limits for FIRST at 1.4 GHz (22 cm) are used for all sources undetected in the FIRST survey, using the RMS value at the expected position in the field (shown in Fig. 4.13). At frequencies shorter than the break in the radio spectra ( $\nu \sim 1$  GHz), I assume a prior for the slope of  $\alpha = -0.8$ , typical of synchrotron emission (Condon, 1992; Carilli & Yun, 1999; Lacki et al., 2010) for all sources except W2305. Using the gradient of the fit between 30 GHz and  $\sim 1$  THz, I attempt to estimate the dominant processes within this frequency range.

From the SEDs of the six Hot DOGs in Fig. 4.7, most of the 20 – 30 GHz JVLA continuum flux lies along the  $S \propto \nu^{-3}$ , suggesting that the values are produced via thermal processes consistent with a dust spectrum. W0126 and W2305 are exceptions to this, and W2305 has a significant FIRST detection, likely caused by synchrotron emission, possibly dominating the thermal processes of the JVLA observations. The JVLA continuum flux at  $\nu \sim 29.30$  GHz for W0126 lies beyond the break in the spectrum, which could be caused by a number of factors, such as additional dust clouds at different radii from the central, obscured AGN, or boosting from star formation activity in the host galaxy. W0126 could also be producing a similar spectra observed in GHz Peak Spectrum (GPS) galaxies (Bicknell et al., 1997; O’Dea, 1998), with a strong radio peak in the spectra at  $\sim 30$  GHz, potentially due to free-free absorption through an obscuring torus. This is less likely, however, given that GPS galaxies have large radio-luminosities (O’Dea, 1998), which is not seen in FIRST imaging of this galaxy. The  $\sim 30$  GHz emission from this galaxy, therefore, likely comes from a more complex spectrum than a single temperature, blackbody model. The  $\sim 30$  GHz flux for W0126 is close to the FIRST 1.4 GHz RMS flux limit, suggesting that the spectrum should decrease at frequencies less than the JVLA observations. For the other galaxies undetected in FIRST (W0116, W0831 and W1322), the fits at  $\nu \lesssim 30$  GHz ( $\lambda \gtrsim 10^{-2}$  m) are close to the detection limits of FIRST at 1.4 GHz, suggesting that deeper observations at 1.4 GHz

## CHAPTER 4. JVLA OBSERVATIONS OF COLD GAS AROUND HOT DOGS

---

could be used to understand the nature of the synchrotron emission in these galaxies.

To determine error in the slope (the normalisation and the break value) a corner plot is produced for each fit, shown in Fig. 4.8. The priors used to constrain the values to ensure realistic values in the final fits were:  $K > 0$ ,  $0 < x_c < 1e11$  and  $\alpha$ , where  $K$  is the normalisation,  $x_c$  is the frequency of the break in the power-law in GHz, and  $\alpha$  is the power-law index of the dust emission (given by  $S_\nu \propto \nu^{-\alpha}$ ). Fig. 4.8 shows that the fits for the single breaks generally have well-defined values for the three parameters used in the fits, suggesting that the values are not produced randomly, although there is a large variance in the possible values for several of the galaxies. While this could suggest that the parameters of the fits need additional constraints, with the number of fluxes available in this frequency range, it is unlikely that without further FIR and radio observations the constraint on these values will be significantly improved.

To determine the maximum level of the free-free emission of these galaxies, observed between the thermal-dust dominated emission and the synchrotron emission as a flat slope with a power-law distribution of  $S_\nu \propto \nu^{0.1}$  (Kennicutt, 1983), I attempt to fit double-broken power-laws to the 1.4 GHz–600 GHz (22 cm–450  $\mu\text{m}$ ) data, shown in Fig. 4.9, and the  $\chi^2$  values for the double-broken power-laws are shown in Table 4.3. The additional break and spectral slope for these fits produce an additional two parameters, which were initially believed to significantly affect the reliability of the fit given that the number of data points at FIR–radio frequencies is  $\sim 5 \pm 2$ , close to the number of parameters used. However, as shown in Fig. 4.10, which shows a typical example of a corner plot for a double-broken power-law for the FIR to radio emission, the normalisation ( $A$ ), spectral slope ( $\alpha$ ) and second break ( $x_{c2}$ ) appear to be well constrained. A greater dispersion is observed in Fig. 4.10 compared to Fig. 4.8, in which the value of  $x_{c1}$  does not appear to have any constraints, and this is likely due to the lack of data at the radio frequencies. Less dispersion is observed in Fig. 4.8, suggesting that the additional

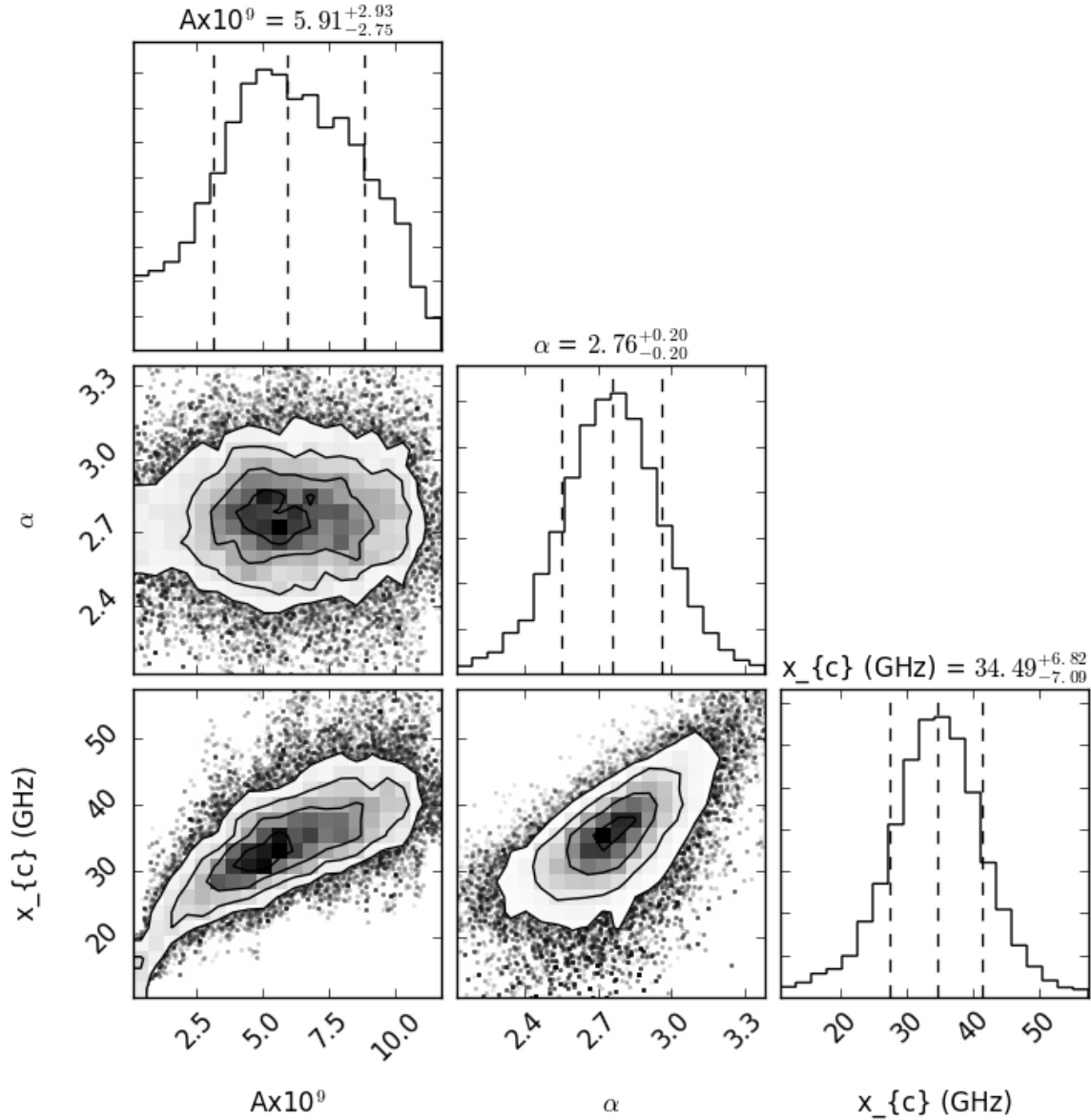


Figure 4.8: Corner plot for single broken power-law for example galaxy (W0410), which shows the fitting of the parameters. Here,  $A$  is the normalisation,  $\alpha$  is the spectral index of the FIR-to-radio data, and  $x_c$  is the break value in GHz. Dashed lines show the median $\pm 1\sigma$  values of the fits.

## CHAPTER 4. JVLA OBSERVATIONS OF COLD GAS AROUND HOT DOGS

---

parameter may produce an unsuitable fit for the amount of data present. Therefore, the maximum value of the free-free emission from the double-broken power-law is unlikely to be realistic.

Both Fig. 4.7 and Fig. 4.9 show the same single-broken power-law fit for the data at  $\nu \gtrsim 600$  GHz. Generally, the power-law fits the data well between 600 GHz to  $\sim 0.1$  THz, however an increasing deviation is observed from the fit at near-IR and optical regimes, suggesting that a single power-law fit for the data in this frequency range is not suitable. It should be noted that for W0831, there is a distinct lack of agreement in the upper limits given by Herschel data at  $60 \mu\text{m}$  and  $160 \mu\text{m}$ , suggesting that the model does not accurately represent the observations. Furthermore, in both Fig. 4.7 and Fig. 4.9 for W0126, the flux at  $22 \mu\text{m}$  is significantly greater than the fit would suggest. The lack of fit at these frequencies could be due to the activity of the dust and different layers of obscuration around these luminous IR galaxies. Dust at significantly greater temperatures at these frequencies compared to lower frequency data (mid- to far-IR) could account for the disparity, and could suggest that these galaxies have a more complex obscuring torus, as previously discussed in Assef et al. (2015). Jones et al. (2014) showed that the 10 Hot DOGs in their sample were not well fitted by any AGN template, with the single Polletta torus template (Polletta et al., 2007) providing the best fit, but still required additional extinction within the first two WISE bands, further suggesting that these galaxies require a more complex obscuring torus to understand their emission. While additional power-law fits could better constrain the luminosity at these frequencies, this would not be able to explain the nature of the dust at these frequencies.

To understand the nature of the dust at different frequencies, and better constrain the fitting parameters used to model the galaxies in the sample, a single of blackbody curve was fitted to the  $100 \mu\text{m} - 30$  GHz data, given by the relation  $S_\nu \propto \nu^{3+\beta} / (e^{\frac{h\nu}{k_B T_{\text{dust}}}} - 1)$

# CHAPTER 4. JVLA OBSERVATIONS OF COLD GAS AROUND HOT DOGS

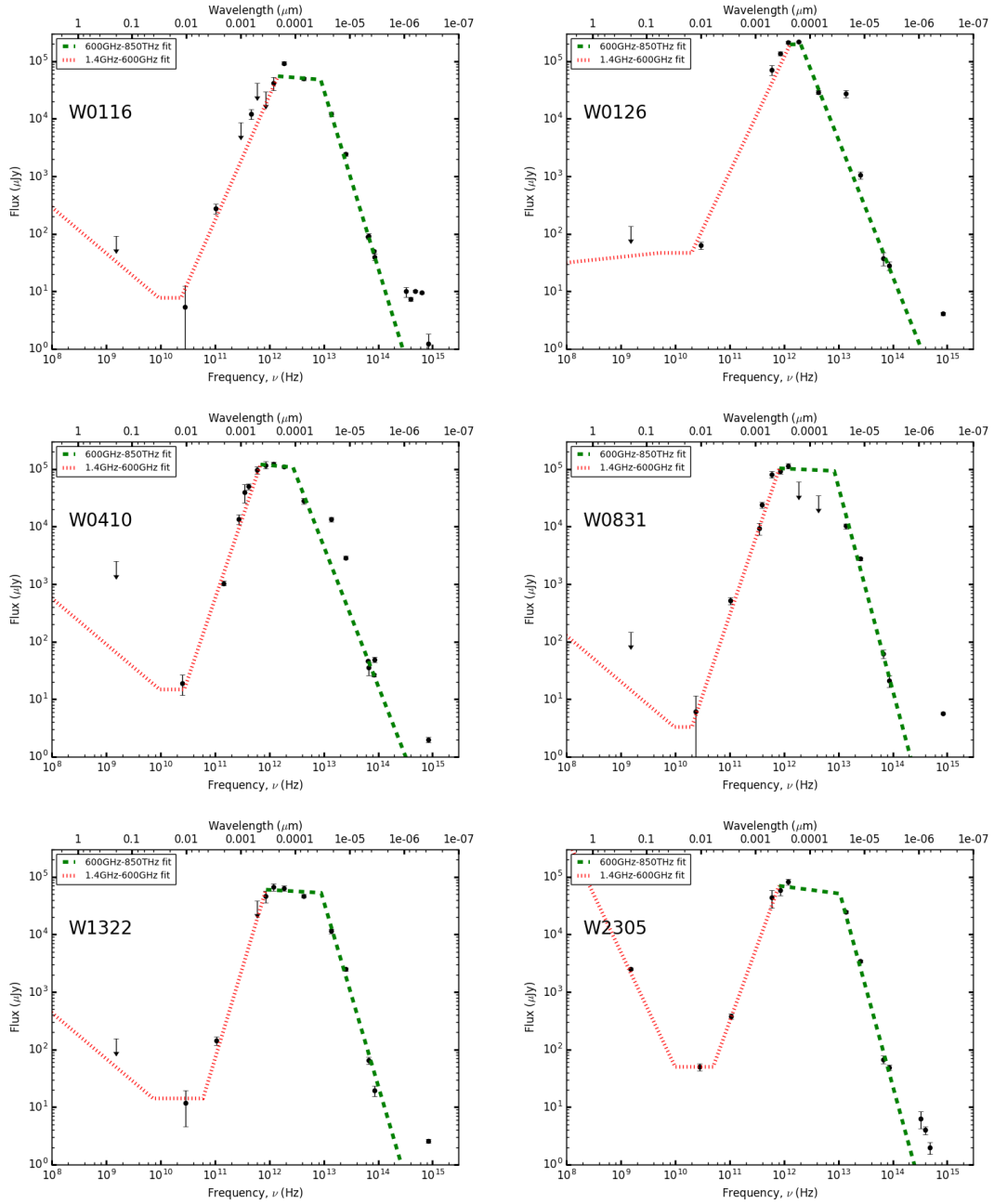


Figure 4.9: SEDs of the six Hot DOGs (left to right, top to bottom: W0116, W0126, W0410, W0831, W1322 and W2305). Unlike Fig. 4.7, double broken power-law fits have been used to fit the FIR-to-radio data (red dotted line) for each galaxy instead of single broken power-law fits and a single broken power-law has been used to fit the optical-to-FIR data (green dashed line).

CHAPTER 4. JVLA OBSERVATIONS OF COLD GAS AROUND HOT DOGS

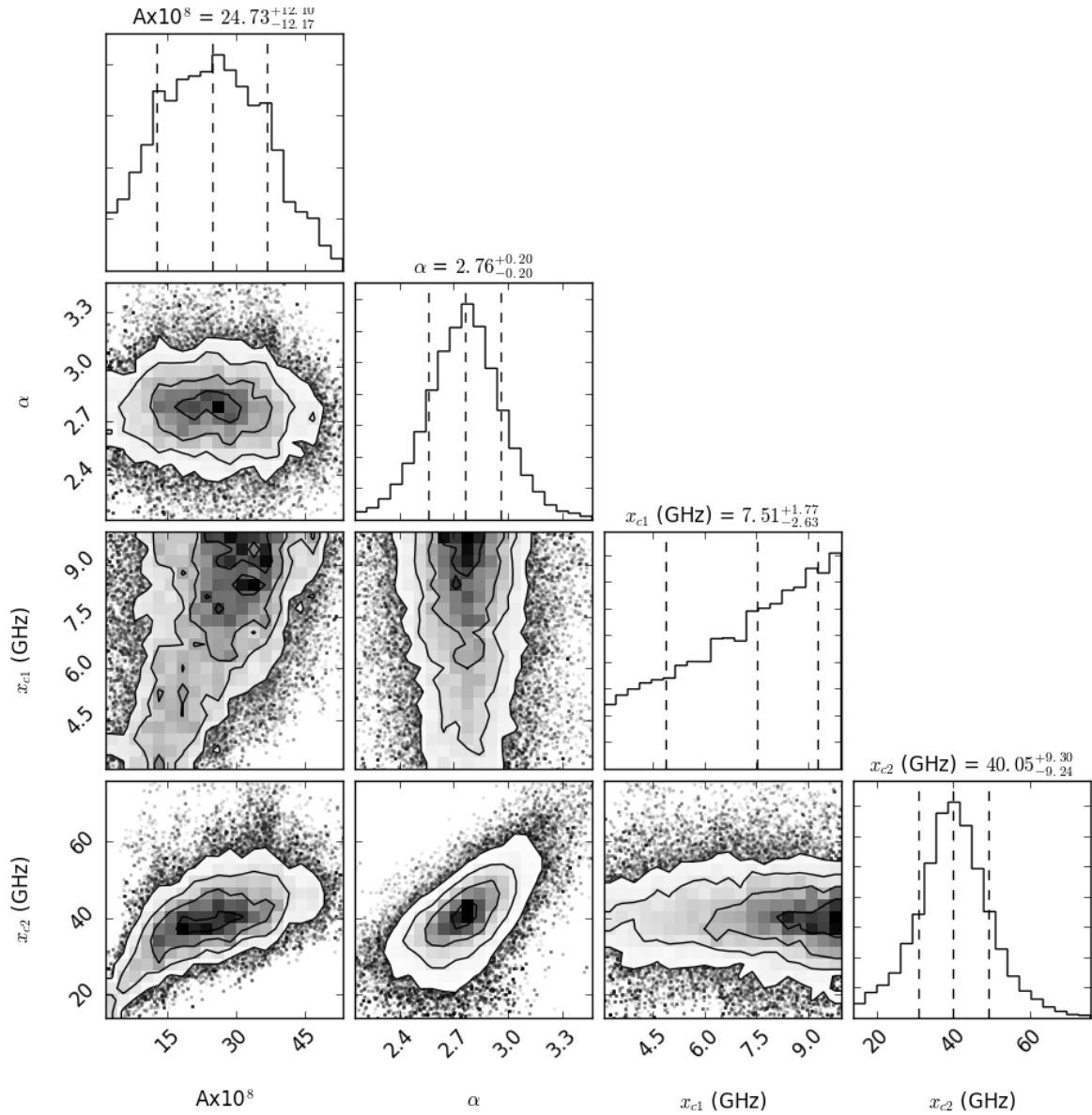


Figure 4.10: Corner plot for double broken power-law for example galaxy (W0410), which shows the fitting of the parameters. Here, A is the normalisation,  $\alpha$  is the spectral index of the FIR-to-radio data,  $x_{c1}$  and  $x_{c2}$  are the break values in GHz. Dashed lines show the median  $\pm 1\sigma$  values of the fits.

## CHAPTER 4. JVLA OBSERVATIONS OF COLD GAS AROUND HOT DOGS

---

(Hildebrand, 1983) where  $T_{\text{dust}}$  is the temperature of the dust and  $\beta$  is the emissivity index. To model the synchrotron emission at  $\nu \lesssim 30$  GHz, a single power-law distribution is fitted to the FIRST, JVLA and ALMA data. To simplify the fitting process,  $\beta$  is fixed at 1.5 (Blain et al., 2003; Wu et al., 2012), which should help to constrain the error in the normalisation and temperature parameters, as shown in Fig. 4.12. Initially, the  $\beta$  parameter was allowed to vary for the FIR-radio blackbody fit, however it was found that this significantly affected the fitting of the normalisation (A) and temperature (K) parameters, and excluding the parameter appeared to improve the fits for all Hot DOGs in the sample. For all galaxies undetected in the FIRST catalogue, the slope is fixed at  $\alpha = -0.8$ , typical for synchrotron emission (Condon, 1992; Carilli & Yun, 1999; Lacki et al., 2010). Using the synchrotron and FIR-radio fits, I attempt to better determine the maximum level of the free-free emission compared to the estimates from the double-broken power-law in Fig. 4.9. The fluxes for the free-free emission, shown in Table 4.4, are only the maximum values, and are affected by the assumption of the value of  $\alpha = -0.8$  and the error in the parameters for the FIR-radio blackbody model (shown in Fig. 4.11). The  $\chi^2$  values for the modified blackbody and synchrotron power-law fits are shown in Table 4.3.

# CHAPTER 4. JVLA OBSERVATIONS OF COLD GAS AROUND HOT DOGS

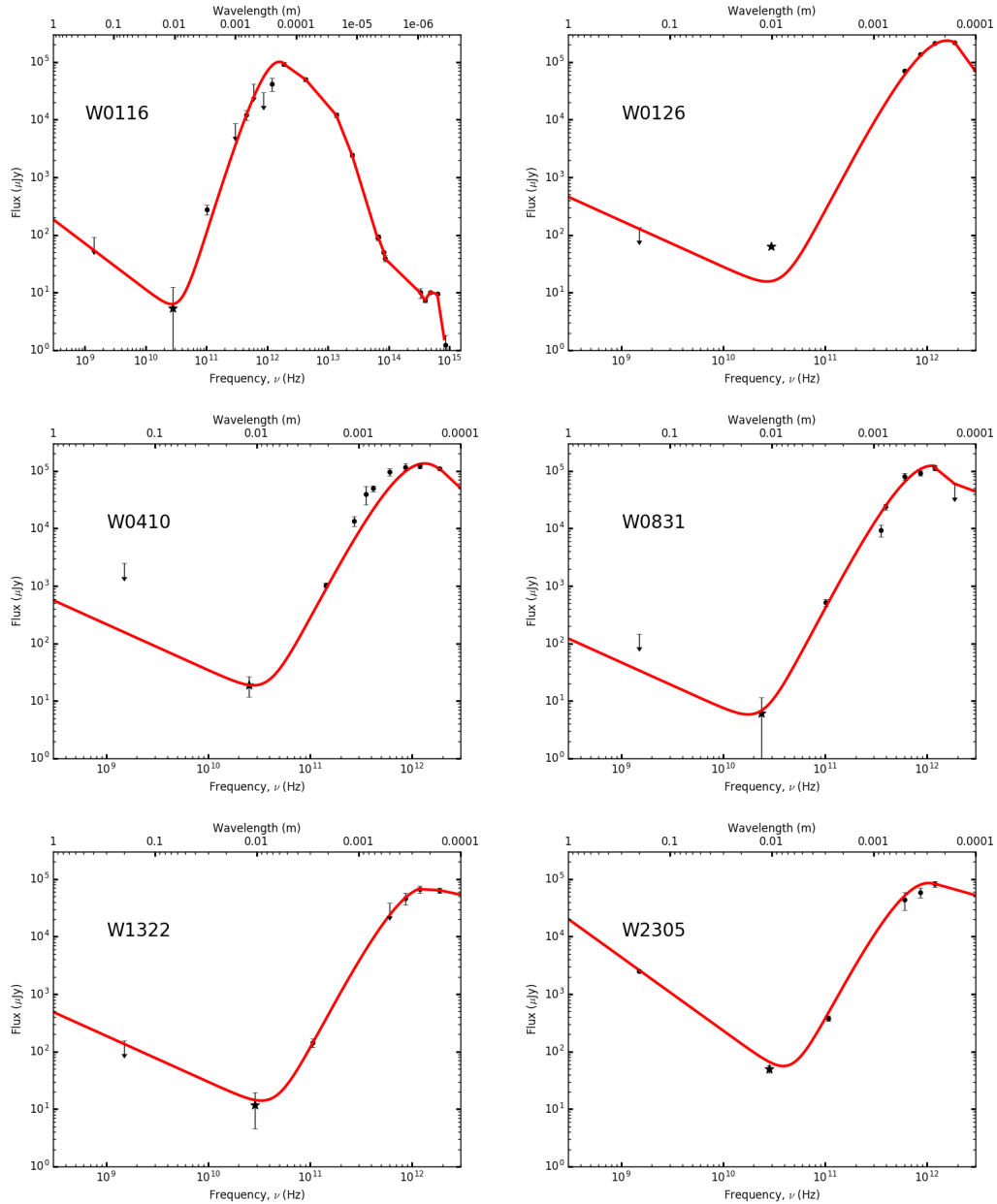


Figure 4.11: SEDs of the six Hot DOGs (left to right, top to bottom: W0116, W0126, W0410, W0831, W1322 and W2305). Observed frame SEDs of the six Hot DOGs in the sample. A single temperature blackbody was fitted to the  $160\ \mu\text{m}$  to 2 cm data, and further power-laws were added to fit the remaining data. Radio data, constrained by ALMA, VLA and FIRST data, is fitted by a single power-law ( $S_\nu \propto \nu^{-0.8}$ ), except for W2305, and the resultant curve is shown by a solid red line. A star has been used to denote the JVLA data in each SED.

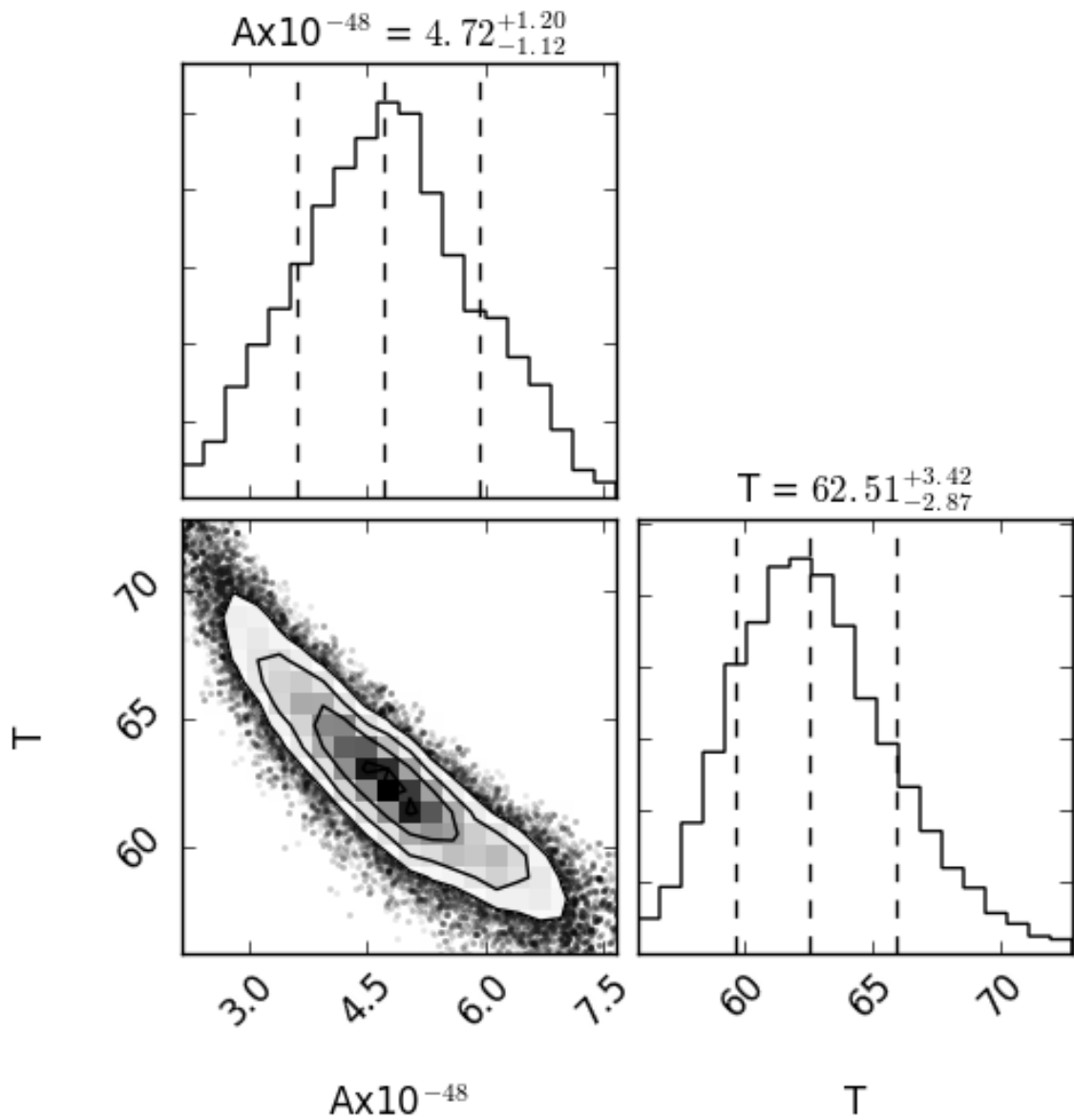


Figure 4.12: The fitted FIR-radio SED parameters for a member of the sample (W0410) using the single-temperature blackbody model. Dashed lines show the  $-1\sigma$ , median and  $1\sigma$ . The  $A$  parameter is the normalisation and  $T$  is the temperature (K).

ID	$\chi^2$ Broken Power-law (1.4 GHz – 600 GHz)	$\chi^2$ Broken Power-law (600 GHz – 850 THz)	$\chi^2$ Double Broken Power-law (1.4 GHz – 600 GHz)	$\chi^2$ Modified Blackbody (1.4 GHz – 100 THz)	$\chi^2$ Power-law (1.4 GHz – 0.3 THz)
W0116	5.47	7.71	9.42	4.85	8.80
W0126	16.05	49.34	14.33	14.95	30.83
W0410	10.70	35.95	10.47	9.68	44.93
W0831	7.77	11.11	8.13	5.28	29.04
W1322	5.34	10.91	2.42	0.82	15.73
W2305	4.79	13.32	4.53	13.16	37.77

Table 4.3:  $\chi^2$  values for the fits of the spectral energy distributions for each of the Hot DOGs in the sample. The second and third columns show the  $\chi^2$  values for the SED fits in Fig. 4.7, the fourth column shows the  $\chi^2$  values for the double broken power-law in Fig. 4.9 and the final two columns show the  $\chi^2$  values for the modified blackbody and synchrotron power-law fits in Fig. 4.11.

## CHAPTER 4. JVLA OBSERVATIONS OF COLD GAS AROUND HOT DOGS

---

The integrated spectrum can be used to estimate the luminosities of the galaxies in the sample using:

$$L = \int 4\pi d_L^2 F_\nu d\nu \quad (4.3)$$

where  $d_L$  is the luminosity distance and  $F_\nu$  is the flux at a specific frequency. To produce the blackbody fits shown in Fig. 4.11, the temperature for the FIR-radio ( $160 \mu\text{m} < \lambda < 20 \text{cm}$ ) component is determined, and the data at  $\lesssim 100 \mu\text{m}$  are connected with a series of power-laws, similar to the method used in Wu et al. (2012). The resulting curves are then combined to produce the curves shown in Fig. 4.11, in which W0116 highlights the range over which the luminosity is calculated, while the other SEDs focus on the FIR-radio component. The values of the calculated luminosities are shown in Table 4.4, and are in general agreement with the bolometric luminosity estimate for most of these galaxies with Tsai et al. (2015). For the IR luminosity, measured between  $8 \mu\text{m}$  and  $1 \text{mm}$ , no significant deviation is seen in the luminosity estimate compared with Tsai et al. (2015) for all galaxies in this sample. The small increase is likely due to the data at lower-frequencies included in this work and the small deviation in the blackbody fits between these two works.

For each of the Hot DOGs in the sample, the expected temperature is shown from the blackbody fit for  $160 \mu\text{m}$  to  $2 \text{cm}$  ( $15 \text{GHz}$  to  $1.88 \text{THz}$ ), with  $1\sigma$  errors in Table 4.4. I find lower dust temperatures, when comparing  $T_{160 \mu\text{m}-20 \text{cm}}$  using the blackbody fits with Wu et al. (2012) for W0116 and W0410. Wu et al. (2012) used the same blackbody fitting method, but for  $2 \mu\text{m}$  to  $1 \text{mm}$  data, and found dust temperatures of  $123 \pm 8 \text{K}$  and  $82 \pm 5 \text{K}$  for W0116 and W0410 respectively,  $1 - 2$  times the values shown in Table 4.4. This result is expected, however, given that the data at  $\lambda > 1 \text{mm}$  should trace colder gas, and suggests that these results do not overestimate the temperature of the dust components in this range.

Table 4.4: The fitted temperatures for the FIR-radio blackbody curve in Fig. 4.11 and the inferred 21 cm and 850  $\mu\text{m}$  fluxes. All values in this table are inferred from the fits in Fig. 4.11. The maximum possible flux contribution are shown for the free-free emission ( $S_{\text{ff}}$ ). The seventh column gives the maximum fluxes for the free-free emission of the Hot DOGs using the synchrotron and FIR-radio models. The final column shows the  $q_{\text{IR}}$  values, discussed in Section 4.4.2, using Eqn. 4.4. Data marked with ( $^{\alpha}$ ) have fitted points which can be compared with observations.

ID	$T_{160\mu\text{m}-2\text{cm}}$ (K)	$S_{21\text{cm}}$ ( $\mu\text{Jy}$ )	$S_{850\mu\text{m}}$ ( $\mu\text{Jy}$ )	$S_{\text{ff}}$ ( $\mu\text{Jy}$ )	$L_{\text{bol}}$ ( $10^{13}L_{\odot}$ )	$L_{\text{IR}}$ ( $10^{13}L_{\odot}$ )	$q_{\text{IR,SED}}$
W0116	$68_{-6}^{+5}$	56.0	5800	6.32	13.4	9.09	2.79
W0126	$66_{-3}^{+3}$	138.2	10000	15.58	15.4	10.6	3.01
W0410	$62_{-3}^{+3}$	169.9	13000	18.68	17.4	11.0	2.16
W0831	$59_{-5}^{+6}$	36.7	19000 $^{\alpha}$	5.82	19.0	11.3	2.56
W1322	$58_{-7}^{+8}$	146.8	5900	14.02	10.5	6.88	2.82
W2305	$47_{-3}^{+4}$	2910 $^{\alpha}$	14000	50.62	14.8	8.88	0.79

## CHAPTER 4. JVLA OBSERVATIONS OF COLD GAS AROUND HOT DOGS

---

From the blackbody/power-law SED fits for  $\nu \lesssim 10$  GHz ( $\gtrsim 1$  cm), using a spectral slope of  $\alpha = -0.8$ , the value of the flux at 22 cm can be estimated, as shown in Table 4.4. The results suggest that the fluxes are significantly fainter than the limits of FIRST (and NVSS for W0410), and it is likely that significantly deeper observations of these galaxies at 1.4 GHz are needed to understand the synchrotron processes at this frequency. Additional radio-continuum observations between 1.4 GHz and  $\sim 30$  GHz would also constrain the free-free flux and the star formation rates, similar to methods used in Thomson et al. (2014) for two SMGs at similar redshifts to the galaxies in the sample. The 1.4 GHz flux estimates from Fig. 4.11 suggest that most of the Hot DOGs in the sample are not radio-loud.

From Fig. 4.11, W2305 is the only Hot DOG in the sample with significant 1.4 GHz radio components compared to the other Hot DOGs in this sample. As previously discussed, the spectral index for the synchrotron component in this galaxy was allowed to vary, and a value of  $\alpha = -1.3$  is observed, significantly lower than the  $\alpha = -0.8$  value assumed for the other Hot DOGs and previous work on normal galaxies (Condon, 1992). This spectral index is significantly lower than the value determined by Magnelli et al. (2015) using a stacking analysis of  $z \sim 2$  galaxies, and could suggest that W2305 is a radio-loud Hot DOG.

## 4.4 Discussion

### 4.4.1 30-GHz Emission from Hot DOGs

The VLA data for six Hot DOGs are near the expected continuum flux from a dust-emission power-law ( $S \propto \nu^{2+\beta}$ ), suggesting that dust emission could dominate at these

frequencies, providing  $\sim 60 - 70\%$  of the flux on average. At 1.4 GHz, there should be a distinct lack of emission in 5/6 galaxies in the sample, as shown in Fig. 4.11. To attempt to understand whether there is any emission beneath the noise level of FIRST, I stack the FIRST images for W0116, W0126, W0831 and W1322. The Root-Mean-Square (RMS) values for the individual images are a third of the 1.4 GHz flux for W2305, however there is no stacked detection (Fig. 4.13), suggesting that the 1.4 GHz emission of these galaxies is substantially lower than the detection limit of FIRST. It is unlikely that the dust emission from these Hot DOGs is suppressing the synchrotron processes at 1.4 GHz, and it is more likely that these Hot DOGs are relatively radio-quiet compared to W2305.

#### 4.4.2 FIR-Radio Correlation

The FIR-radio correlation has been widely used to identify star formation properties of galaxies at high redshift (see Lacki & Thompson, 2010, for a review). Star formation drives the correlation, in which dust-obscured stellar emission produces flux in the FIR, while supernovae (SNe) from the same stars with masses  $M_{\odot} \gtrsim 8M_{\odot}$  produce synchrotron emission at  $\sim 1.4$  GHz. The  $q_{IR}$  value is used to compare the difference in the emission, given by:

$$q_{IR} = \log_{10} \left( \frac{S_{FIR}}{3.75 \times 10^{12} \times S_{1.4\text{GHz}}} \right), \quad (4.4)$$

where  $S_{FIR}$  is the rest-frame FIR flux in  $\text{W m}^{-2}$ , and  $S_{1.4\text{GHz}}$  is the flux at rest-frame 1.4 GHz in  $\text{W m}^{-2} \text{Hz}^{-1}$ . The correlation is well documented locally (van der Kruit, 1971; Helou et al., 1985; Condon, 1992; Yun et al., 2001), and extending to higher

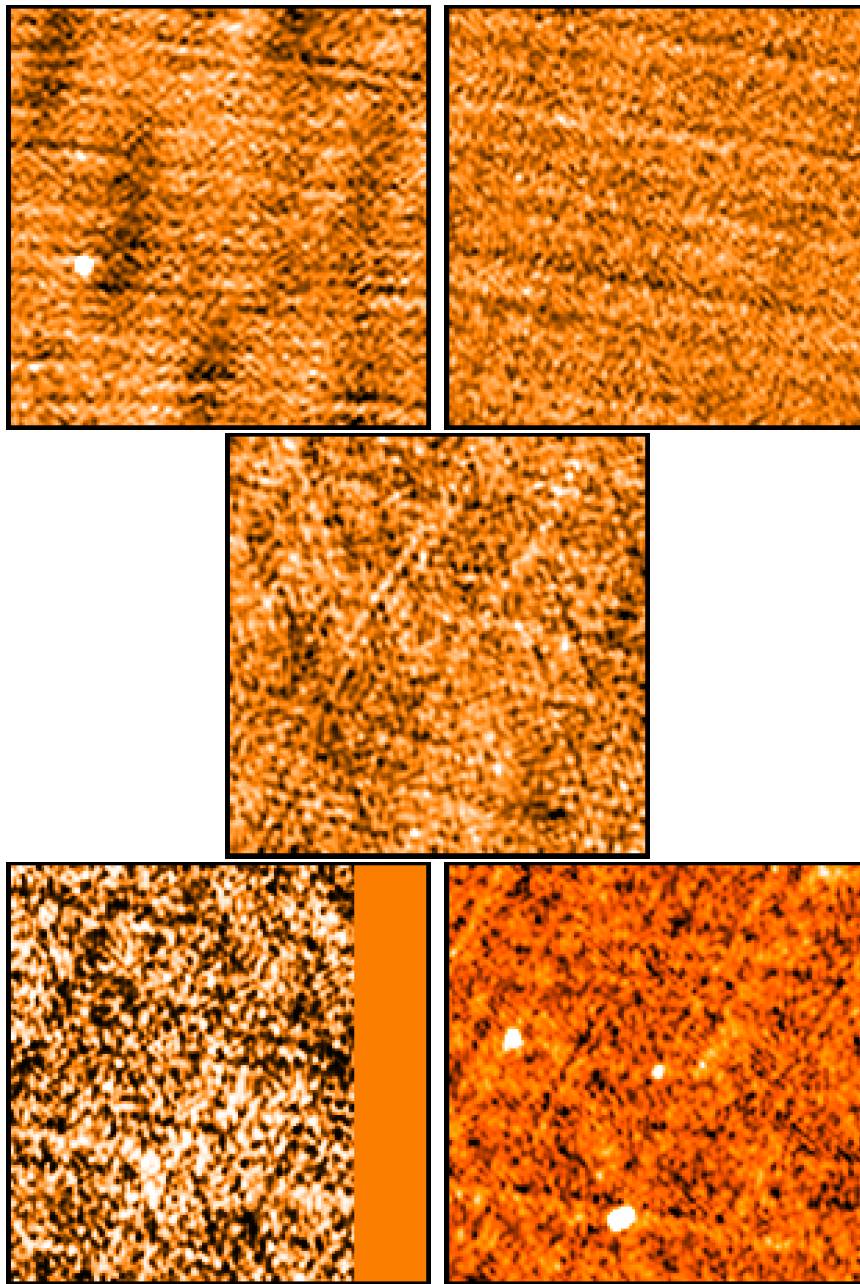


Figure 4.13: Cutout images centred on the expected position of the Hot DOGs in the sample (W0116, W0126, W0831, W1322 and W2305). W0410 does not appear in the FIRST catalogue. All images are  $4.5' \times 4.5'$  in size. The right-hand portion of the image containing the expected position of W1322 is blank due to the image being at the edge of the FIRST survey.

## CHAPTER 4. JVLA OBSERVATIONS OF COLD GAS AROUND HOT DOGS

---

redshifts (Lacki et al., 2010; Ivison et al., 2010), with Thomson et al. (2014) finding  $q_{IR} = 2.56 \pm 0.05$  using ALMA 870  $\mu\text{m}$  observations for  $\sim 50$   $z \gtrsim 2$  SMGs. Ivison et al. (2010) found a similar  $q_{IR} = 2.54 \pm 0.12$  for Herschel 250  $\mu\text{m}$ -selected galaxies at  $z > 1$ , and Boyle et al. (2007) discovered that the correlation was constant down to  $\mu\text{Jy}$  fluxes for radio-quiet quasars.

To obtain an estimate of the value for  $q_{IR}$  for the Hot DOGs in this sample, I assume  $S \propto \nu^\alpha$ , where  $\alpha = -0.8$ , for synchrotron emission to extrapolate the expected value at 1.4 GHz. This extrapolation is necessary due to an undetected flux estimate from the FIRST/NVSS catalogues for these galaxies, and has been calculated using the values from the upper limits in FIRST/NVSS, and detections in ALMA and this work. It should be noted that, as previously discussed, Laor et al. (2019) suggest that galaxies with a higher Eddington luminosity may have steeper spectral indices, and could suggest that I have underestimated the 1.4 GHz fluxes of this sample. However without additional observations, the true value of the rest-frame 1.4 GHz emission cannot be determined. There is no significant deviation in the  $q_{IR}$  values for these galaxies using the  $L_{\text{FIR}}$  values from Tsai et al. (2015), which is expected given that the  $L_{\text{FIR}}$  values deviate by only  $\sim 10 - 20\%$  at most.

To compute the  $q_{IR}$  values for the Hot DOGs in this sample, I use the SED fits of the FIR within the wavelength range 8–1000  $\mu\text{m}$  (Ivison et al., 2010), as shown in Table 4.2. As shown in Fig. 4.11, there is a FIRST detection for only W2305. For the galaxies undetected in FIRST, W0831 is the only galaxy with  $q_{IR}$  estimates in agreement with previous findings with  $q_{IR} = 2.56$ , while W0116 also has  $q_{IR}$  within the  $2\sigma$  limits from Ivison et al. (2010), suggesting that these two galaxies may be only radio-quiet with respect to the FIRST limits. The other Hot DOGs undetected in FIRST have minimum  $q_{IR}$  values significantly above the  $2\sigma$  limits from Ivison et al. (2010), suggesting that these Hot DOGs are radio-quiet with respect to their FIR emission. The lack of radio-

## CHAPTER 4. JVLA OBSERVATIONS OF COLD GAS AROUND HOT DOGS

---

emission from these undetected galaxies is unusual, given that the obscured emission in the FIR from the presence of an AGN should be expected to also radiatively boost the radio emission. The higher  $q_{IR}$  values from W0126, W0410 and W1322 are likely due to dust significantly boosting the FIR emission, while the radio emission is unaffected. The  $q_{IR}$  value for W2305 ( $q_{IR} = 0.79 \pm 0.22$ ) is at least an order of magnitude smaller than the mean  $z = 2$  value from Ivison et al. (2010), suggesting that W2305 is more radio-loud than expected for SMGs, and the galaxies in this sample of Hot DOGs are all different from the population observed in previous work on the high-redshift FIR-radio correlation.

Schleicher & Beck (2013) and Schober et al. (2016) suggest a break-down of the FIR-radio correlation at high redshifts due to more effective electron cooling by Bremsstrahlung emission in the cosmic microwave background. This is unlikely to be the cause of the increased  $q_{IR}$  values in the NVSS/FIRST undetected galaxies in the sample, given that the radiation field of the galaxies will dominate over the cosmic microwave background, and this effect should only dominate at  $z \gtrsim 5$ . The higher  $q_{IR}$  values for the Hot DOGs in this sample are likely due to the increased FIR emission from the dust-obscured AGN shown in previous work (Assef et al., 2015; Díaz-Santos et al., 2016), such that the AGN boosts the FIR-emission from young stars compared to normal galaxies.

If the central AGN is radio-quiet, the observed  $q_{IR}$  values from these galaxies would be dramatically increased. This is unexpected and it is likely that the dust has boosted the FIR emission above what would be expected, while the 1.4 GHz emission is similar to that of a normal galaxy at this redshift. A lack of synchrotron emission could also suggest an abundance of young stars that have not undergone a SNe event within these galaxies, and could suggest that these galaxies are still forming stars, which could explain the lower rest-frame 115.3 GHz continuum fluxes observed in Table 4.2. Magnelli et al. (2015) and Delhaize et al. (2017) suggest a weak redshift dependence in

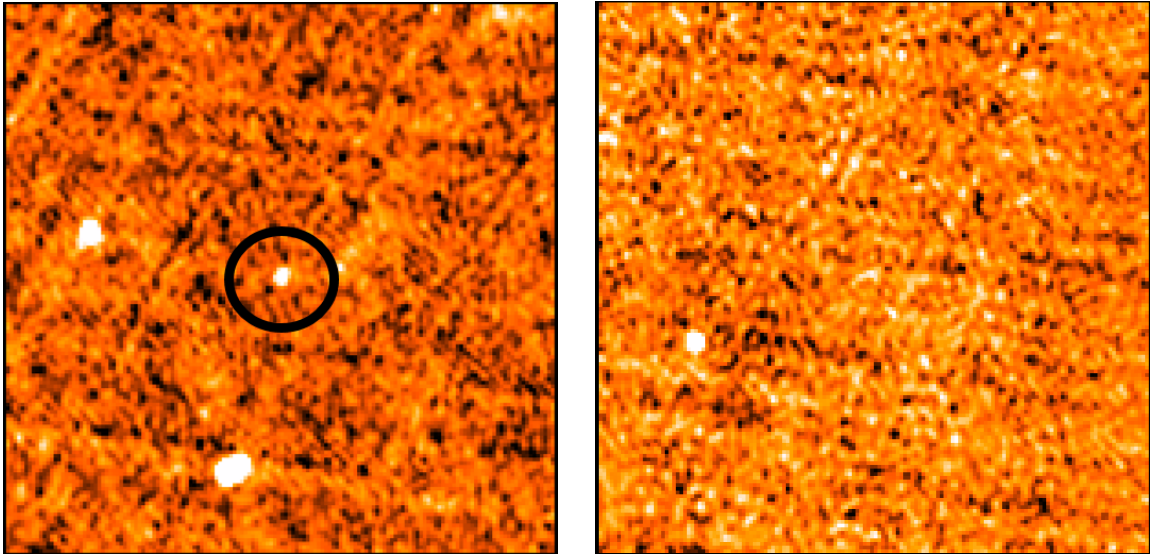


Figure 4.14: Left: Image of the W2305 field using FIRST image cutout service. The Hot DOG in the field has been ringed. Right: Stacked FIRST images of W0116, W0126, W0831 and W1322, showing that no net flux is visible at 1.4GHz. W0410 has not been included in this process as it does not appear in the FIRST catalogue and both images constitute  $4.5' \times 4.5'$  fields.

the FIR-radio correlation of the form  $q_{IR}(z) = q_{IR}(1+z)^{-\beta}$ , where  $\beta \sim 0.15$ . Using the values from Ivison et al. (2010), a value of  $q_{IR}(z) \sim 2 \pm 0.15$  is expected for the Hot DOGs in this sample, significantly louder in the radio than the FIRST limits suggest. These results were derived for star-forming galaxies, and so the FIR may be significantly enhanced by AGN emission in the sample, increasing the expected FIR emission beyond the radio emission produced from SNe. This agrees with previous results from SED fits of Hot DOGs (Jones et al., 2014; Assef et al., 2015), and further suggests that the AGN in these galaxies are radio-quiet.

To understand whether the  $q_{IR}$  values for this sample are typical for Hot DOGs or other classes of object, I compare the values with both high and low redshift galaxies, comparing  $q_{IR}$  values determined using the FIR luminosity between  $8 - 1000 \mu\text{m}$ . I compare with 10 Hot DOGs from Jones et al. (2014), which used  $850 \mu\text{m}$  SCUBA-2

## CHAPTER 4. JVLA OBSERVATIONS OF COLD GAS AROUND HOT DOGS

---

data to search for companion SMGs around Hot DOGs. W0831 is common to both works, and the Hot DOGs in Jones et al. (2014) are expected to have similar radio properties to the Hot DOGs in this work. To understand whether the  $q$ -values are typical of other dusty galaxies at this redshift, I compare with DSFGs from Shu et al. (2016), which have redshifts  $z = 2 - 4$ , and also with 52 ALMA  $870 \mu\text{m}$  selected SMGs in the Extended Chandra Deep Field South with a redshift range of  $z_{\text{phot}} \sim 0.4 - 4.7$  (median  $z = 2.125$ ). The results are shown in Fig. 4.15, which illustrates the distribution of the  $q_{IR}$  values with respect to the redshifts.

To determine how the radio-properties of the JVLA-observed Hot DOGs are associated with the radio-WISE selected galaxies, which have similar WISE selection criteria but are selected with conditions on their 21 cm FIRST emission, I repeat the method shown in Fig. 4.15 for the Hot DOGs in this sample and from Jones et al. (2014) with the radio-WISE selected galaxies from Jones et al. (2015) and Lonsdale et al. (2015). To estimate the K-corrected 1.4 GHz flux from the comparison sample, I use a K-correction factor of  $(1+z)^{-(1+\alpha)}$ , where  $z$  is the redshift of the galaxy and  $\alpha$  is the spectral index, assumed to be  $\alpha = -0.8$  (Novak et al., 2017). The results are shown in Fig. 4.16, and indicates a distinct difference between the two populations. The radio-WISE selected galaxies from Jones et al. (2015) and Lonsdale et al. (2015) are in general agreement, despite the range of redshifts in the two samples. As shown in Fig. 4.15, there is agreement between the two samples of Hot DOGs, however there is a large disparity between the  $q$ -values for the Hot DOGs and the radio-WISE selected galaxies, which are significantly lower than the expected range indicated by Ivison et al. (2010). This is likely due to the additional constraints on the radio emission from these galaxies, producing excess radio emission than expected from the population of  $250 \mu\text{m}$  selected SMGs in Ivison et al. (2010). The  $q$ -value for W2305 is in general agreement with the  $q$ -values for the radio-WISE selected galaxies, further suggesting that this galaxy is a

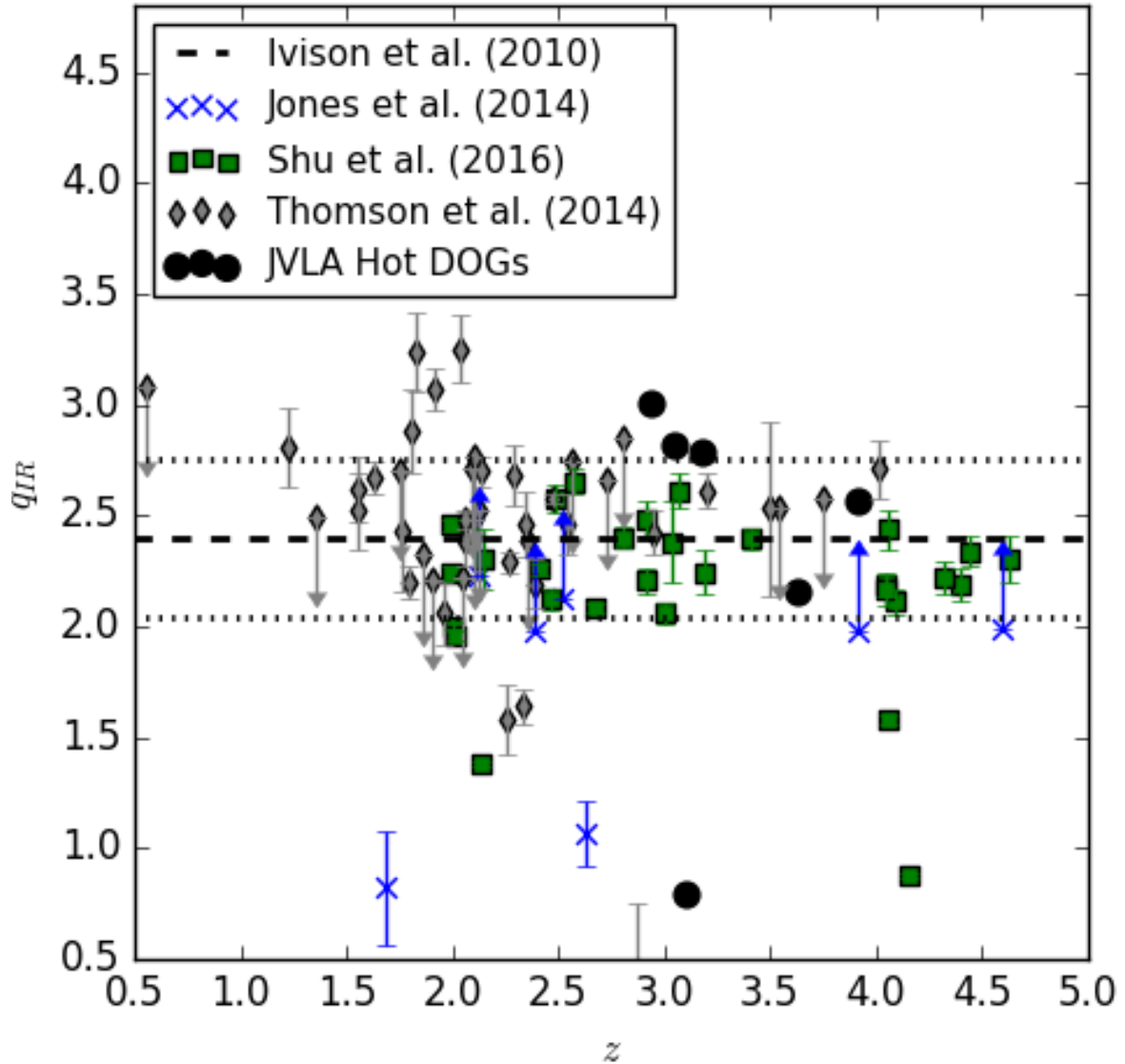


Figure 4.15: Comparison of  $q_{IR}$  values derived using rest-frame  $L_{8-1000 \mu\text{m}}$  and  $S_{1.4 \text{ GHz}}$  for the Hot DOGs in this sample (black circles) against previously observed Hot DOGs (Jones et al., 2014) (blue crosses).  $L_{8-1000 \mu\text{m}}$  was derived using the fits from the SEDs in Fig. 4.11. Comparison samples are shown by green squares and grey diamonds for (Shu et al., 2016) and (Thomson et al., 2014) respectively. A black dashed line and black dotted lines illustrate the median value and the  $\pm 2\sigma$  values for  $250 \mu\text{m}$  selected galaxies in the GOODS-N field (Ivison et al., 2010).

radio-loud Hot DOG. This suggests that Hot DOGs could be radio-quiet counterparts to the radio-WISE selected galaxies, and only the FIRST-detected Hot DOG in this sample is likely to be a radio-loud Hot DOG, rather than a different class of galaxy. All of the spectroscopic redshifts of the radio-WISE selected galaxies in Jones et al. (2014) are much lower than the redshifts of the Hot DOGs in this sample. If these galaxies are linked in the galaxy evolution paradigm, this could suggest that most of the Hot DOGs in this sample are in a radio-quiet phase of their evolution, becoming more radio powerful at lower redshifts, and W2305 could be the interim stage between these two classes of galaxy. To understand this further, deep radio observations of a greater number of dust obscured galaxies need to be made at different redshifts to ascertain the evolution of these galaxies.

## 4.5 Summary

The results from the JVLA observations of six WISE-selected, dusty, luminous obscured galaxies are:

- This work has produced redshifts in agreement with previous work by Tsai et al. (2015) for four Hot DOGs. For W0410, a redshift is found outside the predicted error margins from previous work, but in agreement with new findings using ALMA. There is no CO(1–0) emission line in the spectra of W0126 at the frequency corresponding to  $z = 2.937$  (Tsai et al., 2015), suggesting an incorrect redshift designation for this galaxy.
- It was found that W2305 has additional 115.3 GHz CO(1–0) radio companions, unlike the other Hot DOGs in the sample. W2305 likely has compact radio

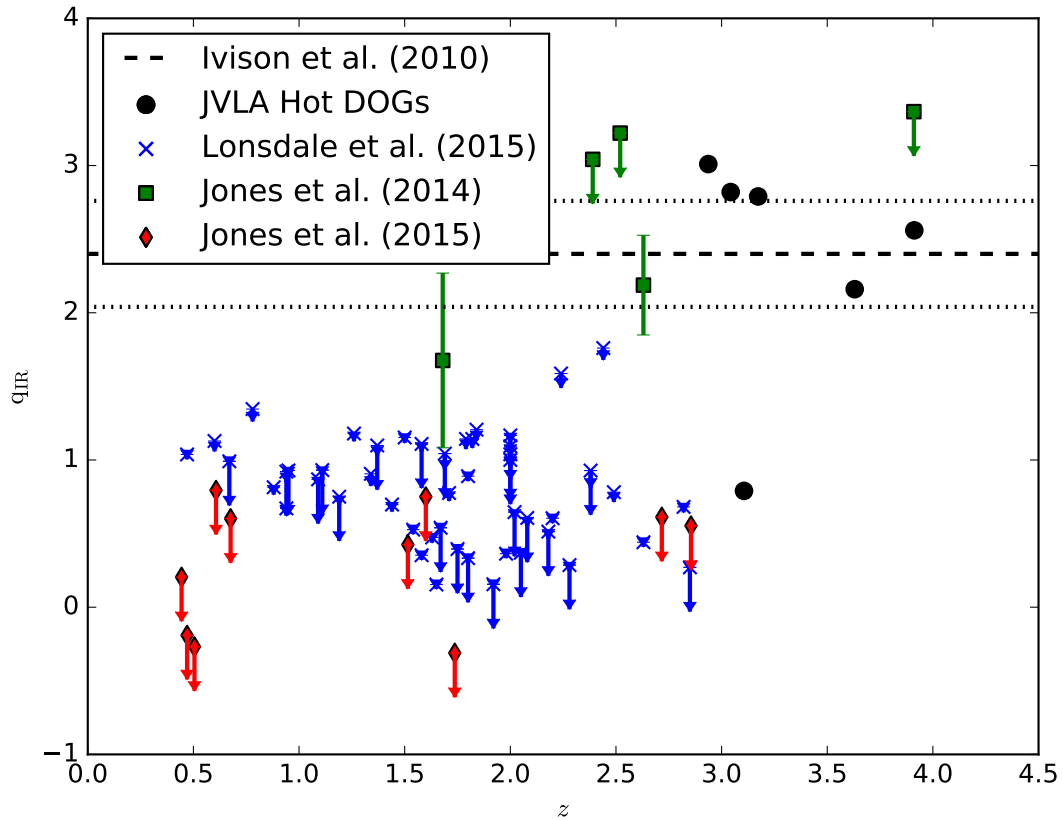


Figure 4.16: Comparison of the  $q_{\text{IR}}$  values with respect to the estimated redshift of radio-WISE selected galaxies in Lonsdale et al. (2015) (blue crosses) and Jones et al. (2015) (red diamonds) compared to JVLA-observed Hot DOGs (black dots) and Hot DOGs in Jones et al. (2014) (green squares). A horizontal line has been included for the median  $\pm 2\sigma$  values (dotted and dashed lines respectively).

## CHAPTER 4. JVLA OBSERVATIONS OF COLD GAS AROUND HOT DOGS

---

emission, rather than jets extending from the host galaxy, and is more radio-loud than the other Hot DOGs in the sample.

- SEDs of the six Hot DOGs in this sample were produced from pre-existing data in conjunction with observations from the JVLA and ALMA. Broken power-law fits of these SEDs suggest that four of the Hot DOGs in the sample are dominated by dust at the frequencies of the JVLA-observations. W0126 and W2305 are likely to have additional free-free and synchrotron components respectively, increasing their fluxes above the expectation for dust-dominated processes.
- $q_{\text{IR}}$  values are calculated for the six Hot DOGs, and I find that the values using  $250 \mu\text{m}$  fluxes do not agree with previous estimates for galaxies at these redshifts. This suggests that these galaxies are radio-quiet but with strong FIR emission not observed at lower redshifts. Dust processes from the obscured AGN within these galaxies may be dominating the supernovae emission at 1.4 GHz.

Future radio observations will attempt to probe the 21 cm Hydrogen emission line in the early universe in an attempt to map the initial perturbations that created the galaxies that are seen today. The Square Kilometer Array (SKA; Bull et al., 2018) is a future radio telescope expected to be running from 2023 (completed 2030), which will use an array of antennae with a maximum baseline of 1 km. The array will be situated in two sites, West Australia and South Africa, observing in a continuous frequency range of 1 MHz to 30 GHz upon completion, and will offer unprecedented resolution necessary to observe the distant universe and provide an insight into galaxy evolution (Murphy, 2009).

# Chapter 5

## Conclusions and Future Prospects

This thesis contains observations of two subsets of heavily dust obscured, high redshift, luminous IR AGN: radio-WISE selected galaxies (Chapter 3) and Hot DOGs (Chapter 4), focusing on their environments and their intrinsic properties.

Chapter 3 was based on work by Penney et al. (2019), using *Spitzer* IRAC  $5.12' \times 5.12'$  observations of 33 fields containing radio-WISE selected galaxies. The results of these observations show that these galaxies inhabit moderately overdense regions of IRAC-selected  $[3.6] - [4.5] > -0.1$  galaxies compared to blank fields from SpUDS and S-COSMOS. Analysing galaxies using this colour selection as a function of distance from the central radio-WISE selected galaxy, there is an enhancement in the density within  $0.5'$ , suggesting that these galaxies could be interacting with galaxies in their local environment on relatively small scales. To understand whether redder IRAC-selected galaxies produced the significant peak shown in Fig. 3.13, an overdensity of galaxies with  $[3.6] - [4.5] > 0.4$  were uncovered. While the density of the galaxies does not explain the observed peak in Fig. 3.13, the results suggest that the fields centered on radio-WISE

## CHAPTER 5. CONCLUSIONS AND FUTURE PROSPECTS

---

selected galaxies contain a uniform overdensity of red IRAC-selected galaxies compared to blank fields. Given the proximity to the radio-WISE selected galaxy, it is likely that the luminous, dust obscured galaxy is interacting with the surrounding environment to produce the observed reddening.

With the advent of the James Webb Space Telescope, observations of fields centered on these luminous, dust obscured galaxies will be more sensitive to the dust in these environments on scales of  $\sim 100$  kpc, helping to understand how these dust obscured, luminous IR galaxies formed and how they interact with their local environment. Deep observations to produce photometric redshifts of the Group-II galaxies would need to be extensively long to produce a complete sample with firm photometric redshifts. Deep observations to determine the spectroscopic redshift may be more suitable, given the faintness at  $3.6 \mu\text{m}$  and  $4.5 \mu\text{m}$ , and could help to determine whether the observed uniform overdensity of Group-II galaxies is associated with the radio-WISE selected galaxy. Future work by Ferris et al. (in prep.) will use optical spectroscopy to determine the SMBH and host masses of these galaxies, and could put estimates as to the level of obscuration necessary to produce the red-IRAC colours ( $[3.6] - [4.5] > 0.5$ ) seen in this work.

Chapter 4 is based on work by Penney et al. (in prep.) using JVLA observations of 6 luminous Hot DOGs selected from the HyLIRG sample of Tsai et al. (2015), looking at their cold gas emission at  $\sim 30$  GHz. The results show that 5/6 of these galaxies have CO(J=1-0) emission lines, with 3 consistent with previous redshift estimates (Tsai et al., 2015). A single galaxy shows a lack of any emission line at the expected frequency, suggesting a possibly incorrect redshift. The  $\sim 30$  GHz continuum values are also calculated, and suggest that the JVLA observations in this work could trace the free-free and dust dominated emission of the galaxy. To understand the radio-processes of these galaxies, the 1.4 GHz emission is taken from the FIRST survey for 5/6 galaxies

## CHAPTER 5. CONCLUSIONS AND FUTURE PROSPECTS

---

and NVSS for W0410, and there appears to be a lack of emission at this frequency for all but W2305. Comparing the 1.4 GHz emission to the FIR emission using the FIR-radio correlation, the FIRST-undetected Hot DOGs appear far fainter than previous work, suggesting that these galaxies are dominated by dust-obscured AGN emission rather than dusty star-formation. The central, obscured AGN in these FIRST-undetected Hot DOGs are likely to be radio-quiet while boosting the FIR emission of the host-galaxy, producing  $q_{\text{IR}}$ -values far larger than previous estimates. In contrast, the only FIRST detected Hot DOG in the sample, W2305, has significantly greater  $q_{\text{IR}}$ -values compared to previous work, suggesting that this galaxy is a radio-loud Hot DOG. Fig. 4.13 shows that the 1.4 GHz emission from W2305 does not appear in lobes, suggesting that the emission is still confined to the host galaxy, similar to the radio-WISE selected galaxies. However, W2305 is not as radio-loud as the radio-WISE selected galaxies, and is likely only a radio-loud Hot DOG.

Higher CO transitions are generally brighter than the CO(J=1-0) transition, and additional transitions can help to place constraints on the motion and mass of the cold, star-forming gas. Further radio observations are currently being employed by Lopez et al. (in prep.) to determine the higher CO transitions of several of the Hot DOGs in this work. When used in tandem with these results, these observations could be used to understand the nature of the star formation properties of these galaxies. Deep observations between  $1.4 \text{ GHz} \lesssim \nu \lesssim 30 \text{ GHz}$  could be used to constrain the upper limits of the free-free and synchrotron emission in these galaxies. These observations would be able to determine the exact  $q_{\text{IR}}$ -values of these galaxies, and help to understand the factor by which the IR-emission is boosted by the central AGN. Deeper 1.4 GHz observations would be able to understand the nature of potential jets from these galaxies, and whether the central AGN is radio-quiet.

Using previous work on both subsets of luminous, dust-obscured galaxies in this thesis,

the result suggest that the radio-WISE selected galaxies have higher mid-IR fluxes and redder IRAC [3.6] – [4.5] colours compared to Hot DOGs from Wu et al. (2012), as shown in Fig. 3.5. Comparing the 850  $\mu\text{m}$  fluxes between Hot DOGs and radio-WISE selected galaxies, the Hot DOGs generally have greater sub-millimeter fluxes and significantly greater  $q_{\text{IR}}$ -values. These results suggest that these two subsets are part of different classes of galaxies, with the Hot DOGs dominating in the FIR and sub-millimeter wavelengths, and radio-WISE selected galaxies dominant in the mid-IR and radio. Given that the spectroscopic redshifts of the radio-WISE selected galaxies in Chapter 3 are lower than the Hot DOGs in Chapter 4, this could imply that the Hot DOGs are younger counterparts, with lower radio emission. However, a larger sample of spectroscopically confirmed galaxies at a wide range of redshifts is needed to confirm whether these galaxies are linked.

Radio observations of galaxies selected to have significant quantities of dust obscuration have provided a unique insight into the properties of dust-obscured galaxies. Follow-up observations using *Spitzer* show that a subset of these galaxies inhabit significantly overdense environments of red IRAC-selected objects, similar to radio-loud AGN, suggesting that the radio-WISE galaxies could be radio-intermediate counterparts of the RLAGN. Radio observations of a subset of luminous Hot DOGs from Tsai et al. (2015) show that these galaxies are significantly more radio-quiet than expected, suggesting that the central, luminous, dust obscured AGN is boosting the FIR and sub-millimeter emission and deeper 1.4 GHz observations could help to understand the synchrotron processes of these high redshift, luminous IR galaxies.

# Appendix A

## Abbreviations

ACA = Atacama Compact Array

AGN = Active Galactic Nuclei

ALMA = Atacama Large Millimeter/Sub-Millimeter Array

Arcsec =  $1/60$  arcmin =  $1/3600$  degrees

Arcmin = 1 arc-minute =  $1/60$  degrees

$c$  = Speed of light ( $299,792,458 \text{ m s}^{-1}$ )

CARLA = Clusters Around Radio-Loud AGN

COSMOS = Cosmic Evolution Survey

cm = centimeter

## APPENDIX A. ABBREVIATIONS

---

DOG = Dust Obscured Galaxy

DSFGs = Dusty Star Forming Galaxies

EAZY = Easy and Accurate  $Z_{\text{phot}}$  from Yale

EVLA = Expanded Very Large Array

JVLA = Karl G. Jansky Very Large Array

FAST = Fitting and Assessment of Synthetic Templates

FIRST = Faint Images of the Radio Sky at Twenty-cm

FTS = Fourier Transform Spectrometer

FWHM = Full-Width at Half Maximum

FWZI = Full-Width at Zero Intensity

G = Gravitational Constant ( $6.67408 \times 10^{-11} \text{ m}^3 \text{ kg}^{-1} \text{ s}^{-2}$ )

GHz = Giga-Hertz ( $10^9 \text{ Hz}$ )

GPS = GHz Peaked Spectrum

Hot DOG = Hot Dust Obscured Galaxy

HyLIRG = Hyper-Luminous Infra-Red Galaxy

Hz = Hertz ( $\text{s}^{-1}$ )

## APPENDIX A. ABBREVIATIONS

---

HzRG = High Redshift Radio-Galaxy

ICM = Intra-Cluster Medium

IGM = Intergalactic Medium

IR = Infra-Red

IRAC = Infra-Red Array Camera

IRS = Infra-Red Spectrometer

IRSA = Infra-Red Science Archive

JWST = James Webb Space Telescope

JVLA = Karl-Jansky Very Large Array

Jy = Jansky ( $10^{-26}$  Watts m Hz<sup>-1</sup> )

K = Kelvin

kg = kilo-grams

km = kilometer

kpc = kilo-parsecs

LIRG = Luminous Infra-Red Galaxy

MIPS = Multiband Imaging Photometer for Spitzer

## APPENDIX A. ABBREVIATIONS

---

MOPEX = Mosaicker and Point Source Extractor

Mpc = Mega Parsec ( $3.09 \times 10^{26}$  m)

mm = millimeter

MHz = Mega-Hertz ( $10^6$  Hz)

NASA = National Aeronautics and Space Administration

NRAO = National Radio Astronomy Observatory

NVSS = NRAO VLA Sky Survey

PSF = Point Spread Function

PV = Position-Velocity

RLAGN = Radio-Loud Active Galactic Nuclei

RMS = Root Mean Square

SCUBA = Submillimetre Common-User Bolometer Array

SDSS = Sloan Digital Sky Survey

SED = Spectral Energy Distribution

SERVS = *Spitzer* Extragalactic Representative Volume Survey

SKA = Square Kilometer Array

## APPENDIX A. ABBREVIATIONS

---

SNR = Signal to Noise Ratio

SMA = Sub-Millimeter Array

SMBH = Super-Massive Black Hole

SMG = Sub-Millimeter Galaxy

*Spitzer* = The Spitzer Space Telescope

SpUDS = *Spitzer* UKIDSS Ultra-Deep Survey

THz = Tera-Hertz ( $10^{15}$  Hz)

UV = Ultra-Violet

UKIDSS = UKIRT Infra-Red Deep Sky Survey

UKIRT = United Kingdom Infra-Red Telescope

ULIRG = Ultra-Luminous Infra-Red Galaxy

VLA = Very Large Array

W = Watts ( $\text{kg m}^2 \text{s}^{-3}$ )

WISE = Wide-Field Infra-Red Survey Explorer

$z$  = Redshift

## Appendix B

# Properties of *Spitzer*-observed Radio-WISE Selected Galaxies

## APPENDIX B. PROPERTIES OF *SPITZER*-OBSERVED RADIO-WISE SELECTED GALAXIES

WISE Designation	RA (J2000)	DEC (J2000)	3.6 $\mu\text{m}$ (mag)	4.5 $\mu\text{m}$ (mag)	12 $\mu\text{m}$ (mag)	22 $\mu\text{m}$ (mag)	Redshift
W0304-3108	03:04:27.45	-31:08:38.40	17.82 $\pm$ 0.005	16.78 $\pm$ 0.002	14.84 $\pm$ 0.04	13.81 $\pm$ 0.07	1.54
W0354-3308	03:54:48.22	-33:08:27.24	19.04 $\pm$ 0.01	17.78 $\pm$ 0.003	15.17 $\pm$ 0.04	14.22 $\pm$ 0.13	1.37
W0519-0813	05:19:05.81	-08:13:20.03	19.20 $\pm$ 0.01	18.47 $\pm$ 0.005	16.17 $\pm$ 0.13	14.79 $\pm$ 0.26	2.05
W0525-3614	05:25:33.50	-36:14:40.92	19.84 $\pm$ 0.02	19.21 $\pm$ 0.01	16.08 $\pm$ 0.08	14.80 $\pm$ 0.23	1.69
W0526-3225	05:26:24.72	-32:25:00.84	19.70 $\pm$ 0.01	18.55 $\pm$ 0.01	14.40 $\pm$ 0.03	12.83 $\pm$ 0.05	1.98
W0549-3739	05:49:30.07	-37:39:39.95	19.89 $\pm$ 0.02	18.93 $\pm$ 0.006	16.22 $\pm$ 0.09	14.87 $\pm$ 0.23	1.71
W0613-3407	06:13:48.05	-34:07:29.29	19.18 $\pm$ 0.01	18.13 $\pm$ 0.004	15.39 $\pm$ 0.05	14.19 $\pm$ 0.13	2.18
W0630-2121	06:30:27.82	-21:20:58.92	19.69 $\pm$ 0.01	18.91 $\pm$ 0.01	15.37 $\pm$ 0.06	14.58 $\pm$ 0.23	1.44
W0642-2728	06:42:28.80	-27:28:01.20	18.92 $\pm$ 0.01	18.10 $\pm$ 0.004	17.17 $\pm$ NA	15.08 $\pm$ NA	1.34
W0719-3349	07:19:12.72	-33:49:44.77	19.86 $\pm$ 0.02	18.65 $\pm$ 0.01	15.70 $\pm$ 0.07	14.76 $\pm$ 0.25	1.63
W0729+6544	07:29:02.64	65:44:29.40	19.46 $\pm$ 0.005	18.48 $\pm$ 0.01	15.24 $\pm$ 0.05	13.77 $\pm$ 0.10	2.24
W0823-0624	08:23:11.28	-06:24:08.42	18.21 $\pm$ 0.01	17.26 $\pm$ 0.003	14.96 $\pm$ 0.04	13.80 $\pm$ 0.10	1.75
W1308-3447	13:08:17.04	-34:47:54.24	18.74 $\pm$ 0.01	17.88 $\pm$ 0.004	15.16 $\pm$ 0.05	13.96 $\pm$ 0.09	1.65
W1343-1136	13:43:31.44	-11:36:09.72	19.31 $\pm$ 0.01	18.48 $\pm$ 0.01	15.90 $\pm$ 0.08	14.82 $\pm$ 0.22	2.49
W1400-2919	14:00:50.16	-29:19:24.60	18.21 $\pm$ 0.002	17.10 $\pm$ 0.002	14.61 $\pm$ 0.03	13.67 $\pm$ 0.08	1.67
W1412-2020	14:12:43.20	-20:20:11.04	18.42 $\pm$ 0.01	17.40 $\pm$ 0.003	15.22 $\pm$ 0.04	13.98 $\pm$ 0.11	1.82
W1434-0235	14:34:19.68	-02:35:43.87	18.89 $\pm$ 0.01	17.90 $\pm$ 0.004	15.63 $\pm$ 0.06	14.67 $\pm$ 0.20	1.92
W1500-0649	15:00:48.72	-06:49:39.83	18.61 $\pm$ 0.01	17.55 $\pm$ 0.003	14.47 $\pm$ 0.03	13.36 $\pm$ 0.07	1.50
W1513-2210	15:13:10.32	-22:10:04.44	19.05 $\pm$ 0.01	18.08 $\pm$ 0.004	15.38 $\pm$ 0.07	13.82 $\pm$ 0.15	2.20
W1517 + 3523 $^\alpha$	15:17:58.56	35:23:54.24	18.02 $\pm$ 0.01	16.80 $\pm$ 0.002	14.27 $\pm$ 0.03	13.11 $\pm$ 0.05	1.52
W1541-1144	15:41:41.76	-11:44:09.24	19.34 $\pm$ 0.01	18.21 $\pm$ 0.005	15.34 $\pm$ 0.07	13.75 $\pm$ 0.11	1.58
W1634-1721	16:34:26.88	-17:21:39.60	18.92 $\pm$ 0.01	18.08 $\pm$ 0.005	15.78 $\pm$ 0.10	14.62 $\pm$ 0.25	2.08
W1641-0548	16:41:07.20	-05:48:26.86	18.35 $\pm$ 0.01	17.29 $\pm$ 0.003	15.25 $\pm$ 0.06	14.55 $\pm$ 0.2	1.84
W1653-0102	16:53:05.28	-01:02:30.59	18.71 $\pm$ 0.01	18.10 $\pm$ 0.005	15.51 $\pm$ 0.08	14.64 $\pm$ 0.23	2.02
W1702-0811	17:02:04.56	-08:11:07.41	20.31 $\pm$ 0.03	19.19 $\pm$ 0.01	15.40 $\pm$ 0.10	13.88 $\pm$ 0.18	2.85
W1703-0517	17:03:24.96	-05:17:43.19	19.52 $\pm$ 0.01	18.39 $\pm$ 0.01	15.61 $\pm$ 0.12	13.86 $\pm$ 0.18	1.80
W1717 + 5313 $^\alpha$	17:17:06.00	53:13:42.60	17.84 $\pm$ 0.005	16.96 $\pm$ 0.002	14.72 $\pm$ 0.03	13.79 $\pm$ 0.07	2.72
W1936-3354	19:36:22.56	-33:54:20.52	19.31 $\pm$ 0.01	18.25 $\pm$ 0.005	15.50 $\pm$ 0.07	14.46 $\pm$ 0.20	2.24
W1951-0420	19:51:41.28	-04:20:24.50	19.66 $\pm$ 0.02	18.78 $\pm$ 0.01	15.50 $\pm$ 0.08	14.05 $\pm$ 0.13	1.58
W1958-0746	19:58:01.68	-07:46:09.30	18.95 $\pm$ 0.01	17.94 $\pm$ 0.004	15.25 $\pm$ 0.07	14.05 $\pm$ 0.12	1.80
W2000-2803	20:00:48.48	-28:02:51.36	19.78 $\pm$ 0.02	18.39 $\pm$ 0.005	15.20 $\pm$ 0.07	14.24 $\pm$ 0.19	2.28
W2021-2611	20:21:48.00	-26:12:00.00	20.96 $\pm$ 0.04	19.82 $\pm$ 0.01	16.40 $\pm$ 0.16	14.43 $\pm$ 0.19	2.44
W2059-3541	20:59:47.04	-35:41:34.45	19.10 $\pm$ 0.01	18.08 $\pm$ 0.004	15.31 $\pm$ 0.06	14.60 $\pm$ 0.26	2.38

Table B.1: 33 WISE-Selected Radio-Loud objects in the centre of the field, including the position, and photometry from the IRAC and WISE W3 and W4 bands with error. Galaxies marked with  $\alpha$  by their designation can be found in (Jones et al., 2015), which details their expected IR luminosity that is not available in this work. For information on obtaining the spectroscopic redshifts for all radio-WISE selected objects, see previous work (Lonsdale et al., 2015). Error margins for IRAC bands are calculated using Source Extractor (see Section 3.2.2). Positions, WISE magnitudes and errors were taken from the WISE All-Sky Catalogue.

# Bibliography

- Aird, J., Coil, A. L., Georgakakis, A., Nandra, K., Barro, G., & Pérez-González, P. G. (2015). The evolution of the X-ray luminosity functions of unabsorbed and absorbed AGNs out to  $z \sim 5$ . *Monthly Notices of the Royal Astronomical Society*, 451:1892–1927.
- Aird, J., Nandra, K., Laird, E. S., Georgakakis, A., Ashby, M. L. N., Barmby, P., Coil, A. L., Huang, J.-S., Koekemoer, A. M., Steidel, C. C., & Willmer, C. N. A. (2010). The evolution of the hard X-ray luminosity function of AGN. *Monthly Notices of the Royal Astronomical Society*, 401:2531–2551.
- Alam, S., Albareti, F. D., Allende Prieto, C., Anders, F., Anderson, S. F., Anderton, T., Andrews, B. H., Armengaud, E., Aubourg, É., Bailey, S., & et al. (2015). The Eleventh and Twelfth Data Releases of the Sloan Digital Sky Survey: Final Data from SDSS-III. *Astrophysical Journal Supplement Series*, 219:12.
- Alexander, D. M. & Hickox, R. C. (2012). What drives the growth of black holes? *New Astronomy Reviews*, 56:93–121.
- Antonucci, R. R. J. & Miller, J. S. (1985). Spectropolarimetry and the nature of NGC 1068. *Astrophysical Journal*, 297:621–632.
- Aravena, M., Hodge, J. A., Wagg, J., Carilli, C. L., Daddi, E., Dannerbauer, H., Lentati, L., Riechers, D. A., Sargent, M., & Walter, F. (2014). CO(1-0) line imaging

- of massive star-forming disc galaxies at  $z = 1.5 - 2.2$ . *Monthly Notices of the Royal Astronomical Society*, 442:558–564.
- Aravena, M., Murphy, E. J., Aguirre, J. E., Ashby, M. L. N., Benson, B. A., Bothwell, M., Brodwin, M., Carlstrom, J. E., Chapman, S. C., Crawford, T. M., de Breuck, C., Fassnacht, C. D., Gonzalez, A. H., Greve, T. R., Gullberg, B., Hezaveh, Y., Holder, G. P., Holzzapfel, W. L., Keisler, R., Malkan, M., Marrone, D. P., McIntyre, V., Reichardt, C. L., Sharon, K., Spilker, J. S., Stalder, B., Stark, A. A., Vieira, J. D., & Weiß, A. (2013). Large gas reservoirs and free-free emission in two lensed star-forming galaxies at  $z = 2.7$ . *Monthly Notices of the Royal Astronomical Society*, 433:498–505.
- Aravena, M., Spilker, J. S., Bethermin, M., Bothwell, M., Chapman, S. C., de Breuck, C., Furstenuau, R. M., González-López, J., Greve, T. R., Litke, K., Ma, J., Malkan, M., Marrone, D. P., Murphy, E. J., Stark, A., Strandet, M., Vieira, J. D., Weiss, A., Welikala, N., Wong, G. F., & Collier, J. D. (2016). A survey of the cold molecular gas in gravitationally lensed star-forming galaxies at  $z > 2$ . *Monthly Notices of the Royal Astronomical Society*, 457(4):4406–4420.
- Assef, R. J., Eisenhardt, P. R. M., Stern, D., Tsai, C.-W., Wu, J., Wylezalek, D., Blain, A. W., Bridge, C. R., Donoso, E., Gonzales, A., Griffith, R. L., & Jarrett, T. H. (2015). Half of the Most Luminous Quasars May Be Obscured: Investigating the Nature of WISE-Selected Hot Dust-Obscured Galaxies. *Astrophysical Journal*, 804:27.
- Bardeau, S., Soucail, G., Kneib, J.-P., Czoske, O., Ebeling, H., Hudelot, P., Smail, I., & Smith, G. P. (2007). A CFH12k lensing survey of X-ray luminous galaxy clusters. II. Weak lensing analysis and global correlations. *Astronomy and Astrophysics*, 470:449–466.

- Barnes, J. E. & Hernquist, L. (1992). Dynamics of interacting galaxies. *Annual Review of Astronomy and Astrophysics*, 30:705–742.
- Barnes, J. E. & Hernquist, L. (1996). Transformations of Galaxies. II. Gasdynamics in Merging Disk Galaxies. *Astrophysical Journal*, 471:115.
- Barnes, J. E. & Hernquist, L. (1998). Transformations of Galaxies. II. Gasdynamics in Merging Disk Galaxies: Addendum. *Astrophysical Journal*, 495:187–188.
- Begelman, M. C. (2003). Evidence for Black Holes. *Science*, 300:1898–1904.
- Bennert, N., Canalizo, G., Jungwiert, B., Stockton, A., Schweizer, F., Peng, C. Y., & Lacy, M. (2008). Evidence for Merger Remnants in Early-Type Host Galaxies of Low-Redshift QSOs. *Astrophysical Journal*, 677:846–857.
- Bertin, E. & Arnouts, S. (1996). SExtractor: Software for source extraction. *American Association Pharmaceutical Scientists*, 117:393–404.
- Best, P. N., Lehnert, M. D., Miley, G. K., & Röttgering, H. J. A. (2003). Red galaxy overdensities and the varied cluster environments of powerful radio sources with  $z \sim 1.6$ . *Monthly Notices of the Royal Astronomical Society*, 343:1–21.
- Bicknell, G. V., Dopita, M. A., & O’Dea, C. P. O. (1997). Unification of the Radio and Optical Properties of Gigahertz Peak Spectrum and Compact Steep-Spectrum Radio Sources. *Astrophysical Journal*, 485:112–124.
- Blain, A. W., Barnard, V. E., & Chapman, S. C. (2003). Submillimetre and far-infrared spectral energy distributions of galaxies: the luminosity-temperature relation and consequences for photometric redshifts. *Monthly Notices of the Royal Astronomical Society*, 338:733–744.
- Blain, A. W., Smail, I., Ivison, R. J., Kneib, J.-P., & Frayer, D. T. (2002). Submillimeter galaxies. *Physics Reports*, 369:111–176.

- Blandford, R. D. & Königl, A. (1979). Relativistic jets as compact radio sources. *Astrophysical Journal*, 232:34–48.
- Blandford, R. D. & Rees, M. J. (1978). Extended and compact extragalactic radio sources - Interpretation and theory. *Physica Scripta*, 17:265–274.
- Bolatto, A. D., Wolfire, M., & Leroy, A. K. (2013). The CO-to-H<sub>2</sub> Conversion Factor. *Annual Review of Astronomy and Astrophysics*, 51:207–268.
- Boyle, B. J., Cornwell, T. J., Middelberg, E., Norris, R. P., Appleton, P. N., & Smail, I. (2007). Extending the infrared radio correlation. *Monthly Notices of the Royal Astronomical Society*, 376(3):1182–1188.
- Brammer, G. B., van Dokkum, P. G., & Coppi, P. (2008). EAZY: A Fast, Public Photometric Redshift Code. *Astrophysical Journal*, 686:1503–1513.
- Bridge, C. R., Blain, A., Borys, C. J. K., Petty, S., Benford, D., Eisenhardt, P., Farrah, D., Griffith, R. L., Jarrett, T., Lonsdale, C., Stanford, S. A., Stern, D., Tsai, C.-W., Wright, E. L., & Wu, J. (2013). A New Population of High-z, Dusty Ly $\alpha$  Emitters and Blobs Discovered by WISE: Feedback Caught in the Act? *Astrophysical Journal*, 769:91.
- Bruzual, G. & Charlot, S. (2003). Stellar population synthesis at the resolution of 2003. *Monthly Notices of the Royal Astronomical Society*, 344:1000–1028.
- Bull, P., Camera, S., Kelley, K., Padmanabhan, H., Pritchard, J., Raccanelli, A., Riemer-Sørensen, S., Shao, L., Andrianomena, S., Athanassoula, E., Bacon, D., Barkana, R., Bertone, G., Bonvin, C., Bosma, A., Brüggén, M., Burigana, C., Böehm, C., Calore, F., Cembranos, J. A. R., Clarkson, C., Connors, R. M. T., de la Cruz-Dombriz, Á., Dunsby, P. K. S., Fornengo, N., Gaggero, D., Harrison, I., Larena, J., Ma, Y.-Z., Maartens, R., Méndez-Isla, M., Mohanty, S. D., Murray, S. G., Parkinson,

- D., Pourtsidou, A., Quinn, P. J., Regis, M., Saha, P., Sahlén, M., Sakellariadou, M., Silk, J., Trombetti, T., Vazza, F., Venumadhav, T., Vidotto, F., Villaescusa-Navarro, F., Wang, Y., Weniger, C., Wolz, L., Zhang, F., Gaensler, B. M., & Weltman, A. (2018). Fundamental Physics with the Square Kilometer Array. *arXiv e-prints*.
- Calzetti, D., Armus, L., Bohlin, R. C., Kinney, A. L., Koornneef, J., & Storchi-Bergmann, T. (2000). The Dust Content and Opacity of Actively Star-forming Galaxies. *Astrophysical Journal*, 533:682–695.
- Caputi, K. I., Cirasuolo, M., Dunlop, J. S., McLure, R. J., Farrah, D., & Almaini, O. (2011). The stellar mass function of the most-massive galaxies at  $3 \leq z < 5$  in the UKIDSS Ultra Deep Survey. *Monthly Notices of the Royal Astronomical Society*, 413:162–176.
- Carilli, C. L. (2008). SKA Key science project: Radio observations of cosmic reionization and first light. *arXiv e-prints*, page arXiv:0802.1727.
- Carilli, C. L. & Yun, M. S. (1999). The Radio-to-Submillimeter Spectral Index as a Redshift Indicator. *Astrophysical Journal Letters*, 513:L13–L16.
- Casey, C. M. (2016). The Ubiquity of Coeval Starbursts in Massive Galaxy Cluster Progenitors. *Astrophysical Journal*, 824:36.
- Casey, C. M., Narayanan, D., & Cooray, A. (2014). Dusty star-forming galaxies at high redshift. *Physics Reports*, 541:45–161.
- Castignani, G., Chiaberge, M., Celotti, A., Norman, C., & De Zotti, G. (2014). Cluster Candidates around Low-power Radio Galaxies at  $z \sim 1-2$  in COSMOS. *Astrophysical Journal*, 792:114.
- Chapman, S. C., Smail, I., Ivison, R. J., Helou, G., Dale, D. A., & Lagache, G. (2002). Optically Faint Counterparts to the Infrared Space Observatory FIRBACK 170 Mi-

- cron Population: Discovery of Cold, Luminous Galaxies at High Redshift. *Astrophysical Journal*, 573:66–74.
- Chiaberge, M., Gilli, R., Lotz, J. M., & Norman, C. (2015). Radio Loud AGNs are Mergers. *Astrophysical Journal*, 806:147.
- Chiang, Y.-K., Overzier, R., & Gebhardt, K. (2013). Ancient Light from Young Cosmic Cities: Physical and Observational Signatures of Galaxy Proto-clusters. *Astrophysical Journal*, 779:127.
- Chiang, Y.-K., Overzier, R. A., Gebhardt, K., & Henriques, B. (2017). Galaxy Proto-clusters as Drivers of Cosmic Star Formation History in the First 2 Gyr. *Astrophysical Journal Letters*, 844:L23.
- Combes, F., García-Burillo, S., Braine, J., Schinnerer, E., Walter, F., & Colina, L. (2011). Galaxy evolution and star formation efficiency at  $0.2 < z < 0.6$ . *Astronomy and Astrophysics*, 528:A124.
- Condon, J. J. (1992). Radio emission from normal galaxies. *Annual Review of Astronomy and Astrophysics*, 30:575–611.
- Condon, J. J., Cotton, W. D., Greisen, E. W., Yin, Q. F., Perley, R. A., Taylor, G. B., & Broderick, J. J. (1998). The NRAO VLA Sky Survey. *Astronomical Journal*, 115:1693–1716.
- Conselice, C. J. (2014). The Evolution of Galaxy Structure Over Cosmic Time. *Annual Review of Astronomy and Astrophysics*, 52:291–337.
- Cooke, E. A., Hatch, N. A., Stern, D., Rettura, A., Brodwin, M., Galametz, A., Wylezalek, D., Bridge, C., Conselice, C. J., De Breuck, C., Gonzalez, A. H., & Jarvis, M. (2016). A Mature Galaxy Cluster at  $z=1.58$  around the Radio Galaxy 7C1753+6311. *Astrophysical Journal*, 816:83.

- Cox, T. J., Jonsson, P., Somerville, R. S., Primack, J. R., & Dekel, A. (2008). The effect of galaxy mass ratio on merger-driven starbursts. *Monthly Notices of the Royal Astronomical Society*, 384:386–409.
- Daddi, E., Dannerbauer, H., Liu, D., Aravena, M., Bournaud, F., Walter, F., Riechers, D., Magdis, G., Sargent, M., Béthermin, M., Carilli, C., Cibinel, A., Dickinson, M., Elbaz, D., Gao, Y., Gobat, R., Hodge, J., & Krips, M. (2015). CO excitation of normal star-forming galaxies out to  $z = 1.5$  as regulated by the properties of their interstellar medium. *Astronomy and Astrophysics*, 577:A46.
- Dannerbauer, H., Daddi, E., Riechers, D. A., Walter, F., Carilli, C. L., Dickinson, M., Elbaz, D., & Morrison, G. E. (2009). Low Milky-Way-Like Molecular Gas Excitation of Massive Disk Galaxies at  $z \sim 1.5$ . *Astrophysical Journal Letters*, 698:L178–L182.
- Dannerbauer, H., Kurk, J. D., De Breuck, C., Wylezalek, D., Santos, J. S., Koyama, Y., Seymour, N., Tanaka, M., Hatch, N., Altieri, B., Coia, D., Galametz, A., Kodama, T., Miley, G., Röttgering, H., Sanchez-Portal, M., Valtchanov, I., Venemans, B., & Ziegler, B. (2014). An excess of dusty starbursts related to the Spiderweb galaxy. *Astronomy and Astrophysics*, 570:A55.
- Davidson, K. & Netzer, H. (1979). The emission lines of quasars and similar objects. *Reviews of Modern Physics*, 51:715–766.
- De Breuck, C., Bertoldi, F., Carilli, C., Omont, A., Venemans, B., Röttgering, H., Overzier, R., Reuland, M., Miley, G., Ivison, R., & van Breugel, W. (2004). A multi-wavelength study of the proto-cluster surrounding the  $z = 4.1$  radio galaxy TN J1338-1942. *Astronomy and Astrophysics*, 424:1–12.
- de Graauw, T., Helmich, F. P., Phillips, T. G., Stutzki, J., Caux, E., Whyborn, N. D., Dieleman, P., Roelfsema, P. R., Aarts, H., Assendorp, R., Bachiller, R., Baechtold,

W., Barcia, A., Beintema, D. A., Belitsky, V., Benz, A. O., Bieber, R., Boogert, A., Borys, C., Bumble, B., Caïs, P., Caris, M., Cerulli-Irelli, P., Chattopadhyay, G., Cherednichenko, S., Ciechanowicz, M., Coeur-Joly, O., Comito, C., Cros, A., de Jonge, A., de Lange, G., Delforges, B., Delorme, Y., den Boggende, T., Desbat, J.-M., Diez-González, C., di Giorgio, A. M., Dubbeldam, L., Edwards, K., Eggens, M., Erickson, N., Evers, J., Fich, M., Finn, T., Franke, B., Gaier, T., Gal, C., Gao, J. R., Gallego, J.-D., Gauffre, S., Gill, J. J., Glenz, S., Golstein, H., Goulooze, H., Gunsing, T., Güsten, R., Hartogh, P., Hatch, W. A., Higgins, R., Honingh, E. C., Huisman, R., Jackson, B. D., Jacobs, H., Jacobs, K., Jarchow, C., Javadi, H., Jellema, W., Justen, M., Karpov, A., Kasemann, C., Kawamura, J., Keizer, G., Kester, D., Klapwijk, T. M., Klein, T., Kollberg, E., Kooi, J., Kooiman, P.-P., Kopf, B., Krause, M., Krieg, J.-M., Kramer, C., Kruizenga, B., Kuhn, T., Laauwen, W., Lai, R., Larsson, B., Leduc, H. G., Leinz, C., Lin, R. H., Liseau, R., Liu, G. S., Loose, A., López-Fernandez, I., Lord, S., Luinge, W., Marston, A., Martín-Pintado, J., Maestrini, A., Maiwald, F. W., McCoey, C., Mehdi, I., Megej, A., Melchior, M., Meinsma, L., Merkel, H., Michalska, M., Monstein, C., Moratschke, D., Morris, P., Muller, H., Murphy, J. A., Naber, A., Natale, E., Nowosielski, W., Nuzzolo, F., Olberg, M., Olbrich, M., Orfei, R., Orleanski, P., Ossenkopf, V., Peacock, T., Pearson, J. C., Peron, I., Phillip-May, S., Piazzo, L., Planesas, P., Rataj, M., Ravera, L., Risacher, C., Salez, M., Samoska, L. A., Saraceno, P., Schieder, R., Schlecht, E., Schlöder, F., Schmülling, F., Schultz, M., Schuster, K., Siebertz, O., Smit, H., Szczerba, R., Shipman, R., Steinmetz, E., Stern, J. A., Stokroos, M., Teipen, R., Teyssier, D., Tils, T., Trappe, N., van Baaren, C., van Leeuwen, B.-J., van de Stadt, H., Visser, H., Wildeman, K. J., Wafelbakker, C. K., Ward, J. S., Wesselius, P., Wild, W., Wulff, S., Wunsch, H.-J., Tielens, X., Zaal, P., Zirath, H., Zmuidzinas, J., & Zwart, F. (2010). The Herschel-Heterodyne Instrument for the Far-Infrared (HIFI). *Astronomy and Astrophysics*, 518:L6.

- Delhaize, J., Smolčić, V., Delvecchio, I., Novak, M., Sargent, M., Baran, N., Magnelli, B., Zamorani, G., Schinnerer, E., Murphy, E. J., Aravena, M., Berta, S., Bondi, M., Capak, P., Carilli, C., Ciliegi, P., Civano, F., Ilbert, O., Karim, A., Laigle, C., Le Fèvre, O., Marchesi, S., McCracken, H. J., Salvato, M., Seymour, N., & Tasca, L. (2017). The VLA-COSMOS 3 GHz Large Project: The infrared-radio correlation of star-forming galaxies and AGN to  $z \lesssim 6$ . *Astronomy and Astrophysics*, 602:A4.
- Dempsey, J. T., Friberg, P., Jenness, T., Tilanus, R. P. J., Thomas, H. S., Holland, W. S., Bintley, D., Berry, D. S., Chapin, E. L., Chrysostomou, A., Davis, G. R., Gibb, A. G., Parsons, H., & Robson, E. I. (2013). SCUBA-2: on-sky calibration using submillimetre standard sources. *Monthly Notices of the Royal Astronomical Society*, 430:2534–2544.
- Dey, A., Soifer, B. T., Desai, V., Brand, K., Le Floc’h, E., Brown, M. J. I., Jannuzi, B. T., Armus, L., Bussmann, S., Brodwin, M., Bian, C., Eisenhardt, P., Higdon, S. J., Weedman, D., & Willner, S. P. (2008). A Significant Population of Very Luminous Dust-Obscured Galaxies at Redshift  $z \sim 2$ . *Astrophysical Journal*, 677:943–956.
- Díaz-Santos, T., Assef, R. J., Blain, A. W., Tsai, C. W., Aravena, M., Eisenhardt, P., Wu, J., Stern, D., & Bridge, C. (2016). The Strikingly Uniform, Highly Turbulent Interstellar Medium of the Most Luminous Galaxy in the Universe. *Astrophysical Journal Letters*, 816(1):L6.
- Donoso, E., Li, C., Kauffmann, G., Best, P. N., & Heckman, T. M. (2010). Clustering of radio galaxies and quasars. *Monthly Notices of the Royal Astronomical Society*, 407:1078–1089.
- Downes, D. & Solomon, P. M. (1998). Rotating Nuclear Rings and Extreme Starbursts in Ultraluminous Galaxies. *Astrophysical Journal*, 507:615–654.

- Dressler, A. (1980). Galaxy morphology in rich clusters - Implications for the formation and evolution of galaxies. *Astrophysical Journal*, 236:351–365.
- Dressler, A., Oemler, Jr., A., Couch, W. J., Smail, I., Ellis, R. S., Barger, A., Butcher, H., Poggianti, B. M., & Sharples, R. M. (1997). Evolution since  $z = 0.5$  of the Morphology-Density Relation for Clusters of Galaxies. *Astrophysical Journal*, 490:577–591.
- Dunlop, J., Akiyama, M., Alexander, D., Almaini, O., Borys, C., Bouwens, R., Bremer, M., Cimatti, A., Cirasuolo, M., Clewley, L., Conselice, C., Coppin, K., Dalton, G., Damen, M., Dunne, L., Dye, S., Eales, S., Edge, A., Egami, E., Fall, M., Farrah, D., Ferguson, H., Finoguenov, A., Foucaud, S., Franx, M., Furusawa, H., Huang, J., Ibar, E., Illingworth, G., Ivison, R., Jarvis, M., Labbe, I., Lawrence, A., Maddox, S., McLure, R., Mortier, A., Oliver, S., Ouchi, M., Page, M., Papovich, C., Quadri, R., Rawlings, S., Rieke, G., Schiminovich, D., Sekiguchi, K., Serjeant, S., Simpson, C., Smail, I., Stanway, E., Taylor, A., Watson, M., Williams, R., Yamada, T., van Breukelen, C., & van Dokkum, P. (2007). A Spitzer Public Legacy survey of the UKIDSS Ultra Deep Survey. Spitzer Proposal.
- Dunlop, J. S. & Peacock, J. A. (1990). The Redshift Cut-Off in the Luminosity Function of Radio Galaxies and Quasars. *Monthly Notices of the Royal Astronomical Society*, 247:19.
- Eggen, O. J., Lynden-Bell, D., & Sandage, A. R. (1962). Evidence from the motions of old stars that the Galaxy collapsed. *Astrophysical Journal*, 136:748.
- Eisenhardt, P. R. M., Wu, J., Tsai, C.-W., Assef, R., Benford, D., Blain, A., Bridge, C., Condon, J. J., Cushing, M. C., Cutri, R., Evans, II, N. J., Gelino, C., Griffith, R. L., Grillmair, C. J., Jarrett, T., Lonsdale, C. J., Masci, F. J., Mason, B. S., Petty, S., Sayers, J., Stanford, S. A., Stern, D., Wright, E. L., & Yan, L. (2012). The

- First Hyper-luminous Infrared Galaxy Discovered by WISE. *Astrophysical Journal*, 755:173.
- Elbaz, D. & Cesarsky, C. J. (2003). A Fossil Record of Galaxy Encounters. *Science*, 300:270–274.
- Evans, D. A., Reeves, J. N., Hardcastle, M. J., Kraft, R. P., Lee, J. C., & Virani, S. N. (2010). The Hard X-ray View of Reflection, Absorption, and the Disk-Jet Connection in the Radio-loud AGN 3C 33. *Astrophysical Journal*, 710:859–868.
- Event Horizon Telescope Collaboration, Akiyama, K., Alberdi, A., Alef, W., Asada, K., Azulay, R., Baczko, A.-K., Ball, D., Baloković, M., Barrett, J., & et al. (2019). First M87 Event Horizon Telescope Results. I. The Shadow of the Supermassive Black Hole. *Astrophysical Journal Letters*, 875:L1.
- Falomo, R. & Ulrich, M.-H. (2000). Optical imaging and spectroscopy of BL Lac objects. *Astronomy and Astrophysics*, 357:91–100.
- Fan, L., Knudsen, K. K., Fogasy, J., & Drouart, G. (2018). ALMA Detections of CO Emission in the Most Luminous, Heavily Dust-obscured Quasars at  $z > 3$ . *Astrophysical Journal Letters*, 856(1):L5.
- Fan, X., Strauss, M. A., Schneider, D. P., Gunn, J. E., Lupton, R. H., Becker, R. H., Davis, M., Newman, J. A., Richards, G. T., White, R. L., Anderson, Jr., J. E., Annis, J., Bahcall, N. A., Brunner, R. J., Csabai, I., Hennessy, G. S., Hindsley, R. B., Fukugita, M., Kunszt, P. Z., Ivezić, Ž., Knapp, G. R., McKay, T. A., Munn, J. A., Pier, J. R., Szalay, A. S., & York, D. G. (2001). High-Redshift Quasars Found in Sloan Digital Sky Survey Commissioning Data. IV. Luminosity Function from the Fall Equatorial Stripe Sample. *Astronomical Journal*, 121:54–65.

- Fanaroff, B. L. & Riley, J. M. (1974). The morphology of extragalactic radio sources of high and low luminosity. *Monthly Notices of the Royal Astronomical Society*, 167:31P–36P.
- Farouki, R. T. & Shapiro, S. L. (1982). Simulations of merging disk galaxies. *Astrophysical Journal*, 259:103–115.
- Fath, E. A. (1909). The Spectra of Some Spiral Nebulae and Globular Star Clusters. *Popular Astronomy*, 17:504–508.
- Fazio, G. G., Hora, J. L., Allen, L. E., Ashby, M. L. N., Barmby, P., Deutsch, L. K., Huang, J.-S., Kleiner, S., Marengo, M., Megeath, S. T., Melnick, G. J., Pahre, M. A., Patten, B. M., Polizotti, J., Smith, H. A., Taylor, R. S., Wang, Z., Willner, S. P., Hoffmann, W. F., Pipher, J. L., Forrest, W. J., McMurty, C. W., McCreight, C. R., McKelvey, M. E., McMurray, R. E., Koch, D. G., Moseley, S. H., Arendt, R. G., Mentzell, J. E., Marx, C. T., Losch, P., Mayman, P., Eichhorn, W., Krebs, D., Jhabvala, M., Gezari, D. Y., Fixsen, D. J., Flores, J., Shakoorzadeh, K., Jungo, R., Hakun, C., Workman, L., Karpati, G., Kichak, R., Whitley, R., Mann, S., Tollestrup, E. V., Eisenhardt, P., Stern, D., Gorjian, V., Bhattacharya, B., Carey, S., Nelson, B. O., Glaccum, W. J., Lacy, M., Lowrance, P. J., Laine, S., Reach, W. T., Stauffer, J. A., Surace, J. A., Wilson, G., Wright, E. L., Hoffman, A., Domingo, G., & Cohen, M. (2004). The Infrared Array Camera (IRAC) for the Spitzer Space Telescope. *Astrophysical Journal Supplement Series*, 154:10–17.
- Felten, J. E. & Morrison, P. (1966). Omnidirectional Inverse Compton and Synchrotron Radiation from Cosmic Distributions of Fast Electrons and Thermal Photons. *Astrophysical Journal*, 146:686.
- Foyle, K., Rix, H.-W., Walter, F., & Leroy, A. K. (2010). ARM AND INTER-

ARM STAR FORMATION IN SPIRAL GALAXIES. *The Astrophysical Journal*, 725(1):534–541.

Gardner, J. P., Mather, J. C., Clampin, M., Doyon, R., Greenhouse, M. A., Hammel, H. B., Hutchings, J. B., Jakobsen, P., Lilly, S. J., Long, K. S., Lunine, J. I., McCaughrean, M. J., Mountain, M., Nella, J., Rieke, G. H., Rieke, M. J., Rix, H.-W., Smith, E. P., Sonneborn, G., Stiavelli, M., Stockman, H. S., Windhorst, R. A., & Wright, G. S. (2006). The James Webb Space Telescope. *Space Science Reviews*, 123:485–606.

Geller, M. J., Diaferio, A., Rines, K. J., & Serra, A. L. (2013). Measuring the Mass Distribution in Galaxy Clusters. *Astrophysical Journal*, 764:58.

Genzel, R., Burkert, A., Bouché, N., Cresci, G., Förster Schreiber, N. M., Shapley, A., Shapiro, K., Tacconi, L. J., Buschkamp, P., Cimatti, A., Daddi, E., Davies, R., Eisenhauer, F., Erb, D. K., Genel, S., Gerhard, O., Hicks, E., Lutz, D., Naab, T., Ott, T., Rabien, S., Renzini, A., Steidel, C. C., Sternberg, A., & Lilly, S. J. (2008). From Rings to Bulges: Evidence for Rapid Secular Galaxy Evolution at  $z \sim 2$  from Integral Field Spectroscopy in the SINS Survey. *Astrophysical Journal*, 687:59–77.

Gott, III, J. R. & Gunn, J. E. (1971). The Coma Cluster as an X-Ray Source: Some Cosmological Implications. *Astrophysical Journal Letters*, 169:L13.

Greve, T. R., Ivison, R. J., & Papadopoulos, P. P. (2003). Gas and Dust in the Extremely Red Object ERO J164502+4626.4. *Astrophysical Journal*, 599:839–846.

Greve, T. R., Stern, D., Ivison, R. J., De Breuck, C., Kovács, A., & Bertoldi, F. (2007). Wide-field mid-infrared and millimetre imaging of the high-redshift radio galaxy, 4C41.17. *Monthly Notices of the Royal Astronomical Society*, 382:48–66.

## BIBLIOGRAPHY

---

Griffin, M. J., Abergel, A., Abreu, A., Ade, P. A. R., André, P., Augueres, J.-L., Babbedge, T., Bae, Y., Baillie, T., Baluteau, J.-P., Barlow, M. J., Bendo, G., Benielli, D., Bock, J. J., Bonhomme, P., Brisbin, D., Brockley-Blatt, C., Caldwell, M., Cara, C., Castro-Rodriguez, N., Cerulli, R., Chaniel, P., Chen, S., Clark, E., Clements, D. L., Clerc, L., Coker, J., Communal, D., Conversi, L., Cox, P., Crumb, D., Cunningham, C., Daly, F., Davis, G. R., de Antoni, P., Delderfield, J., Devin, N., di Giorgio, A., Didschuns, I., Dohlen, K., Donati, M., Dowell, A., Dowell, C. D., Duband, L., Dumaye, L., Emery, R. J., Ferlet, M., Ferrand, D., Fontignie, J., Fox, M., Franceschini, A., Frerking, M., Fulton, T., Garcia, J., Gastaud, R., Gear, W. K., Glenn, J., Goizel, A., Griffin, D. K., Grundy, T., Guest, S., Guillemet, L., Hargrave, P. C., Harwit, M., Hastings, P., Hatziminaoglou, E., Herman, M., Hinde, B., Hristov, V., Huang, M., Imhof, P., Isaak, K. J., Israelsson, U., Ivison, R. J., Jennings, D., Kiernan, B., King, K. J., Lange, A. E., Latter, W., Laurent, G., Laurent, P., Leeks, S. J., Lellouch, E., Levenson, L., Li, B., Li, J., Lilienthal, J., Lim, T., Liu, S. J., Lu, N., Madden, S., Mainetti, G., Marliani, P., McKay, D., Mercier, K., Molinari, S., Morris, H., Moseley, H., Mulder, J., Mur, M., Naylor, D. A., Nguyen, H., O'Halloran, B., Oliver, S., Olofsson, G., Olofsson, H.-G., Orfei, R., Page, M. J., Pain, I., Panuzzo, P., Papageorgiou, A., Parks, G., Parr-Burman, P., Pearce, A., Pearson, C., Pérez-Fournon, I., Pinsard, F., Pisano, G., Podosek, J., Pohlen, M., Polehampton, E. T., Poulighen, D., Rigopoulou, D., Rizzo, D., Roseboom, I. G., Roussel, H., Rowan-Robinson, M., Rownd, B., Saraceno, P., Sauvage, M., Savage, R., Savini, G., Sawyer, E., Scharnberg, C., Schmitt, D., Schneider, N., Schulz, B., Schwartz, A., Shafer, R., Shupe, D. L., Sibthorpe, B., Sidher, S., Smith, A., Smith, A. J., Smith, D., Spencer, L., Stobie, B., Sudiwala, R., Sukhatme, K., Surace, C., Stevens, J. A., Swinyard, B. M., Trichas, M., Tourette, T., Triou, H., Tseng, S., Tucker, C., Turner, A., Vaccari, M., Valtchanov, I., Vigroux, L., Virique, E., Voellmer, G., Walker, H., Ward, R., Waskett, T., Weilert, M., Wesson, R., White, G. J., Whitehouse, N., Wil-

- son, C. D., Winter, B., Woodcraft, A. L., Wright, G. S., Xu, C. K., Zavagno, A., Zemcov, M., Zhang, L., & Zonca, E. (2010). The Herschel-SPIRE instrument and its in-flight performance. *Astronomy and Astrophysics*, 518:L3.
- Harris, A. I., Baker, A. J., Frayer, D. T., Smail, I., Swinbank, A. M., Riechers, D. A., van der Werf, P. P., Auld, R., Baes, M., Bussmann, R. S., Buttiglione, S., Cava, A., Clements, D. L., Cooray, A., Dannerbauer, H., Dariush, A., De Zotti, G., Dunne, L., Dye, S., Eales, S., Fritz, J., González-Nuevo, J., Hopwood, R., Ibar, E., Ivison, R. J., Jarvis, M. J., Maddox, S., Negrello, M., Rigby, E., Smith, D. J. B., Temi, P., & Wardlow, J. (2012). Blind Detections of CO J = 1-0 in 11 H-ATLAS Galaxies at  $z = 2.1-3.5$  with the GBT/Zpectrometer. *Astrophysical Journal*, 752(2):152.
- Hatch, N. A., Overzier, R. A., Kurk, J. D., Miley, G. K., Röttgering, H. J. A., & Zirm, A. W. (2009). The growth and assembly of a massive galaxy at  $z \sim 2$ . *Monthly Notices of the Royal Astronomical Society*, 395:114–125.
- Hatch, N. A., Wylezalek, D., Kurk, J. D., Stern, D., De Breuck, C., Jarvis, M. J., Galametz, A., Gonzalez, A. H., Hartley, W. G., Mortlock, A., Seymour, N., & Stevens, J. A. (2014). Why  $z < 1$  radio-loud galaxies are commonly located in protoclusters. *Monthly Notices of the Royal Astronomical Society*, 445:280–289.
- Heckman, T. M. (1980). Star formation and activity in the nuclei of barred galaxies. *Astronomy and Astrophysics*, 88:365.
- Heckman, T. M., Smith, E. P., Baum, S. A., van Breugel, W. J. M., Miley, G. K., Illingworth, G. D., Bothun, G. D., & Balick, B. (1986). Galaxy collisions and mergers - The genesis of very powerful radio sources? *Astrophysical Journal*, 311:526–547.
- Helou, G., Soifer, B. T., & Rowan-Robinson, M. (1985). Thermal infrared and non-thermal radio - Remarkable correlation in disks of galaxies. *Astrophysical Journal Letters*, 298:L7–L11.

- Hernquist, L. (1989). Tidal triggering of starbursts and nuclear activity in galaxies. *Nature*, 340:687–691.
- Hernquist, L. (1992). Structure of merger remnants. I - Bulgeless progenitors. *Astrophysical Journal*, 400:460–475.
- Hernquist, L. (1993). N-body realizations of compound galaxies. *Astrophysical Journal Supplement Series*, 86:389–400.
- Hildebrand, R. H. (1983). The Determination of Cloud Masses and Dust Characteristics from Submillimetre Thermal Emission. *Quarterly Journal of the Royal Astronomical Society*, 24:267.
- Ho, L. C., Filippenko, A. V., & Sargent, W. L. W. (1997). A Search for “Dwarf” Seyfert Nuclei. V. Demographics of Nuclear Activity in Nearby Galaxies. *Astrophysical Journal*, 487:568–578.
- Ho, P. T. P., Moran, J. M., & Lo, K. Y. (2004). The Submillimeter Array. *Astrophysical Journal Letters*, 616:L1–L6.
- Hoekstra, H., Bartelmann, M., Dahle, H., Israel, H., Limousin, M., & Meneghetti, M. (2013). Masses of Galaxy Clusters from Gravitational Lensing. *Space Science Reviews*, 177:75–118.
- Holland, W. S., Robson, E. I., Gear, W. K., Cunningham, C. R., Lightfoot, J. F., Jenness, T., Ivison, R. J., Stevens, J. A., Ade, P. A. R., Griffin, M. J., Duncan, W. D., Murphy, J. A., & Naylor, D. A. (1999). SCUBA: a common-user submillimetre camera operating on the James Clerk Maxwell Telescope. *Monthly Notices of the Royal Astronomical Society*, 303:659–672.
- Hopkins, P. F., Cox, T. J., Hernquist, L., Narayanan, D., Hayward, C. C., & Murray, N. (2013). Star formation in galaxy mergers with realistic models of stellar feedback

- and the interstellar medium. *Monthly Notices of the Royal Astronomical Society*, 430:1901–1927.
- Hopkins, P. F., Hernquist, L., Cox, T. J., Di Matteo, T., Robertson, B., & Springel, V. (2006). A Unified, Merger-driven Model of the Origin of Starbursts, Quasars, the Cosmic X-Ray Background, Supermassive Black Holes, and Galaxy Spheroids. *Astrophysical Journal Supplement Series*, 163:1–49.
- Hopkins, P. F., Hernquist, L., Cox, T. J., & Kereš, D. (2008). A Cosmological Framework for the Co-Evolution of Quasars, Supermassive Black Holes, and Elliptical Galaxies. I. Galaxy Mergers and Quasar Activity. *Astrophysical Journal Supplement Series*, 175:356–389.
- Houck, J. R., Roellig, T. L., van Cleve, J., Forrest, W. J., Herter, T., Lawrence, C. R., Matthews, K., Reitsema, H. J., Soifer, B. T., Watson, D. M., Weedman, D., Huisjen, M., Troeltzsch, J., Barry, D. J., Bernard-Salas, J., Blacken, C. E., Brandl, B. R., Charmandaris, V., Devost, D., Gull, G. E., Hall, P., Henderson, C. P., Higdon, S. J. U., Pirger, B. E., Schoenwald, J., Sloan, G. C., Uchida, K. I., Appleton, P. N., Armus, L., Burgdorf, M. J., Fajardo-Acosta, S. B., Grillmair, C. J., Ingalls, J. G., Morris, P. W., & Teplitz, H. I. (2004). The Infrared Spectrograph (IRS) on the Spitzer Space Telescope. *Astrophysical Journal Supplement Series*, 154:18–24.
- Hubble, E. P. (1925). Cepheids in spiral nebulae. *The Observatory*, 48:139–142.
- Hubble, E. P. (1926). Extragalactic nebulae. *Astrophysical Journal*, 64.
- Hubble, E. P. (1936). *Realm of the Nebulae*.
- Hwang, C.-Y. & Chang, M.-Y. (2009). A Catalog of Morphologically Identified Merging Galaxies. *Astrophysical Journal Supplement Series*, 181:233–237.

- Iguchi, S., Morita, K.-I., Sugimoto, M., Vilaró, B. V., Saito, M., Hasegawa, T., Kawabe, R., Tatematsu, K., Sakamoto, S., Kiuchi, H., Okumura, S. K., Kosugi, G., Inatani, J., Takakuwa, S., Iono, D., Kamazaki, T., Ogasawara, R., & Ishiguro, M. (2009). The Atacama Compact Array (ACA). *Publications of the Astronomical Society of Japan*, 61:1–12.
- Iverson, R. J., Magnelli, B., Ibar, E., Andreani, P., Elbaz, D., Altieri, B., Amblard, A., Arumugam, V., Auld, R., Aussel, H., Babbedge, T., Berta, S., Blain, A., Bock, J., Bongiovanni, A., Boselli, A., Buat, V., Burgarella, D., Castro-Rodríguez, N., Cava, A., Cepa, J., Chantal, P., Cimatti, A., Cirasuolo, M., Clements, D. L., Conley, A., Conversi, L., Cooray, A., Daddi, E., Dominguez, H., Dowell, C. D., Dwek, E., Eales, S., Farrah, D., Förster Schreiber, N., Fox, M., Franceschini, A., Gear, W., Genzel, R., Glenn, J., Griffin, M., Gruppioni, C., Halpern, M., Hatziminaoglou, E., Isaak, K., Lagache, G., Levenson, L., Lu, N., Lutz, D., Madden, S., Maffei, B., Magdis, G., Mainetti, G., Maiolino, R., Marchetti, L., Morrison, G. E., Mortier, A. M. J., Nguyen, H. T., Nordon, R., O'Halloran, B., Oliver, S. J., Omont, A., Owen, F. N., Page, M. J., Panuzzo, P., Papageorgiou, A., Pearson, C. P., Pérez-Fournon, I., Pérez García, A. M., Poglitsch, A., Pohlen, M., Popesso, P., Pozzi, F., Rawlings, J. I., Raymond, G., Rigopoulou, D., Riguccini, L., Rizzo, D., Rodighiero, G., Roseboom, I. G., Rowan-Robinson, M., Saintonge, A., Sanchez Portal, M., Santini, P., Schulz, B., Scott, D., Seymour, N., Shao, L., Shupe, D. L., Smith, A. J., Stevens, J. A., Sturm, E., Symeonidis, M., Tacconi, L., Trichas, M., Tugwell, K. E., Vaccari, M., Valtchanov, I., Vieira, J., Vigroux, L., Wang, L., Ward, R., Wright, G., Xu, C. K., & Zemcov, M. (2010). The far-infrared/radio correlation as probed by Herschel. *Astronomy and Astrophysics*, 518:L31.
- Iverson, R. J., Papadopoulos, P. P., Smail, I., Greve, T. R., Thomson, A. P., Xilouris, E. M., & Chapman, S. C. (2011). Tracing the molecular gas in distant submillimetre

- galaxies via CO(1-0) imaging with the Expanded Very Large Array. *Monthly Notices of the Royal Astronomical Society*, 412:1913–1925.
- Jansky, K. G. (1933). Radio Waves from Outside the Solar System. *Nature*, 132:66.
- John, T. L. (1988). Continuous absorption by the negative hydrogen ion reconsidered. *Astronomy and Astrophysics*, 193:189–192.
- Jones, S. F., Blain, A. W., Assef, R. J., Eisenhardt, P., Lonsdale, C., Condon, J., Farrah, D., Tsai, C.-W., Bridge, C., Wu, J., Wright, E. L., & Jarrett, T. (2017). Overdensities of SMGs around WISE-selected, ultraluminous, high-redshift AGNs. *Monthly Notices of the Royal Astronomical Society*, 469:4565–4577.
- Jones, S. F., Blain, A. W., Lonsdale, C., Condon, J., Farrah, D., Stern, D., Tsai, C.-W., Assef, R. J., Bridge, C., Kimball, A., Lacy, M., Eisenhardt, P., Wu, J., & Jarrett, T. (2015). Submillimetre observations of WISE/radio-selected AGN and their environments. *Monthly Notices of the Royal Astronomical Society*, 448:3325–3338.
- Jones, S. F., Blain, A. W., Stern, D., Assef, R. J., Bridge, C. R., Eisenhardt, P., Petty, S., Wu, J., Tsai, C.-W., Cutri, R., Wright, E. L., & Yan, L. (2014). Submillimetre observations of WISE-selected high-redshift, luminous, dusty galaxies. *Monthly Notices of the Royal Astronomical Society*, 443:146–157.
- Joseph, R. D. & Wright, G. S. (1985). Recent star formation in interacting galaxies. II - Super starburst in merging galaxies. *Monthly Notices of the Royal Astronomical Society*, 214:87–95.
- Kellermann, K. I., Sramek, R., Schmidt, M., Shaffer, D. B., & Green, R. (1989). VLA observations of objects in the Palomar Bright Quasar Survey. *Astronomical Journal*, 98:1195–1207.

- Kennicutt, R. (1983). The origin of the nonthermal radio emission in normal disk galaxies. *Astronomy and Astrophysics*, 120:219–222.
- Khalatyan, A., Cattaneo, A., Schramm, M., Gottlöber, S., Steinmetz, M., & Wisotzki, L. (2008). Is AGN feedback necessary to form red elliptical galaxies? *Monthly Notices of the Royal Astronomical Society*, 387:13–30.
- King, A. (2003). Black Holes, Galaxy Formation, and the  $M_{BH}-\sigma$  Relation. *Astrophysical Journal Letters*, 596:L27–L29.
- Kirkpatrick, J. D., Gelino, C. R., Cushing, M. C., Mace, G. N., Griffith, R. L., Skrutskie, M. F., Marsh, K. A., Wright, E. L., Eisenhardt, P. R., McLean, I. S., Mainzer, A. K., Burgasser, A. J., Tinney, C. G., Parker, S., & Salter, G. (2012). Further Defining Spectral Type “Y” and Exploring the Low-mass End of the Field Brown Dwarf Mass Function. *Astrophysical Journal*, 753:156.
- Kodama, T. & Bower, R. (2003). The  $K_s$ -band luminosity and stellar mass functions of galaxies in  $z \sim 1$  clusters. *Monthly Notices of the Royal Astronomical Society*, 346:1–12.
- Kormendy, J. & Bender, R. (2012). A Revised Parallel-sequence Morphological Classification of Galaxies: Structure and Formation of S0 and Spheroidal Galaxies. *Astrophysical Journal Supplement Series*, 198:2.
- Kormendy, J. & Kennicutt, Jr., R. C. (2004). Secular Evolution and the Formation of Pseudobulges in Disk Galaxies. *Annual Review of Astronomy and Astrophysics*, 42:603–683.
- Kravtsov, A. V. & Borgani, S. (2012). Formation of Galaxy Clusters. *Annual Review of Astronomy and Astrophysics*, 50:353–409.

- Kurk, J., Röttgering, H., Pentericci, L., & Miley, G. (2000). Deep Ly $\alpha$  Imaging of Radio Galaxy 1138-262 at redshift 2. 2. In Mazure, A., Le Fèvre, O., & Le Brun, V., editors, *Clustering at High Redshift*, volume 200 of *Astronomical Society of the Pacific Conference Series*, page 424.
- Kurk, J. D., Pentericci, L., Röttgering, H. J. A., & Miley, G. K. (2004). A search for clusters at high redshift. III. Candidate H $\alpha$  emitters and EROs in the PKS 1138-262 proto-cluster at  $z = 2.16$ . *Astronomy and Astrophysics*, 428:793–815.
- Lacki, B. C. & Thompson, T. A. (2010). The Physics of the Far-infrared-Radio Correlation. II. Synchrotron Emission as a Star Formation Tracer in High-redshift Galaxies. *Astrophysical Journal*, 717:196–208.
- Lacki, B. C., Thompson, T. A., & Quataert, E. (2010). The Physics of the Far-infrared-Radio Correlation. I. Calorimetry, Conspiracy, and Implications. *Astrophysical Journal*, 717:1–28.
- Lacy, M., Wilson, G., Masci, F., Storrie-Lombardi, L. J., Appleton, P. N., Armus, L., Chapman, S. C., Choi, P. I., Fadda, D., Fang, F., Frayer, D. T., Heinrichsen, I., Helou, G., Im, M., Laine, S., Marleau, F. R., Shupe, D. L., Soifer, B. T., Squires, G. K., Surace, J., Teplitz, H. I., & Yan, L. (2005). The Infrared Array Camera Component of the Spitzer Space Telescope Extragalactic First Look Survey. *Astrophysical Journal Supplement Series*, 161:41–52.
- Lambas, D. G., Alonso, S., Mesa, V., & O’Mill, A. L. (2012a). Galaxy interactions. I. Major and minor mergers. *Astronomy and Astrophysics*, 539:A45.
- Lambas, D. G., Alonso, S., Mesa, V., & O’Mill, A. L. (2012b). Galaxy interactions. I. Major and minor mergers. *Astronomy and Astrophysics*, 539:A45.

- Landy, S. D. & Szalay, A. S. (1993). Bias and variance of angular correlation functions. *Astrophysical Journal*, 412:64–71.
- Laor, A., Baldi, R. D., & Behar, E. (2019). What drives the radio slopes in radio-quiet quasars? *Monthly Notices of the Royal Astronomical Society*, 482(4):5513–5523.
- Larson, R. B. (2003). The physics of star formation. *Reports on Progress in Physics*, 66:1651–1697.
- Le Fevre, O., Deltorn, J. M., Crampton, D., & Dickinson, M. (1996). Clustering around the Radio Galaxy MRC 0316-257 at  $Z = 3.14$ . *Astrophysical Journal Letters*, 471:L11.
- Lilly, S. J., Le Brun, V., Maier, C., Mainieri, V., Mignoli, M., Scodreggio, M., Zamorani, G., Carollo, M., Contini, T., Kneib, J.-P., Le Fèvre, O., Renzini, A., Bardelli, S., Bolzonella, M., Bongiorno, A., Caputi, K., Coppa, G., Cucciati, O., de la Torre, S., de Ravel, L., Franzetti, P., Garilli, B., Iovino, A., Kampczyk, P., Kovac, K., Knobel, C., Lamareille, F., Le Borgne, J.-F., Pello, R., Peng, Y., Pérez-Montero, E., Ricciardelli, E., Silverman, J. D., Tanaka, M., Tasca, L., Tresse, L., Vergani, D., Zucca, E., Ilbert, O., Salvato, M., Oesch, P., Abbas, U., Bottini, D., Capak, P., Cappi, A., Cassata, P., Cimatti, A., Elvis, M., Fumana, M., Guzzo, L., Hasinger, G., Koekemoer, A., Leauthaud, A., Maccagni, D., Marinoni, C., McCracken, H., Memeo, P., Meneux, B., Porciani, C., Pozzetti, L., Sanders, D., Scaramella, R., Scarlata, C., Scoville, N., Shopbell, P., & Taniguchi, Y. (2009). The zCOSMOS 10k-Bright Spectroscopic Sample. *Astrophysical Journal Supplement Series*, 184:218–229.
- Lonsdale, C. J., Farrah, D., & Smith, H. E. (2006). *Ultraluminous Infrared Galaxies*, page 285. Springer Praxis Books.
- Lonsdale, C. J., Lacy, M., Kimball, A. E., Blain, A., Whittle, M., Wilkes, B., Stern, D., Condon, J., Kim, M., Assef, R. J., Tsai, C.-W., Efstathiou, A., Jones, S., Eisenhardt, P., Bridge, C., Wu, J., Lonsdale, C. J., Jones, K., Jarrett, T., & Smith, R.

- (2015). Radio Jet Feedback and Star Formation in Heavily Obscured, Hyperluminous Quasars at Redshifts  $\sim 0.5$ -3. I. ALMA Observations. *Astrophysical Journal*, 813:45.
- Lonsdale, C. J., Whittle, M., Trapp, A., Patil, P., Lonsdale, C. J., Thorp, R., Lacy, M., Kimball, A. E., Blain, A., Jones, S., & Kim, M. (2016). Small jets in radio-loud hot DOGs. *Astronomische Nachrichten*, 337:194.
- Lotz, J. M., Jonsson, P., Cox, T. J., & Primack, J. R. (2008). Galaxy merger morphologies and time-scales from simulations of equal-mass gas-rich disc mergers. *Monthly Notices of the Royal Astronomical Society*, 391(3):1137–1162.
- Lynden-Bell, D. (1969). Galactic Nuclei as Collapsed Old Quasars. *Nature*, 223:690–694.
- Madau, P., Ferguson, H. C., Dickinson, M. E., Giavalisco, M., Steidel, C. C., & Fruchter, A. (1996). High-redshift galaxies in the Hubble Deep Field: colour selection and star formation history to  $z \sim 4$ . *Monthly Notices of the Royal Astronomical Society*, 283:1388–1404.
- Magnelli, B., Ivison, R. J., Lutz, D., Valtchanov, I., Farrah, D., Berta, S., Bertoldi, F., Bock, J., Cooray, A., Ibar, E., Karim, A., Le Floch, E., Nordon, R., Oliver, S. J., Page, M., Popesso, P., Pozzi, F., Rigopoulou, D., Riguccini, L., Rodighiero, G., Rosario, D., Roseboom, I., Wang, L., & Wuyts, S. (2015). The far-infrared/radio correlation and radio spectral index of galaxies in the SFR- $M_*$  plane up to  $z \sim 2$ . *Astronomy and Astrophysics*, 573:A45.
- Makovoz, D. & Marleau, F. R. (2005). Point-Source Extraction with MOPEX. *Publications of the Astronomical Society of the Pacific*, 117:1113–1128.
- Mancone, C. L. & Gonzalez, A. H. (2012). EzGal: A Flexible Interface for Stellar

- Population Synthesis Models. *Publications of the Astronomical Society of the Pacific*, 124:606.
- Matthews, T. A. & Sandage, A. R. (1963). Optical Identification of 3C 48, 3C 196, and 3C 286 with Stellar Objects. *Astrophysical Journal*, 138:30.
- McMullin, J. P., Waters, B., Schiebel, D., Young, W., & Golap, K. (2007). CASA Architecture and Applications. In Shaw, R. A., Hill, F., & Bell, D. J., editors, *Astronomical Data Analysis Software and Systems XVI*, volume 376 of *Astronomical Society of the Pacific Conference Series*, page 127.
- McMurtry, C. W., Allen, T. S., Moore, A. C., Forrest, W. J., & Pipher, J. L. (2005). Characterization of 2.5 micron HgCdTe VIRGO/VISTA detector array. In Grycewicz, T. J. & Marshall, C. J., editors, *Focal Plane Arrays for Space Telescopes II*, volume 5902 of *Proceedings of SPIE*, pages 152–160.
- Messier, C. (1781). Catalogue des Nébuleuses et des Amas d'Étoiles (Catalog of Nebulae and Star Clusters). Technical report.
- Metropolis, N., Rosenbluth, A. W., Rosenbluth, M. N., Teller, A. H., & Teller, E. (1953). Equation of State Calculations by Fast Computing Machines. *The Journal of Chemical Physics*, 21:1087–1092.
- Mihos, J. C. & Hernquist, L. (1994). Ultraluminous starbursts in major mergers. *Astrophysical Journal Letters*, 431:L9–L12.
- Miley, G. K., Overzier, R. A., Zirm, A. W., Ford, H. C., Kurk, J., Pentericci, L., Blakeslee, J. P., Franx, M., Illingworth, G. D., Postman, M., Rosati, P., Röttgering, H. J. A., Venemans, B. P., & Helder, E. (2006). The Spiderweb Galaxy: A Forming Massive Cluster Galaxy at  $z \sim 2$ . *Astrophysical Journal Letters*, 650:L29–L32.

- Moore, B., Katz, N., Lake, G., Dressler, A., & Oemler, A. (1996). Galaxy harassment and the evolution of clusters of galaxies. *Nature*, 379:613–616.
- Moorwood, A., Cuby, J.-G., Biereichel, P., Brynnel, J., Delabre, B., Devillard, N., van Dijsseldonk, A., Finger, G., Gemperlein, H., Gilmozzi, R., Herlin, T., Huster, G., Knudstrup, J., Lidman, C., Lizon, J.-L., Mehrgan, H., Meyer, M., Nicolini, G., Petr, M., Spyromilio, J., & Stegmeier, J. (1998). ISAAC sees first light at the VLT. *The Messenger*, 94:7–9.
- Mortlock, D. J., Warren, S. J., Venemans, B. P., Patel, M., Hewett, P. C., McMahon, R. G., Simpson, C., Theuns, T., Gonzáles-Solares, E. A., Adamson, A., Dye, S., Hambly, N. C., Hirst, P., Irwin, M. J., Kuiper, E., Lawrence, A., & Röttgering, H. J. A. (2011). A luminous quasar at a redshift of  $z = 7.085$ . *Nature*, 474:616–619.
- Morton, D. C. & Noreau, L. (1994). A compilation of electronic transitions in the CO molecule and the interpretation of some puzzling interstellar absorption features. *Astrophysical Journal Supplement Series*, 95:301–343.
- Muldrew, S. I., Hatch, N. A., & Cooke, E. A. (2015). What are protoclusters? - Defining high-redshift galaxy clusters and protoclusters. *Monthly Notices of the Royal Astronomical Society*, 452:2528–2539.
- Murphy, E. J. (2009). The Far-Infrared-Radio Correlation at High Redshifts: Physical Considerations and Prospects for the Square Kilometer Array. *Astrophysical Journal*, 706:482–496.
- Naab, T., Johansson, P. H., & Ostriker, J. P. (2009). Minor Mergers and the Size Evolution of Elliptical Galaxies. *Astrophysical Journal Letters*, 699:L178–L182.
- Naab, T., Khochfar, S., & Burkert, A. (2006). Properties of Early-Type, Dry Galaxy

- Mergers and the Origin of Massive Elliptical Galaxies. *Astrophysical Journal Letters*, 636:L81–L84.
- Napier, P. J. (2006). *The EVLA Project: Ten Times More Capability for the VLA*, volume 356 of *Astronomical Society of the Pacific Conference Series*, page 65.
- Navarro, J. F., Frenk, C. S., & White, S. D. M. (1997). A Universal Density Profile from Hierarchical Clustering. *Astrophysical Journal*, 490:493–508.
- Navarro, J. F., Ludlow, A., Springel, V., Wang, J., Vogelsberger, M., White, S. D. M., Jenkins, A., Frenk, C. S., & Helmi, A. (2010). The diversity and similarity of simulated cold dark matter haloes. *Monthly Notices of the Royal Astronomical Society*, 402:21–34.
- Negroponte, J. & White, S. D. M. (1983). Simulations of mergers between disc-halo galaxies. *Monthly Notices of the Royal Astronomical Society*, 205:1009–1029.
- Netzer, H. (2013). *The Physics and Evolution of Active Galactic Nuclei*.
- Neugebauer, G., Habing, H. J., van Duinen, R., Aumann, H. H., Baud, B., Beichman, C. A., Beintema, D. A., Boggess, N., Clegg, P. E., de Jong, T., Emerson, J. P., Gautier, T. N., Gillett, F. C., Harris, S., Hauser, M. G., Houck, J. R., Jennings, R. E., Low, F. J., Marsden, P. L., Miley, G., Olmon, F. M., Pottasch, S. R., Raimond, E., Rowan-Robinson, M., Soifer, B. T., Walker, R. G., Wesselius, P. R., & Young, E. (1984). The Infrared Astronomical Satellite (IRAS) mission. *Astrophysical Journal Letters*, 278:L1–L6.
- Nielbock, M., Müller, T., Klaas, U., Altieri, B., Balog, Z., Billot, N., Linz, H., Okumura, K., Sánchez-Portal, M., & Sauvage, M. (2013). The Herschel PACS photometer calibration. A time dependent flux calibration for the PACS chopped point-source photometry AOT mode. *Experimental Astronomy*, 36:631–660.

- Novak, M., Smolčić, V., Delhaize, J., Delvecchio, I., Zamorani, G., Baran, N., Bondi, M., Capak, P., Carilli, C. L., Ciliegi, P., Civano, F., Ilbert, O., Karim, A., Laigle, C., Le Fèvre, O., Marchesi, S., McCracken, H., Miettinen, O., Salvato, M., Sargent, M., Schinnerer, E., & Tasca, L. (2017). The VLA-COSMOS 3 GHz Large Project: Cosmic star formation history since  $z = 5$ . *Astronomy and Astrophysics*, 602:A5.
- Nyland, K., Lacy, M., Sajina, A., Pforr, J., Farrah, D., Wilson, G., Surace, J., Häußler, B., Vaccari, M., & Jarvis, M. (2017). An Application of Multi-band Forced Photometry to One Square Degree of SERVS: Accurate Photometric Redshifts and Implications for Future Science. *Astrophysical Journal Supplement Series*, 230:9.
- O’Dea, C. P. (1998). The Compact Steep-Spectrum and Gigahertz Peaked-Spectrum Radio Sources. *Publications of the Astronomical Society of the Pacific*, 110:493–532.
- Okabe, N., Smith, G. P., Umetsu, K., Takada, M., & Futamase, T. (2013). LoCuSS: The Mass Density Profile of Massive Galaxy Clusters at  $z = 0.2$ . *Astrophysical Journal Letters*, 769:L35.
- Oliver, S., Waddington, I., Gonzalez-Solares, E., Surace, J., Fang, F., Shupe, D., Jarrett, T., Lonsdale, C., Xu, C. ., Farrah, D., Salaman, M., Rowan-Robinson, M., Siana, B., & Smith, H. E. . (2004). Angular Clustering of Galaxies at 3.6 Microns from the Spitzer Wide-area Infrared Extragalactic (SWIRE) Survey. *Astrophysical Journal Supplement Series*, 154:30–34.
- Overzier, R. A. (2016). The realm of the galaxy protoclusters. A review. *The Astronomy and Astrophysics Review*, 24:14.
- Padovani, P. & Giommi, P. (1995). The connection between x-ray- and radio-selected BL Lacertae objects. *Astrophysical Journal*, 444:567–581.

- Papovich, C. (2008). The Angular Clustering of Distant Galaxy Clusters. *Astrophysical Journal*, 676:206–217.
- Park, C. & Hwang, H. S. (2009). Interactions of Galaxies in the Galaxy Cluster Environment. *Astrophysical Journal*, 699:1595–1609.
- Peñaloza, C. H., Clark, P. C., Glover, S. C. O., Shetty, R., & Klessen, R. S. (2017). Using CO line ratios to trace the physical properties of molecular clouds. *Monthly Notices of the Royal Astronomical Society*, 465:2277–2285.
- Penney, J. I., Blain, A. W., Wylezalek, D., Hatch, N. A., Lonsdale, C., Kimball, A., Assef, R. J., Condon, J. J., Eisenhardt, P. R. M., Jones, S. F., Kim, M., Lacy, M., Muldrew, S. I., Petty, S., Sajina, A., Silva, A., Stern, D., Diaz-Santos, T., Tsai, C.-W., & Wu, J. (2019). The environments of luminous radio-WISE selected infrared galaxies. *Monthly Notices of the Royal Astronomical Society*, 483:514–528.
- Pentericci, L., Kurk, J. D., Röttgering, H. J. A., Miley, G. K., van Breugel, W., Carilli, C. L., Ford, H., Heckman, T., McCarthy, P., & Moorwood, A. (2000). A search for clusters at high redshift. II. A proto cluster around a radio galaxy at  $z=2.16$ . *Astronomy and Astrophysics*, 361:L25–L28.
- Perley, R. A., Chandler, C. J., Butler, B. J., & Wrobel, J. M. (2011). The Expanded Very Large Array: A New Telescope for New Science. *Astrophysical Journal Letters*, 739:L1.
- Peterson, B. & Wilkes, B. (2000). *Active Galaxies: Unified Model*, page 1586.
- Pilbratt, G. L., Riedinger, J. R., Passvogel, T., Crone, G., Doyle, D., Gageur, U., Heras, A. M., Jewell, C., Metcalfe, L., Ott, S., & Schmidt, M. (2010). Herschel Space Observatory. An ESA facility for far-infrared and submillimetre astronomy. *Astronomy and Astrophysics*, 518:L1.

- Poglitsch, A., Waelkens, C., Geis, N., Feuchtgruber, H., Vandenbussche, B., Rodriguez, L., Krause, O., Renotte, E., van Hoof, C., Saraceno, P., Cepa, J., Kerschbaum, F., Agnèse, P., Ali, B., Altieri, B., Andreani, P., Augueres, J.-L., Balog, Z., Barl, L., Bauer, O. H., Belbachir, N., Benedettini, M., Billot, N., Boulade, O., Bischof, H., Blommaert, J., Callut, E., Cara, C., Cerulli, R., Cesarsky, D., Contursi, A., Creten, Y., De Meester, W., Doublier, V., Doumayrou, E., Duband, L., Exter, K., Genzel, R., Gillis, J.-M., Grözinger, U., Henning, T., Herreros, J., Huygen, R., Inuscio, M., Jakob, G., Jamar, C., Jean, C., de Jong, J., Katterloher, R., Kiss, C., Klaas, U., Lemke, D., Lutz, D., Madden, S., Marquet, B., Martignac, J., Mazy, A., Merken, P., Montfort, F., Morbidelli, L., Müller, T., Nielbock, M., Okumura, K., Orfei, R., Ottensamer, R., Pezzuto, S., Popesso, P., Putzeys, J., Regibo, S., Reveret, V., Royer, P., Sauvage, M., Schreiber, J., Stegmaier, J., Schmitt, D., Schubert, J., Sturm, E., Thiel, M., Tofani, G., Vavrek, R., Wetzstein, M., Wieprecht, E., & Wiezorrek, E. (2010). The Photodetector Array Camera and Spectrometer (PACS) on the Herschel Space Observatory. *Astronomy and Astrophysics*, 518:L2.
- Polletta, M., Tajer, M., Maraschi, L., Trinchieri, G., Lonsdale, C. J., Chiappetti, L., Andreon, S., Pierre, M., Le Fèvre, O., Zamorani, G., Maccagni, D., Garcet, O., Surdej, J., Franceschini, A., Alloin, D., Shupe, D. L., Surace, J. A., Fang, F., Rowan-Robinson, M., Smith, H. E., & Tresse, L. (2007). Spectral Energy Distributions of Hard X-Ray Selected Active Galactic Nuclei in the XMM-Newton Medium Deep Survey. *Astrophysical Journal*, 663:81–102.
- Postman, M., Franx, M., Cross, N. J. G., Holden, B., Ford, H. C., Illingworth, G. D., Goto, T., Demarco, R., Rosati, P., Blakeslee, J. P., Tran, K.-V., Benítez, N., Clampin, M., Hartig, G. F., Homeier, N., Ardila, D. R., Bartko, F., Bouwens, R. J., Bradley, L. D., Broadhurst, T. J., Brown, R. A., Burrows, C. J., Cheng, E. S., Feldman, P. D., Golimowski, D. A., Gronwall, C., Infante, L., Kimble, R. A., Krist, J. E.,

- Lesser, M. P., Martel, A. R., Mei, S., Menanteau, F., Meurer, G. R., Miley, G. K., Motta, V., Sirianni, M., Sparks, W. B., Tran, H. D., Tsvetanov, Z. I., White, R. L., & Zheng, W. (2005). The Morphology-Density Relation in  $z \sim 1$  Clusters. *Astrophysical Journal*, 623:721–741.
- Pringle, J. E. & King, A. (2003). *Astrophysical Flows*.
- Richards, E. A. (2000). The Nature of Radio Emission from Distant Galaxies: The 1.4 GHz Observations. *Astrophysical Journal*, 533:611–630.
- Riechers, D. A., Hodge, J., Walter, F., Carilli, C. L., & Bertoldi, F. (2011). Extended Cold Molecular Gas Reservoirs in  $z \sim 3.4$  Submillimeter Galaxies. *Astrophysical Journal Letters*, 739:L31.
- Rieke, G. H., Alonso-Herrero, A., Weiner, B. J., Pérez-González, P. G., Blaylock, M., Donley, J. L., & Marcillac, D. (2009). DETERMINING STAR FORMATION RATES FOR INFRARED GALAXIES. *The Astrophysical Journal*, 692(1):556–573.
- Rieke, G. H., Young, E. T., Engelbracht, C. W., Kelly, D. M., Low, F. J., Haller, E. E., Beeman, J. W., Gordon, K. D., Stansberry, J. A., Misselt, K. A., Cadien, J., Morrison, J. E., Rivlis, G., Latter, W. B., Noriega-Crespo, A., Padgett, D. L., Stapelfeldt, K. R., Hines, D. C., Egami, E., Muzerolle, J., Alonso-Herrero, A., Blaylock, M., Dole, H., Hinz, J. L., Le Floch, E., Papovich, C., Pérez-González, P. G., Smith, P. S., Su, K. Y. L., Bennett, L., Frayer, D. T., Henderson, D., Lu, N., Masci, F., Pesenson, M., Rebull, L., Rho, J., Keene, J., Stolovy, S., Wachter, S., Wheaton, W., Werner, M. W., & Richards, P. L. (2004). The Multiband Imaging Photometer for Spitzer (MIPS). *Astrophysical Journal Supplement Series*, 154:25–29.
- Rigby, E. E., Hatch, N. A., Röttgering, H. J. A., Sibthorpe, B., Chiang, Y. K., Overzier, R., Herbonnet, R., Borgani, S., Clements, D. L., Dannerbauer, H., De Breuck, C., De

- Lucia, G., Kurk, J., Maschietto, F., Miley, G., Saro, A., Seymour, N., & Venemans, B. (2014). Searching for large-scale structures around high-redshift radio galaxies with Herschel. *Monthly Notices of the Royal Astronomical Society*, 437:1882–1893.
- Robertson, B., Bullock, J. S., Cox, T. J., Di Matteo, T., Hernquist, L., Springel, V., & Yoshida, N. (2006). A Merger-driven Scenario for Cosmological Disk Galaxy Formation. *Astrophysical Journal*, 645:986–1000.
- Salpeter, E. E. (1964). Accretion of Interstellar Matter by Massive Objects. *Astrophysical Journal*, 140:796–800.
- Sambruna, R. M. (1997). Soft X-Ray Properties of Flat-Spectrum Radio Quasars. *Astrophysical Journal*, 487:536–554.
- Sanders, D. B. & Mirabel, I. F. (1996). Luminous Infrared Galaxies. *Annual Review of Astronomy and Astrophysics*, 34:749.
- Sanders, D. B., Soifer, B. T., Elias, J. H., Madore, B. F., Matthews, K., Neugebauer, G., & Scoville, N. Z. (1988a). Ultraluminous infrared galaxies and the origin of quasars. *Astrophysical Journal*, 325:74–91.
- Sanders, D. B., Soifer, B. T., Elias, J. H., Neugebauer, G., & Matthews, K. (1988b). Warm ultraluminous galaxies in the IRAS survey - The transition from galaxy to quasar? *Astrophysical Journal Letters*, 328:L35–L39.
- Sarazin, C. L., Irwin, J. A., & Bregman, J. N. (2001). Chandra X-Ray Observations of the X-Ray Faint Elliptical Galaxy NGC 4697. *Astrophysical Journal*, 556:533–555.
- Sarazin, C. L. & Kempner, J. C. (2000). Nonthermal Bremsstrahlung and Hard X-Ray Emission from Clusters of Galaxies. *Astrophysical Journal*, 533:73–83.
- Sawicki, M. (2002). The 1.6 Micron Bump as a Photometric Redshift Indicator. *Astronomical Journal*, 124:3050–3060.

- Schleicher, D. R. G. & Beck, R. (2013). A new interpretation of the far-infrared - radio correlation and the expected breakdown at high redshift. *Astronomy and Astrophysics*, 556:A142.
- Schmidt, M. (1963). 3C 273 : A Star-Like Object with Large Red-Shift. *Nature*, 197:1040.
- Schober, J., Schleicher, D. R. G., & Klessen, R. S. (2016). Galactic Synchrotron Emission and the Far-infrared-Radio Correlation at High Redshift. *Astrophysical Journal*, 827:109.
- Schweizer, F. (1982). Colliding and merging galaxies. I - Evidence for the recent merging of two disk galaxies in NGC 7252. *Astrophysical Journal*, 252:455–460.
- Schweizer, F. & Seitzer, P. (1998). Ages and Metallicities of Young Globular Clusters in the Merger Remnant NGC 7252. *Astronomical Journal*, 116:2206–2219.
- Scoville, N., Capak, P., Giavalisco, M., Sanders, D., Yan, L., Aussel, H., Ilbert, O., Salvato, M., Mobasher, B., & Le Floch, E. (2007). IRAC Deep Survey Of COSMOS. In Storrie-Lombardi, L. J. & Silbermann, N. A., editors, *The Science Opportunities of the Warm Spitzer Mission Workshop*, volume 943 of *American Institute of Physics Conference Series*, pages 221–228.
- Seyfert, C. K. (1943). Nuclear Emission in Spiral Nebulae. *Astrophysical Journal*, 97:28.
- Sharon, C. E., Riechers, D. A., Hodge, J., Carilli, C. L., Walter, F., Weiß, A., Knudsen, K. K., & Wagg, J. (2016). A Total Molecular Gas Mass Census in  $z \sim 2-3$  Star-forming Galaxies: Low-J CO Excitation Probes of Galaxies' Evolutionary States. *Astrophysical Journal*, 827:18.
- Shu, X. W., Elbaz, D., Bourne, N., Schreiber, C., Wang, T., Dunlop, J. S., Fontana, A., Leiton, R., Pannella, M., Okumura, K., Michałowski, M. J., Santini, P., Merlin,

- E., Buitrago, F., Bruce, V. A., Amorin, R., Castellano, M., Derriere, S., Comastri, A., Cappelluti, N., Wang, J. X., & Ferguson, H. C. (2016). Identification of  $z \gtrsim 2$  Herschel 500  $\mu\text{M}$  Sources Using Color Deconfusion. *Astrophysical Journal Supplement Series*, 222:4.
- Silva, A., Sajina, A., Lonsdale, C., & Lacy, M. (2015). ALMA Detected Overdensity of Sub-millimeter Sources Around WISE/NVSS-selected  $z \sim 2$  Dusty Quasars. *Astrophysical Journal Letters*, 806:L25.
- Silverman, J. D., Green, P. J., Barkhouse, W. A., Kim, D.-W., Kim, M., Wilkes, B. J., Cameron, R. A., Hasinger, G., Jannuzi, B. T., Smith, M. G., Smith, P. S., & Tananbaum, H. (2008). The Luminosity Function of X-Ray-selected Active Galactic Nuclei: Evolution of Supermassive Black Holes at High Redshift. *Astrophysical Journal*, 679:118–139.
- Simpson, C. & Eisenhardt, P. (1999). The Detection and Photometric Redshift Determination of Distant Galaxies Using SIRTf’s Infrared Array Camera. *Publications of the Astronomical Society of the Pacific*, 111:691–701.
- Sklias, P., Zamojski, M., Schaerer, D., Dessauges-Zavadsky, M., Egami, E., Rex, M., Rawle, T., Richard, J., Boone, F., Simpson, J. M., Smail, I., van der Werf, P., Altieri, B., & Kneib, J. P. (2014). Star formation histories, extinction, and dust properties of strongly lensed  $z \sim 1.5 - 3$  star-forming galaxies from the Herschel Lensing Survey. *Astronomy and Astrophysics*, 561:A149.
- Slipher, V. M. (1917). The spectrum and velocity of the nebula N.G.C. 1068 ( M 77). *Lowell Observatory Bulletin*, 3:59–62.
- Smith, E. P., Heckman, T. M., Bothun, G. D., Romanishin, W., & Balick, B. (1986). On the nature of QSO host galaxies. *Astrophysical Journal*, 306:64–89.

- Smith, G. P., Kneib, J.-P., Smail, I., Mazzotta, P., Ebeling, H., & Czoske, O. (2005). A Hubble Space Telescope lensing survey of X-ray luminous galaxy clusters - IV. Mass, structure and thermodynamics of cluster cores at  $z=0.2$ . *Monthly Notices of the Royal Astronomical Society*, 359:417–446.
- Solomon, P. M., Downes, D., Radford, S. J. E., & Barrett, J. W. (1997). The Molecular Interstellar Medium in Ultraluminous Infrared Galaxies. *Astrophysical Journal*, 478:144–161.
- Somerville, R. S., Primack, J. R., & Faber, S. M. (2001). The nature of high-redshift galaxies. *Monthly Notices of the Royal Astronomical Society*, 320:504–528.
- Springel, V. & Hernquist, L. (2005). Formation of a Spiral Galaxy in a Major Merger. *Astrophysical Journal Letters*, 622:L9–L12.
- Steidel, C. C., Adelberger, K. L., Dickinson, M., Giavalisco, M., Pettini, M., & Kellogg, M. (1998). A Large Structure of Galaxies at Redshift  $Z$  approximately 3 and Its Cosmological Implications. *Astrophysical Journal*, 492:428–438.
- Steidel, C. C., Adelberger, K. L., Shapley, A. E., Erb, D. K., Reddy, N. A., & Pettini, M. (2005). Spectroscopic Identification of a Protocluster at  $z=2.300$ : Environmental Dependence of Galaxy Properties at High Redshift. *Astrophysical Journal*, 626:44–50.
- Stern, D., Assef, R. J., Benford, D. J., Blain, A., Cutri, R., Dey, A., Eisenhardt, P., Griffith, R. L., Jarrett, T. H., Lake, S., Masci, F., Petty, S., Stanford, S. A., Tsai, C.-W., Wright, E. L., Yan, L., Harrison, F., & Madsen, K. (2012). Mid-infrared Selection of Active Galactic Nuclei with the Wide-Field Infrared Survey Explorer. I. Characterizing WISE-selected Active Galactic Nuclei in COSMOS. *Astrophysical Journal*, 753:30.

- Stern, D., Eisenhardt, P., Gorjian, V., Kochanek, C. S., Caldwell, N., Eisenstein, D., Brodwin, M., Brown, M. J. I., Cool, R., Dey, A., Green, P., Jannuzi, B. T., Murray, S. S., Pahre, M. A., & Willner, S. P. (2005). Mid-Infrared Selection of Active Galaxies. *Astrophysical Journal*, 631:163–168.
- Stern, D., Holden, B., Stanford, S. A., & Spinrad, H. (2003). Confirmation of a Radio-selected Galaxy Overdensity at  $z=1.11$ . *Astronomical Journal*, 125:2759–2768.
- Stevens, J. A., Ivison, R. J., Dunlop, J. S., Smail, I. R., Percival, W. J., Hughes, D. H., Röttgering, H. J. A., van Breugel, W. J. M., & Reuland, M. (2003). The formation of cluster elliptical galaxies as revealed by extensive star formation. *Nature*, 425:264–267.
- Sunyaev, R. A. & Zeldovich, Y. B. (1972). The Observations of Relic Radiation as a Test of the Nature of X-Ray Radiation from the Clusters of Galaxies. *Comments on Astrophysics and Space Physics*, 4:173.
- Tacconi, L. J., Genzel, R., Smail, I., Neri, R., Chapman, S. C., Ivison, R. J., Blain, A., Cox, P., Omont, A., Bertoldi, F., Greve, T., Förster Schreiber, N. M., Genel, S., Lutz, D., Swinbank, A. M., Shapley, A. E., Erb, D. K., Cimatti, A., Daddi, E., & Baker, A. J. (2008). Submillimeter Galaxies at  $z \sim 2$ : Evidence for Major Mergers and Constraints on Lifetimes, IMF, and CO-H<sub>2</sub> Conversion Factor. *Astrophysical Journal*, 680:246–262.
- Takizawa, M. (2002). Evolution of Hard X-Ray Radiation from Clusters of Galaxies: Bremsstrahlung or Inverse Compton Scattering? *Publications of the Astronomical Society of Japan*, 54:363–371.
- Taylor, M. B. (2005). TOPCAT & STIL: Starlink Table/VOTable Processing Software. In Shopbell, P., Britton, M., & Ebert, R., editors, *Astronomical Data Analysis Soft-*

*ware and Systems XIV*, volume 347 of *Astronomical Society of the Pacific Conference Series*, page 29.

- Thomson, A. P., Ivison, R. J., Simpson, J. M., Swinbank, A. M., Smail, I., Arumugam, V., Alexander, D. M., Beelen, A., Brandt, W. N., Chandra, I., Dannerbauer, H., Greve, T. R., Hodge, J. A., Ibar, E., Karim, A., Murphy, E. J., Schinnerer, E., Sirothia, S., Walter, F., Wardlow, J. L., & van der Werf, P. (2014). An ALMA survey of submillimetre galaxies in the Extended Chandra Deep Field South: radio properties and the far-infrared/radio correlation. *Monthly Notices of the Royal Astronomical Society*, 442:577–588.
- Thomson, A. P., Ivison, R. J., Smail, I., Swinbank, A. M., Weiss, A., Kneib, J.-P., Papadopoulos, P. P., Baker, A. J., Sharon, C. E., & van Moorsel, G. A. (2012). VLA imaging of  $^{12}\text{CO}$   $J = 1-0$  and free-free emission in lensed submillimetre galaxies. *Monthly Notices of the Royal Astronomical Society*, 425:2203–2211.
- Toomre, A. (1977). Theories of spiral structure. *Annual Review of Astronomy and Astrophysics*, 15:437–478.
- Toomre, A. & Toomre, J. (1972). Galactic Bridges and Tails. *Astrophysical Journal*, 178:623–666.
- Trenti, M. & Stiavelli, M. (2008). Cosmic Variance and Its Effect on the Luminosity Function Determination in Deep High-z Surveys. *Astrophysical Journal*, 676:767–780.
- Treu, T., Ellis, R. S., Kneib, J.-P., Dressler, A., Smail, I., Czoske, O., Oemler, A., & Natarajan, P. (2003). A Wide-Field Hubble Space Telescope Study of the Cluster Cl 0024+16 at  $z = 0.4$ . I. Morphological Distributions to 5 Mpc Radius. *Astrophysical Journal*, 591:53–78.

- Tsai, C.-W., Eisenhardt, P. R. M., Wu, J., Stern, D., Assef, R. J., Blain, A. W., Bridge, C. R., Benford, D. J., Cutri, R. M., Griffith, R. L., Jarrett, T. H., Lonsdale, C. J., Masci, F. J., Moustakas, L. A., Petty, S. M., Sayers, J., Stanford, S. A., Wright, E. L., Yan, L., Leisawitz, D. T., Liu, F., Mainzer, A. K., McLean, I. S., Padgett, D. L., Skrutskie, M. F., Gelino, C. R., Beichman, C. A., & Juneau, S. (2015). The Most Luminous Galaxies Discovered by WISE. *Astrophysical Journal*, 805:90.
- Urry, C. M. & Padovani, P. (1995). Unified Schemes for Radio-Loud Active Galactic Nuclei. *Publications of the Astronomical Society of the Pacific*, 107:803.
- van der Kruit, P. C. (1971). Observations of core sources in Seyfert and normal galaxies with the Westerbork synthesis radio telescope at 1415 MHz. *Astronomy and Astrophysics*, 15:110–122.
- van Dokkum, P. G. (2005). The Recent and Continuing Assembly of Field Elliptical Galaxies by Red Mergers. *Astronomical Journal*, 130:2647–2665.
- van Dokkum, P. G. & van der Marel, R. P. (2007). The Star Formation Epoch of the Most Massive Early-Type Galaxies. *Astrophysical Journal*, 655:30–50.
- Vanderplas, J., Connolly, A., Ivezić, Ž., & Gray, A. (2012). Introduction to astroml: Machine learning for astrophysics. In *Conference on Intelligent Data Understanding (CIDU)*, pages 47–54.
- Veilleux, S., Cecil, G., & Bland-Hawthorn, J. (2005). Galactic Winds. *Annual Review of Astronomy and Astrophysics*, 43:769–826.
- Venemans, B. P., Röttgering, H. J. A., Miley, G. K., van Breugel, W. J. M., de Breuck, C., Kurk, J. D., Pentericci, L., Stanford, S. A., Overzier, R. A., Croft, S., & Ford, H. (2007). Protoclusters associated with  $z > 2$  radio galaxies . I. Characteristics of high redshift protoclusters. *Astronomy and Astrophysics*, 461:823–845.

- Vito, F., Brandt, W. N., Stern, D., Assef, R. J., Chen, C.-T. J., Brightman, M., Comastri, A., Eisenhardt, P., Garmire, G. P., Hickox, R., Lansbury, G., Tsai, C.-W., Walton, D. J., & Wu, J. W. (2018). Heavy X-ray obscuration in the most luminous galaxies discovered by WISE. *Monthly Notices of the Royal Astronomical Society*, 474:4528–4540.
- Waddington, I., Oliver, S. J., Babbedge, T. S. R., Fang, F., Farrah, D., Franceschini, A., Gonzalez-Solares, E. A., Lonsdale, C. J., Rodighiero, G., Rowan-Robinson, M., Shupe, D. L., Surace, J. A., Vaccari, M., & Xu, C. K. (2007). Clustering of galaxies at 3.6  $\mu\text{m}$  in the Spitzer Wide-area Infrared Extragalactic legacy survey. *Monthly Notices of the Royal Astronomical Society*, 381:1437–1449.
- White, R. L., Becker, R. H., Helfand, D. J., & Gregg, M. D. (1997). A Catalog of 1.4 GHz Radio Sources from the FIRST Survey. *Astrophysical Journal*, 475:479–493.
- White, S. D. M. & Rees, M. J. (1978). Core condensation in heavy halos - A two-stage theory for galaxy formation and clustering. *Monthly Notices of the Royal Astronomical Society*, 183:341–358.
- Williams, C. C., Giavalisco, M., Porciani, C., Yun, M. S., Pope, A., Scott, K. S., Austermann, J. E., Aretxaga, I., Hatsukade, B., Lee, K.-S., Wilson, G. W., Cybulski, R., Hughes, D. H., Kawabe, R., Kohno, K., Perera, T., & Schloerb, F. P. (2011). On the Clustering of Submillimeter Galaxies. *Astrophysical Journal*, 733:92.
- Willott, C. J., Rawlings, S., & Blundell, K. M. (2001). Extremely red galaxy counterparts to 7C radio sources. *Monthly Notices of the Royal Astronomical Society*, 324:1–17.
- Wooten, A. & Thompson, A. R. (2009). The Atacama Large Millimeter/Submillimeter Array. *IEEE Proceedings*, 97:1463–1471.

- Wright, E. L., Eisenhardt, P. R. M., Mainzer, A. K., Ressler, M. E., Cutri, R. M., Jarrett, T., Kirkpatrick, J. D., Padgett, D., McMillan, R. S., Skrutskie, M., Stanford, S. A., Cohen, M., Walker, R. G., Mather, J. C., Leisawitz, D., Gautier, III, T. N., McLean, I., Benford, D., Lonsdale, C. J., Blain, A., Mendez, B., Irace, W. R., Duval, V., Liu, F., Royer, D., Heinrichsen, I., Howard, J., Shannon, M., Kendall, M., Walsh, A. L., Larsen, M., Cardon, J. G., Schick, S., Schwalm, M., Abid, M., Fabinsky, B., Naes, L., & Tsai, C.-W. (2010). The Wide-field Infrared Survey Explorer (WISE): Mission Description and Initial On-orbit Performance. *Astronomical Journal*, 140:1868–1881.
- Wu, J., Bussmann, R. S., Tsai, C.-W., Petric, A., Blain, A., Eisenhardt, P. R. M., Bridge, C. R., Benford, D. J., Stern, D., Assef, R. J., Gelino, C. R., Moustakas, L., & Wright, E. L. (2014). Interferometric Follow-up of WISE Hyper-luminous Hot, Dust-obscured Galaxies. *Astrophysical Journal*, 793:8.
- Wu, J., Tsai, C.-W., Sayers, J., Benford, D., Bridge, C., Blain, A., Eisenhardt, P. R. M., Stern, D., Petty, S., Assef, R., Bussmann, S., Comerford, J. M., Cutri, R., Evans, II, N. J., Griffith, R., Jarrett, T., Lake, S., Lonsdale, C., Rho, J., Stanford, S. A., Weiner, B., Wright, E. L., & Yan, L. (2012). Submillimeter Follow-up of WISE-selected Hyperluminous Galaxies. *Astrophysical Journal*, 756:96.
- Wylezalek, D., Galametz, A., Stern, D., Vernet, J., De Breuck, C., Seymour, N., Brodwin, M., Eisenhardt, P. R. M., Gonzalez, A. H., Hatch, N., Jarvis, M., Rettura, A., Stanford, S. A., & Stevens, J. A. (2013). Galaxy Clusters around Radio-loud Active Galactic Nuclei at  $1.3 < z < 3.2$  as Seen by Spitzer. *Astrophysical Journal*, 769:79.
- Wylezalek, D., Vernet, J., De Breuck, C., Stern, D., Brodwin, M., Galametz, A., Gonzalez, A. H., Jarvis, M., Hatch, N., Seymour, N., & Stanford, S. A. (2014). The

## BIBLIOGRAPHY

---

Galaxy Cluster Mid-infrared Luminosity Function at  $1.3 < z < 3.2$ . *Astrophysical Journal*, 786:17.

Yun, M. S., Reddy, N. A., & Condon, J. J. (2001). Radio Properties of Infrared-selected Galaxies in the IRAS 2 Jy Sample. *Astrophysical Journal*, 554:803–822.

Zwicky, F. (1933). On a New Type of Reasoning and Some of Its Possible Consequences. *Physical Review*, 43:1031–1033.